NORTHWESTERN UNIVERSITY

Harnessing Molecular Precision Through DNA Dendrons for Therapeutics and Materials Design

A DISSERTATION

SUBMITTED TO THE GRADUATE SCHOOL
IN PARTIAL FULFILLMENT OF THE REQUIREMENTS

for the degree

DOCTOR OF PHILOSOPHY

Field of Chemistry

By

Max Everett Distler

EVANSTON, ILLINOIS

December 2022

ABSTRACT

Harnessing Molecular Precision Through DNA Dendrons in Therapeutics and Materials Design

Max Everett Distler

DNA is extremely versatile and powerful, both as a construct in biological applications and as a ligand in materials design due to the fact that its recognition properties can be programmed through sequence and length. Spherical nucleic acids (SNAs), nanoparticles surrounded by a dense shell of DNA or RNA, are a privileged class of structures that have found widespread use in therapeutics, diagnostics, polymer synthesis, and colloidal crystal engineering. These materials, however, are typically limited to isotropic and heterogeneous DNA ligand presentation. Therefore, although SNAs have highlighted the importance of nucleic acid architecture on corresponding properties, it is impossible to use them to probe such relationships at the molecular level.

Herein, this thesis describes methods for programming DNA ligand architecture with molecular precision and investigates how this control enables new capabilities in both therapeutics and materials design. Chapter one introduces the role of DNA in nanochemistry, the properties of DNA architectures that have led to significant scientific advances, and the current limitations in controlling DNA presentation at the nanoscale. Chapter two describes the synthesis of a molecularly well-defined DNA dendron and establishes a foundational understanding of how the dendron structure dictates its biological properties. Chapter three investigates the structure-function relationships that impact DNA dendron vaccine function in a molecularly defined manner. In chapter four, the knowledge learned in the previous chapter is used to explore the structure-function relationships of antiviral SNA vaccines in the context of SARS-CoV-2 in humanized mice. Chapter five investigates how DNA dendrons can be utilized in colloidal crystal engineering as foundational building blocks. Specifically, DNA dendrimers of different sizes and valencies are

explored as structure-directing agents. Chapter six, investigates a new approach to DNA dendrimer synthesis that enables the encoding of anisotropic orthogonal interactions, allowing for unique structural control over colloidal alloys. Finally, chapter seven provides a summary of the key conclusions drawn and the lessons learned through this research as well as an overview of important future directions. Collectively, these chapters explore how control over DNA architecture at the molecular level can lead to novel and advanced capabilities in the fields of therapeutics and materials design. In biology, it has expanded the foundational understanding of multivalent DNA architectures, while introducing a molecularly defined approach to therapeutics design. In materials, it has led to key insights as to how DNA ligand architecture can be a tool to guide NP assembly, thereby introducing novel structural programmability for the design of modern materials.

ACKNOWLEDGMENTS

I am most fortunate to have a plethora of people to acknowledge so I ask for your indulgence.

During the past four years, my growth as a scientist and as a person would not have been possible without the support, mentorship, and collaboration of faculty, mentors, colleagues, friends, and family, as well as the resources made available by Northwestern University and the International Institute for Nanotechnology. Professor Chad Mirkin fosters a rich learning environment, where one is surrounded by a community of scientists who are all working to answer important and interesting scientific questions. His mentorship has guided my growth as a scientist, mentor, and leader, and I am so grateful for his steadfast support and his constant challenging of me to be a better scientist. I will incorporate his wisdom and advice in all of my future endeavors. Professors Nathan Gianneschi and Joseph Hupp both served as members of my committee and have been incredible resources throughout my time here, providing invaluable scientific advice that has guided me to ask more meaningful scientific questions. Professor Milan Mrksich served as the chair of my qualifying exam committee, and I thank him for the great questions and feedback he provided at that stage of my PhD.

I was fortunate to begin my PhD under the mentorship of Professor Katherine Bujold. She immersed me in the world of scientific research and taught by example, how to be a meticulous scientist and a kind lab mate. Her approach to science and lab management remains the model for how I conduct my lab work. Upon starting my graduate work, Dr. Oliver Hayes quickly became one of my closest mentors and friends. From him I learned what being a scientist is about: the constant drive to learn, understand, explain, and manipulate the world around us. His curiosity and kindness were infectious and have had a direct impact on my growth as a scientist, a leader, a mentor, and a friend. His approach to life is something I embrace every day.

During my graduate career, I had the distinct pleasure of learning from and working with Professor Benjamin Partridge. In addition to his unbridled willingness to help and teach laboratory and writing skills, he is a very close friend. Our friendship has kept me sane and motivated through the hard times and helped me celebrate the good times. I know he will be an incredible professor. Professor Michelle Teplensky also played a key role in my development as a scientist and as a person. Her immense knowledge of biology and immunology was vital to the success of my projects (as well as those of many others). I tried to learn as much from her as possible, and her future students are fortunate for the wealth of information she will provide. In addition to being a remarkable scientist, Michelle is an amazing person and friend. I also thank Dr. Edmund Cheng. They say that you become more like the people you work with. That was my hope when I started working with Edmund. He is an incredible role model, and his approach to science is something I try to apply in the lab every day.

I learned much from collaborating with experts on various projects. Dr. Byeongdu Lee and Eric Wayne Roth provided valuable insights and technical skills that enabled several projects to move from conception to completion. I am extremely grateful to have had the opportunity to learn from and work with them.

Throughout my graduate studies, I had the distinct honor of mentoring talented young scientists: Catherine Davidson, Kathleen Ngo, and John Cavaliere. These gifted graduate students have taught me more than I could have ever taught them. I want to thank them for always coming to lab with a positive attitude and great questions. I cannot wait to witness the incredible scientists they will become. The Mirkin group is filled with kind and supportive people that are always ready to offer guidance and insight. I give special thanks to Dr. Caroline Kusmierz, Ben Coleman, David Xu, Katie Landy, Michael Evangelopoulos, Namrata Ramani, Dr. Peter Winegar, Dr. Wenjie Zhou, Yuanwei Li, Zhenyu Henry Han, Dr. Yuwei Gu, Dr. Kyle Gibson, and Dr. Sergej Kudruk for their support, friendship, and positivity throughout. I also acknowledge the incredible team of research and office staff that Chad has assembled, who keep the lab running day in and day out: Dr. Tanushri Sengupta, Dr. Sarah Petrosko, Dr. Jenny Orbeck, Pam Watson, Bethany Hexom, Dr. Sara Rupich, and Elizabeth Forest. This group has answered questions, provided advice, and ensured my success as a graduate student. I would not be at this point without their help and guidance. Every project presented in this thesis required a vast amount of oligonucleotides that were synthesized, in part, by our DNA technicians, Vinzenz Mayer, Jennifer Delgado, Matt Capek, and Robert Stawicki. I thank them all.

I have had an incredible support system outside of the lab, comprised of friends who have become family over the years. Thank you to Spencer Tang, Benjamin Galinski, Aaron Stone, Lauren Conte, Tatum LeClair, Rachel Alpert, Corinne Noonan, and Taylor Forman for providing laughs, love, and encouragement throughout even the most challenging times over the past four years. I also wish to thank Elizabeth Zushma, my high school chemistry teacher, for her constant support and unwavering belief in me.

Finally, I give my deepest thanks to my parents, Michael and Linda Distler, and my sister, Amanda Distler, who have been my foundation throughout this entire journey. They have consistently supported me throughout my life and inspired me to pursue passions, embrace challenges and failures, and respect everyone.

PREFACE

This dissertation is submitted for the degree of Doctor of Philosophy at Northwestern University. The research reported herein was conducted under the supervision of Professor Chad A. Mirkin in the Department of Chemistry, between November 2018 and August 2022. The following work is original.

This work was or will be presented in:

Distler, M. E.; Teplensky, M. H.; Bujold, K. E.; Kusmierz, C. D.; Evangelopoulos, M.; Mirkin, C. A., DNA Dendrons as Agents for Intracellular Delivery. J. *Am. Chem. Soc*. 2021, 143, 13513-13518.

Distler, M. E.; Cavaliere, J.; Teplensky, M. H.; Evangelopoulos, M.; Mirkin, C. A., DNA Dendron-Based Molecular Vaccines. 2022, *Submitted.*

Teplensky, M. H.*; Distler, M. E.*; Kusmierz, C. D.; Evangelopoulos, M.; Gula, H.; Elli, D.; Tomatsidou, A.; Nicolaescu, V.; Gelarden, I.; Yeldandi, A.; Batlle, D.; Missiakas, D.; Mirkin, C. A., Spherical nucleic acids as an infectious disease vaccine platform. *Proc. Natl. Acad. Sci.* 2022, 119, e2119093119.

Cheng, H. F.*; Distler, M. E.*; Lee, B.; Zhou, W.; Weigand, S.; Mirkin, C. A., Nanoparticle Superlattices through Template-Encoded DNA Dendrimers. *J. Am. Chem. Soc*. 2021, 143, 17170-17179.

Distler, M. E.; Landy, K. M.; Gibson, K. J.; Lee, B.; Weigand, S.; Mirkin, C. A., Symmetry-Breaking Dendrimer Synthons in Colloidal Crystal Engineering with DNA 2022, *Submitted.*

*Equal Author Contribution

LIST OF ABBREVIATIONS

1D	One dimensional
2D	Two dimensional
3D	Three dimensional
2WJ	Two-way junction
3WJ	Three-way junction
3BD	3 branched dendron
6BD	6 branched dendron
9BD	9 branched dendron
A	Adenine
ACE2	Angiotensin-converting enzyme 2
Au	Gold
BMDC	Bone marrow-derived dendritic cell
bp	Base pair
C	Cytosine
CCM	Complementary contact model
CD (11,27,80,86)	Cluster of differentiation
CMC	Critical micelle concentration
CPG	Controlled pore glass
CpG	cytosine-phosphate-guanine
CPP	Cell penetrating peptide
Cy3	Cyanine-3
DBCO	Dibenzocyclooctyne
DC	Dendritic Cell
D*h*	Hydrodynamic diameter
DJ PAE	DNA junction programmable atom equivalent
DLS	Dynamic light scattering
DNA	Deoxyribonucleic Acids
DOPC	1,2-Dioleoyl-sn-glycero-3-phosphocholine
dsDNA	double stranded DNA
EDS	Energy-dispersive X-ray spectroscopy
EE	Electron equivalents
ELISA	Enzyme-linked immunosorbent assay
FCC	Face centered cubic
FK	Frank-Kasper
G	Guanine
GT	Graphite-type
HPLC	High-performance liquid chromatography
HPV	Human papillomavirus
Ig	Immunoglobulin
IgG	Immunoglobulin-G

IL-6	Interleukin-6
IVIS	*In vivo* imaging system
MALDI-TOF MS	Matrix assisted laser desorption/ionization time-of-flight mass spectrometry
MFI	Median fluorescence intensity
MHC	Major histocompatibility complex
NP	Nanoparticle
Ova	Ovalbumin 1 peptide
PAE	Programmable atom equivalent
PAGE	Polyacrylamide gel electrophoresis
PAMAM	Poly(amidoamine)
PEG	Polyethylene glycol
PO	Phosphate backbone
PS	Phoshorothioate backbone
RBD	Receptor binding domain
RNA	Ribonucleic acid
SAXS	Small angle X-ray scattering
SC	Simple cubic
SDS	Sodium dodecyl sulfate
SH	Simple hexagonal
Si2Sr	Strontium disilicide
siRNA	Small interfering RNA
SNA	Spherical nucleic acid
SPDP	succinimidyl 3-(2-pyridyldithio)propionate
STEM	Scanning transmission electron microscopy
sVNT	Surrogate virus neutralizing test
T	Thymine
Ta1	Thyomosin-alpha-2 peptide
TFF	Tangential flow filtrations
Ti5Ga4	Titanium5Gallium4
TLR-9	Toll like receptor-9
Tm	Melting temperature
TMSD	Toehold mediated strand displacement
TNF-alpha	Tumor necrosis factor - alpha
UV-vis	Ultraviolet-visible light
VSEPR	Valence shell electron pair repulsion

DEDICATION

This thesis is dedicated to my grandparents: Edgar and Mildred Distler and Leonard and Ruth Kahn, who inspired me to pursue my passions and to live life like someone left the gate open.

TABLE OF CONTENTS

Nanoparticle Superlattices Through Template-Encoded DNA Dendrimers

Symmetry-Breaking DNA Dendrimer Synthons in Colloidal Crystal Engineering with DNA

LIST OF FIGURES

LIST OF TABLES

CHAPTER ONE

Directing Nanoparticle Interactions with Their Environments

1.1. The Role of Ligands in Nanochemistry

1.1.1. Guiding Nanoparticle Properties Using Ligands

At the nanoscale, materials have properties that are vastly different from their bulk counterparts. This is best exemplified with elemental Gold (Au). Bulk Au is considered chemically inert, incapable of performing chemical reactions and stable for significant periods of time. However, Au nanoparticles (NPs) display much more interesting properties, such as unique optical and catalytic capabilities.[20-23] Furthermore, by tuning the size and shape of Au NPs, these properties can be altered, for example by changing the wavelength of light with which such particles interact and changing the selectivity of their catalytic reactions.[24-27] However, often overlooked is the role that ligands play in determining NP properties.

Ligands, for the purpose of this work, are defined as molecules that adhere and coat the surface of all NPs and determine NP properties throughout synthesis and application.[5, 28-29] During synthesis, their main function is to stabilize nanoparticle surfaces, which they do in a variety of ways. Most commonly, ligands provide stability through electrostatic or steric effects (**Figure 1.1. A)**.[28, 30] In brief, by using charged ligands, NPs retain their colloidal stability due to repulsive forces and, by using ligands that occupy a significant amount of space, steric effects inhibit aggregation.[5, 28-29] Furthermore, these surface ligands can impact the pH, the growth mechanism, and the rate of reduction, all of which directly impact the size and shape of the resultant nanoparticles (**Figure 1.1. B**).[31-36] Ligands are thus a vital component in determining individual NP properties during synthesis.

Once the NPs are synthesized, the ligands continue to be stabilizing agents for the colloidal NPs, but they also act as the main communicators between the NPs and their surrounding environments.[5, 28-29] Importantly, ligands can be exchanged post synthesis enabling the NP properties to be modified by changing the attached ligand.[37-44] At this stage, the ligands dictate the types of solvents in which the NPs are stable, as well as, how the NPs interact with each other and with other species (**Figure 1.1. C,D**).[5, 28-29] This will prove particularly important when interfacing nanoparticles with different materials (v*ide infra*).

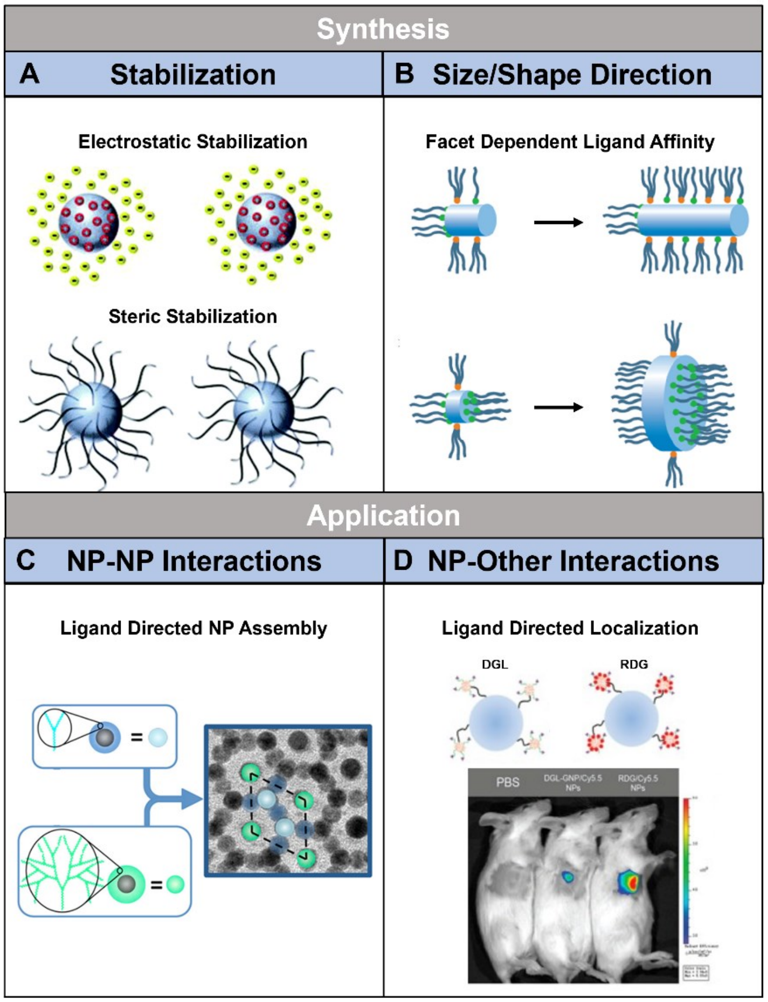

Figure 1.1. Ligands dictate nanoparticle properties during synthesis and applications
(A) During synthesis, ligands provide colloidal stability of the NPs, typically through electrostatic interactions or steric hinderance. Adapted from ref. [5]. (B) Ligands can be applied as size and shape directing agents, due to selective affinity for specific NP facets. Adapted from ref. [15]. (C,D) Ligands dictate how NPs interact with other NPs and their environment. Ligand structure can tune assembly outcomes and biological localization. Adapted from ref. [10, 16].

1.1.2. The Importance of Ligands in Biological Settings

Ligand coatings on NPs have long been known to direct NP properties in biological settings (*e.g.,* pharmacokinetics, therapeutic efficacy, and toxicity).[45-47] Ligands, such as polymers, carbohydrates, peptides, and proteins, have been used to increase NP stability and enhance NP function.[29] Specifically, depending on the selected ligand, circulation time[48], cellular localization[49-50], organismal localization[51-53], and resistance to degradation[48, 54] can all be tuned. Ligands are typically selected based on the desired properties but can be classified into two types: those that improve NP circulation and stability, and those that improve NP function.

One of the most commonly used ligands for circulation and stability, both in research and in the clinic, is the polymer, polyethylene glycol (PEG).[55] Due to its biocompatibility, solubility in aqueous and many organic solvents, and its ability to stabilize NPs from aggregation, it has been widely adopted for use in coating inorganic NPs and proteins that interface with biology.[29] The PEG coating prevents proteins from interacting with the NP cores, decreasing the rate of core degradation and increasing its circulation time in serum (**Figure 1.2. A**).[56-61] Despite its widespread use, however, PEG has shortcomings. Specifically, while PEG prevents degradative proteins from breaking down the NP cores, it also prevents other protein interactions, inhibiting cellular uptake of the NPs. Furthermore, it has been demonstrated that over time, the body is able to produce an immune response against PEG, limiting its use in long-term treatments.[62-65]

The second category of ligands used in biological systems is selected due to the ability to improve NP function or introduce new functionalities. These ligands usually take the form of biomolecules that are known to interact with naturally occurring proteins, such as peptides, proteins, and carbohydrates.[29] The interactions can be leveraged to drive organismal and cellular localization, uptake, and function.[29] One of the most well-known examples of this ligand type is the class of cell penetrating peptides (CPPs).[66] CPPs are short amino acid sequences that are typically arginine or lysine rich, leading to a net positive charge.[66-69] The positive charge of the CPP is known to disrupt the cell membrane and facilitate cellular uptake of a peptide-coated NP (**Figure 1.2. B**). This approach has been utilized for the delivery of inorganic NPs, polymer NPs, liposomes, and proteins, and has led to therapeutic responses including gene knockdown and gene editing in the cytosol and nucleus, respectively.[66, 70-71] Nevertheless, despite all that has been achieved with CPPs, they are notoriously cytotoxic, limiting their clinical translation to only a few approved examples.[71-73]

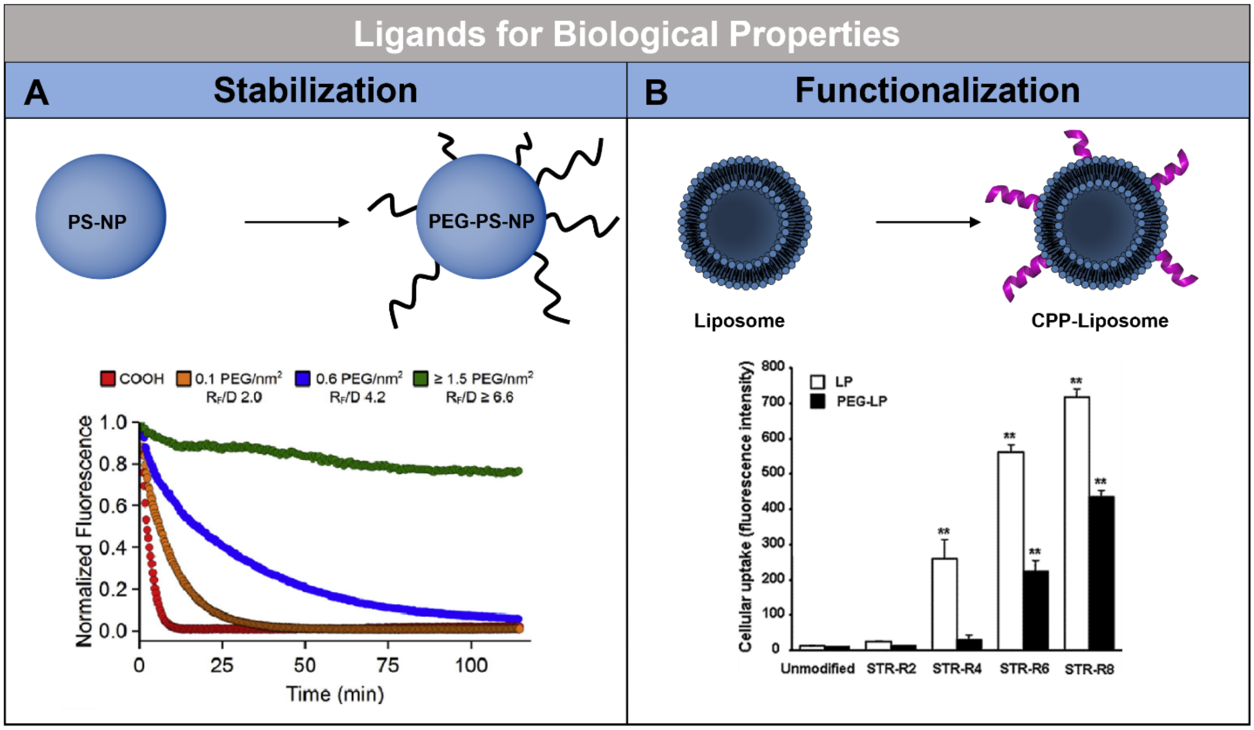

Figure 1.2. Different ligands offer various benefits in biological settings
(A) PEGylation has been widely adopted for interfacing nanomaterials with biology. It has been shown that PEGylation of polystyrene (PS) NPs extends the circulation half-life of the NP, *in vivo*. Adapted from ref [11]. (B) CPPs are commonly used to facilitate cellular uptake of nanomaterials. Here, CPP conjugated liposomes exhibit highly efficient cellular uptake. Adapted from ref [17].

While both ligand types, stabilizing and functionalizing, are useful in specific applications, ligands that have capabilities from both groups (*e.g.,* increasing stability, resistance to degradation, cellular uptake, and function) are extremely valuable. This is a major benefit of a different ligand not previously discussed –oligonucleotides– which will be discussed in detail in **section 1.2.2**.

1.1.3. Ligands in Nanoparticle Assembly and Materials Design

Just as ligands can dictate NP interactions in biology, they can also direct interactions between other NPs. Such capabilities enable NP assembly into one, two, or three dimensional (1D, 2D, 3D) materials (**Figure 1.3. B**).[74-75] NP assembly is a key pillar in the development of new materials because individual NPs can be combined to create architectures with unique structures and properties.[74-75] For example, NP assembly has led to the creation of materials with unique plasmonic, photoluminescent, and magnetic properties.[76-79] Ligand mediated NP assembly can be driven by many factors including supramolecular interactions, electrostatics, dipole-dipole interactions, and ligand interdigitation (**Figure 1.3. A**).[4, 29] Typically, polymeric ligands are used for NP assembly due to their diversity in size, charge, and hydrophilicity, allowing for the programming of the interactions that drive assembly.[74, 80-81]

Once NPs are coated with a desired ligand, they can be assembled. This is typically achieved by either evaporation-driven assembly or slow-cooling/annealing mediated assembly.[75] During assembly formation, ligands play a key role in directing the shape and size of the resultant structures.[75, 82] Furthermore, ligands can introduce stimuli responsiveness into NP assemblies.

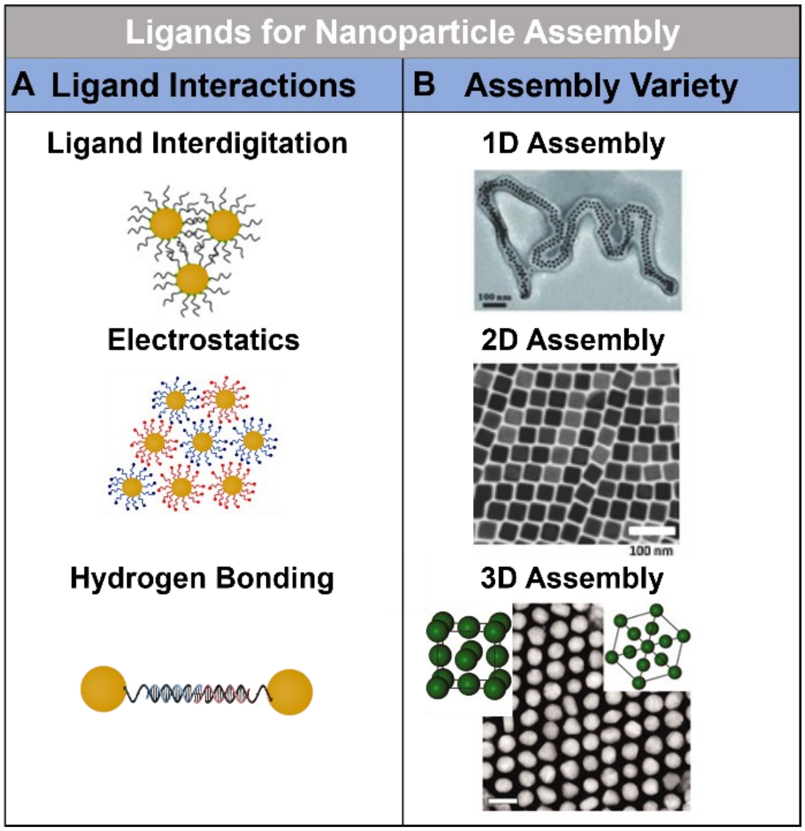

Figure 1.3. Ligands can be used to form NP assemblies
(A) NP-NP interactions can be tuned based on the selected ligand. The most common ligand interactions used in assembly are ligand interdigitation, electrostatics, and hydrogen bonding. Adapted from ref. [4]. (B) a vast library of NP assemblies have been achieved spanning 1D, 2D, and 3D architectures. Adapted from refs. [6-8].

Most commonly, the stimuli are temperature- or pH-dependent and lead to the shrinking/swelling of the architectures. [83-86] Nevertheless, the major shortcoming of using typical polymeric ligands to direct NP assembly is the lack of specificity and programmability. For example, polymers provide little control over specificity, meaning that ligand coated nanoparticles can interact with any other particles so long as they are chemically complementary. As a result, programming NP assemblies to have distinct structural and functional properties is challenging, when using common polymeric ligands. However, a notable exception to this rule is the use of oligonucleotides, biopolymers that enable unique control over specificity, length, and interaction strength. This will be discussed further in **section 1.2.3**.

1.2. Oligonucleotides as Ligands for Biology and NP Assembly

1.2.1 Oligonucleotides as NP Ligands

Deoxyribonucleic acid (DNA), a type of oligonucleotide, consists of four bases: Adenine (A), Cytosine (C), Guanine (G), and Thymine (T) (**Figure 1.4. A**).[87] These four bases are capable of encoding all of the genetic information necessary for life. However, once a procedure for DNA synthesis was developed, it was quickly realized that DNA can be much more than just the blueprint for life. Indeed, by interfacing DNA with biological systems and NPs, new capabilities in therapeutics, diagnostics, and materials design have been achieved. The widespread use of DNA as a ligand emerged due to three beneficial properties. The first is that DNA has an accessible synthesis. In the 1960s, Letsinger and coworkers developed an automated, solid-phase synthesis of DNA, an approach that has been widely adopted in labs around the world.[88-89] The resultant DNA products can be readily purified, characterized, and ready to use in just four days. The second benefit is its modular design. During DNA synthesis, the specific sequence as well as the length of the desired strand can be programmed. Furthermore, specific chemical functional groups can be incorporated into the DNA sequence, enabling post synthetic modifications to be made. This is particularly useful for functionalization of NPs with DNA strands. The third major benefit of working with DNA is its selective hybridization. Specifically, DNA molecules interact with each other through Watson-Crick base pairing, a hydrogen-bond based recognition system whereby nucleobases A and T form two connective hydrogen bonds and nucleobases C and G form three connective hydrogen bonds.[87] Due to the differences in the number of hydrogen bonds and the control over DNA sequences, DNA strands can be synthesized to have specific interaction strengths between complementary strands based on the number of Gs and Cs in the sequence, as well as the length of the sequence. Hydrogen bonding between complementary base pairs (bp) is termed hybridization and results in the formation of double stranded DNA (dsDNA).

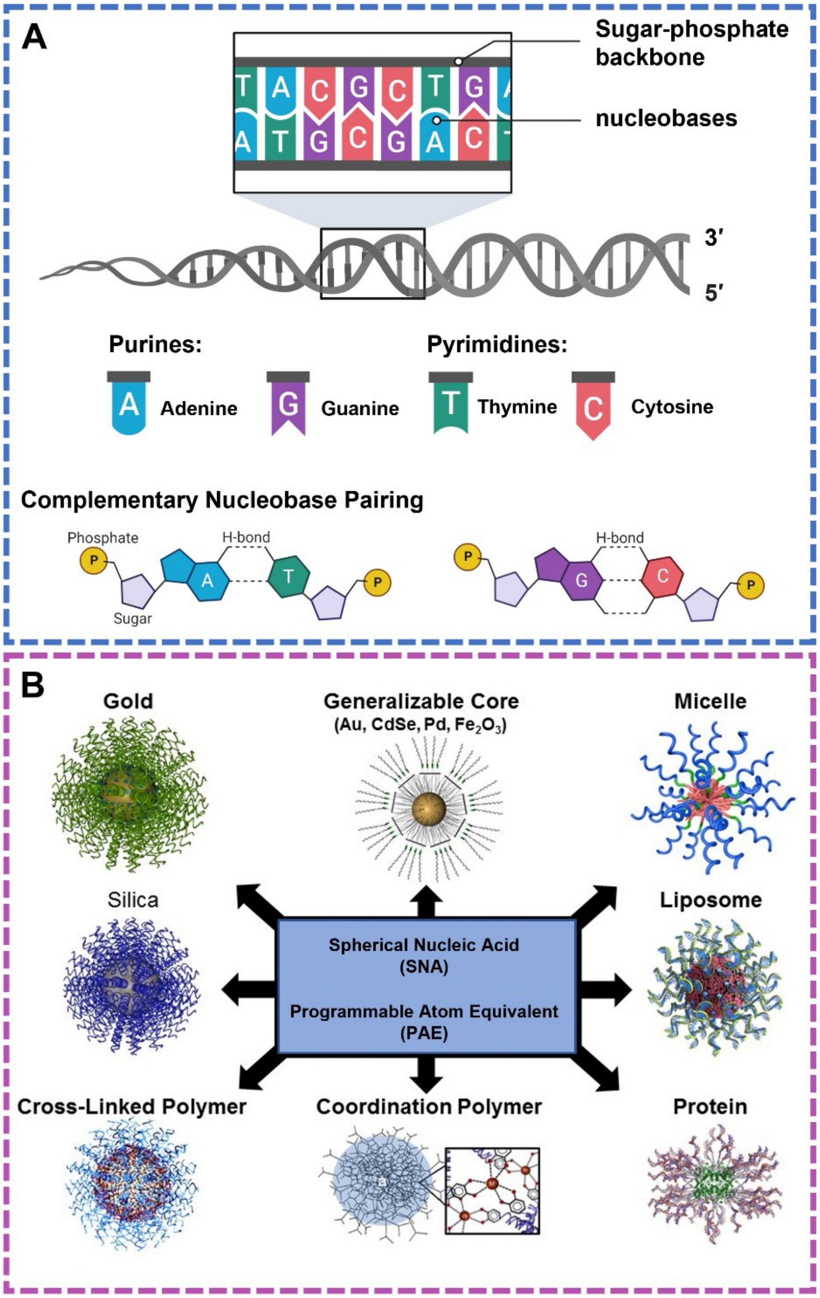

Figure 1.4. DNA as a ligand
(A) The structure of DNA enables it to be a powerful, sequence specific, NP ligand. (B) DNA can be conjugated to a variety of NP surfaces, enabling unique biological and material properties to be applied to a wide array of NP cores.

DNA was first established as an NP ligand when Alivisatos and coworkers[90], and Mirkin and coworkers[91] were investigating how nanomaterials (*e.g.,* Au NPs) could be controllably assembled using DNA-DNA hybridization. These original studies were the first demonstrations of how DNA can be used as a ligand to program interactions between NPs and their environments. Due to the chemical addressability of oligonucleotides, a variety of chemical functional groups can be added to DNA strands, making NP functionalization possible. By taking advantage of the inherent DNA properties discussed above, novel capabilities have been achieved, which will be detailed in **sections 1.2.2. and 1.2.3**.

A variety of techniques have been developed to conjugate DNA to NP surfaces regardless of NP composition (**Figure 1.4. B**). Commonly used gold (Au) and silver (Ag) NPs are easily functionalized with DNA by incorporating either terminal thiol or dithiol functional groups on the DNA strands, which can form Au-Thiol or Ag-Thiol bonds that link the DNA to the NP surface.[90-92] Due to the rising interest in the use of DNA as an NP ligand, techniques to functionalize other NP types with DNA have been developed. An example is the generalizable approach that enables the functionalization of nearly any inorganic NP with DNA. This approach works by coating the NP with an azide-functionalized polymer and reacting dibenzocyclooctyne (DBCO) modified DNA to form a covalent bond.[93] Methods to functionalize organic NPs with DNA have also emerged. For example, liposome cores and micelles can be functionalized through intercalation of DNA that contains a hydrophobic functional group, such as cholesterol or lipid tails.[94-95] Finally, methods to functionalize proteins have been developed, which involve conjugating DNA to reactive, surface accessible amino acids, such as lysine and cysteine.[96] As a result, virtually any NP of interest, organic or inorganic, can be functionalized with DNA, enabling the development of new therapeutics, diagnostics, and materials, as discussed below.[97-99]

1.2.2. DNA Functionalized NPs Enable New Capabilities in Biology

With the development of functionalization techniques to attach DNA to NP surfaces, the Mirkin lab and others have shown that such architectures have unique biological properties.[100] These structures, termed spherical nucleic acids (SNAs), are defined as NPs with a dense shell of radially oriented oligonucleotides. SNAs interact with living matter in markedly different ways from their linear DNA counterparts. The dense shell of DNA enables rapid cellular uptake in over 60 different cell types, which occurs through engagement with type-A scavenger receptors located on many cell surfaces.[101] In addition to the improved cellular uptake of SNAs over linear DNA, the dense shell sterically and electrostatically inhibits degradative proteins, resulting in superior SNA stability, *in vitro* and *in vivo*.[102-103] Furthermore, the oligonucleotides themselves can be designed to have therapeutic functions. Indeed, SNAs capable of immune suppression, immune activation, gene knockdown, gene editing, and sensing, have all been developed by modifying the oligonucleotide sequences of the DNA shell.[104-106] Importantly, properties arising from the DNA shell are independent of the NP core employed. As a result, gold NPs, polymer vesicles, liposomes, and proteins have all been used as SNA cores.[94-96, 107]

The modularity in SNA design has enabled significant breakthroughs in the structure-function relationships that guide therapeutic design. Among the most notable is the work investigating rational vaccinology – the concept that vaccine structure plays a significant role in defining vaccine efficacy.[106, 108] In order to investigate such structure-function relationships, a highly modular nanoscale architecture is required, wherein a single component can be modified individually to test the effects of each design parameter on vaccine function. The SNA is an ideal architecture for this task. By tuning SNA design, the effects of component ratios, attachment chemistry, and core stability can all be explored independently.[109-112] As a result, a deeper understanding of the structure-function relationships that guide vaccine efficacy have been defined.

1.2.3. DNA Ligands for NP Assembly

The inherent properties of DNA ligands have also revolutionized how NP assembly is achieved, providing a method to easily tune interparticle distances and interaction strengths within the assembly. DNA-functionalized NPs are synthesized *via* the same methods outlined in **section 1.2.2.** and their assembly is facilitated by DNA hybridization of complementary sequences on adjacent DNA functionalized NPs.[90-91] When used in NP assembly, DNA functionalized NPs are referred to as programmable atom equivalents (PAEs) because the DNA hybridization events mimic the overlapping of electron orbitals in atomic bonds. Utilizing DNA, two different types of NP assemblies have been achieved – discrete assemblies and extended colloidal crystals.

Discrete assemblies consist of a defined, small number of NPs and typically lack extended structural periodicity (**Figure 1.5. A**). They have mostly been utilized to create interesting 1D, 2D, and 3D assemblies with optical properties or interactions between functional nanoparticle building blocks.[113-114] Discrete assemblies can be programmed via judicious DNA design. Specifically, longer DNA sequences ($\geq$12 bases) have strong interaction strengths with their complementary strands.[113-114] As a result, the hybridization events between adjacent NPs thermodynamically locks the NPs into specific locations, inhibiting reorganization and formation of extended assemblies.

The second type of DNA mediated NP assemblies are colloidal crystals, which are defined by their extended structures consisting of several hundred NP building blocks in periodic crystalline patterns (**Figure 1.5. B**). Many analogies can be drawn between atomic crystals and colloidal crystals and by exploring the capabilities of colloidal crystal engineering with DNA, we can develop a deeper understanding of both. The field of colloidal crystal engineering with DNA has rapidly developed and key concepts have been codified into design rules that enable the programming of crystal phase symmetries, lattice parameters, crystal habits, and thermostabilities.[115-117] Furthermore, this approach enables features of the NP (*i.e.,* size, shape, and

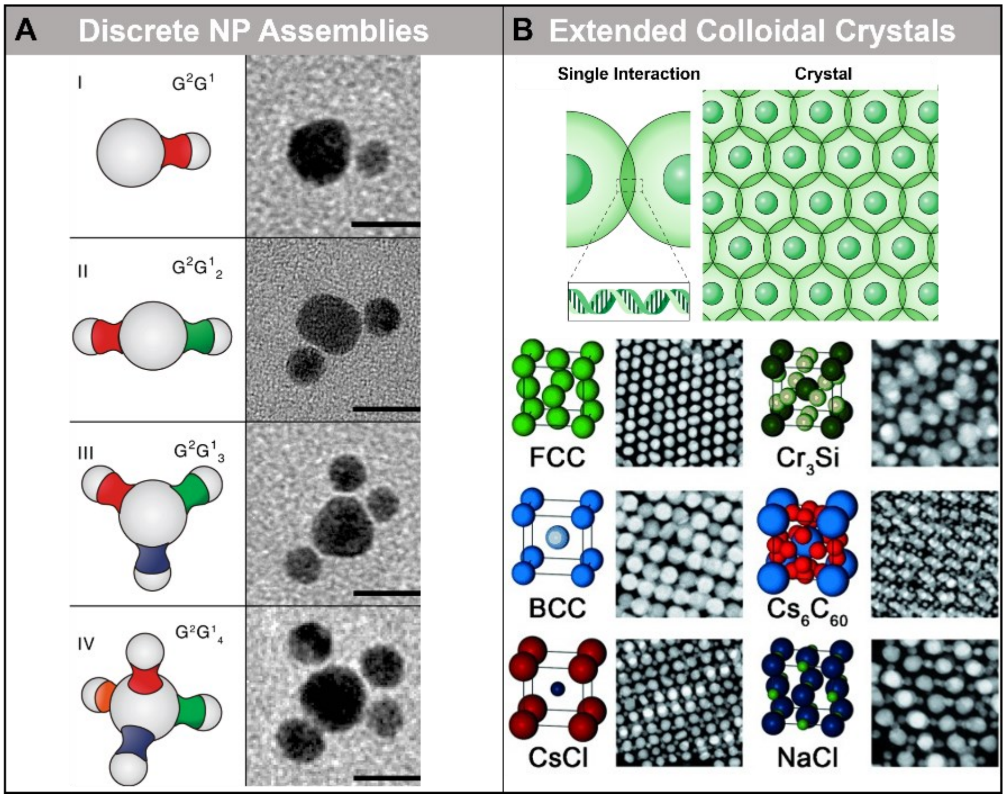

Figure 1.5. DNA mediated nanoparticle assembly
(A) Discrete nanoparticle assembles have been programmed by synthesizing nanoparticles with a limited number of DNA strands per particle that form strong hybridization events with complementary DNA sequences. Adapted from ref. [12]. (B) Extended colloidal crystals are synthesized from PAEs with a high DNA coverage density and low interaction strengths to promote the formation of the most thermodynamically favorable crystal structure. Adapted from refs. [18-19].

composition) and the DNA to be modulated independent of each other. As a result, researchers have synthesized crystal structures with over 70 different crystal symmetries.[18]

1.3. Controlling DNA Ligand Architecture

1.3.1. Methods to Program DNA Ligand Presentation

Current DNA functionalization methods typically result in NPs that have disperse isotropic distributions of DNA on their surfaces. This is mainly due to the inherent chemical isotropy of many nanoparticle cores. While much has been achieved with isotopically functionalized NPs, if the final goal is to make DNA-based structures by design, then more precise control over DNA ligand architecture is required. Specifically, ligand architecture can be divided into three parameters – (1) ligand valency (the number of DNA interactions that can occur), (2) anisotropy (the directionality of DNA interactions that can occur), and (3) orthogonality (the type of unique DNA interactions that can occur) (**Figure 1.6.**). Such control over all three parameters would mean that DNA can be used to encode specific and directional interactions, truly enabling nanoscale materials to be made by design. Advances in synthesizing nanoparticles with controlled DNA ligand architecture have led to programmed formation of discrete assemblies with specific numbers of binding partners and precise directional interactions.[2, 118-119] Furthermore, it has been shown that ligand number, position, and local density play critical roles in biodistribution, cell activation, and cellular uptake.[120-122] Methods have been developed to program DNA ligand valency, position, and orthogonality, but very few have achieved control over all three. For example, through judicious DNA design and meticulous DNA functionalization, researchers are able to synthesize inorganic NPs with a defined number of DNA strands (valency control).[3] While this approach has been effective for desired applications, it often produces NPs with disperse valences and does not allow for the programming of anisotropic or orthogonal interactions. A second approach utilizes polymer coatings to selectively block the surfaces of inorganic NPs, thereby promoting DNA functionalization on the portion of the NP that is not covered.[118] This method can program anisotropic interactions, but offers little with regard to valency and orthogonality. The only method that enables control over all three parameters requires a protein core due to the inherent chemical isotropy of protein surfaces and the ability to mutate desired amino acids. As a result, proteins allow the direct programming of the valency, anisotropy, and orthogonality of the DNA conjugated to the protein surface.[123] Though extremely promising and effective, protein mutagenesis and expression are not trivial tasks. This approach is not easily scalable in terms of the amount of material that can be synthesized and in terms of the complexity

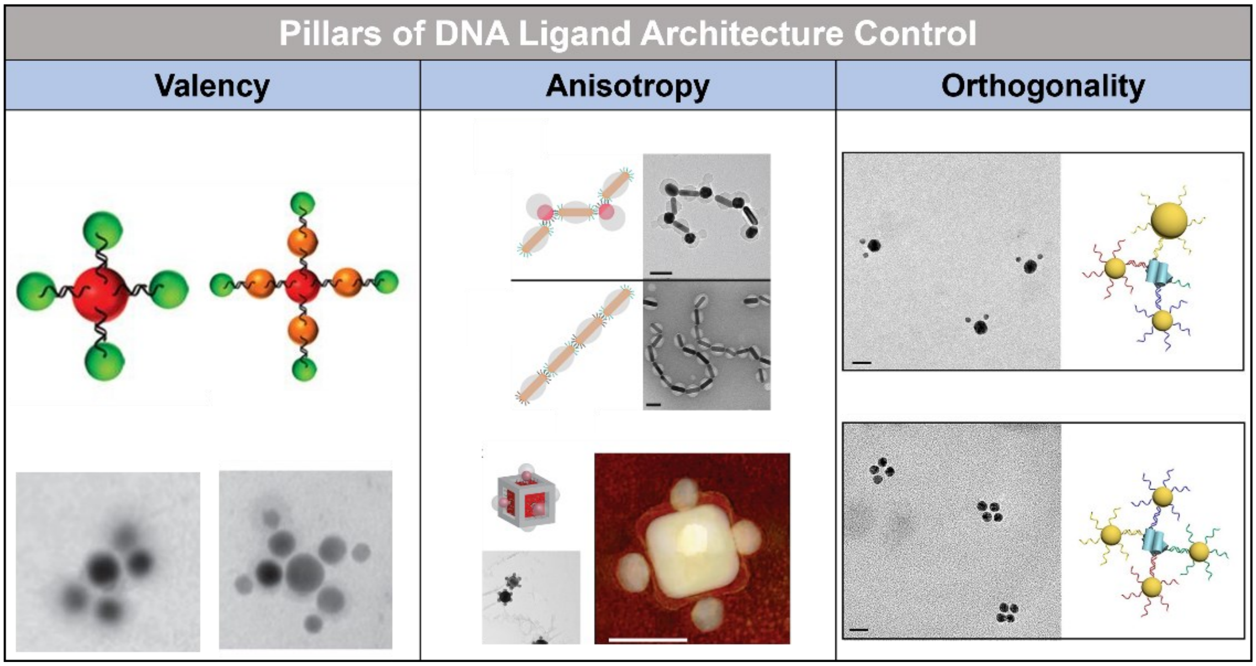

Figure 1.6. The pillars of DNA ligand architecture
There are three major parameters that need to be controlled in order to program materials by design with DNA: valency (the number of DNA interactions that can form), anisotropy (the directionality of the interactions that can form), and orthogonality (the types of unique interactions that can form). The ability to fine-tune each of these pillars will enable us to expand far beyond what is currently attainable in therapeutics and materials design. Adapted from refs. [1-3].

of the resultant structures. Therefore, an easily scalable and generalizable approach to control DNA ligand architecture is required to access programmable materials by design.

1.3.2. Remaining Challenges

When it comes to SNAs and PAEs, the functionalization methods and inherent isotropy of many NP cores means that no two SNAs or PAEs are identical and there is limited control over DNA ligand architecture. Therefore, fundamental questions about structure/function relationships of SNAs and PAEs remain unanswered and their architectural designs remain unevolved. Ultimately, understanding DNA ligand architecture, along with the ability to manipulate it will lead to enhanced programmability and customization of properties for biological function and nanoparticle assembly. This thesis directly addresses these shortcomings and presents the development of a novel approach to realize fine-tuned and molecularly-defined control over DNA ligand architecture at the nanoscale.

1.4. Thesis Overview

The body of work presented herein focuses on developing a novel approach to achieving fine-tuned, molecularly defined control over DNA ligand architecture and studying how this control is utilized to access new capabilities in therapeutics and materials design. To this end, we developed and explored dendritic DNA molecules as highly modular, molecularly defined structures and established key design parameters that impact their therapeutic functions, as a delivery agent and as a cancer vaccine, and assembly properties, in the form of DNA dendrimer PAEs. This thesis teaches how control over DNA ligand architecture can introduce new capabilities across fields. In biological settings, we outline the lower limit of DNA valency that is necessary to achieve rapid cellular uptake, resistance to degradation, and enhanced cargo delivery. Furthermore, we define design rules necessary to create functional cancer vaccines from these DNA dendron molecules and functional infectious disease vaccines from the SNA platform. In materials design, we utilize the DNA dendron and bottom-up assembly to create molecularly defined DNA dendrimers with unique control over ligand valency, anisotropy, and orthogonality, enabling the exploration of how these different parameters can be tuned to access new crystal structures and compositions. These lessons advance the fields of therapeutic development, molecular medicine, and colloidal crystal engineering with DNA by addressing overarching challenges in both fields that are associated with the cellular delivery of biomolecules, vaccine structure and function, synthetically breaking symmetry, and multicomponent colloidal alloys.

Chapter two explores the design and synthesis of DNA dendrons and their utilization for the cellular delivery of therapeutically relevant, biomolecular cargo. Inspired by high-density nucleic acid nanostructures, such as SNAs, we hypothesized that small clusters of nucleic acids, in the form of DNA dendrons, could be conjugated to biomolecules and facilitate their cellular uptake (**Figure 1.7. A**). We show that DNA dendrons are internalized by 90% of dendritic cells after just 1 h of treatment, with a >20-fold increase in DNA delivery per cell compared with their linear

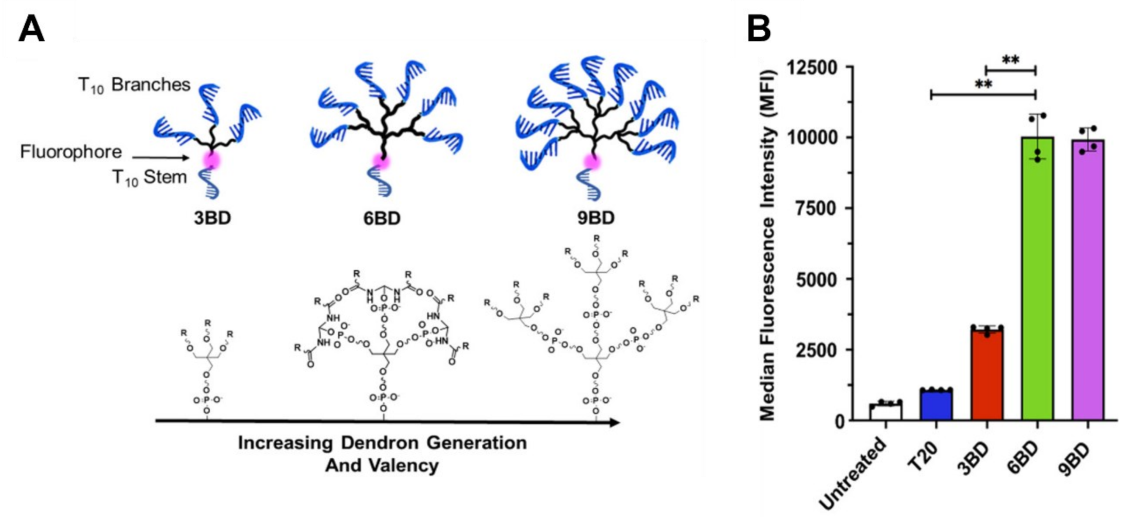

Figure 1.7. DNA dendrons as agents for intracellular delivery.
(A,B) DNA dendrons were designed as molecularly defined mimics of the SNA architecture and enable similar properties, such as highly efficient cellular uptake.

counterparts (**Figure 1.7. B**). This effect is due to the interaction of the DNA dendrons with scavenger receptor-A on cell surfaces, which results in their rapid endocytosis. Moreover, when conjugated to peptides at a single attachment site, dendrons enhance the cellular delivery and activity of both the model ovalbumin 1 peptide and the therapeutically-relevant thymosin alpha 1 peptide. These findings show that high-density, multivalent DNA ligands play a significant role in dictating cellular uptake of biomolecules and consequently will expand the scope of deliverable biomolecules to cells.

Chapter three builds upon the foundational DNA dendron work in chapter two and leverages the modularity of the DNA dendron to develop design rules for the structure-function relationships that dictate DNA dendron-based molecular vaccine function. Vaccine structure plays a critical role in therapeutic efficacy – a concept termed rational vaccinology. In order to establish vaccine design rules, a highly modular platform is required. If vaccine design can be modulated in a molecularly defined manner, then a deeper understanding of vaccine structure and function can be achieved. Here, we report a single molecule DNA dendron-based molecular vaccine that is capable of

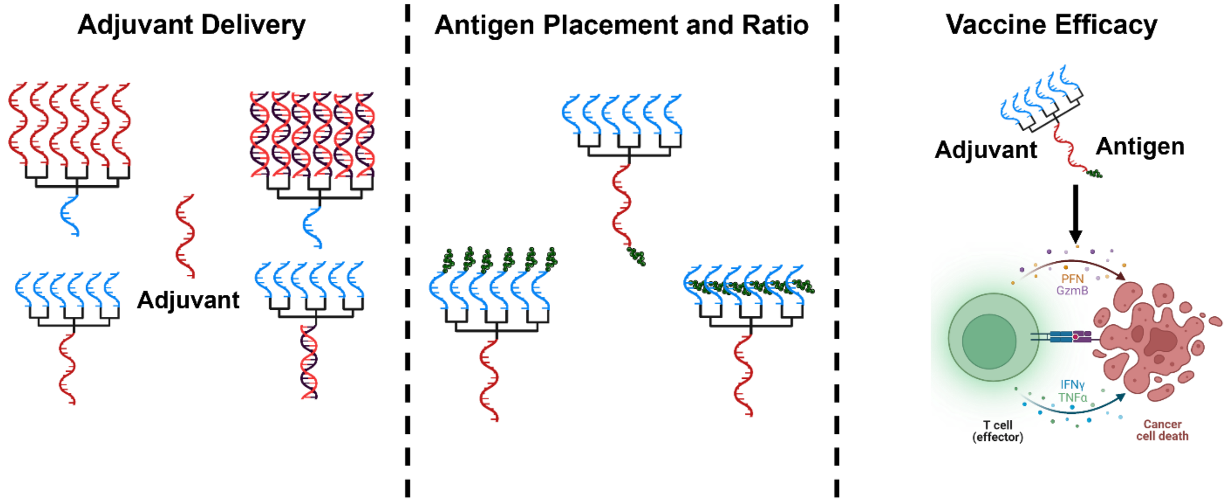

Figure 1.8. DNA dendron molecular vaccines
DNA dendrons were used to study structure-function relationships of molecular cancer vaccines, specifically with regard to the delivery of functional adjuvant and antigen components to produce a potent anticancer immune response.

cellular uptake, immune activation, and immune targeting (**Figure 1.8.**). We leveraged the modularity of the DNA dendron design to determine the most effective structure for delivery of immune activating DNA sequences and antigenic peptides. We investigated how peptide placement and antigen:adjuvant ratios impact uptake, activation, and immune response, both *in vitro* and *in vivo*. The DNA dendrons were then used as treatment in a mouse cervical cancer model. We found that tuning dendron design can maximize immune activation and lead to a strong and specific immune response against the target cancer cells, thereby inhibiting tumor growth and extending mouse survival.

Observing how vaccine structure can impact its function, we then applied the lessons learned from chapter three to the design of an infectious disease vaccine using the SNA platform, which is reported in **Chapter four**. Despite recent efforts demonstrating that organization and presentation of vaccine components are just as important as composition in dictating vaccine efficacy, antiviral vaccines have long focused solely on the identification of the immunological target. Here, we describe a study aimed at exploring how vaccine component presentation in the context of SNAs can be used to elicit and maximize an antiviral response. Using SARS-CoV-2 (the virus that

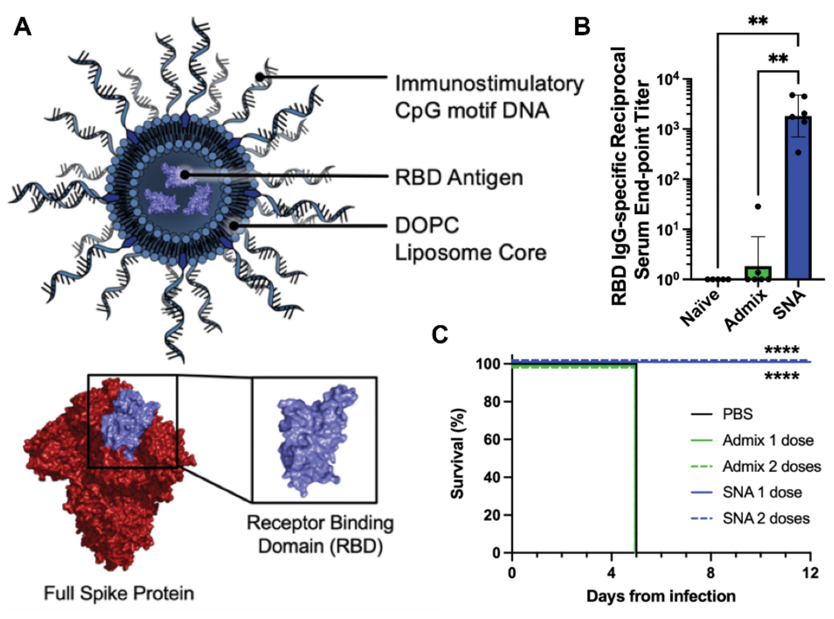

Figure 1.9. SNA infectious disease vaccine design
(A) The SNA platform was utilized to explore structure-function relationships that dictate infectious disease vaccine design, specifically against SARS-CoV-2. (B, C) We demonstrate that by fine-tuning the SNA design, a potent and effective immune response can be raised both *in vitro* and *in vivo*.

causes COVID-19) as a topical example of an infectious disease with an urgent need for rapid vaccine development, we designed an antiviral SNA vaccine, encapsulating the receptor-binding domain (RBD) subunit into a liposome and decorating the core with a dense shell of CpG motif toll-like receptor 9 (TLR-9) agonist oligonucleotides (**Figure 1.9. A**). This vaccine induced memory B cell formation in human cells, and *in vivo* administration into mice generated robust binding and neutralizing antibody titers (**Figure 1.9. B**). Moreover, the SNA vaccine outperformed multiple simple mixtures of antigen and adjuvant that incorporated clinically used adjuvants. Through modular changes to SNA structure, we uncovered key relationships and proteomic insights between adjuvant and antigen ratios, concepts potentially translatable across vaccine platforms and disease models. Importantly, when humanized angiotensin-converting enzyme 2 (ACE2) transgenic mice were challenged *in vivo* against a lethal dose of live virus, only mice that previously received the SNA vaccine had a 100% survival rate and lungs that were clear of virus by plaque analysis (**Figure 1.9. C**). This work underscores the potential for SNAs to be implemented as an easily adaptable and generalizable platform to fight infectious disease and demonstrates the importance of structure and presentation in the design of next-generation antiviral vaccines.

In **Chapter five**, we explore how the dendron can be used as a molecularly defined building block in NP assembly that offers unique structural control. The chemical interactions that lead to the emergence of hierarchical structures are often highly complex and difficult to program. Here, the synthesis of a series of superlattices based upon 30 different structurally reconfigurable DNA dendrimers is reported, each of which presents a well-defined number of single-stranded oligonucleotides (*i.e.,* sticky ends) on its surface (**Figure 1.10.**). Such building blocks assemble with complementary DNA-functionalized Au NPs to yield five distinct crystal structures, depending upon choice of dendrimer and defined by phase symmetry. These DNA dendrimers can associate to form micelle-dendrimers, whereby the extent of association can be modulated based upon surfactant concentration and dendrimer length to produce a low-symmetry Ti_5Ga_4-type phase that had yet to be reported in the field of colloidal crystal engineering. Taken together, colloidal crystals that feature three different types of particle bonding interactions—template–dendron, dendrimer–dendrimer, and DNA–modified AuNP-dendrimer—are reported, illustrating how sequence-defined recognition and dynamic association can be combined to yield complex hierarchical materials.

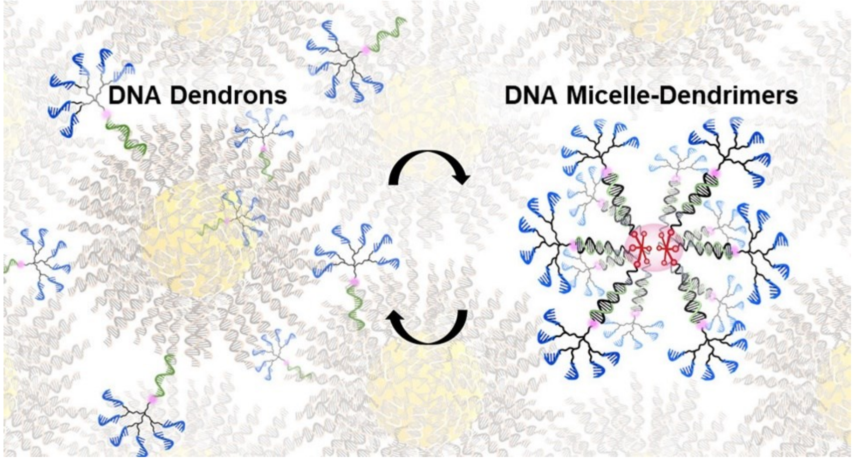

Figure 1.10. Template-encoded DNA dendrimers for NP assembly. DNA dendrons were used to build DNA dendrimer PAEs that provide unprecedented control over DNA ligand valency and distribution, enabling programmability over colloidal crystal outcomes.

In **Chapter six**, we build upon the lessons learned and capabilities gained in chapter five and develop a new type of DNA dendrimer that expands on what is currently possible in the field of colloidal crystal engineering with DNA. Breaking symmetry in colloidal crystals is challenging due to the inherent chemical and structural isotropy of many nanoscale building blocks. If a non-particle component could be used to anisotropically encode orthogonal recognition properties, the scope of structural and compositional possibilities of colloidal crystals can expand beyond what has been possible to date with purely particle-based systems. Here, we report the synthesis and characterization of novel DNA dendrimers that function as symmetry-breaking synthons, capable of programming anisotropic and orthogonal interactions within colloidal crystals (**Figure 1.11.**). When the DNA dendrimers have identical sticky ends, they hybridize with DNA-functionalized nanoparticles to yield three distinct colloidal crystals, dictated by dendrimer size, including a structure not previously reported in the field of colloidal crystal engineering, Si_2Sr. When used as symmetry-breaking synthons (when the sticky ends deliberately consist of orthogonal sequences), the synthesis of binary and ternary colloidal alloys with structures that can only be realized through directional interactions are possible. Furthermore, by modulating the extent of shape anisotropy within the DNA dendrimers, the local distribution of the nanoparticles within the crystals can be directed.

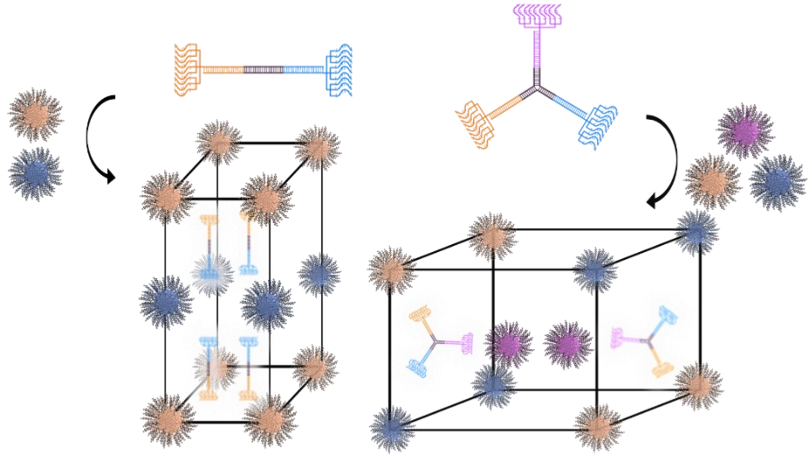

Figure 1.11. Symmetry-breaking DNA dendrimer synthons
A new type of DNA dendrimer is introduced that consists of a DNA junction core and DNA dendron arms. As a result, anisotropic, orthogonal interactions can be controllably encoded within a colloidal crystal, enabling unique low symmetry structures and complex multicomponent assemblies.

Chapter seven summarizes the key conclusions from the body of work presented in this thesis and provides reflections on how this work has impacted the fields of therapeutics and materials design. We found that the DNA dendron can function as a molecularly defined mimic of SNAs, privy to the typical SNA properties, but offers additional properties of its own. We demonstrated its use as a potentially universal tag for the cellular delivery of nanoscale materials. We leveraged its modularity to study structure-function relationships of cancer vaccines with molecular precision. Lastly, we applied these lessons to develop a functional SNA-based infectious disease vaccine. Toward materials design, we utilized the DNA dendron to develop PAEs that offer programmability over valency, anisotropy, and orthogonality and we investigated how this level of control can lead to novel structural outcomes. Finally, we highlight the future questions and challenges that this work offers the opportunity to explore.

CHAPTER TWO

DNA Dendrons as Agents for Intracellular Delivery

Material in this chapter is based upon published work:

Distler, M. E.; Teplensky, M. H.; Bujold, K. E.; Kusmierz, C. D.; Evangelopoulos, M.; Mirkin, C. A., DNA Dendrons as Agents for Intracellular Delivery. *J. Am. Chem. Soc.* **2021,** *143*, 13513-13518.

2.1. Current Methods and Challenges for the Cellular Delivery of Biomolecules

Deoxyribonucleic acids (DNA), peptides, and proteins are attractive candidates in developing novel diagnostic probes[124] and therapeutics[125] due to their chemical, structural, and functional properties. Nevertheless, their uses in this capacity and translation clinically are still greatly limited by their low cellular uptake, arising from their hydrophilicity, charge, and rapid degradation.[126-128] Methods have been developed to circumvent these shortcomings and promote uptake, such as the use of lipoplexes[129], cell-penetrating peptides[130-131], and nanoparticle complexes.[132-135] While these methods are effective in increasing cellular uptake, they can be cytotoxic and unstable, limiting their applicability *in vivo*.[133, 136-138]

Spherical nucleic acids (SNAs), nanoparticles with a dense shell of radially oriented oligonucleotides, are a promising class of nanostructures that interact with living matter in markedly different ways from linear strands. Through engagement with type-A scavenger receptors, SNAs exhibit rapid cellular uptake in over 60 different cell types,[139] a property stemming from the dense arrangement of oligonucleotides. Furthermore, the DNA shell sterically inhibits degradative proteins, resulting in superior SNA stability *in vivo*.[102-103] The properties arising from the DNA shell are independent of the nanoparticle core employed and translatable across different classes of oligonucleotides. Indeed, gold, polymer vesicles, liposomes, and most recently, proteins[107, 140-142] have been used as cores functionalized with immunostimulatory DNA, antisense DNA, RNA, and small-interfering RNA.[143-145]

While SNAs have been utilized as a platform for various probes and therapeutics, in some respects their three-dimensional architectures impose unnecessary limitations by requiring dense isotropic functionalization in order to access these advantageous properties. As a result, small molecules, DNA/RNA, peptides, and small proteins, which have a limited number of conjugation sites, lack reliable and biocompatible methods for cellular delivery. We hypothesized that a structure consisting of one portion of an SNA would be able to engage scavenger receptors in much the same way as the full SNA architecture. To test this hypothesis, we synthesized DNA dendrons, molecularly well-defined clusters of DNA radiating from a single branching point and functionalized them with nucleic acid and peptide cargo to explore their cellular uptake properties.

2.2. Design and Synthesis of DNA Dendrons

DNA dendrons have been previously synthesized through two approaches: hybridization-mediated assembly[146-152] and solid-phase covalent methods.[151, 153] Hybridization based approaches depend on non-covalent interactions, making them susceptible to degradation in biological environments due to dehybridization and structural rearrangement.[146] In contrast, solid-phase DNA synthesis using phosphoramidite chemistry enables the synthesis of defined, covalently-linked structures.[153] However, the current state-of-the-art covalent syntheses of DNA dendrons typically exhibit low yields, which are exacerbated by multiple required purification steps. We identified the causes of low yields to be intermolecular steric hindrance, intramolecular steric and electrostatic hindrance, and solid support-DNA steric hindrance. By systematically addressing these issues, we synthesized DNA dendrons with size, length, and generation control at greater than 10% yield post purification, an over 20-fold increase compared to previous attempts[151] at controlled dendron synthesis. A more in-depth discussion can be found below (**Table 2.1**).

The current state-of-the-art covalent syntheses of DNA dendrons typically exhibit low yields. A robust, high-yielding synthesis of covalently-linked DNA dendrons, suitable for biological applications, was developed by addressing the three synthetic parameters discussed above. To decrease intermolecular steric hindrance, 2000 Å dT CPG beads were used over the more commonly used, smaller 1000 Å Unylinker CPG beads. The effect was two-fold: a large pore diameter decreased intermolecular steric hinderance caused by adjacent dendrons while also enhancing reagent diffusion, thereby increasing coupling yield. Second, intramolecular steric hindrance and electrostatic repulsion between the dendron branches was reduced by incorporating hexaethylene glycol phosphoramidites near the branching units. This resulted in increased dendron molecular flexibility and spacing between DNA branches. Finally, steric hindrance between the surface of the CPG bead and growing dendron was mitigated by increasing the length of the dendron stem, thereby pushing it farther from the CPG surface and providing more space for the

Table 2.1. DNA dendron yield improvement

Strand Name	DNA Sequence (Phosphate Backbone)	MW (kDa)	% Yield
6A_1xT_1000A	5’ TTTTTTTTTT-D-Tr-TTTTT 3’	21.19	0.52
6B_2xT_1000A	5’ TTTTTTTTTT-D-Tr-TTTTT 3’	21.19	5.6
6C_2xT_1000A	5’ TTTTTTTTTT-D-Tr-TTTTTTTTTT 3’	22.71	8.5
6D_2xT_2000A	5’ TTTTTTTTTT-D-Tr-TTTTTTTTTT 3’	22.71	11.1
6E_2xT_2000A	5’ TTTTTTTTTT-Sp-D-Sp-Tr-TTTTTTTTTT 3’	25.81	12.0

1xT: synthesis was conducted at the standard thymine concentration
2xT: synthesis was conducted at double the standard thymine concentration
1000A: synthesis was conducted using 1000 angstrom CPG beads
2000A: synthesis was conducted using 2000 angstrom CPG beads
D: 1,3-bis-[5-(4,4'-dimethoxytrityloxy)pentylamido]propyl-2-[(2-cyanoethyl)-(N,N-diisopropyl)]-phosphoramidite (Symmetric Doubler)
Tr: Tris-2,2,2-[3-(4,4'-dimethoxytrityloxy)propyloxymethyl]methyleneoxypropyl-[(2-cyanoethyl)-(N,N-diisopropyl)]-phosphoramidite (Long Stem Trebler)
Sp: 18-O-Dimethoxytritylhexaethyleneglycol,1-[(2-cyanoethyl)-(N,N-diisopropyl)]-phosphoramidite (Spacer phosphoramidite 18)
Amino dT: 5'-Dimethoxytrityl-5-[N-(trifluoroacetylaminohexyl)-3-acrylimido]-2'-deoxyUridine,3'-[(2-cyanoethyl)-(N,N-diisopropyl)]-phosphoramidite (Amino-Modifier C6 dT)
DBCO dT: 5'-Dimethoxytrityl-5-[(6-oxo-6-(dibenzo[b,f]azacyclooct-4-yn-1-yl)-capramido-N-hex-6-yl)-3-acrylimido]-2'-deoxyUridine,3'-[(2-cyanoethyl)-(N,N-diisopropyl)]-phosphoramidite (DBCO dT CE)
Cy3: 1-[3-(4-monomethoxytrityloxy)propyl]-1'-[3-[(2-cyanoethyl)-(N,N-diisopropyl) phosphoramidityl]propyl]-3,3,3',3'-tetramethylindocarbocyanine chloride (Cyanine 3)

growing dendron. Furthermore, by doubling (2xT) the concentration of nucleic acid phosphoramidites compared to typical reagent concentrations (1xT), coupling on the branching end of the dendrons was more successful, resulting in higher yields. These efforts are supported by a nearly 2000% increase in yield and provide a robust synthetic procedure for the synthesis of DNA dendrons with size, length, and generation control.

DNA dendrons were synthesized containing either three (3BD), six (6BD) or nine (9BD) branches (**Figure 2.1. a**). A fluorophore was incorporated between the branched region and the stem to be used as a fluorescent label in *in vitro* and *in vivo* studies (*vide infra*). All dendrons were characterized by matrix-assisted laser desorption/ionization time-of-flight mass spectrometry (MALDI-TOF) and denaturing polyacrylamide gel electrophoresis (PAGE) to confirm mass and purity (**Figure 2.1. b, c; Table 2.2**). MALDI-TOF revealed expected mass increments of approximately 10 kDa with increasing dendron valency. Denaturing PAGE showed single bands for each purified dendron and an expected decrease in electrophoretic mobility as branch number increases. Moreover, through this work, non-standard phosphoramidites containing functional groups for bioconjugation, such as primary amines, can be introduced on both the stem and branch positions without a decrease in yield.

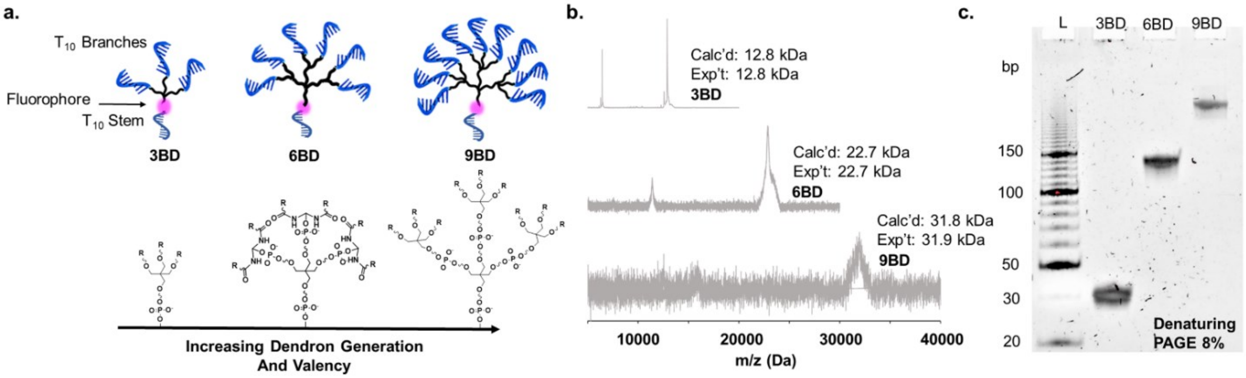

Figure 2.1. DNA dendron design and characterization
(a) DNA dendrons consist of a 10-base oligodeoxynucleotide stem, a branching region producing three, six, or nine total branches, and 10-bases on each branch. The number of branches can be tuned by changing the branching unit and dendron generation. (b,c) Dendron synthesis and purification were confirmed by MALDI-TOF and denaturing PAGE.

2.3. Cellular Uptake Properties of DNA Dendrons

We hypothesized that increasing DNA dendron valency would lead to higher uptake by cells, facilitated by the increased interaction of the dense DNA branches with scavenger receptor-A on cell surfaces. To test this hypothesis, murine bone marrow-derived dendritic cells (BMDCs) were treated with 50 nM fluorophore-labeled linear T20 strands or a 3BD, 6BD, or 9BD dendron for 1 hour in serum-containing media. Cellular uptake was assessed by measuring the fluorescence frequency and intensity of treated cells via flow cytometry. We observed that the T20 linear strand is taken up by just 29% of DCs (**Figure 2.2.a**). This amount significantly rises with increasing DNA dendron valency, as 3BD is taken up by ap-proximately 60% of cells and 6BD and 9BD are taken up by about 90% of cells (**Figure 2.2.a**). To determine the relative amount of DNA taken up per cell, we analyzed the median fluorescence intensity (MFI) of the fluorophore signal in cells

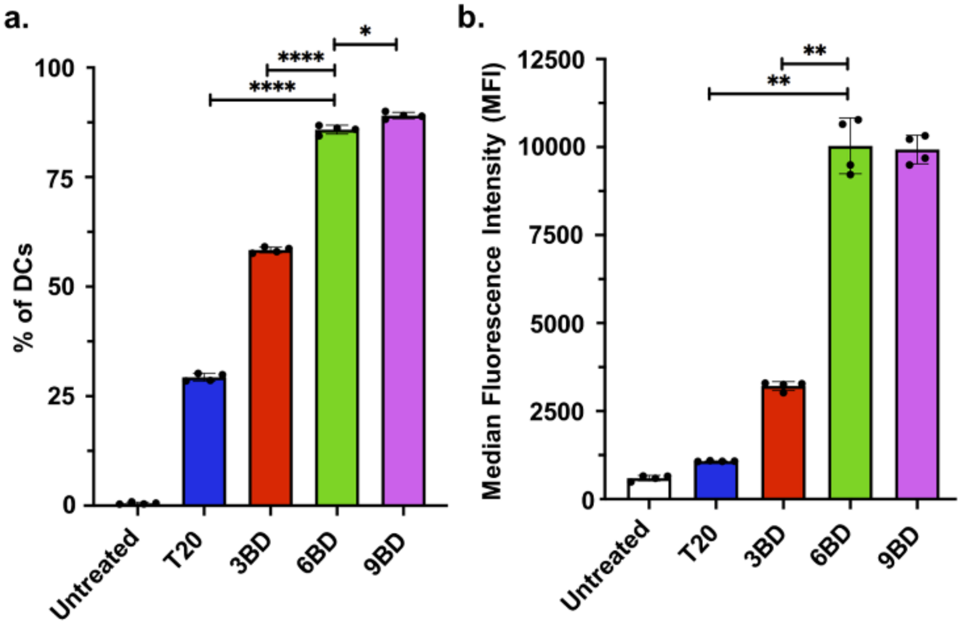

Figure 2.2. Ex vivo DNA dendron uptake in murine bone-marrow derived dendritic cells (DCs) compared to a linear control

(a) Frequency of DNA positive cells amongst the DC population shows that higher valency DNA dendrons (6BD and 9BD) are endocytosed by a greater percentage of the population compared to low valency dendrons (3BD) and a linear control (T20). (b) The median fluorescence intensity (MFI) of DNA positive cells indicates that not only are DNA dendrons taken up by more cells, but are also taken up more per cell than their linear counterparts. Only relevant significances against 6BD and 9BD are shown for clarity. *p<0.05, **p<0.01, ****p<0.0001.

positive for DNA. Valency dependence is even more pronounced by this metric. A cluster of three DNA strands (3BD) resulted in a greater than 5-fold increase in MFI compared to the T20 linear control. Moreover, almost a 20-fold increase in MFI was measured for cells treated with 6BD and 9BD compared to the T20 strand (**Figure 2.2.b**). These experiments show that DNA dendrons are not only taken up by a greater percentage of cells, but also that more DNA dendrons are taken up per cell, compared to their linear counterparts. Furthermore, this observation indicates that six DNA branches is the minimum valency required to achieve highly efficient (>90%) cellular uptake.

Table 2.2. DNA sequences used in this study

Strand Name	DNA Sequence (Phosphate Backbone)	MW (kDa)
T_{20}-Cy3	5’ TTTTTTTTT-Cy3-TTTTTTTTTT 3’	6.22
T_{20} - Amino	5’ TTTTTTTTTTTTTTTTTTT-Amino dT 3’	6.12
T_{20}-Amino-Cy3	5’ TTTTTTTTT-Cy3-TTTTTTTTT-Amino dT 3’	6.68
T_{20} - DBCO	5’ TTTTTTTTTTTTTTTTTTT-DBCO 3’	6.49
3BD	5’ TTTTTTTTTT-Tr-Cy3-TTTTTTTTT 3’	12.80
3BD - Amino	5’ TTTTTTTTTT-Tr-Cy3-TTTTTTTT-Amino dT 3’	13.5
6BD	5’ TTTTTTTTTT-D-Tr-Cy3-TTTTTTTTT 3’	22.70
6BD - Amino	5’ TTTTTTTTTT-D-Tr-Cy3-TTTTTTTT-Amino dT 3’	23.68
9BD	5’ TTTTTTTTTT-Tr-Tr-Cy3-TTTTTTTTT 3’	31.80
9BD - Amino	5’ TTTTTTTTTT-Tr-Tr-Cy3-TTTTTTTT-Amino dT 3’	33.03

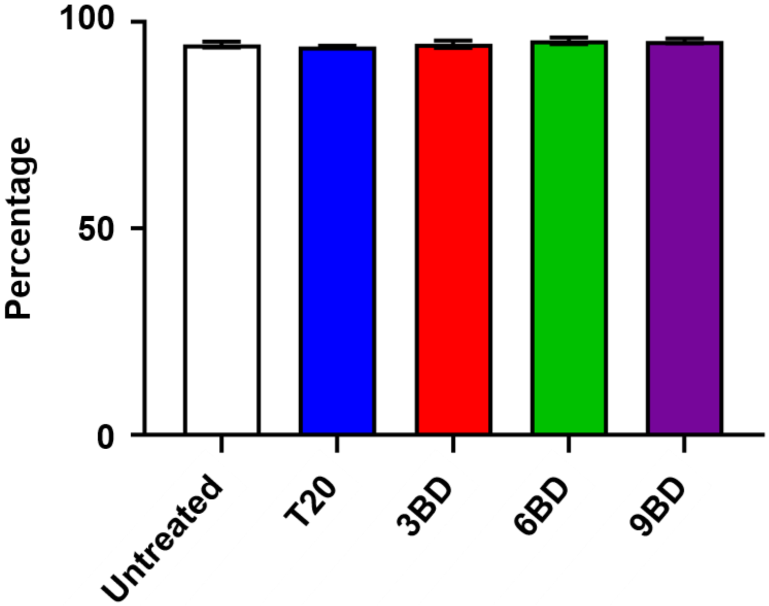

Figure 2.3. Cell viability measurements
No significant changes in cell viability were measured after treatment of dendritic cells with DNA dendrons at 250 nM, as determined by flow cytometry. Similar viability data was observed in all cell experiments conducted.

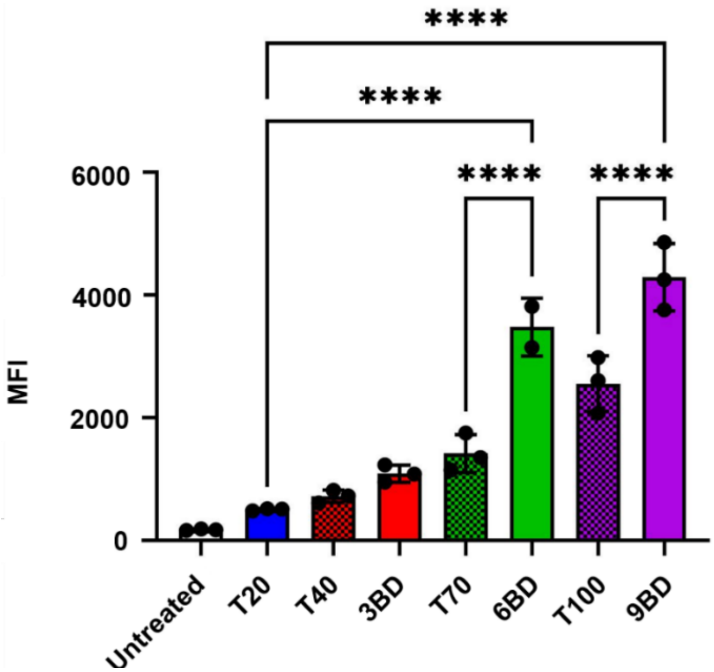

Figure 2.4. DNA dendrons compared to linear strands of equal bases
Cells were treated with 250 nM of DNA for 1 h. The significant increase in MFI of cells treated with 6BD and 9BD indicates that the multivalent architecture promotes cellular uptake. Crucially, linear strands of equal DNA content to the dendrons are prohibitively more difficult to synthesize than the DNA dendrons. Not all significances are shown for clarity., ****p<0.0001.

Crucially, we observed that the DNA dendrons are not cytotoxic (**Figure 2.3.)** and that the efficient uptake is a result of the dendron architecture and not solely due to the increase in DNA content (**Figure 2.4.**). These conclusions were further validated in another cell line, C166 endothelial cells (**Figure 2.5.**). We confirmed that the dendrons are taken up through scavenger receptor-A mediated endocytosis, following the same uptake mechanism as the SNA (**Figure 2.6.**). Moreover, we observed that DNA dendrons are significantly more resistant to serum nucleases compared to their linear counterparts—a result of their dense DNA clusters sterically preventing enzymatic degradation (**Figure 2.7.**). Together, these findings demonstrate that DNA dendrons exhibit the superior cellular uptake and resistance to nuclease degradation required for therapeutic applications.

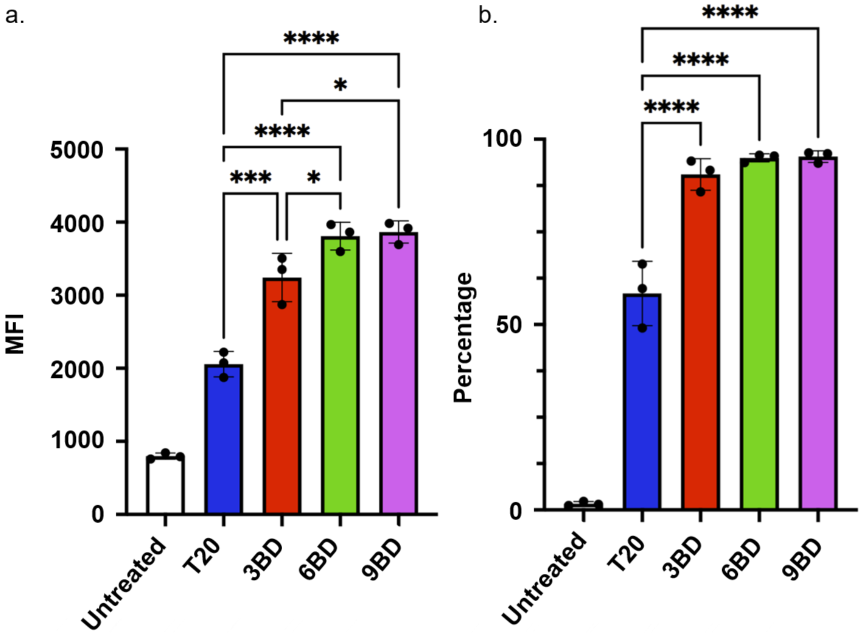

Figure 2.5. DNA dendron uptake by C166 endothelial cells
(a) 6BD and 9BD achieve significantly greater uptake than the 3BD and T20 linear control as measured by the mean fluorescence intensity of cells treated with DNA. (b) Greater than 90% of cells take up the DNA dendrons, a significant increase compared to the T20 control. Not all significances are shown for clarity. *$p<0.05$, ***$p<0.001$, ****$p<0.0001$.

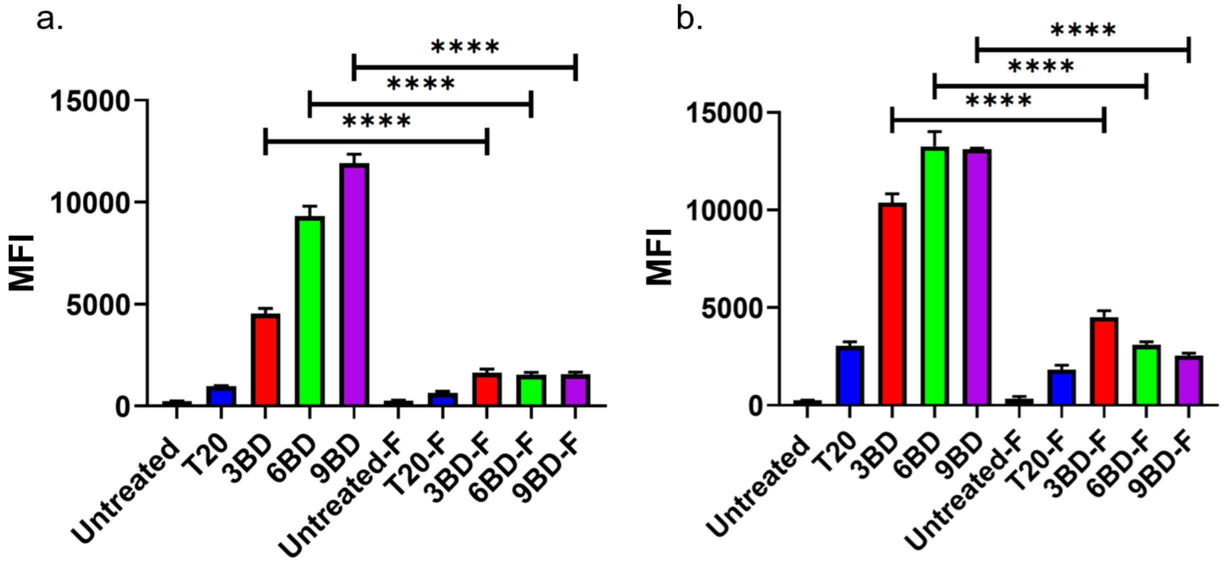

Figure 2.6. DNA dendron uptake by scavenger receptor A
Median fluorescence intensity (MFI) of cells treated with fluorescently tagged DNA at (a) 50 nM or (b) 250 nM for 1 h. Fucoidan treated groups are denoted with an F. Not all significances are shown for clarity. ****p<0.0001.

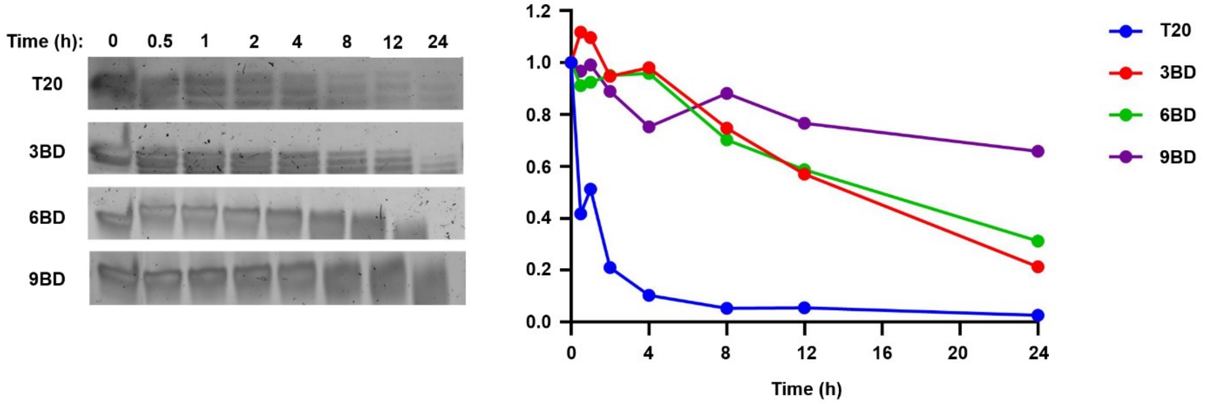

Figure 2.7. DNA dendron resistance to degradation
Representative denaturing PAGE of multiple time points show the dendron's increased resistance to degradation versus a linear control (left). Densitometry analysis of stained gels indicate that high valency DNA dendrons have greater resistance to serum nucleases compared to linear DNA. Data is representative of three experimental replicates conducted in triplicate.

2.4. Dendron-Mediated Delivery of a Model Peptide

Having established that DNA dendrons are efficiently taken up by cells, we hypothesized that conjugating DNA dendrons to functional biomolecules would induce rapid and effective cellular delivery of those biomolecular cargoes. Specifically, peptides have the potential to be powerful therapeutics due to their vast structural and functional properties; however, since they are small amino acid chains with varied charge, dense surface functionalization is difficult and can lead to a loss of peptide function.[65] As a result, they are typically delivered as unmodified therapeutics, leaving them prone to rapid degradation and limited cellular uptake.[154] The Ovalbumin 1 peptide ($Ova_{257-264}$, designated herein as Ova) was chosen as a model system because it is well characterized and its cellular processing can be readily measured with commercially available reagents (**Table 2.3.**).[155] We used a fluorophore-tagged Ova peptide and conjugated it to the dendron through a cysteine residue at the *N*-terminus *via* a disulfide exchange reaction utilizing a pyridyl-disulfide containing crosslinker. DNA-Ova conjugates were synthesized for each of the T_{20}, 3BD, 6BD, and 9BD strands, purified by denaturing PAGE, and characterized by MALDI-TOF (**Figure 2.8.**). MALDI-TOF revealed expected mass increases of ~1.5 kDa between DNA and DNA-Ova conjugates, accounting for the added mass of the conjugated Ova peptide.

Table 2.3. Peptides used in this study

	Peptide Sequence	**Calculated MW (Da)**
Ova	N’-FITC-SIINFEKLC-COOH	1569
Ta1	N’-acetyl-SDAAVDTSSEITTKDLKEKKEVVEEAENC-COOH	3211

We hypothesized that increasing DNA dendron valency would improve the cellular delivery of the DNA-conjugated Ova peptide, facilitated by the DNA dendron. Thus, we compared the signal of DNA and peptide for a simple mixture (DNA and peptide mixed but not conjugated, termed admix), T_{20}, 3BD, 6BD, and 9BD conjugates. By measuring the MFI of cells treated with 50 nM of each sample, we determined the extent of uptake of the DNA and peptide per cell. By this metric, we observed that the 6BD and 9BD conjugates are superior to the admix and T_{20} conjugate, with an ~30-fold increase in MFI of both DNA and peptide compared to admix (**Figure 2.9.b**). Furthermore, assessing cells containing double positive signals for both DNA and peptide reveals that only 3% of cells treated with the admix solution contained both (**Figure 2.9.c**). In contrast, with the T_{20} conjugate, both peptide and DNA are delivered to 38% of the cells, demonstrating the importance of covalently coupling the two agents to improve co-delivery. Importantly, with the use of any of the dendron conjugates, this double positive signal increases to greater than 50%; indeed, the 6BD conjugate delivers both peptide and DNA to over 70% of the cells (**Figure 2.9.c**). Crucially, peptide conjugation does not impact the mechanism by which dendrons enter cells (**Figure 2.10.**). Based on literature precedent[156-160], the observed differences

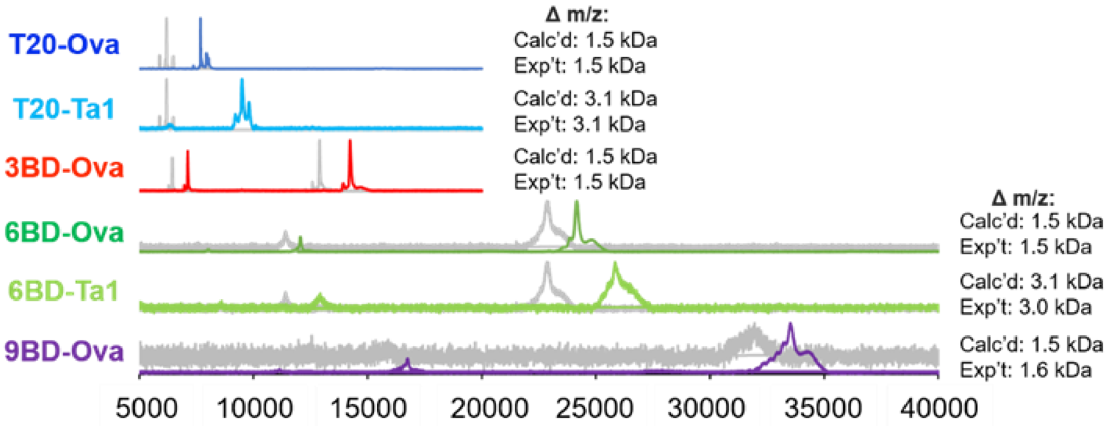

Figure 2.8. MALDI-TOF characterization of each DNA-peptide conjugate
T20-Ova, T20-Ta1, 3BD-Ova, 6BD-Ova, 6BD-Ta1, and 9BD-Ova (top to bottom). The calculated changes in m/z correctly match the observed shifts from the unconjugated DNA (gray) and the peptide conjugates (color).

in uptake between 6BD-Ova and 9BD-Ova at this time point are likely due to differences in the size of the conjugate, which has been shown to play an important role in DC processing of antigens. Overall, these results are a powerful demonstration of the potential that DNA dendrons have to deliver biomolecular conjugates to cells.

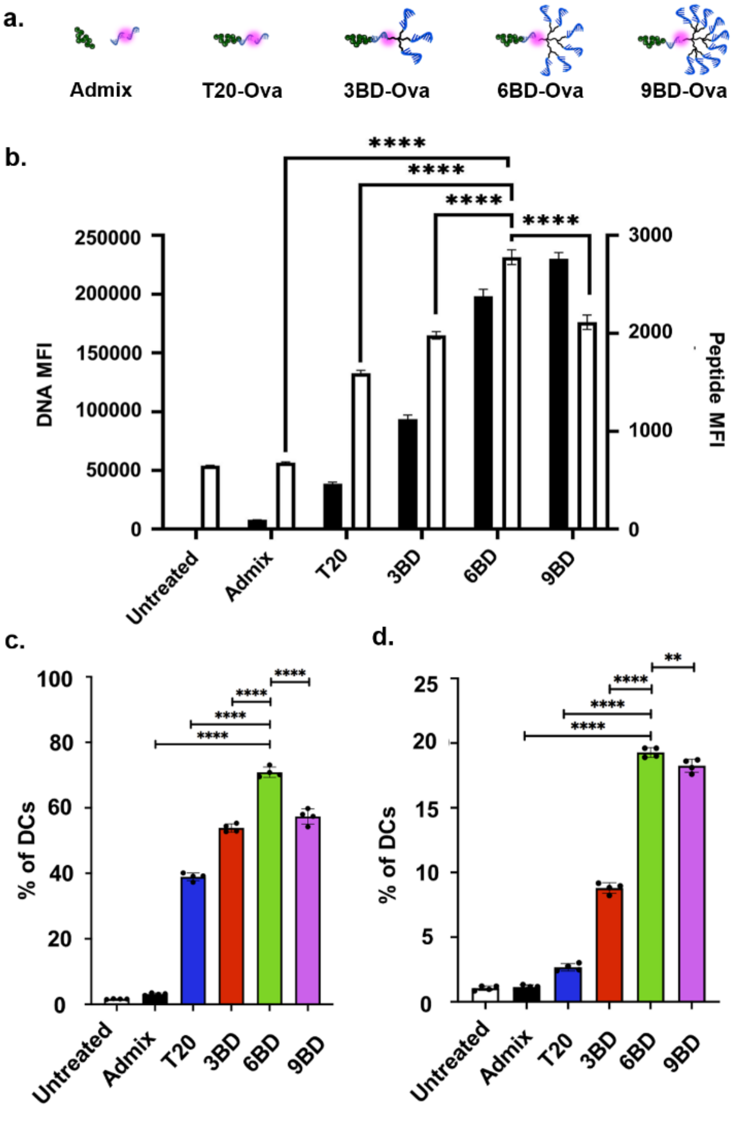

Figure 2.9. Dendron-mediated delivery of Ova
(a) Depiction of DNA-Ova conjugates. (b) The individual MFI for both the DNA (black) and peptide (white) show significantly greater uptake of both 6BD and 9BD compared to other structures, as determined by flow cytometry. (c) 6BD delivers both DNA and peptide to a greater percentage of cells compared to low valency dendrons and the admix solution, as determined by flow cytometry, measuring double-positive signals. (d) By measuring the fluorescence signal of an antibody that recognizes Ova-MHC binding using flow cytometry, 6BD and 9BD enable more efficient Ova peptide processing compared to lower valency conjugates and admix. Not all significances are shown for clarity. $^{**}p<0.01$, $^{****}p<0.0001$.

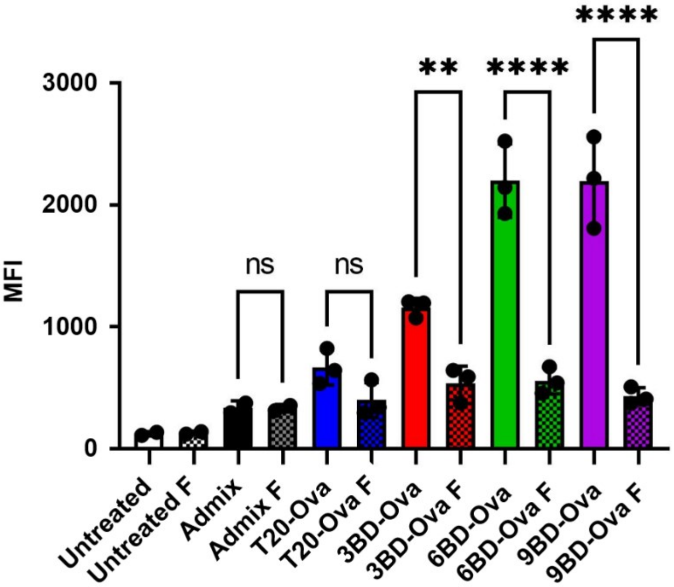

Figure 2.10. DNA dendron-Ova conjugate uptake by scavenger receptor A
Median fluorescence intensity (MFI) of cells treated with fluorescently tagged DNA at 250 nM for 1 h. Fucoidan treated groups are denoted with an F. Not all significances are shown for clarity. $**p<0.005$, $****p<0.0001$.

To investigate whether DNA dendron conjugation affected the cellular processing of the peptide, we measured the frequency at which the Ova peptide binds to a receptor, the major histocompatibility complex (MHC). The MHC is responsible for recognizing immunogenic peptides and, based on those peptide sequences, teaching other immune cells what to target.[155] We quantified the percentage of cells that have the Ova peptide bound to MHC using a commercially available antibody, and observed that increasing the valency of dendron conjugates significantly increased Ova-MHC complexation. While cells treated with the T_{20} conjugate have a 2-fold increase in MHC bound Ova compared to admix, those treated with higher valency 6BD and 9BD conjugates yield a 15-fold increase in MHC bound Ova, ultimately displaying the Ova peptide on *ca.* 20% of the DC population (**Figure 2.9.d**). This enhancement is due to the dendrons' ability to induce rapid uptake while simultaneously preventing extracellular peptide degradation. Importantly, these findings validate that dendron conjugation does not impede the cellular processing of the peptide. The Ova peptide requires trafficking to the ER in order to be properly processed by the cell, which was confirmed by confocal microscopy (**Figure 2.11.**). This observation is attributed to the metastability of the disulfide bond connecting the peptide to the dendron, since reducing conditions intracellularly lead to dendron cleavage and release of the peptide for MHC binding. From these results, we conclude that the 6BD and 9BD dendrons are capable of carrying biomolecules, which have been extremely difficult to deliver in the past, into cells and that dendron-delivered peptides are taken up and recognized by the cell for subsequent processing. Furthermore, these DNA dendron-peptide conjugates provide a novel route to develop powerful peptide-based vaccines, as demonstrated by their enhanced uptake and function when compared to admix solutions, a common clinical vaccine formulation.[161-162]

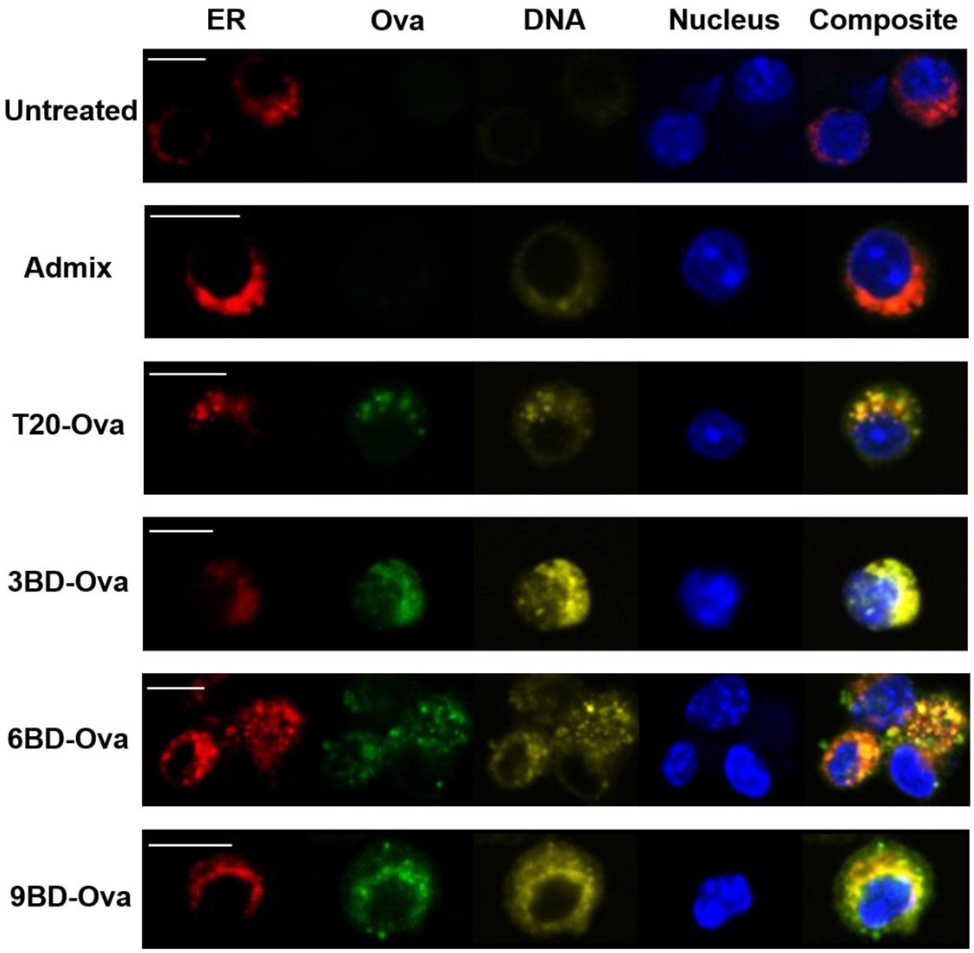

Figure 2.11. Representative confocal images of cells treated with DNA-Ova conjugates
Images show clear colocalization of samples within the cell, as well as within the ER of cells. Scale bar = 10 µm.

2.5. Dendron-Mediated Delivery of a Therapeutically Relevant Peptide

The Ova peptide, however, is a model system. To determine whether comparable improvements in uptake and function are observed when delivering a clinically relevant peptide, we investigated how dendron-mediated delivery of the thymosin alpha 1 peptide (Ta1) impacts cellular response. Ta1 is a peptide that is naturally produced by the thymus gland and is essential for an active immune response by functioning as an adjuvant and binding to toll-like receptor-9.[163] It is clinically used to treat hepatitis, cancer, HIV-AIDS, and Covid-19, due to its vast, self-regulating immune cell activation.[164-171] Its ability to activate immune cells for cytokine production and stem cell differentiation without causing cytokine storms has led to its widespread use to treat immunocompromised patients.[164-173] We assessed whether the dendron can be used to deliver Ta1 more effectively and efficiently such that a more potent downstream therapeutic response is observed compared to an unmodified Ta1 peptide, the current clinical formulation. As 6BD conjugates were most effective for the delivery of the model peptide, Ova, we selected this dendron to use in all future studies. Compared to Ta1 on its own and a T_{20}-Ta1 conjugate, DCs treated with the 6BD-Ta1 conjugate expressed significantly higher levels of the co-stimulatory marker CD86, a result of immune cell activation (**Figure 2.12.a**).

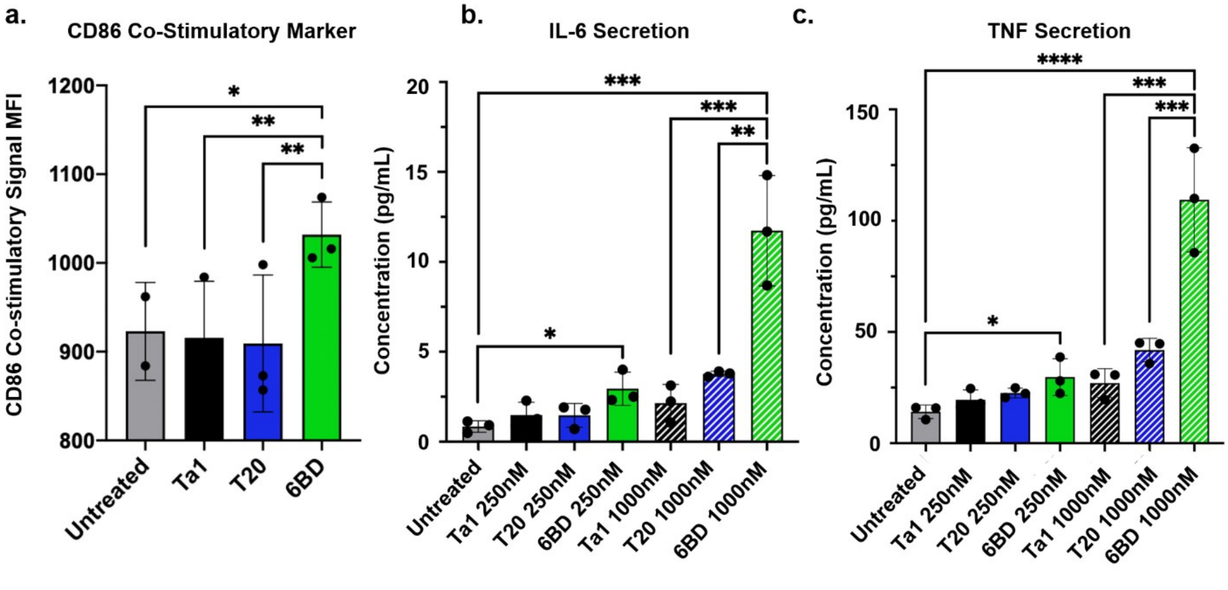

Figure 2.12. DNA dendron mediated delivery of the clinically- relevant peptide, Ta1
(a) Enhanced immune cell activation, as evidenced by CD86 costimulatory marker expression, for cells treated with 6BD-Ta1. (b,c) Enhanced downstream effects are observed when delivering Ta1 as a dendron conjugate as evidenced by increased secretion of cytokines, interleukin-6, and tumor necrosis factor. Both cytokines are indicative of widespread immune activation. *$p<0.05$, **$p<0.01$, ***$p<0.001$, ****$p<0.0001$.

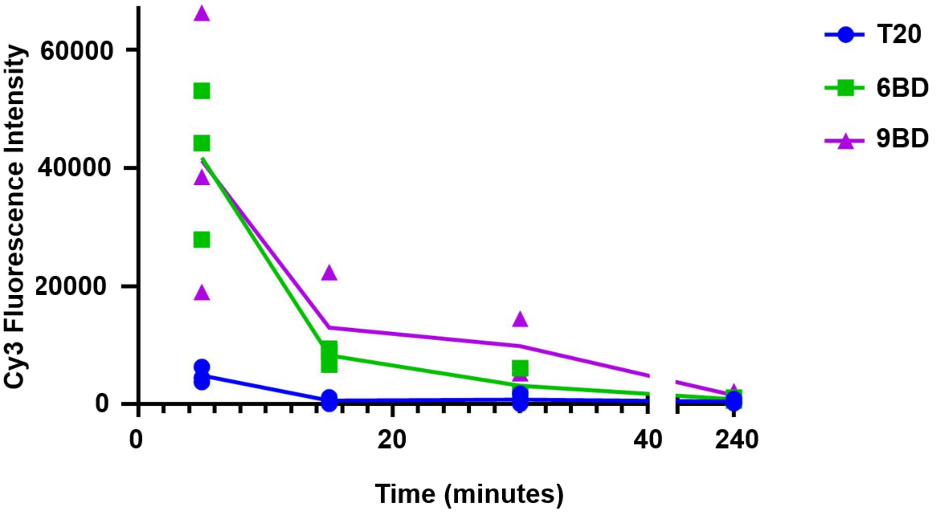

Figure 2.13. In vivo pharmacokinetics of DNA dendrons and a linear control
The clearance of T_{20}, 6BD, and 9BD were studied by measuring the fluorescence in plasma. Raw data points as well as the geometric mean at each time point are depicted.

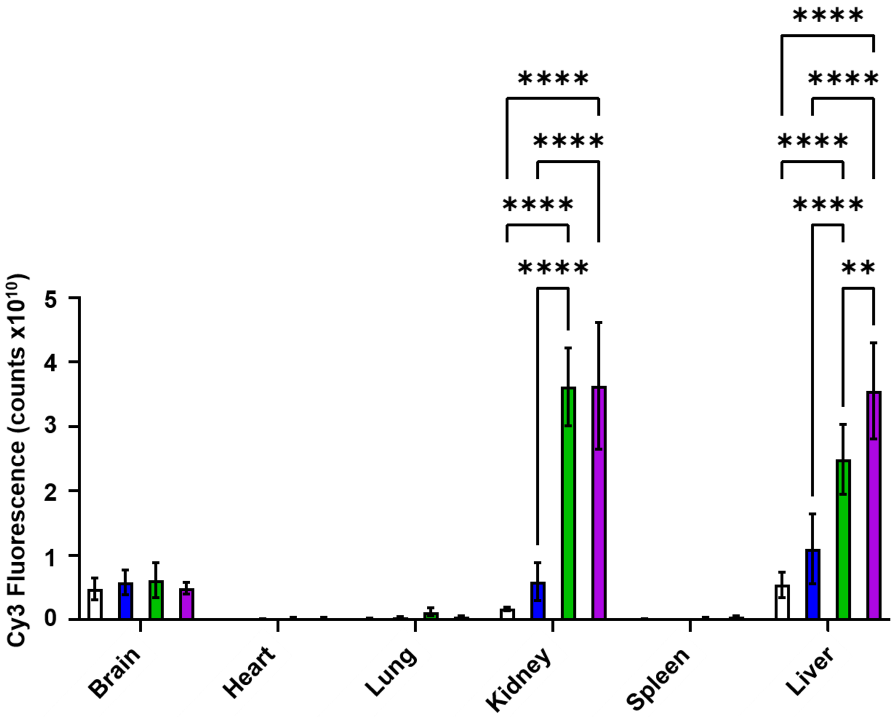

Figure 2.14. In vivo biodistribution
Biodistribution was determined by NIRF imaging studies using a Caliper Life Sciences In Vivo Imaging System (IVIS) to determine the extent of DNA dendron accumulation in main organs after 1-hour post-injection. Female CD1 mice (28-30 g) were administered intravenously at a dose of 3 nmoles / mouse. Mice (n = 3) were humanely euthanized by cardiac perfusion with 1x PBS while anesthetized. Tissues were harvested and fixed in 4% paraformaldehyde. Organs were imaged using an IVIS system and data was quantified by measuring fluorescence counts with the Living Image software (Fig. S8).

By measuring downstream cytokine secretion, we studied the impact of Ta1 delivery on additional immune cell signaling. We found that the 6BD-Ta1 conjugate significantly out-competed both the unmodified Ta1 peptide and the T_{20} conjugate, at various concentrations, in inducing secretion of interleukin 6 (IL-6) and tumor necrosis factor α (TNF-α) (**Figure 2.12. b, c**), cytokines important for widespread immune activation.[174-175] Ultimately, this shows that the 6BD dendron is capable of delivering functional, therapeutically relevant peptides more efficiently and effectively than current clinical formulations, resulting in a stronger, downstream cellular response. Supported by *in vivo* pharmacokinetic and biodistribution studies (**Figure 2.13., 2.14.)**, these dendrons hold potential for future clinical applications. We have further shown that the DNA dendron can be used as a tag for the cellular delivery of small proteins and as a way to maximize the DNA loading on proteins that have a limited number of reactive surface residues. These results are presented in **appendix 1**.

In conclusion, we have developed a general approach to deliver functional biomolecules into cells utilizing molecularly defined DNA dendrons. Their ease of synthesis and functionalization points to their potential for use as cellular delivery agents for a variety of materials (i.e. small molecules, DNA/RNA, peptides, and proteins). Indeed, DNA dendrons provide a simple, effective, and biocompatible approach to deliver various diagnostic and therapeutic materials to living systems that were previously difficult, if not impossible, to deliver to cells. Therefore, the DNA dendron is poised to have a significant impact on the development of next generation diagnostic tools, vaccines, and therapeutics.

CHAPTER THREE

Elucidating DNA Dendron Structure-Function Relationships for Vaccine Design

Material in this chapter is based upon:

Distler, M. E.; Cavaliere, J.; Teplensky, M. H.; Evangelopoulos, M.; Mirkin, C. A., DNA Dendron-Based Molecular Vaccines. **2022,** *Submitted*.

3.1. Investigating Structure-Function Relationships of Cancer Vaccines

Immunotherapy has emerged as a powerful approach to treat cancer due to its ability to train the immune system to attack specific cancer cells and reduce off target effects.[176-180] Cancer vaccines function *via* the delivery of two components: an adjuvant (an immune system activator) and an antigen (an immune system target).[181-182] Nanomaterials are particularly attractive agents for the delivery of adjuvant and antigen components because they provide unprecedented control over vaccine properties.[178, 181-188] Indeed, the rational design of nanoscale therapeutics allows one to tune the biodistribution, codelivery, kinetics of component processing, and temporal degradation of the vaccine, all of which are critical factors that determine vaccine efficacy.[189-194] These findings are the foundation for rational vaccinology and underscore the importance of vaccine structure and architecture in dictating vaccine function.

The SNA, a nanoparticle core functionalized with a dense shell of radially oriented DNA, has emerged as a powerful platform to study concepts in rational vaccinology because it enables fine-tuned control over vaccine structure.[108-110, 112, 195-196] Due to the modularity of the SNA design, key parameters such as adjuvant and antigen ratios,[109] antigen attachment chemistry,[108, 112] and SNA stability[196] can be modified independently, enabling the exploration of important structural considerations. As with many nanoparticle-based systems however, achieving molecularly defined structural control over the SNA is a challenge due to the inherent chemical isotropy of many nanoparticle cores. As a result, SNAs are prone to dispersity, specifically with regards to DNA surface coverage, antigen conjugation, and nanoparticle size, resulting in no two SNAs being identical; thus, codifying resultant structure-function relationships is difficult.[197] DNA dendrons have emerged as a molecularly-defined approach to access SNA properties.[198-199] These dendritic architectures consist of single stranded DNA stems that branch into multiple DNA strands. Similar to the SNA, these multivalent DNA constructs undergo rapid cellular uptake, are resistant to degradation, and elicit an enhanced therapeutic effect of conjugated cargo.[198] We hypothesized that by utilizing the DNA dendron as the basis for a cancer vaccine, structure-function relationships could be probed in a molecularly-defined manner, providing novel insights into vaccine design and function.

Herein, we report the design, synthesis, and application of DNA dendron-based molecular vaccines as potent cancer immunotherapies. We investigated how adjuvant placement and attachment chemistry impacts dendron uptake and adjuvant potency. By conjugating an antigenic peptide, derived from cervical cancer due to human papillomavirus (HPV), to different positions on the dendron architecture, we Investigated how antigen placement impacts cellular uptake and immune activation of the vaccine. Finally, we utilized these structures to train immune cells to target and kill cancer cells, both *in vitro* and *in vivo*, which demonstrated that vaccine efficacy is structure dependent. Taken together, we establish the DNA dendron as a powerful tool to study the fundamental structure-function relationships that govern cancer vaccine efficacy. Further, we demonstrate the DNA dendrons themselves behave as potent vaccines with far-reaching potential as a new class of cancer immunotherapeutics.

3.2. Design, Uptake, and Efficacy of Immune Stimulating DNA Dendrons

The adjuvant is a key component of a vaccine because it leads to immune activation and cellular processing of the antigen target.[200] Previous work has shown that increasing valency of the DNA dendron (and thereby the number of adjuvant sequences) expectedly leads to increased immune activation,[201] however important structural questions, such as the effects of steric hinderance and DNA hybridization are yet to be explored and can have a significant impact on adjuvant function (*vide infra*). When considering multivalent adjuvant delivery and efficacy, steric hinderance can play a crucial role in determining adjuvant potency. To that end, we designed four different six-branched DNA dendrons that contain adjuvant CpG DNA sequences (cytosine-phosphate-guanine that is an agonist to TLR-9): 1. a T10 sequence stem that branches into six CpG sequences (termed Dn6a, for dendron with 6 adjuvant strands), 2. a T10 sequence stem that branches into six CpG complementary sequences that hybridize the CpG sequences (termed Dn6aH, for dendron with 6 adjuvant strands hybridized), 3. a CpG sequence stem that branches into six T10 sequences (termed Dn1a, for dendron with 1 adjuvant strand), and 4. a CpG complement stem that can hybridize the CpG strand and branches into six T10 sequences (termed Dn1aH, for dendron with 1 adjuvant strand hybridized) (**Figure 3.1 A**). These designs enabled us to probe steric effects in different ways. The Dn6a *versus* Dn1a comparison established if

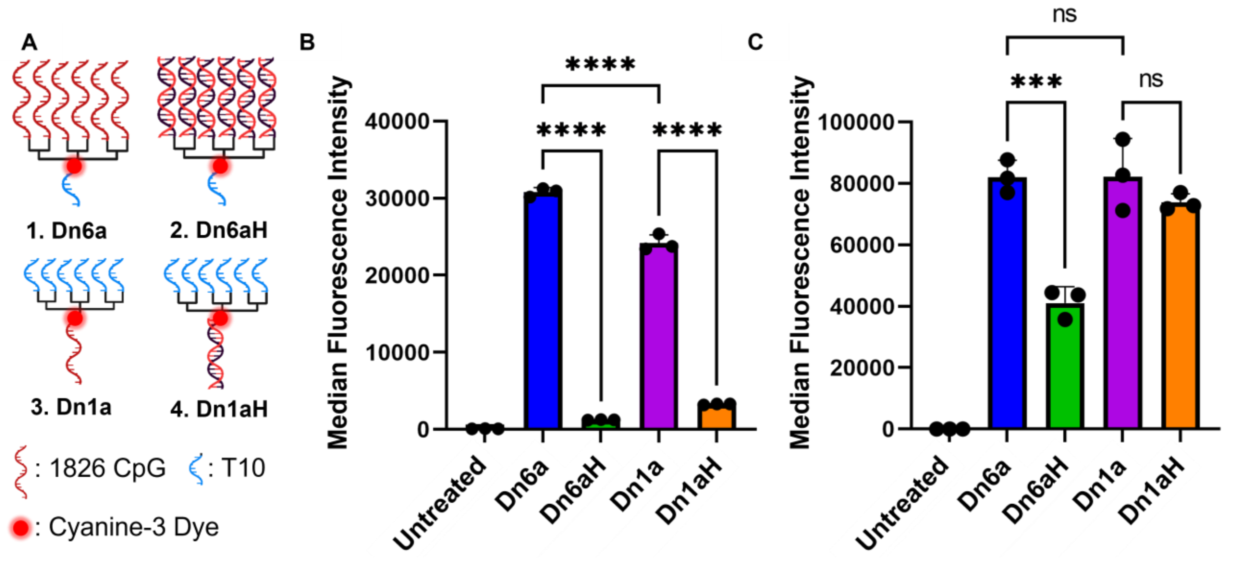

Figure 3.1. Cellular uptake of immune stimulating DNA dendrons
(A) Four different DNA dendron designs were investigated: 6 CpG sequences as the branches and a T10 stem (Dn6a), 6 CpG sequences hybridized to the branches and a T10 stem (Dn6aH), T10 branches and a CpG stem (Dn1a), T10 branches and a CpG sequence hybridized to the stem (Dn1aH). All DNA dendrons were designed to have a cyanine 3 fluorescent dye in the middle of the molecule. (B) Cellular uptake after 1 h incubation at 250 nM shows the unhybridized structures have preferential access to cells. (C) Cellular uptake after 15 h incubation at 1 μM shows this trend holds, with hybridized branches having lower cellular uptake. The MFI +/- standard deviation (SD) is shown. ns = not significant; *** = p<0.001; **** = p<0.0001. Not all significances are shown for clarity.

multivalency truly improves adjuvant function or if the closely packed branches results in impaired activation due to steric/electrostatic hindrance. The hybridized (Dn6aH and Dn1aH) *versus* unhybridized structures (Dn6a and Dn1a) reveal if the dendron molecule itself sterically inhibits proper toll-like receptor 9 (TLR-9) binding and processing and if a supramolecular dendron design is therefore necessary for potent activation. For *in vitro* measurements via flow cytometry, all DNA dendrons were synthesized with a cyanine 3 fluorescent dye in the middle of the structure, which not only allowed for a quantitative assessment of dendron uptake, but also allowed for facile tracking of the dendron throughout synthesis and purification. The DNA dendrons were synthesized through solid-phase automated synthesis, purified by polyacrylamide gel electrophoresis (PAGE), and characterized by PAGE and Matrix Assisted Laser Desorption/Ionization Time of Flight Mass Spectrometry (MALDI-TOF MS) (**Table 3.1**). To form the hybridized structures, CpG can duplex with the DNA dendron branches or stems, when added

Table 3.1. DNA design and characterization

Name	**DNA Sequence (5' - 3')**	**Calc'd MW**	**Exp't MW**
1826 CpG	TCC ATG ACG TTC CTG ACG TT	6059	6057
Dn1a	TTT TTT TTT T D Tr Sp Cy3 TCC ATG ACG TTC CTG ACG TT	26643.94	26701
Dn1aH	TTT TTT TTT T D Tr Sp Cy3 AAC GTC AGG AAC GTC ATG GA	26760.04	26767
Dn6a	TCC ATG ACG TTC CTG ACG TT D Tr Sp Cy3 TTT TTT TTT T	42038.84	42015
Dn6aH	AAC GTC AGG AAC GTC ATG GA D Tr Sp Cy3 TTT TTT TTT T	42735.44	42775
Dn1	TTT TTT TTT T D Tr Sp Cy3 TCC ATG ACG TTC CTG ACG T AmdT	26798.14	26803
Dn6m	TTT TT AmdT TTT T D Tr Sp Cy3 TCC ATG ACG TTC CTG ACG TT	27569.24	27588
Dn6e	AmdT TTT TTT TTT D Tr Sp Cy3 TCC ATG ACG TTC CTG ACG TT	27569.24	27553

Acronyms for Phosphoramidites:
Sp: 18-O-Dimethoxytritylhexaethyleneglycol,1-[(2-cyanoethyl)-(N,N-diisopropyl)]-phosphoramidite (Spacer phosphoramidite 18)
D: 1,3-bis-[5-(4,4'-dimethoxytrityloxy)pentylamido]propyl-2-[(2-cyanoethyl)-(N,N-diisopropyl)]phosphoramidite (Symmetric doubler phosphoramidite)
Tr: Tris-2,2,2-[3-(4,4'-dimethoxytrityloxy)propyloxymethyl]methyleneoxypropyl-[(2-cyanoethyl)-(N,Ndiisopropyl)]-phosphoramidite (Long trebler phosphoramidite)
Cy3: 1-[3-(4-monomethoxytrityloxy)propyl]-1'-[3-[(2-cyanoethyl)-(N,N-diisopropyl) phosphoramidityl]propyl]-3,3,3',3'-tetramethylindocarbocyanine chloride (Cyanine 3 phosphoramidite)
AmdT: 5'-Dimethoxytrityl-5-[N-(trifluoroacetylaminohexyl)-3-acrylimido]-2'-deoxyUridine,3'-[(2-cyanoethyl)-(N,N-diisopropyl)]-phosphoramidite (Amino Modifier C6 dT)

at stoichiometric amounts and annealed from 90 to 20 °C, over 1 h, as characterized by native PAGE (**Figure 3.2**).

First, we determined how each of these DNA dendron designs impacted cellular uptake efficiency. To test this, murine bone-marrow-derived dendritic cells (BMDCs) were treated with 250 nM fluorescently labeled DNA dendrons (1:1 ratio of dendron molecule to fluorescent tag) for 1 h in serum-containing media. Cellular uptake was assessed by measuring the median fluorescence intensity (MFI) of the cyanine-3 fluorophore, in treated cells, via flow cytometry. After 1 h, we observed that hybridization of the CpG sequence led to a significant decrease in cellular uptake (**Figure 3.1. B**), presumably due to a decrease in DNA-scavenger receptor A recognition, which may arise from increased rigidity or steric hinderance. The non-hybridized structures had MFIs over two orders of magnitude greater than those of the hybridized structures,

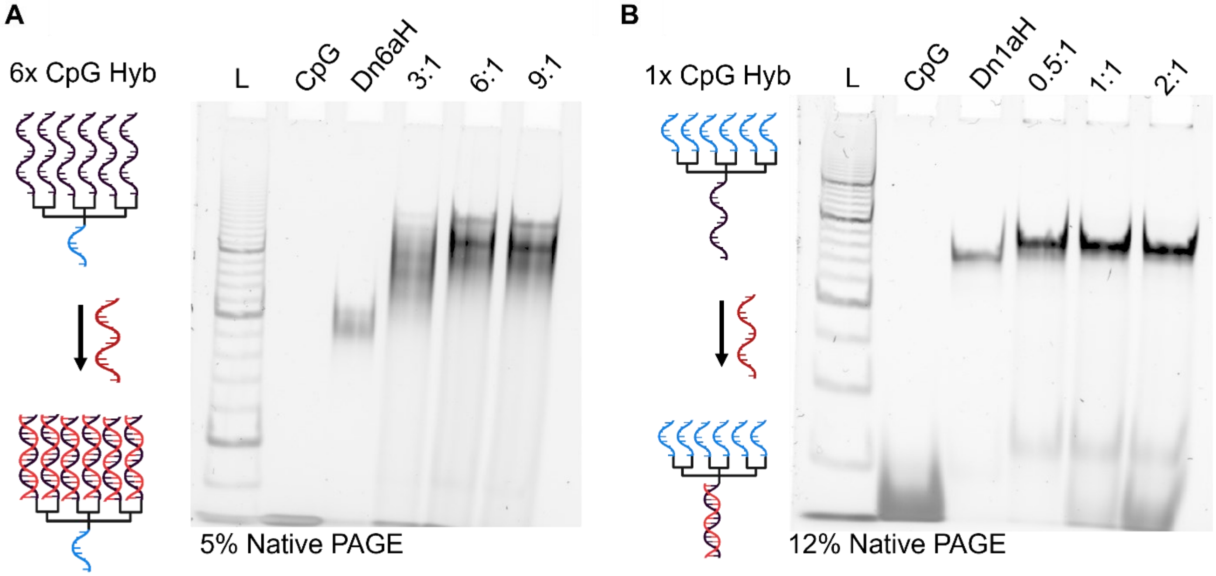

Figure 3.2. Hybridized dendron structure formation
Hybridized dendron design, Dn1aH and Dn6aH, were formed by combining the DNA dendrons with the CpG strands at stoichiometric amounts and annealing from 90-20 °C over 1 h. By tuning the relative amount of CpG added, we determined that a 1:1 ratio of CpG complement to CpG strand works to form the full hybridized structure for Dn6aH (left) and Dn1aH (right).

indicating that dendron uptake is maximized when the branches are single stranded DNA. The Dn6a treated cells also had a 1.2-fold increase in MFI compared to those treated with the Dn1a. This observation can be attributed to the fact that longer DNA sequences can lead to increased uptake efficiencies (**Figure 3.3.**).[198] To measure adjuvant function, a higher concentration and longer timepoint was necessary. We first assessed how these changes impacted cellular uptake. To do so, this experiment was repeated but at a treatment concentration of 1 μM and an incubation time of 15 h. Even at this later timepoint, we see that the non-hybridized structures enter cells in greater quantity than the hybridized forms. Specifically, the Dn6aH structure suffers from low uptake indicating that the double stranded dendron branches significantly inhibits cellular uptake (**Figure 3.1. C**).

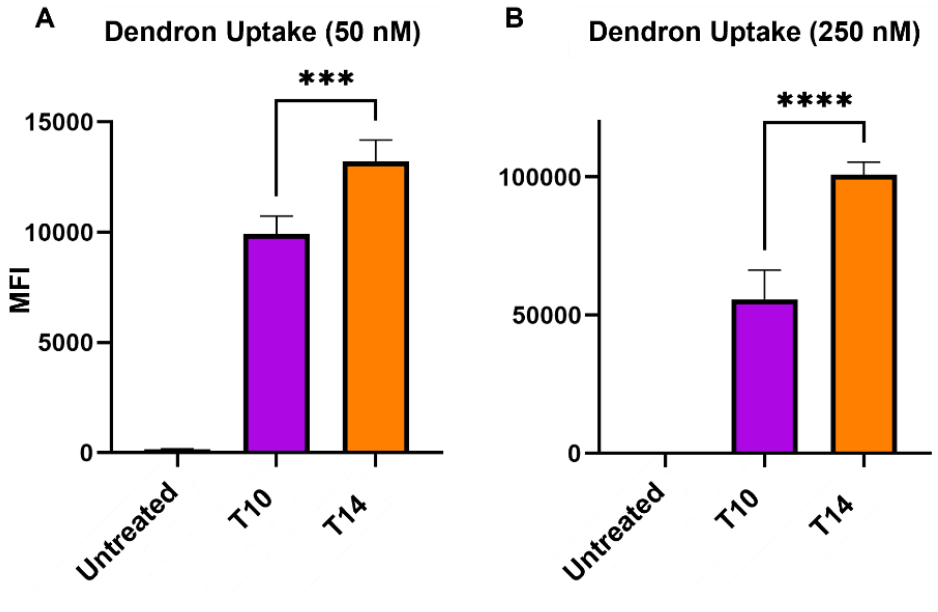

Figure 3.3. Dendron uptake with increasing branch length
Cells were treated with DNA dendrons that contained either T10 branches or T14 branches. Only at early timepoints do we observe that longer branches result in increased cellular uptake at treatment concentrations of 50 and 250 nM after 1 h.

In addition to enhanced cellular delivery of the adjuvant, we confirmed that the dendron architecture does not prohibit adjuvant interactions with TLR-9. To test this, immune activation was measured in response to a linear CpG control or the four dendron designs. Upon TLR-9 activation by CpG adjuvant DNA, immune co-stimulatory markers, such as cluster of differentiation (CD) 86 and CD80 become upregulated and presented on the dendritic cell surface.[202] We can assess which dendrons illicit the greatest immune response by measuring the amount of CD80 and CD86 expressed. To address the fact that the Dn6a and Dn6aH structures deliver 6-fold more CpG per dendron than the Dn1a and Dn1aH structures, this experiment was conducted in two distinct ways. First, cells were treated such that the total dendron concentration was held constant (**Figure 3.4. A**). This meant that the Dn6a and Dn6aH treated cells were receiving 6-fold more CpG, but the amount of dendron molecule drug was the same for each group. Due to the two different CpG concentrations, two linear CpG controls were used to match those concentrations (CpG 1, to match Dn1a, and CpG 6, to match Dn6a). In this case, we observed trends in CD86 and CD80 expression that match the uptake profile of the different groups – the Dn6a, Dn1a, and Dn1aH had no significant differences in CD86 and CD80 expression, while the Dn6aH structure produced significantly less CD86 and CD80 expression amongst murine CD11c+ dendritic cells. This trend held when the percent of cells positive for CD86 and CD80 expression was measured. Specifically, the Dn6a, Dn1a, and Dn1aH induced CD86 expression in nearly 100% of cells, while the Dn6aH structure induced expression in only 80% of cells (**Figure 3.5.**). These observations can be attributed to the lower cellular uptake of the Dn6aH, as discussed above. Furthermore, this indicates that although the Dn6a dendron was delivering 6-fold more CpG than the Dn1a and Dn1aH dendrons, the total immune activation was nearly identical. To further investigate this observation, cells were treated such that the CpG concentration was held constant across treatment groups. Therefore, cells treated with Dn6a and Dn6aH received 1/6th the amount of dendron molecule as those treated with Dn1a and Dn1aH (**Figure 3.4. B**). Interestingly, when the CpG concentration was held constant, a different trend in immune activation emerged. The Dn6a and Dn6aH structures resulted in significantly lower immune activation whereby CD86 and CD80 levels were reduced by approximately 50% and 33%, respectively, compared to the Dn1a and Dn1aH responses (**Figure 3.5.**). This indicates that although the Dn6a dendron presented CpG multivalently, this multivalency did not lead to increased CpG processing and cell activation, suggesting that dendron valency does not impart the proper spatial requirements necessary for multivalent interactions with TLR-9.[203] Taken together, these data reveal that the Dn1a and Dn1aH design is the most efficient dendron design for effective, adjuvant delivery. Due to synthetic ease and molecular precision, the non-hybridized Dn1a structure was selected as the base design moving forward. Moreover, since the branches of the DNA dendron are no longer used as the CpG sequence, they can be leveraged as orthogonal handles to improve cellular uptake (i.e., G-rich sequences) or as secondary functional sequences (e.g., alternative TLR agonist sequences) (**Figure 3.6.)**.

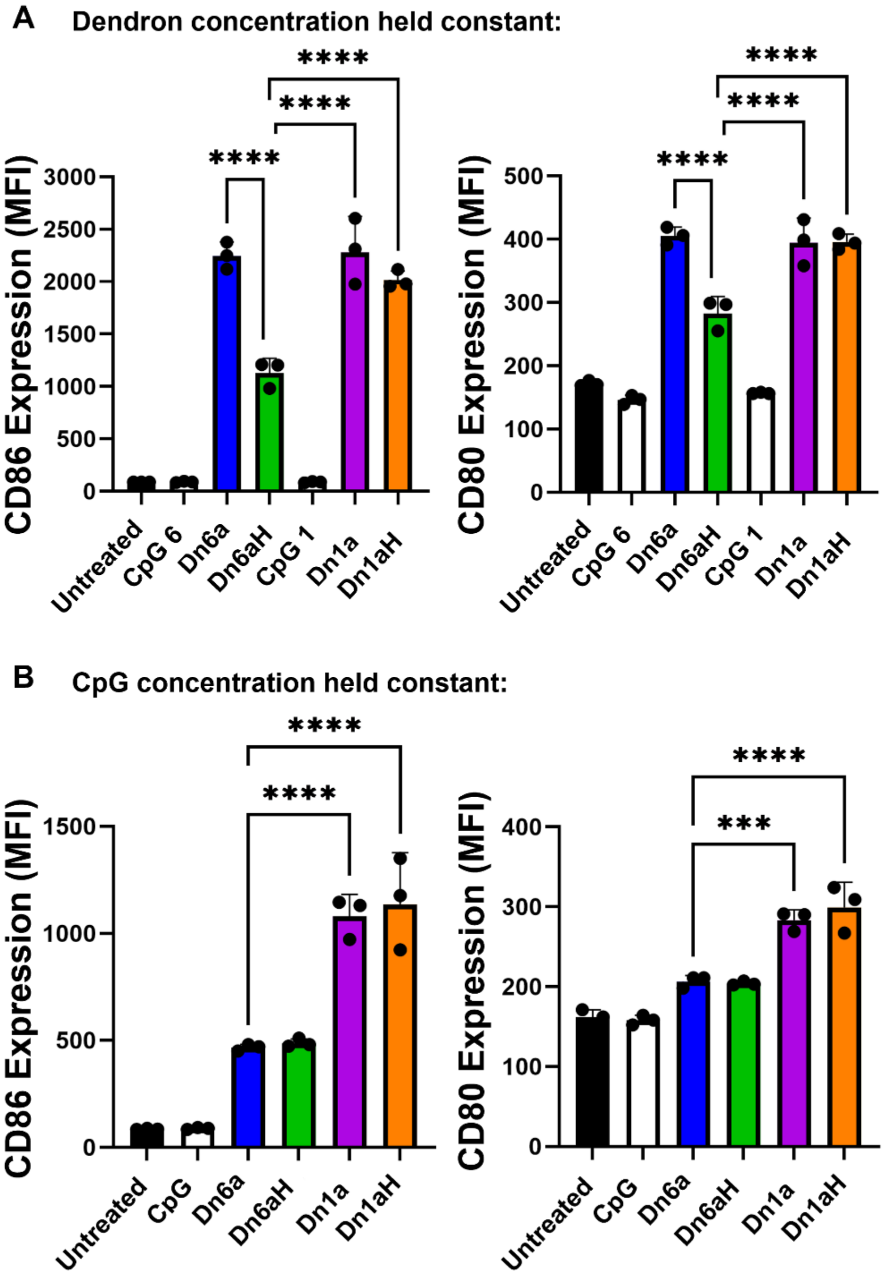

Figure 3.4.. Immune activation after treatment of *ex vivo* murine bone marrow-derived dendritic cells with immune stimulating DNA dendrons

(A) A linear CpG control and the four dendron designs were tested. (B) Median flourescnce intensity (left) and frquency (right) of CD86 expression when the total dendron concentration was held constant. A similar trend was observed as that in the uptake experiment, whereby the unhybridized structures perform better than the hybridized constructs with no signfiicant differences between 6x CpG, 1x CpG, and 1x CpG Hyb despite the 6-fold increase in CpG delivered by the 6x CpG dendron. (C) Median flourescence intensity (left) and frequency (right) of CD86 expression when the total CpG concentration was held constant. Results indicate that the 1x CpG dendron was the most efficient design to deliver functional DNA adjuvant. The MFI +/- standard deviation (SD) is shown. ns = not significant; *** = p<0.001; **** = p<0.0001. Not all significances are shown for clarity.

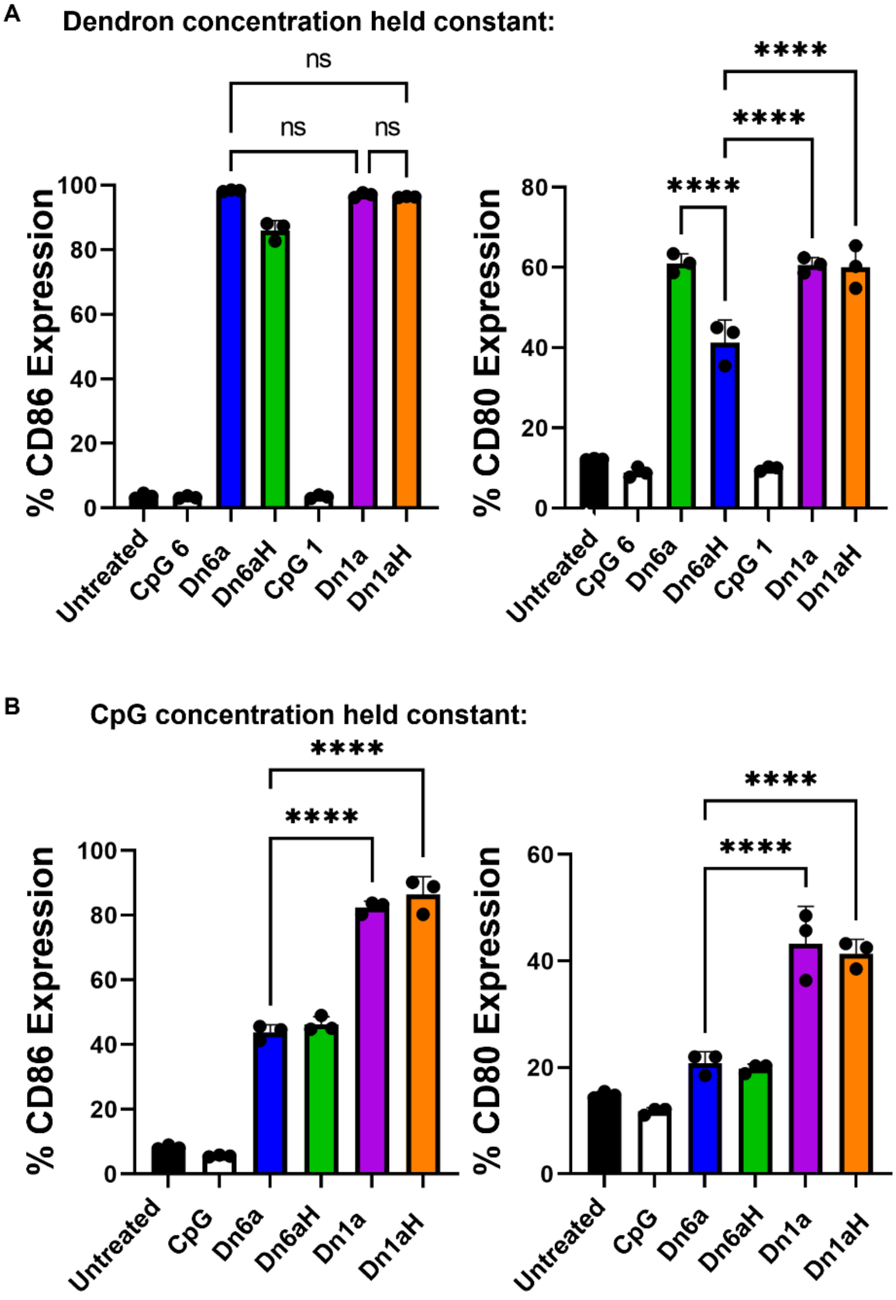

Figure 3.5. Frequency of cells expressing CD86 and CD80 in response to the different dendron designs
These trends match what is observed for the amount of CD86 and CD80 expression, with the greatest differences arising when CpG concentration is held constant.

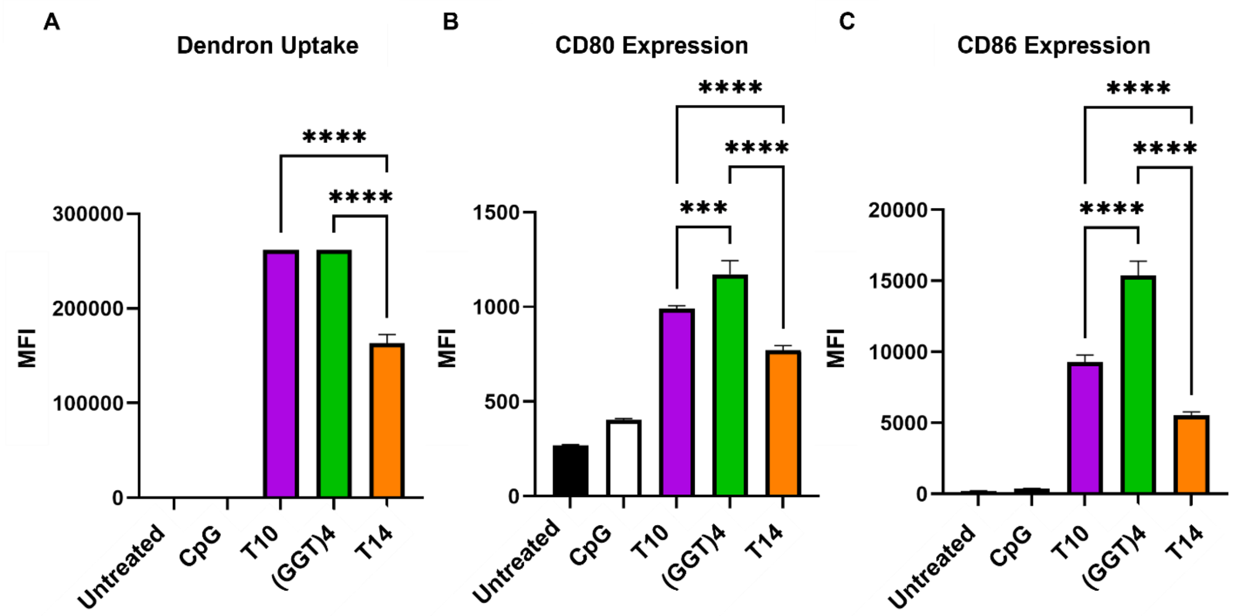

Figure 3.6. Sequence dependent dendron function
Dendritic cells were treated with either CpG linear control, Dn1a with T10 branches, Dn1a with G-rich branches ($(GGT)_4$), and Dn1a with T14 branches, which matches the G-rich sequence in number of bases. After 15 h, we observe that the G-rich branches have comparable uptake to the T10 branches, but results in a significant increase in DC activation (CD80 and CD86 expression).

3.3. Antigen Conjugation and its Effects on Immune Activation

Having established design rules for dendron-mediated adjuvant delivery, we next sought to understand how the placement of the antigenic peptide affects dendron vaccine efficacy. We hypothesized that antigen placement on the dendron would significantly impact dendron uptake and overall vaccine efficacy due to the hydrophobic nature of many peptide antigens[204] and the importance of antigen/adjuvant ratios on vaccine efficacy.[109] To begin exploring the impact of antigen placement, three dendrons were designed, all utilizing the Dn1a dendron identified above for enhanced adjuvant activity. The first contained a primary amine on the 3' end of the dendron stem such that a single antigen could be added to each structure (Dn1E, dendron with 1 epitope). The second design included primary amines on the 5' end of the dendron, thereby producing dendrons with 6 peptides on the ends of the branches (1 peptide / branch) (Dn6Ee, dendron with 6 epitopes on the end). To test whether peptide conjugation to the 5’ end impacted dendron uptake (due to a potential loss of scavenger receptor A binding interactions), the third design had primary amines located in the middle of each branch, enabling the conjugation of six antigen molecules without blocking the multivalent DNA branches (Dn6Em, dendron with 6 epitopes in the middle). The resultant dendrons were purified by PAGE and characterized by MALDI-TOF MS (**Figure 3.7. A**). Interestingly, these dendrons on their own, without conjugated antigens, had distinct uptake and activation properties. Specifically, the dendrons with more primary amine functional groups achieved nearly two-fold increases in cellular uptake (**Figure 3.8.**). This can likely be

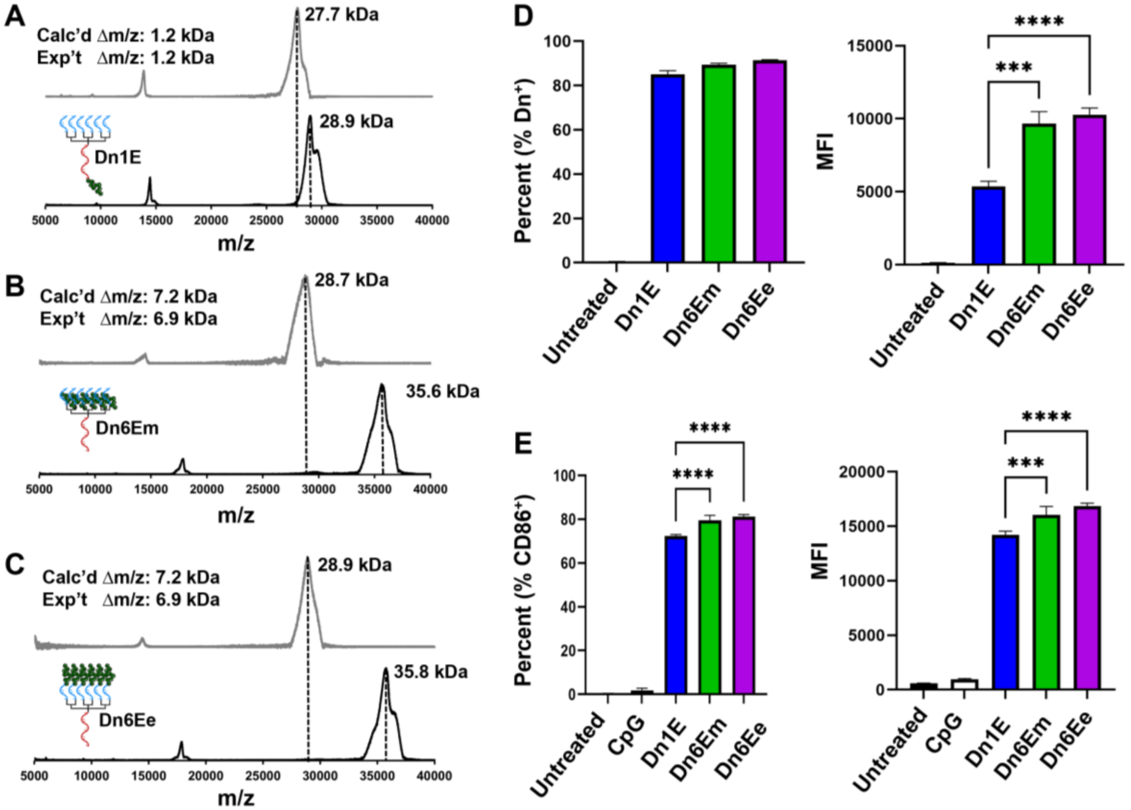

Figure 3.7. Antigenic peptide conjugation and its impact on cellular uptake and immune activation
(A-C) MALDI-TOF MS of dendron-peptide conjugates, post purification, reveal expected mass shifts for each of the synthesized conjugates: Dn1E, Dn6Em, and Dn6Ee. (D) Cellular uptake of the dendron-peptide conjugates after 1 h at 250 nM shows an increase in cellular uptake for the conjugates that contain a greater number of hydrophobic antigenic peptides. (E) Immune activation of dendritic cells after 15 h treatement at 1 µM. Results follow similar trends to the uptake experiment, whereby the Dn6E structures produced a stronger immune response than did the Dn1E structure. The MFI +/- standard deviation (SD) is shown. *** = $p<0.001$; **** = $p<0.0001$. Not all significances are shown for clarity.

attributed to the positive charge of the primary amine in biological conditions, which can facilitate cellular uptake.[205] Nevertheless, when the peptide is conjugated to the dendron through these primary amines, the positive charge is no longer a factor because the primary amine is converted to an amide.

We chose to work with the peptide antigen E649–58 (V10C, sequence: VYDFAFRDLC, **Table 3.2.**) derived from the E6 protein, which is found in cervical cancer cells caused by human papillomavirus (HPV). The peptide contains a single, terminal cysteine amino acid that was used to conjugate to the dendron through a reducible disulfide bond. Specifically, the heterobifunctional crosslinker, succinimidyl 3-(2-pyridyldithio)propionate (SPDP), was used, which contains an activated ester on one end, used for primary amine functionalization, and a pyridyldithiol group on the other end, used for sulfhydryl functionalization. First, the activated ester was reacted with the primary amines on the DNA dendrons, producing pyridyldithiol functionalized strands. Second, the E6 peptide was reacted with the pyridyldithiol to form peptide conjugates. All conjugates were purified by PAGE and characterized by MALDI-TOF MS. MALDI results

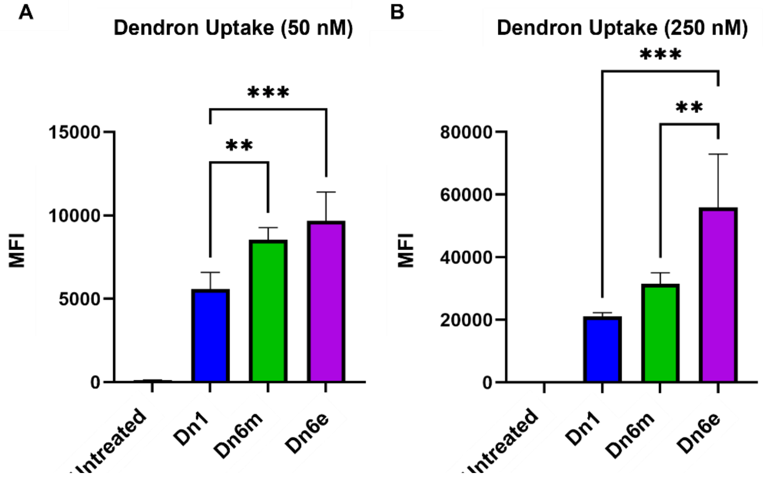

Figure 3.8.. Effects of primary amines on dendron uptake
Dn1, Dn6m, and Dn6e are the dendrons that contain primary amines before peptide conjugation. It appears that these amines can impact the cellular uptake of the dendron. Dn6m and Dn6e both have 6 primary amines and significantly higher cellular uptake than Dn1 which only has 1 primary amine. Furthermore, Dn6e, which has all of the amines on the 5’ terminal end of the dendron was taken up significantly more than the Dn6m, which had amines “buried” in the middle of the branches.

Table 3.2. Peptide sequence used in this study

Name	Amino Acid Sequence (N - C)	MW
$E6^{49-58}$ (V10C)	VYDFAFRDLC	1248

Peptides were obtained through GenScript at ≥95% purity.

indicate that for each of the dendron designs, the expected product was produced and purified successfully because the expected mass shifts between unconjugated and conjugated DNA dendrons (**Figure 3.7. A-C** top *verses* bottom) were observed. Specifically, the Dn1E structure shows a mass shift of 1.2 kDa, while the Dn6E structures show a mass shift of 6.9 kDa, closely matching the expected changes in mass for dendrons with one and six peptides, respectively.

After synthesizing the dendron peptide conjugates, we sought to understand how peptide placement affects cellular uptake. We hypothesized that the increased hydrophobicity as a result of peptide conjugation would facilitate uptake and lead to increased uptake frequency and fluorescence intensity. Using flow cytometry, we found that though the structures were taken up at a similar frequency, the increased number of conjugated peptides led to a clear increase in the amount of dendron per cell, based on the MFI. Cells treated with Dn6Em and Dn6Ee experienced a 100% increase in MFI compared to those treated with the Dn1E structure (**Figure 3.7. D**). A similar trend was observed when measuring immune activation via CD86 expression (**Figure 3.7. E**). We measured a significant increase in the frequency of cells expressing CD86 from 75% to 80%, for those treated with either Dn6Em or Dn6Ee compared to Dn1E. When measuring the amount of CD86 expressed (MFI), we observed a similar trend as seen in the uptake experiments, wherein the Dn6E structures led to the expression of more CD86 than the Dn1E dendron (**Figure 3.7. E**). A similar trend was also observed when measuring the CD80 costimulatory marker (**Figure 3.9.**). These results confirmed the hypothesis that increasing the number of peptides attached leads to increases in cellular uptake. Due to the similarity in uptake and activity for the

Dn6Em and Dn6Ee constructs, we chose to continue experimenting with the Dn6Em structure for synthetic reasons, finding that Dn6Em peptide conjugation consistently had a 30% yield while the Dn6Ee structure had a 15% yield.

We further explored the uptake mechanism of these materials by selectively inhibiting uptake pathways (**Figure 3.10.**). Specifically, cells were pre-treated with either fucoidan (scavenger receptor A inhibitor), methyl-β-cyclodextrin (cholesterol/lipid raft depletion), or incubated at 4 ℃ (inhibits all active transport mechanisms). We observed that inhibiting active transport through incubation at 4 ℃ resulted in the greatest decrease in uptake for each of the peptide conjugates, indicating that these peptides were not facilitating significant passive transport across the cell membranes. After treatment with methyl-β-cyclodextrin, which abstracts hydrophobic cholesterol and lipid rafts from the cell surface, we observed a decrease in cellular uptake, which is likely due to decreased interactions between hydrophobic peptides and hydrophobic components of the cell membrane. Finally, we observed that by inhibiting scavenger

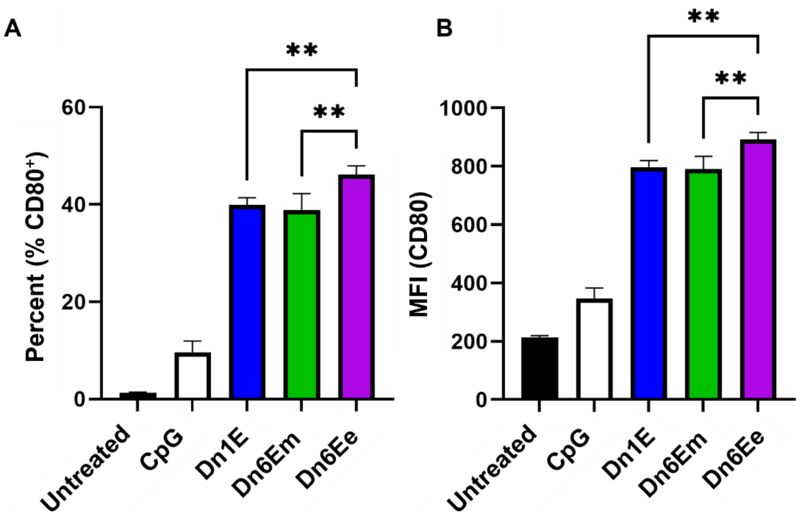

Figure 3.9. CD80 expression in response to dendron-peptide conjugates
Cells treated with the peptide conjugates showed increases in CD80 expression frequency and amount. These trends match what was observed for the CD86 costimulatory marker.

receptor A mediated endocytosis, using fucoidan, the most significant drop (at least 50% in each treatment group) in uptake was observed, indicating that the primary method of dendron uptake was through scavenger receptor A, regardless of where the antigenic peptide was located on the dendron.

3.4. Investigating Vaccine Efficacy Ex Vivo and In Vivo

Before studying vaccine efficacy in vivo, we first confirmed that the DNA dendron vaccines can produce a potent and specific immune response against cervical cancer cells. Mouse peripheral blood mononuclear cells (PBMCs) were treated with the different vaccines. The resultant matured T cells were isolated from the PBMCs and incubated in the presence of TC-1 mouse cervical cancer cells at a 10 to 1 ratio of T-cells to cancer cells. After incubation, cancer cell death was quantified by measuring 7-AAD (necrosis) and Annexin V (early apoptosis). We observed that all tested DNA dendrons produced a potent immune response against the target cancer cells. Cells treated with the Dn1E vaccine killed 30% of the target cancer cells based on

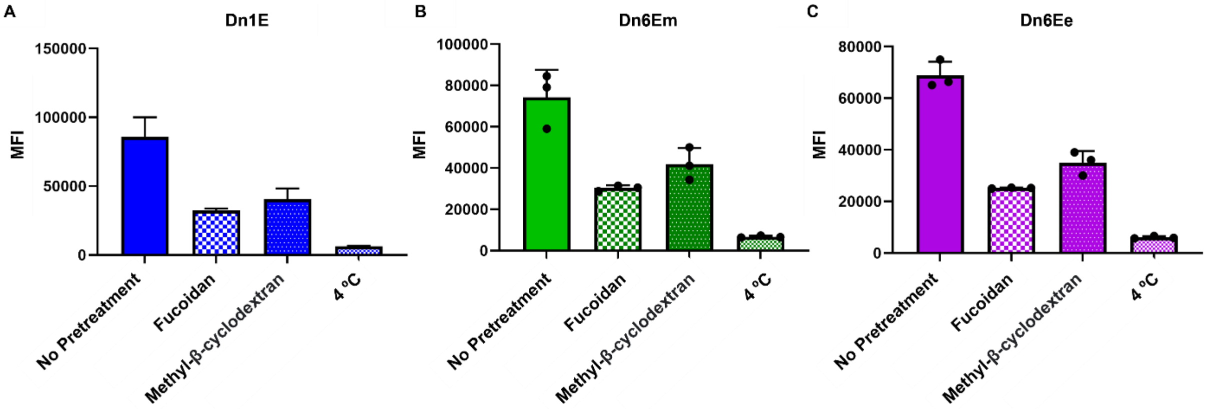

Figure 3.10. Dendron conjugates uptake pathway
Cells were treated with peptide-dendron conjugates after pretreatment with either fucoidan (Scav A inhibitor), methyl-beta-cyclodextrin (lipid raft and cholesterol depletion), or after incubation at 4 °C (active transport inhibitor). Dendrons are significantly taken up by active transport, which is mostly facilitated by Scavenger receptor A and partly by hydrophobic mediated methods.

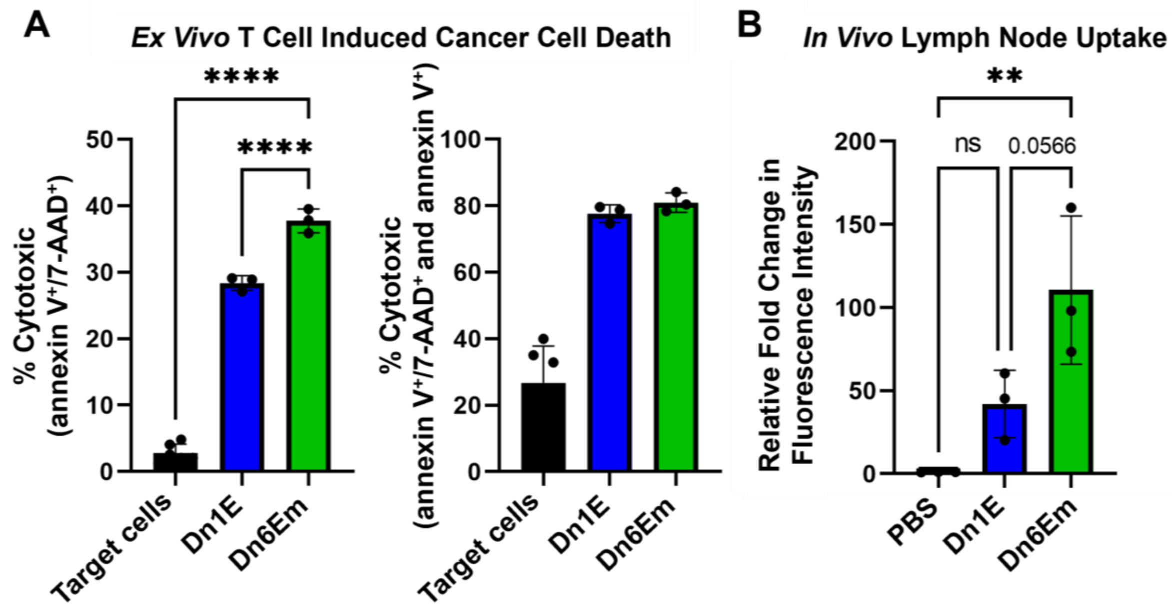

Figure 3.11. ***Ex vivo*** **vaccine efficacy and** ***in vivo*** **vaccine uptake**
(A) Murine PBMCs were treated with the dendron vaccines, mature T cells were then isolated and incubated in the presence of target TC-1 cancer cells, and cell death was quantified in terms of expression of both necrosis and early apoptosis markers (double positive, left) or early apoptosis markers (double and single positive, right). (B) Dendron vaccines were injected subcutaneously into female C57BL/6 mice (n=3) and fluorescence intensity of the lymph nodes was measured after 4 h, using IVIS. Results indicate that the Dn6Em structure was taken up significantly more than the Dn1E structure in vivo. ** = $p<0.01$; *** = $p<0.001$; **** = $p<0.0001$. Not all significances are shown for clarity.

expression of both apoptotic and necrotic markers, while, cells treated with Dn6Em killed 40% of the target cells (figure 4A, left). If the target cells that were expressing only apoptotic markers, indicating that they are undergoing early apoptosis but not yet full necrosis, were included in this measure, we find that both vaccines killed approximately 80% of the target cells (**Figure 3.11. A**, right). Since early apoptosis occurs prior to necrosis, these results suggest that the vaccines produce an immune response at different rates. Therefore, the Dn6Em vaccine seems to result in a potent immune response earlier than the Dn1E vaccine, leading to a greater number of necrotized target cells. This observation is likely due to the increase in antigen loading on the Dn6Em structure, as well as its increased cellular uptake.

To further assess the potential *in vivo* efficacy of the dendron vaccines, we next characterized their *in vivo* uptake properties by the lymph nodes, the biological hub for immune cells responsible for producing immune responses.[206] Female C57BL/6 mice (n=3 per group) received either a saline control (PBS), Dn1E (6 nmol) or Dn6Em (6 nmol), subcutaneously. After 4 h, the mice were sacrificed, and the lymph nodes were collected for imaging of fluorescent signals using an *in vivo* Imaging System (IVIS). We observed that both vaccines localized to one or both of the proximal lymph nodes (**Figure 3.12.**) and that the Dn6Em structure was taken up by

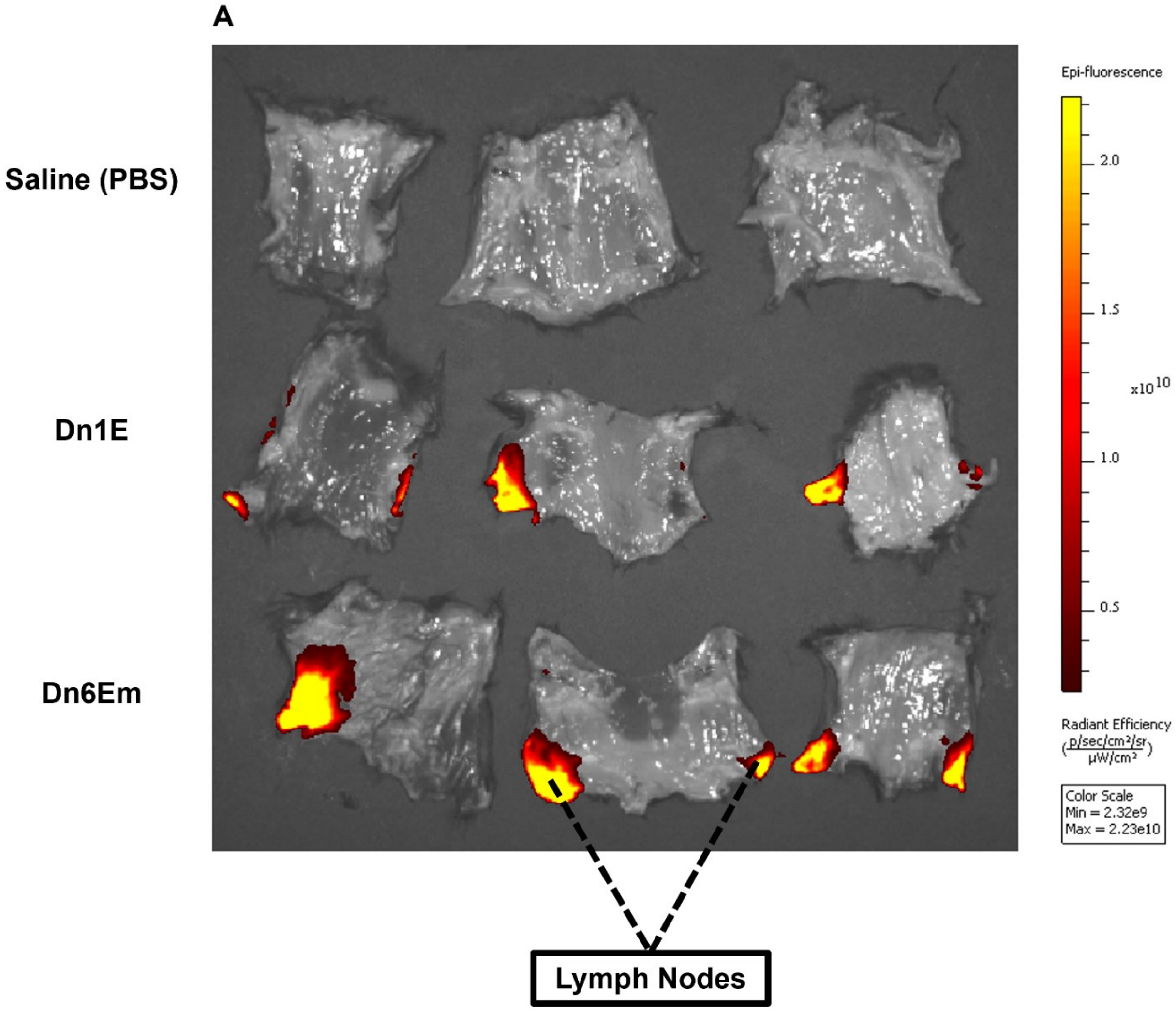

Figure 3.12. Raw lymph node uptake data
Female C57BL/6 mice (8-12 weeks old) were administered a single subcutaneous injection into the abdomen. Treatment dose was maintained at 6nmol. After 4 h, mice were euthanized and the skin containing the lymph nodes was resected. Fluorescence was assessed using an IVIS 200 Spectrum (PerkinElmer) in vivo imaging system with a narrow band excitation of 535 and emission of 580. Quantitative analysis was performed using Living Image software. The raw data presented here shows the Dn6Em Is taken up by the lymph nodes more than the Dn1E vaccine.

the lymph nodes more than the Dn1E vaccine ($p = 0.0566$) and significantly more than the PBS treated mice (**Figure 3.11. B**). This indicates that not only do the vaccines produce a potent immune response *ex vivo*, but they also accumulate at desired immune centers when delivered *in vivo*. Previous research has shown that therapeutic hydrophobicity can significantly enhance lymph node uptake.[207-209] Since the Dn6Em structure has 6-fold more peptides per dendron, those hydrophobic moieties seem to be playing an important role in mediating vaccine uptake. Raw IVIS images can be found in **Figure 3.12**.

To evaluate the *in vivo* therapeutic impacts of the different dendron architectures, we treated TC-1 tumor-bearing female mice (n=5-6) and evaluated tumor growth and animal survival. TC-1 tumor cells (2×10^5) were inoculated subcutaneously into the right flank of C57BL/6 mice and allowed to grow to ~50 mm^3 before the first of four treatments (schedule provided in **Fig 3.13. A**). Animals were treated once per week with Dn1E, admix 1 (simple mixture corresponding to Dn1E adjuvant/antigen ratio), Dn6Em, admix 6 (simple mixture corresponding to Dn6Em adjuvant/antigen ratio), or saline (PBS). Tumor growth was measured every 2-3 days while survival was quantified; animals were sacrificed when tumor burden reached 1500 mm^3. Mice that were treated with Dn6Em exhibited potent suppression of tumor growth (**Fig. 3.13. B,C and 3.14.**). In fact, 100% of animals treated with Dn6Em demonstrated tumor growth inhibition (<100 mm^3 through day 30) and were protected from death through the 44 day study, as tumors did not reach the 1500 mm^3 cut-off during this timeframe (**Fig. 3.13. D**). In contrast, mice treated with the Dn1E dendron failed to exhibit a significant improvement in tumor burden, and only 33% survived to day 44 (median survival – 36.5 days). As expected, animals treated with saline all perished by the conclusion of the study (median survival – 35 days), and animals treated with either of the admix controls were unable to mount a sufficient Immune response to fight off tumor burden effectively.

Spider plots for all groups are provided in Supplementary **Figure 3.14**. This study illustrates the importance of precise structural changes to the dendron architecture to dramatically impact animal survival and tumor burden in vivo.

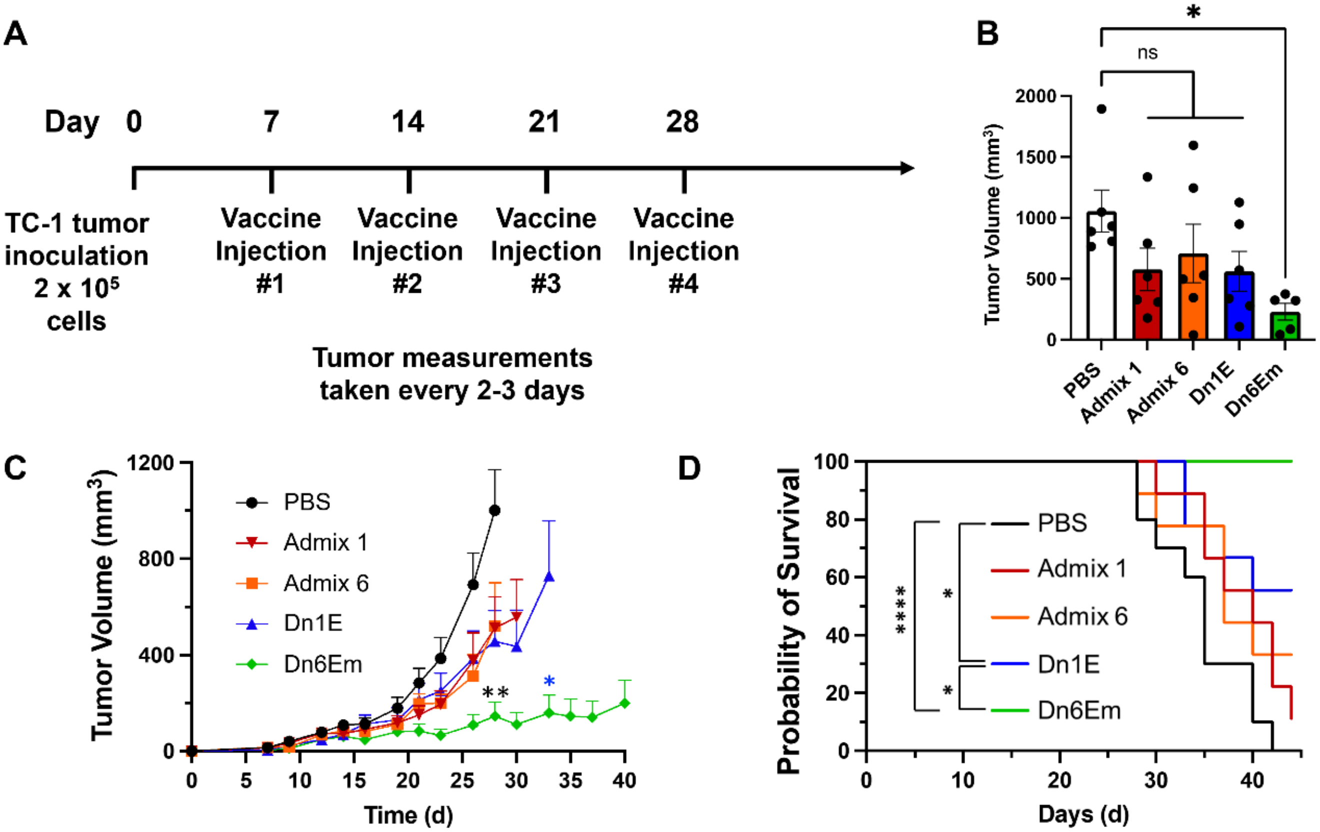

Figure 3.13. Treating tumor-bearing mice that were inoculated with cervical cancer cells
(A) Mice were treated with 2 x 10^5 cancer cells on day 0 and received treatment once/week for four weeks, starting on day 7. Tumor measurements were taken every 2-3 days. (B) Plots of the average tumor volumes show that the Dn6Em structure is the most effective vaccine for inhibiting tumor growth. (C) This inhibition in tumor growth led to a 100% survival rate for Dn6Em throughout the study (44 days). (D) Tumor volumes at day 28, which demonstrate the significant tumor growth inhibition that results from Dn6Em treatment over the other groups. ns = not significant; * = $p<0.05$. Not all significances are shown for clarity.

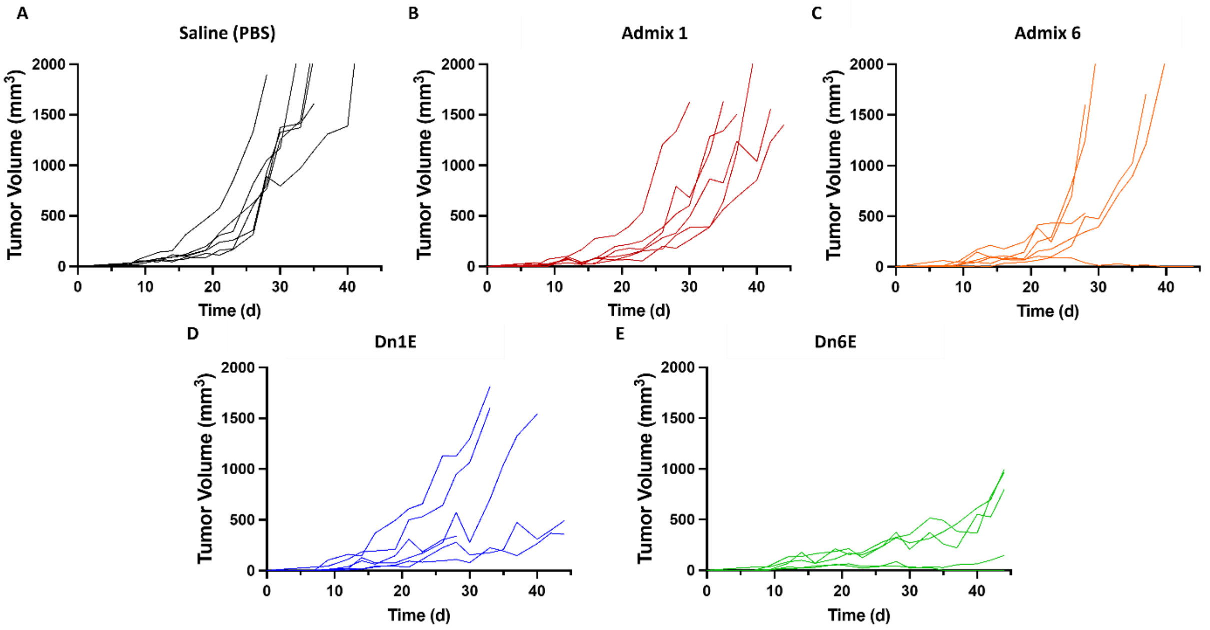

Figure 3.14. Tumor growth spider plots
Female C57BL/6 mice aged 8-12 weeks (Jackson Laboratory) were inoculated with 2 x 10^5 TC-1 tumor cells subcutaneously into the right flank and were allowed to grow to ∼50 mm^3 (7 days) prior to treatment. Treatments were administered at a dose of 60 uM in 100 uL volume by subcutaneous injection into the abdomen once per week, following the schedule provided. Tumor growth was measured every 2-3 days and volume was calculated using the following equation: tumor volume = length × width^2 × 0.5. Animals were euthanized when tumor volumes reached 1,500 mm^3 or when animal health necessitated them to be sacrificed for humane reasons. Presented here are the spider plots of the individual mice in each group.

3.5. Comments on the Rational Design of Molecular Vaccines

This work establishes the DNA dendron as a powerful tool to study the fundamental structure-function relationships that govern cancer vaccine efficacy while simultaneously demonstrating the DNA dendron as a potent platform for immunotherapeutics. DNA dendrons can be readily synthesized to have specific DNA sequences, lengths, and valences. By leveraging this level of control, DNA dendrons containing immune-stimulating CpG sequences were designed and synthesized. We investigated how DNA dendron design impacts the effective delivery of functional CpG sequences, and how to maximize cellular uptake and the resultant immune response *ex vivo*. This investigation led us to find that having the CpG sequence as the dendron stem, and poly-T sequences as the branches led to the most effective delivery of functional adjuvant. Nevertheless, the branch sequences have the potential to be further tuned to improve dendron uptake (e.g., G-rich sequences). By conjugating an antigenic peptide derived from HPV related cervical cancer to the dendron, a molecularly defined cancer vaccine was synthesized. We demonstrated that peptide conjugation to different parts of the dendrons impacts dendron uptake and immune activation. Furthermore, we show that these vaccines produce a robust and specific immune response against the cancer target, both *ex vivo* and *in vivo*. Finally, we demonstrated that DNA dendron molecular vaccines elicit a robust and powerful anti-tumor response, *in vivo*. Taken together, this work explores the structure-function relationships of DNA-dendron based vaccines in a molecularly defined manner. Due to the modularity of this molecular vaccine, these design rules can be applied to develop vaccines that treat a variety of cancers. This is the first demonstration of the capabilities of DNA dendron vaccines.

CHAPTER FOUR

Investigating Infectious Disease Vaccine Design with Spherical Nucleic Acids

Material in this chapter is based upon published work:

Teplensky, M. H.*; Distler, M. E.*; Kusmierz, C. D.; Evangelopoulos, M.; Gula, H.; Elli, D.; Tomatsidou, A.; Nicolaescu, V.; Gelarden, I.; Yeldandi, A.; Batlle, D.; Missiakas, D.; Mirkin, C. A., Spherical nucleic acids as an infectious disease vaccine platform. Proc. Natl. Acad. Sci. 2022, 119, e2119093119.

*Equal Author Contribution

4.1. Current Approaches to Infectious Vaccine Design

Infectious diseases have long threatened humanity due to their ability to rapidly spread and mutate across populations, infecting many people.[210] The rapid and global spread of SARS-CoV-2, the virus that causes COVID-19, emphatically revealed this and highlighted the importance of effective vaccination strategies to mitigate the spread and infectivity of viruses. Vaccination strategies are increasingly important as we consider the potential for emerging infectious diseases still to come.[211-212] The ability to rapidly adapt vaccine platforms through advancement of previous knowledge can be a huge asset. In particular, protein-based subunit vaccines can reduce vaccine production costs, while diminishing vaccine side effects. However, ultimate outcomes of protein-based subunit vaccine performance is difficult to correlate between candidates.[213]

An example of this is the influenza vaccine, which has relied on various simple mixtures of antigenic protein subunit target and adjuvant in solution to induce immune responses.[214] As a result, influenza vaccine effectiveness has varied dramatically by year, with a low of 10% effectiveness in 2004-2005 and a high of 60% effectiveness in 2010-2011.[215-216] This high variability is often attributed to the level of antigenic match between circulating viruses and vaccine strains. However, recent work has shown that the same antigen target can be more or less antigenic depending on the mode of presentation and delivery to the immune system.[216-217] By harnessing this concept, which we have termed *rational vaccinology* [161], we can greatly aid efforts to correlate vaccine design with performance by providing structurally-informed and optimized vaccine platforms that can be readily and quickly adapted to new disease targets.

4.2. Utilizing the SNA to Explore Concepts in Rational Vaccinology

Rational vaccinology has been implemented successfully for vaccines against cancer, where nanoscale changes have dramatically altered immune activation and tumor reduction.[161, 218-219] The application of this approach toward infectious disease has yet to be fully realized, and the potential for it to dramatically impact the success of vaccine development remains untapped. Herein, we have implemented spherical nucleic acid (SNA) nanotechnology as a tool to explore the impact of vaccine presentation when applied to infectious disease using COVID-19 as a case study. SNAs are comprised of a nanoparticle core surrounded by a dense radial arrangement of oligonucleotides.[100, 102, 220] Like many nanovaccine platforms, the SNA is biocompatible and comprised of naturally found molecules in cellular biology. Importantly, however, the SNA provides key advantages over other nanovaccine platforms. Specifically, the SNA platform is highly modular, enabling the elucidation of important structure-function relationships. Moreover, the SNA is effective at entering cells rapidly and in high quantities through scavenger-receptor A mediated endocytosis and is resistant to nuclease degradation due to the dense arrangement of oligonucleotides.[139-140] Moreover, by using a DNA shell containing immunostimulatory CpG motif DNA, SNAs robustly activate the innate immune system through TLR-9 activation [161-162], and exhibit efficient lymph node drainage and high co-delivery of adjuvant and antigen to antigen-presenting cells (APCs).[161, 219] These properties have been harnessed in this work to maximize humoral responses and generate antibodies effective at neutralization in pseudoviral assays, capable of withstanding mutations to still bind the target, and protective in mice against a lethal viral challenge. Overall, we report enhancement in immune response, leading to a 100% survival rate in a lethal viral challenge, which can be achieved through utilization of the SNA's privileged architecture.

4.3. Design and Characterization of SNAs as an Infectious Disease Vaccine

To synthesize SNA vaccines capable of raising robust, prophylactic responses against SARS-CoV-2, we harnessed the modularity of the liposomal SNA to simultaneously deliver encapsulated protein antigen and CpG motif DNA adjuvant. The modularity of the SNA platform enables fine-tuned control over vaccine structure, allowing for the rational design of the most effective vaccine. For these studies, we used the receptor-binding domain (RBD, **Figure 4.1.**) of the SARS-CoV-2 Spike protein as the antigen because this domain is responsible for recognizing and binding to human cell angiotensin-converting enzyme 2 (ACE2) receptor and facilitating cellular entry. SNAs were synthesized using previously established protocols.[161, 221] Briefly, protein antigens were encapsulated in 80-nm liposomes prepared from 1,2-dioleoyl-*sn*-glycero-3-phosphocholine (DOPC) films and purified using tangential flow filtration (TFF) to remove any unencapsulated protein. To form SNAs, protein-encapsulated liposomes were incubated with 3'-cholesterol-modified CpG DNA (**Figure 4.2. A**). The CpG DNA used was either a human or murine TLR9 agonist sequence depending on the experiment (**Table 4.1.**). Successful DNA incorporation and SNA formation was confirmed by dynamic light scattering (DLS) and agarose gel electrophoresis, which shows a decrease in electrophoretic mobility commensurate with DNA

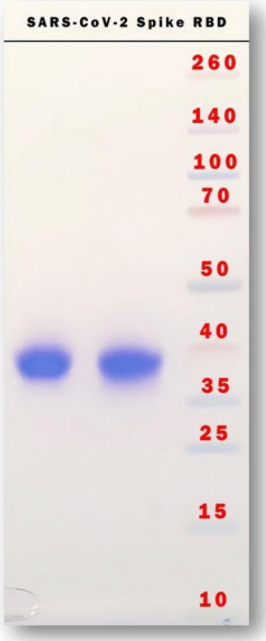

Figure 4.1. SDS PAGE of SARS-CoV-2 spike protein RBD
Protein was expressed in Expi293 and purified by Ni-affinity chromatography. Two different batches of sample are shown for demonstration of reproducible expression and purification. The molecular weight of the protein is 40,315.17 Da.

loading and increased size. (**Figure 4.3.**). The average RBD protein loading per liposome across 10 distinct batches was 4.7 ± 1.6 (**Figure 4.2. B**). This is equivalent to a loading capacity of 0.52 wt/wt%.

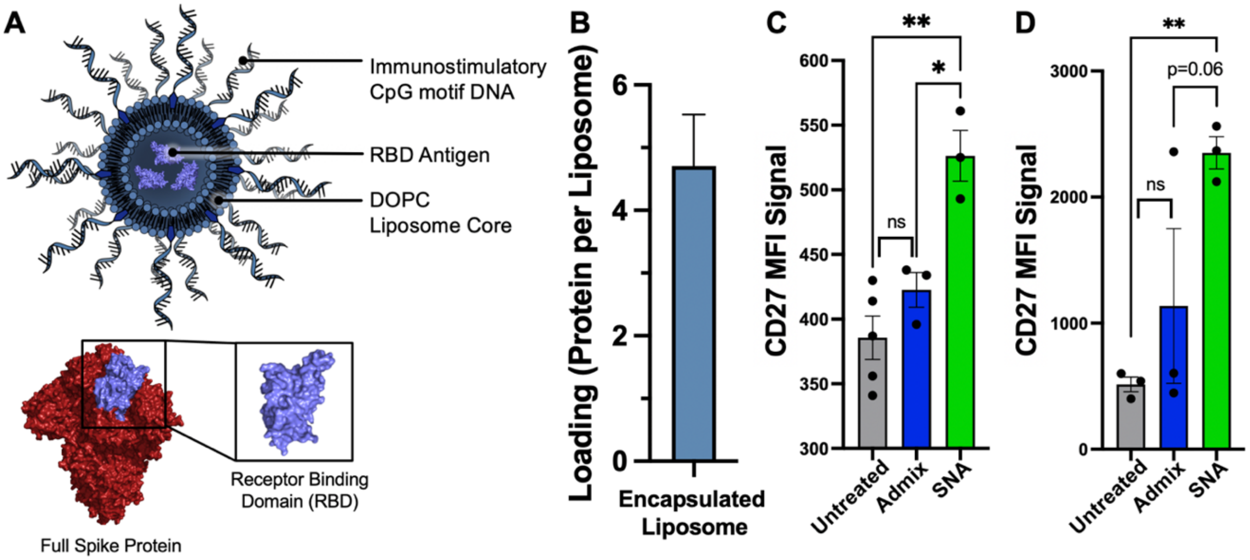

Figure 4.2. A Spherical Nucleic Acid (SNA) vaccine containing receptor binding domain (RBD) antigen is capable of activating B cells *in vitro*

(A) (top) A schematic of the SNA used in this work encapsulating RBD antigen within an 80-nm DOPC liposome core, and radially displaying a shell of TLR9-agonist CpG motif DNA. (bottom) RBD structure (purple) as a subset of the full SARS-CoV-2 Spike protein (red). This representation of the full spike protein and RBD was adapted from PDB ID: 6VXX. (B) Minimal batch-to-batch variation of the amount of RBD protein loaded per liposome (mean and 95% confidence interval shown, n = 10). (C,D) *In vitro* activation of hPBMCs to increase expression of CD27 among CD19$^+$ B cells. Incubation with hPBMCs was performed for both 1 (C) and 3 (D) days. Mean and SEM shown; analysis was done using an ordinary one-way ANOVA followed by a (C) Sidak's or (D) Dunnett's multiple comparisons test. n = 3 – 4 per group. *p<0.05; **p<0.01; ns=non-significant; other p values are shown.

4.4. B-Cell Activation In Vitro in Human Peripheral Blood Mononuclear Cells

A necessary step in effective vaccination is immunological memory carried by memory B cells, as these are easily reactivated upon exposure to antigen.[222-224] Moreover, their activation results in rapid proliferation and differentiation into plasma cells that produce large amounts of

Table 4.1. DNA adjuvants used in this study

Name	Sequence (5' to 3')[3]	Backbone (PS = phosphorothioate)	Calc'd Mass g/mol	Extinction Coefficient L/(mole·cm)[1]
CpG 1826	TCC ATG ACG TTC CTG ACG TT $(\text{Spacer18})_2$ Cholesterol	PS	6364.1	181100
CpG 1826 Cy5 Fluorophore-labeled[2]	TCC ATG ACG TTC CTG ACG TT Cy5 $(\text{Spacer18})_2$ Cholesterol	PS	8405.6	191100
CpG 7909	TCG TCG TTT TGT CGT TTT GTC GTT $(\text{Spacer18})_2$ Cholesterol	PS	7698.2	209400

[1] Calculated using IDT's OligoAnalyzer Tool: https://www.idtdna.com/calc/analyzer
[2] Cy5=1-[3-(4-monomethoxytrityloxy)propyl]-1'-[3-[(2-cyanoethyl)-(N,N- diisopropylphosphoramidityl]propyl]-3,3,3',3'-tetramethylindodicarbocyanine chloride; Stock no. 10-5915 (Glen Research)
[3] Spacer18=18-O-Dimethoxytritylhexaethyleneglycol,1-[(2-cyanoethyl)-(N,N-diisopropyl)]-phosphoramidite; Stock no. 10-1918 (Glen Research)

higher-affinity antibodies.[222-223] SNAs were therefore assessed for their ability to robustly activate naïve B cells in human peripheral blood mononuclear cells (hPBMCs). For these studies, we used SNAs composed of a human CpG 7909 oligonucleotide shell (**Table 4.1**). After one and three days of incubation, cells were measured for the presence of CD27, an activation marker which can contribute to B cell expansion, differentiation, and antibody production.[225-226] A significant difference in CD27 expression was observed when comparing the SNA to simple mixtures of RBD and CpG, termed admix, and when compared to untreated cells (**Figure 4.2. C and D**). This can be attributed to the advantageous properties that emerge when utilizing the SNA architecture, such as improved co-delivery of antigen and adjuvant components, increased and rapid cellular uptake, and enhanced resistance to nuclease degradation.[110, 161, 219] While using human cells, this demonstration of B cell activation is *in vitro,* and does not consider the complexity involved in multi-cell cross talk that leads to robust antibody production. Therefore, we next assessed the

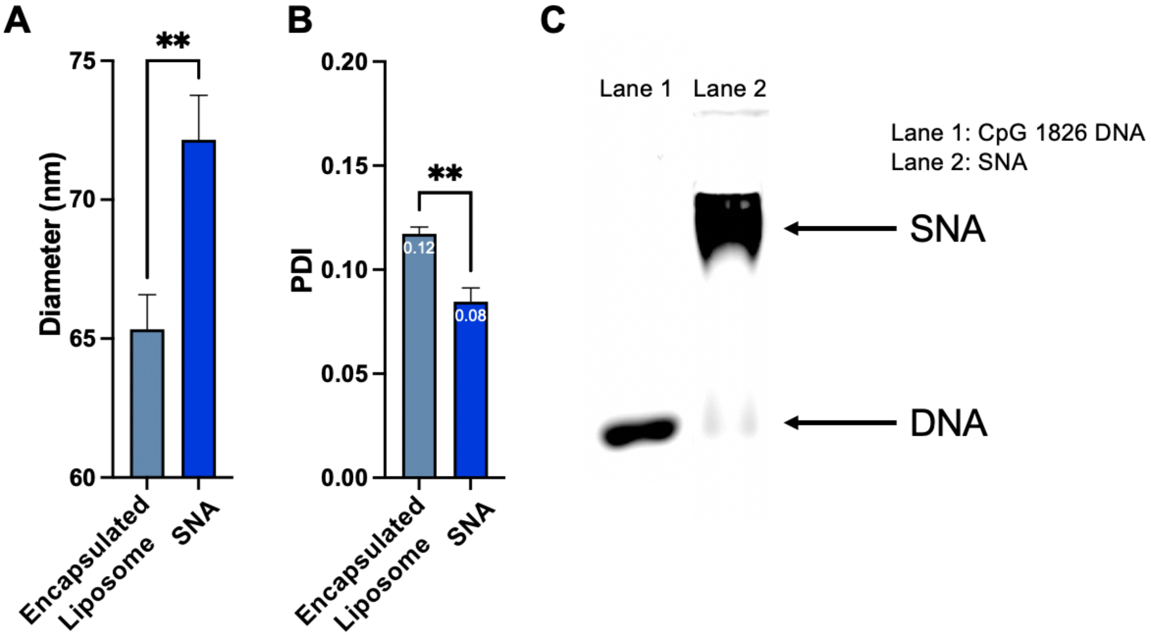

Figure 4.3. SNA formation confirmed through dynamic light scattering (DLS) and agarose gel electrophoresis (A) DLS demonstrates a significant increase in diameter and (B) a decrease in polydispersity index (PDI) as a result of addition of the DNA shell. (C) Agarose gel electrophoresis highlights the mobility shift of DNA as a result of SNA formation.

ability of the SNA to stimulate the adaptive immune system *in vivo* to generate robust, antigen-specific antibody responses.

4.5. In Vivo Antibody Production

We evaluated RBD IgG-specific binding and neutralizing antibody production following a single subcutaneous injection in C57BL/6 mice (n = 3 – 6 per group). RBD-specific binding antibodies were assessed by ELISA on mouse sera collected two weeks post-prime injection. For SNA-immunized mice, we quantified a *ca.* 1000-fold enhancement in the reciprocal serum end-point antibody titer compared to the simple mixture control (**Figure 4.4. A**). Furthermore, SNA-treated mice elicited a potent pseudovirus-neutralizing ability, whereby the generated antibodies inhibited 58% of the interaction between RBD and ACE2 at a 1:10 dilution in a surrogate virus neutralization test (sVNT) assay (**Figure 4.4. B**). Overall, a *ca.* 16.5-fold enhancement of final neutralizing antibody titer was measured for SNA-treated mice compared to those that received admix (**Figure 4.4. C**), which had no detectable inhibition ability (threshold was 30% inhibition as per manufacturer's specifications) (**Figure 4.4. B**).

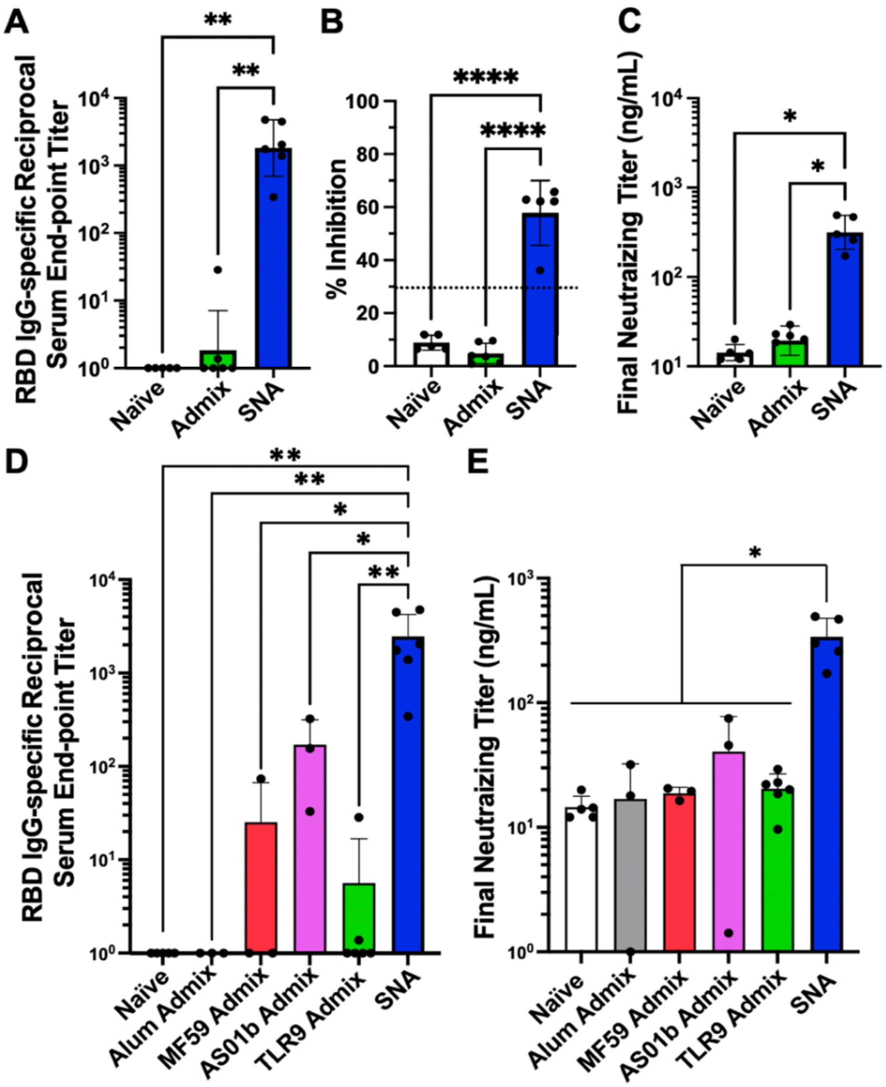

Figure 4.4. SNA structure induces higher levels of antigen-specific binding and neutralizing titers *in vivo*
(A) Samples were quantified via ELISA for the presence of RBD-specific IgG binding antibodies. Reciprocal serum end-point titers were calculated through fitting absorbance at 450nm values to a 4PL Sigmoidal curve. (B) Sera were employed in a pseudovirus inhibition study and were assessed for the inhibition percentage at a 1:10 sera dilution, or (C) were fit to a standard curve to calculate a final neutralizing titer. Dashed line in (B) represents threshold cutoff value for positive inhibition according to manufacturer's protocol. (D) RBD-specific IgG binding antibody measurement of SNA compared with simple mixture immunizations formulated using commercial adjuvants. (E) Final neutralizing titer calculated in a pseudovirus inhibition study and fit to a standard curve. All graphs show mean and SD, n = 3 - 6 per group. Mice were injected with 1.4 nmol by RBD protein and one of the following adjuvants: 44 nmol by CpG DNA (SNA and TLR9 admix groups), 40 μg by Al^{3+} (Alum admix), 25 μL by AddaVax (MF59 admix), 4.2 μg by QS21 and MPLA4 (AS01b admix). Dosing can be found in greater detail in *In Vivo Immunization in Mice.* For panels A, B, D, analysis was done using an ordinary one-way ANOVA followed by a Tukey's multiple comparisons test. For panels C, E, analysis was done using a Brown-Forsythe ANOVA followed by a Dunnett's multiple comparisons test. n = 3 – 4 per group. *p<0.05; **p<0.01; ***p<0.001; ****p<0.0001.

These assays validate that serum antibodies are more robustly produced with SNA immunization compared to admix vaccination, and also that a single dose of the SNA vaccine generates antibodies that can recognize and block a pseudoviral RBD domain from binding to an ACE2 receptor. This underscores the importance of structuring components into an SNA architecture in order to achieve enhanced biological and therapeutic responses, as proteins and DNA alone exhibit poor biodistribution to draining lymph nodes and rapid clearance.[227] By contrast, these results uphold that SNAs effectively deliver cargo to immune cells *in vivo*. Moreover, high neutralizing antibody levels are correlated with protection against infection[228]; therefore, these results establish the potential for SNA vaccines to be a viable vaccination strategy for COVID-19.

4.6. Comparison of SNA Performance to Simple Mixture of RBD and Commercial Adjuvants

To further compare the SNA platform against commercially available alternatives[229], we evaluated how the SNA vaccine compared against mixtures of commercial clinically-used adjuvants and the RBD antigen. Specifically, we employed Alum, MF59, and AS01b as adjuvants. All of these have been used to protect against infectious diseases, including Hepatitis B or Influenza.[230-232] In an assessment of RBD IgG-specific binding antibodies two weeks post-prime, the SNA outperformed all tested simple mixtures of adjuvants, even surpassing the best performing commercial adjuvant AS01b simple mixture by 14-fold. It ultimately reached a reciprocal serum end-point titer of 2464 (**Figure 4.4. D**). The simple mixture formulated with alum admix has undetectable binding antibodies indistinguishable from those raised by naïve mice, and MF59 admix had only one responder out of three mice, which had a reciprocal serum end-point titer of 74, 33-fold lower than SNA vaccination. When comparing the SNA against commercial adjuvant-containing simple mixtures in a pseudoviral neutralizing study (**Figure 4.4. E**), even the best performing group, AS01b admix, only reached 41 ng/mL neutralizing antibodies in sera, whereas the SNA concentration is nearly 9-fold higher, 339 ng/mL. This trend was similarly observed three weeks post-prime (**Figure 4.5.**), where the sera neutralizing antibodies generated from the SNA immunization were highest at 1193 ng/mL, 4-fold greater than the closest admix (AS01b).

4.7. Stoichiometry Between Adjuvant and Antigen Impacts Immune Response

As the SNA modularity can be easily tuned, we sought to understand the impact of the amount of adjuvant DNA loading on the SNA shell. We performed an agarose gel on 80-nm DOPC liposomes to evaluate the range of DNA that could fit on the surface before dissociating[233] (**Figure 4.6.**). This revealed a maximum of *ca.* 200 DNA strands per liposome (surface density of 1.7 pmol/cm^2), which aligns with other liposomal SNA structures.[218, 234] To investigate the adjuvant loading dependence on vaccine efficacy, we varied the DNA surface coverage to synthesize three different SNAs containing 75, 150, and 200 strands per liposome, while keeping the encapsulation of protein in the core constant. This provided three different adjuvant:antigen ratios that were *ca.* 16:1,

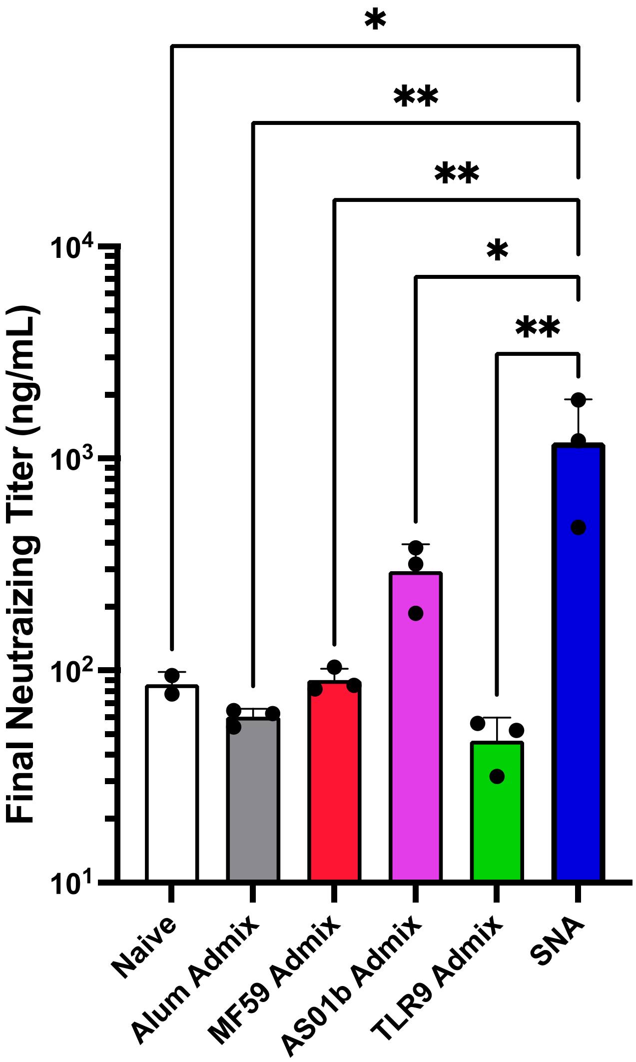

Figure 4.5. Final neutralizing antibody titers
Titers calculated in a pseudovirus inhibition study and fit to a standard curve using sera collected from C57BL/6 mice 21 days post a single prime injection. *$p<0.05$; **$p<0.01$.

32:1, and 43:1, respectively. We hypothesized enhanced loading would propagate an initial innate response, which could enhance an adaptive response. Mice were inoculated with one of the three different SNAs or one of three TLR9 admix controls that matched these adjuvant:antigen ratios. Two weeks post-prime injection, RBD-specific binding and neutralizing antibodies were quantified from sera and were plotted against adjuvant loading to determine any linear relationships (**Figure 4.7. A and B**). There is a strong positive correlation between adjuvant loading and immune response for SNA immunization ($R^2 = 0.99$ for both binding and neutralizing antibodies). Moreover, we assessed the ability of antibodies generated from the best performing SNA (200 adjuvant strands per liposome), to bind to a mutated RBD of an evasive variant, B.1.351.[235] There was a non-significant difference in the reciprocal serum end-point titer when binding to the RBD B.1.351 variant (**Fig. 4.7. C**), when compared to the reciprocal serum end-point titer for binding to wildtype RBD. This promising retention of antibody binding ability leads

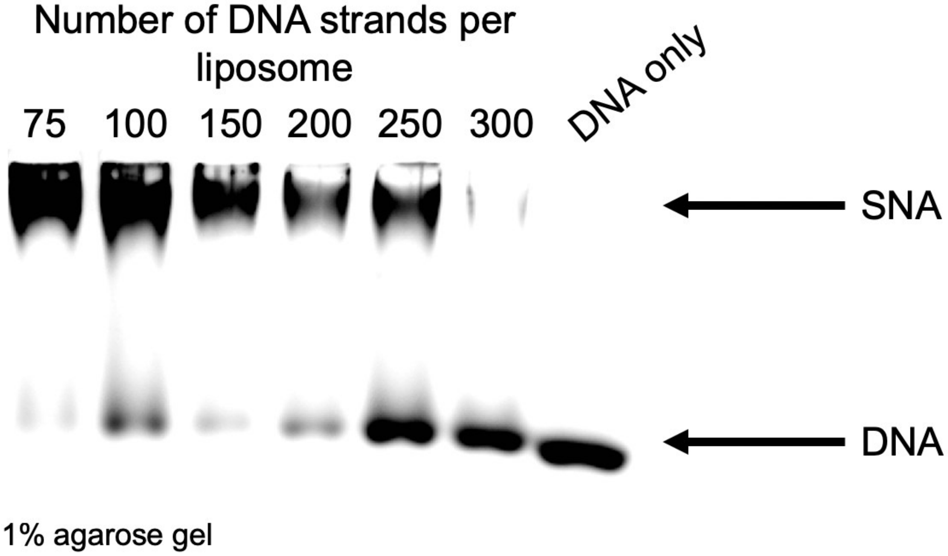

Figure 4.6. Determination of maximum loading of DNA per liposome before dissociation
The last detectable SNA band that also has a low intensity DNA band, indicating low levels of dissociation, is present at a stoichiometry of 200 DNA strands per liposome.

us to propose that the SNA platform can generate robust humoral responses that are resistant to mutational viral changes.

4.8. Identification of Up-Regulated Immunoglobulin Classes Using Proteomics

To understand how the different stoichiometries of adjuvant on the SNA induced different levels of binding and neutralizing antibodies, we performed proteomics to assess the expression of different immunoglobulins. Eighteen immunoglobulins (Igs) were identified amongst all the SNA formulations (75, 150, or 200 adjuvant strands/liposome termed 75 SNA, 150 SNA, and 200 SNA, respectively), with an additional five distinct Ig proteins present in the 200 SNA treatment group (**Figure 4.7. D**). In particular, the five significant proteins have increased fold changes in the 200 SNA immunization compared to 150 SNA (**Figure 4.7. E**). Furthermore, the total spectra of these proteins, an indicator of protein abundance[236], increases as the adjuvant loading increases (**Figure 4.7. F**). The IgM antibody was one of the 18 Ig proteins present among all SNA vaccine groups (**Table 4.2.**) and is the first immunoglobulin class produced in the primary response to antigens.[237] The five significant Igs in the 200 SNA group are involved in antigen binding, positive regulation of B cell activation and B cell receptor signaling, Ig receptor binding and mediated immune response, and overall, the adaptive immune response.[238] This suggests that the increased expression of these proteins and the subsequent processes in which they are involved, results in the measurable increase in immune outputs.

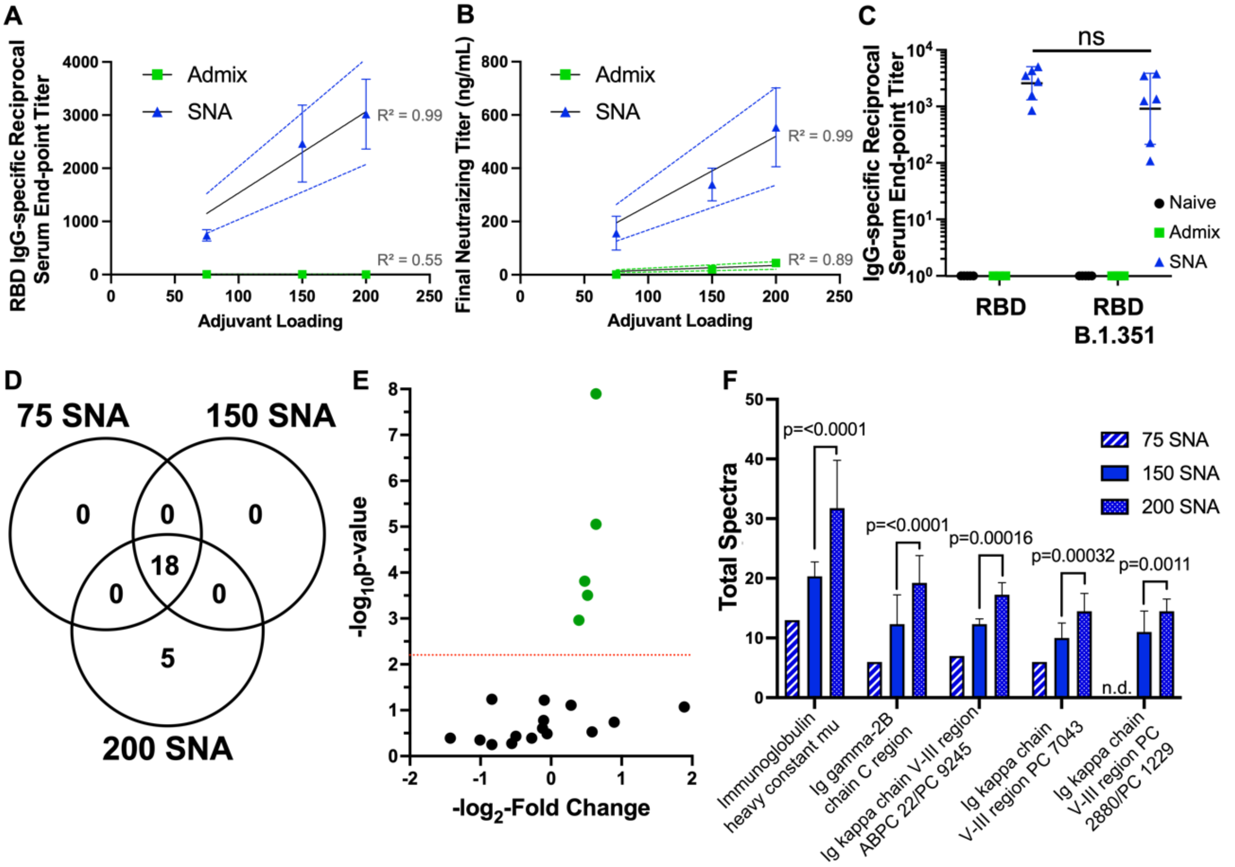

Figure 4.7. SNA vaccines formulated with different loadings of adjuvant DNA as the shell

SNA vaccines formulated with different loadings of adjuvant DNA as the shell demonstrate linear correlations in resulting binding and neutralizing antibody production as a result of differential protein expression. (**A**) RBD-specific IgG binding antibodies shown as the reciprocal serum end-point titer were plotted against adjuvant loading for the 3 different SNA groups. (**B**) The pseudovirus inhibition assay demonstrated the same positive linear relationship between adjuvant loading and the calculated final neutralizing titer. Graphs show mean and SEM for n = 3 - 6 per group. (**C**) Antibodies generated by the different vaccines were assessed for their ability to bind the B.1.351 variant of the RBD protein (RBD-SA). Graph shows mean and SD for n = 3 - 6 per group. Analysis performed doing a two-way ANOVA followed by Sidak's multiple comparisons test. ns = non-significant change in reciprocal serum end-point titer for SNA-raised antibodies. (**D**) Quantitative profile of immunoglobulins between the 3 SNA groups with different loadings of adjuvant DNA on shell. (**E**) Volcano plot showing relative fold change and significance of different Igs when comparing the 200 SNA against the 150 SNA group. Red line indicates significance threshold. (**F**) The five identified upregulated proteins were plotted as a function of total spectra with significance between 200 SNA versus 150 SNA shown. N.d. = not detected. Significance threshold = $p<0.0063$. Mice were injected with the following: SNA 200 and admix equivalent were dosed at 1.4 nmol by RBD protein, 60 nmol by CpG DNA. SNA 150 and admix equivalent was dosed at 1.4 nmol by RBD protein, 44 nmol by CpG DNA. SNA 75 and admix equivalent was dosed at 1.4 nmol by RBD protein, 22 nmol by CpG DNA. Dosing can be found in greater detail in *In Vivo Immunization in Mice*.

Table 4.2. Proteomic analysis of vaccinated mice

Name	Molecular Weight	Fisher's Exact Test (p-value): *($p< 0.0063$)^2	Total Spectra Count (Integer avg for group)		
			75 SNA	150 SNA	200 SNA
Immunoglobulin kappa constant	12 kDa	0.37	4	37	26
Immunoglobulin heavy constant mu	50 kDa	< 0.00010	13	20	32
Ig gamma-2B chain C region	44 kDa	< 0.00010	6	12	19
Ig kappa chain V-III region ABPC 22/PC 9245	12 kDa	0.00016	7	12	17
Ig gamma-1 chain C region, membrane-bound form	43 kDa	0.059	4	14	14
Ig kappa chain V-III region PC 7043	12 kDa	0.00032	6	10	15
Ig kappa chain V-III region PC 2880/PC 1229	12 kDa	0.0011	0	11	15
Ig gamma-3 chain C region	44 kDa	0.17	2	7	6
Ig kappa chain V-V region HP R16.7	12 kDa	0.25	3	4	4
H-2 class I histocompatibility antigen, Q10 alpha chain	37 kDa	0.53	3	8	5
Ig kappa chain V-II region 26-10	12 kDa	0.079	1	4	5
Ig kappa chain V-V region MOPC 173	12 kDa	0.45	1	2	1
Ig heavy chain V region AC38 205.12	13 kDa	0.4	0	3	3
Ig gamma-2A chain C region secreted form	37 kDa	0.32	2	2	2
Ig heavy chain V region 93G7	16 kDa	0.56	0	1	1
Ig heavy chain V-III region HPC76 (Fragment)	12 kDa	0.086	0	0	1
Ig kappa chain V-V region MOPC 41	14 kDa	0.18	0	1	1
Ig heavy chain V region HPCG14	14 kDa	0.29	0	1	1
Polymeric immunoglobulin receptor	85 kDa	0.47	0	0	0
Ig alpha chain C region	37 kDa	1	0	0	0

4.9. Dosing of SNA Vaccine Enhances Immune Responses

We quantified the impact of multiple doses of the best-performing SNA vaccine (200 SNA) on the resulting amplification of immune responses. Many ongoing vaccines that were granted Emergency Use Authorization or are in development have utilized a prime-boost vaccine schedule to enhance immune responses.[239] Therefore, we immunized mice with a prime-boost schedule (boost was two weeks post prime) to assess any elevation in antibody production. We collected sera from the mice two weeks after the boost, which is 4 weeks (28 days) after the initial prime immunization. An increase in both binding antibodies (**Figure 4.8. A**; 6.5-fold increase) and neutralizing antibodies (**Figure 4.8. B**; 126-fold increase) was observed when comparing sera from two doses to that from one. The admix vaccination did improve with a second administration, but levels of binding and neutralizing antibodies were still 4000-fold and 1500-fold lower, respectively, compared to the SNA immunization (**Figure 4.8.**), and proteomics signatures were significantly different (**Figure 4.9.**)

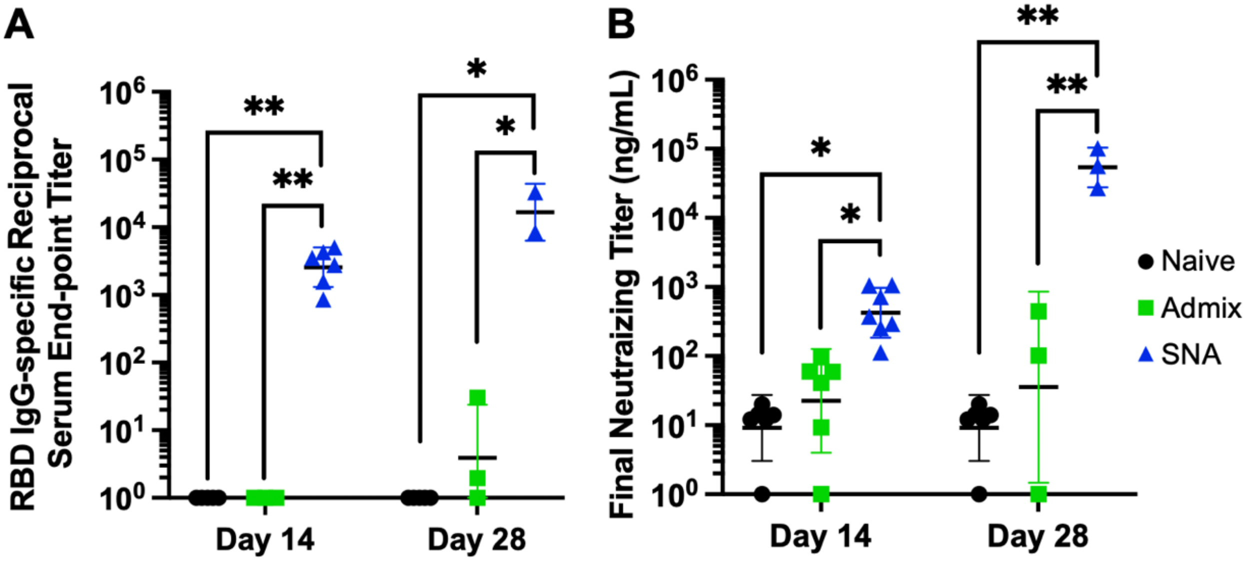

Figure 4.8. The impact of vaccine schedule on efficacy
Prime-boost vaccination with two administrations enhances antibody production for all treatments, while SNA immunization is highest. Levels of (**A**) binding and (**B**) neutralizing antibodies on either day 14 (prime only on d0, sera collection on d14) or on day 28 (prime on d0, boost on d14, sera collection on d28). Graphs show mean and SD for n = 3 - 6 per group. Analysis was done using a two-way ANOVA followed by a Tukey's multiple comparisons test. Only significant comparisons shown. *p<0.05; **p<0.01.

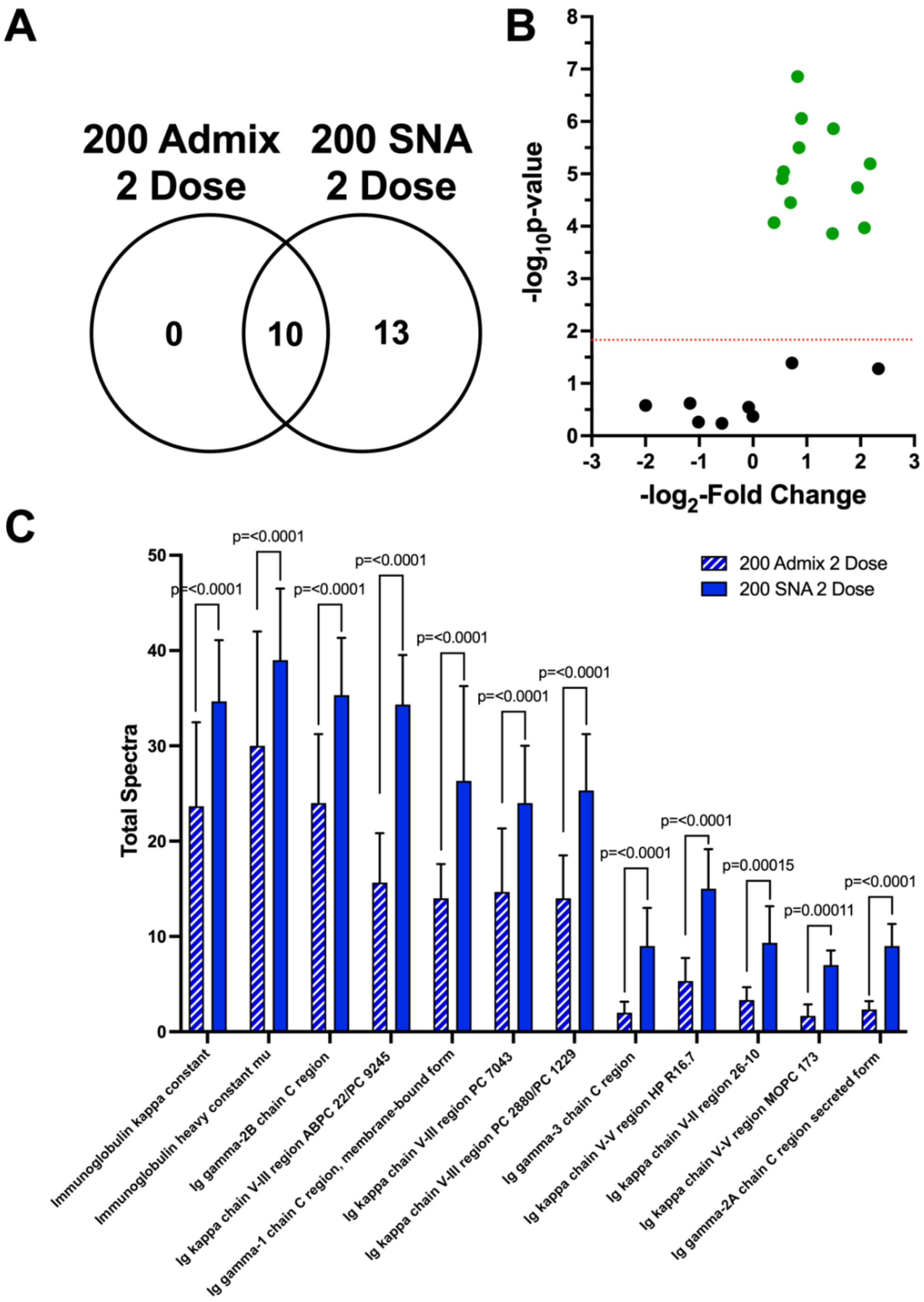

Figure 4.9. Proteomic analysis of 2 dose admix and SNA treatments

A) Quantitative profile of immunoglobulins between the 200 Admix 2 dose group and 200 SNA 2 dose group. (B) Volcano plot showing relative fold change and significance of different Igs when comparing the 200 Admix 2 dose against the 200 SNA 2 dose group. Red line indicates significance threshold. (C) The identified significant upregulated proteins were plotted as a function of total spectra with significance shown. Significance threshold = $p<0.01585$.

4.10. Live Viral In Vivo Challenge Using Transgenic k18-hACE2 Mice

As a direct test of vaccine efficacy, we conducted a viral challenge study using transgenic mice that are susceptible to infection through expression of the human ACE2 protein: k18-hACE2.[240-241] Animals were challenged with a lethal dose of the virus.[242-246] We compared the top performing vaccine design (200 SNA) to the admix vaccine, and also to mice receiving only saline (PBS) as a negative control. Mice were given either one or two doses of the SNA or admix vaccine. Mice (n = 10 per group, comprising 5 females and 5 males) were challenged with virus two weeks after receiving the final vaccine dose (complete schedule in **Figure 4.10. A**). Just prior to viral infection, blood was collected from the mice to verify neutralizing antibody production (**Figure 4.11.**).

After viral infection, animals were monitored twice daily for signs of disease, and weighed daily. Within the first five days post infection, mice that received either saline or one or two doses of admix vaccine experienced a rapid decline in body weight and an increase in clinical score, both of which indicate that the mice were not protected from the virus (**Figure 4.10. B and C**). These animals were euthanized at day 5, as per study protocol, for humane reasons, and lungs were removed to measure viral loads (**Figure 4.10. D and E**). In stark contrast, mice that were treated with either one or two doses of the SNA vaccine displayed no evidence of declining health. Body weight and clinical scores remained stable throughout the entire study, and thus survival of the SNA treated mice was 100% (**Figure 4.10. B-D**). All surviving animals were killed at day 12 post infection. Lungs from sacrificed mice (day 5 for PBS and admix vaccine either dose, and day 12 for SNA vaccine either dose) were collected and quantified for viral titers measured by plaque assay. Mice receiving either one or two doses of SNA vaccine had no measurable viral titers in the lungs (**Figure 4.10. E**). Mice immunized with PBS or either admix dose and sacrificed on day 5, had viral titers around 7×10^1 or $2\text{-}3 \times 10^1$ PFU/mL/mg lung, respectively. Histopathological examination of the lungs, performed following methods used in the same transgenic model[242], showed extensive neutrophil infiltration for mice that did not receive the SNA vaccine (mean = 1.6, 1.85, and 1.95 for PBS-treated, Admix 1, and Admix 2 dose treated mice, respectively) (**Figure 4.10. F**). In mice that received the SNA vaccine, neutrophil infiltration was reduced (mean = 0.7 and 0.15 for 1 and 2 doses, respectively). This indicates that the SNA vaccine is capable of avoiding or greatly attenuating outcomes of severe COVID-19 pneumonia, which is characterized by elevated neutrophil infiltration.[247] Additional histopathological analysis and representative images can be found in the supplementary information (**Figure 4.12.**). Overall, these results emphasize the impact that the SNA vaccine platform, and more broadly rational vaccinology, can have on elevating antiviral vaccine efficacy.

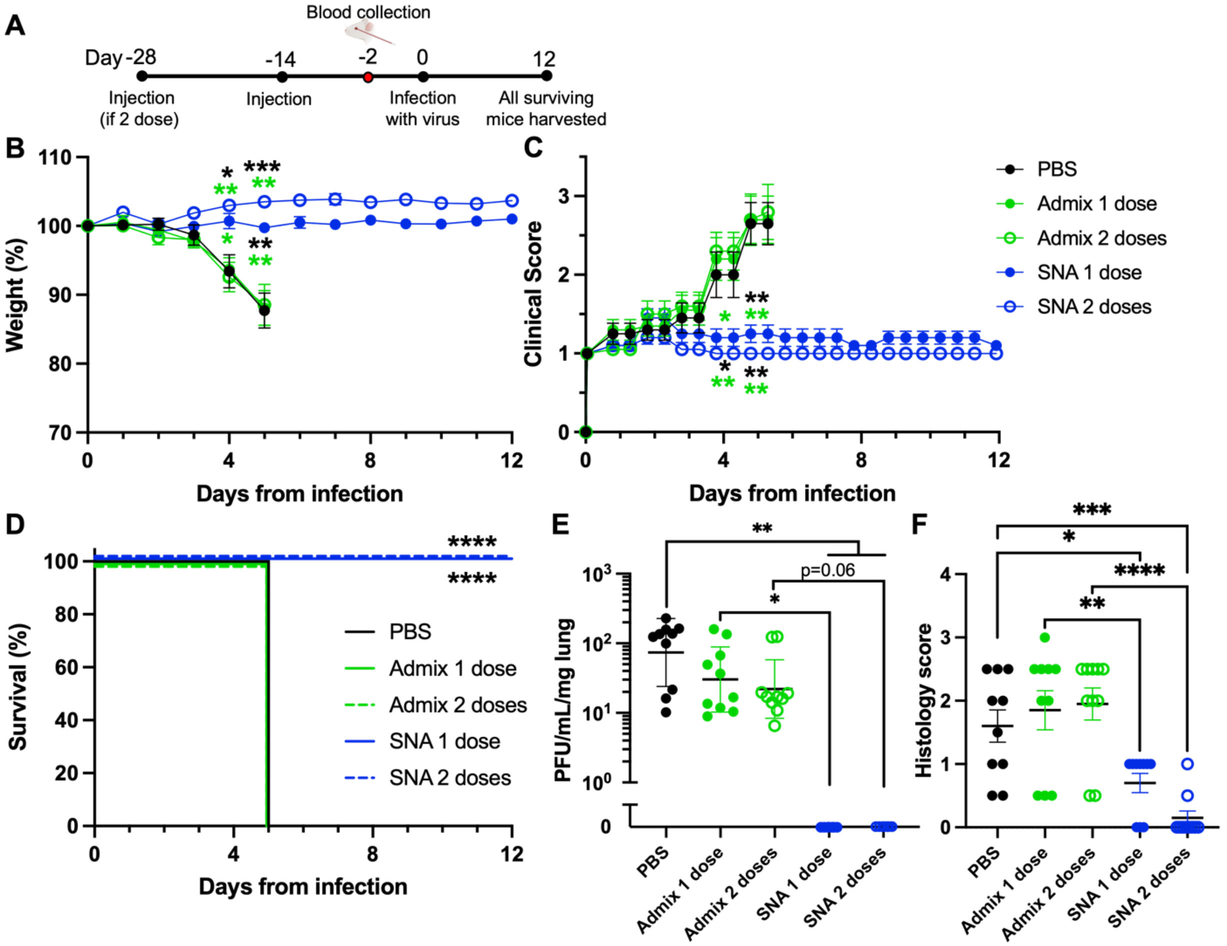

Figure 4.10. *In* Vivo vaccine efficacy

Vaccine effectiveness was tested using k18-hACE2 transgenic mice in a live viral SARS-CoV-2 challenge study. (**A**) Female and male mice (n = 10 total per group, 5 of each gender) were treated with vaccine or control groups and infected with virus as per the schedule. (**B**) Vaccination with SNA of either 1 or 2 doses prevented any body weight loss, (**C**) improved clinical scores, and (**D**) prevented any mortality as compared to vehicle-mice (PBS) or admix mice treated with 1 or 2 doses when infected with SARS-CoV-2. On date of death, lungs were harvested and assessed for (**E**) viral load and (**F**) histopathology. (**E**) No detectable virus was observed for SNA mice treated with 1 or 2 doses. (**F**) Scores of neutrophil infiltration are lower in mice treated with SNA vaccine compared to mice treated with Admix vaccine or untreated. Comparisons made between PBS and all other groups, and Admix 1 dose versus SNA 1 dose, and Admix 2 dose versus SNA 2 dose. For panels **B**,**C**, statistical significance is shown above the date at which the analysis was performed. Colors correspond to the group that the SNA was compared to. Only significant comparisons were shown, and comparisons were made between SNA and PBS or the admix group with the same corresponding number of doses. For panels **B**, **C**, **E**, analysis was done using a Brown-Forsythe ANOVA followed by a Dunnett's multiple comparisons test. Panel **F** analysis was done using an ordinary one-way ANOVA followed by Sidak's multiple comparisons test. Panel **D** was analyzed using a log-rank test. *$p<0.05$; **$p<0.01$; ***$p<0.001$; ****$p<0.0001$.

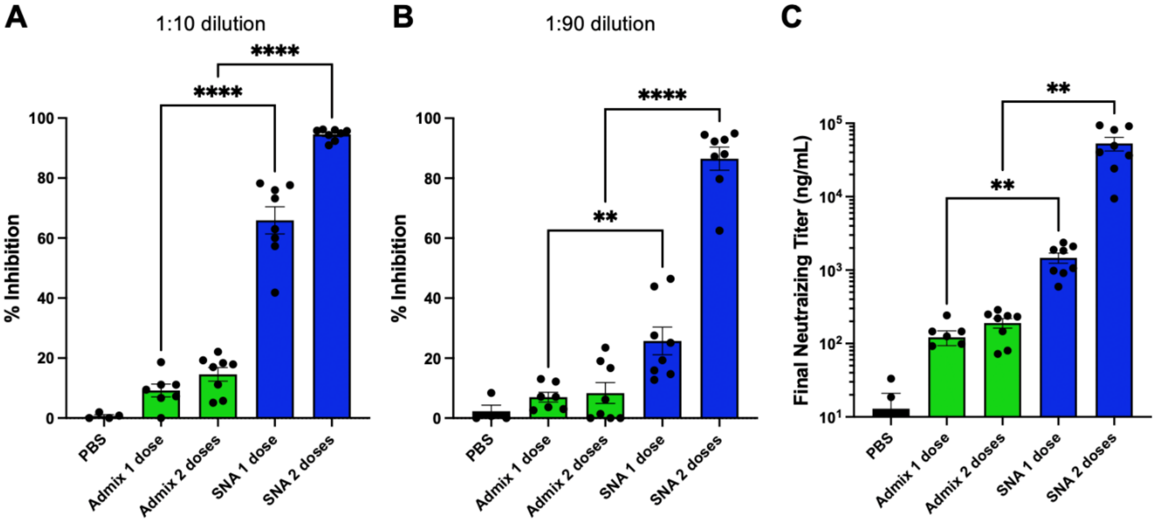

Figure 4.11. Pre-infection antibody production
Sera from k18-hACE2 transgenic mice were collected after immunization with different vaccines just prior to infection with virus to verify neutralizing antibody production. (A,B) Different dilutions of sera were assessed for antibody ability to inhibit RBD binding to ACE2 in a pseudovirus assay. SNA at either dose is significantly more effective at inhibition than admix. (C) Values from assay were fit to a standard curve to calculate a final neutralizing titer. $^{**}p<0.01$; $^{****}p<0.0001$.

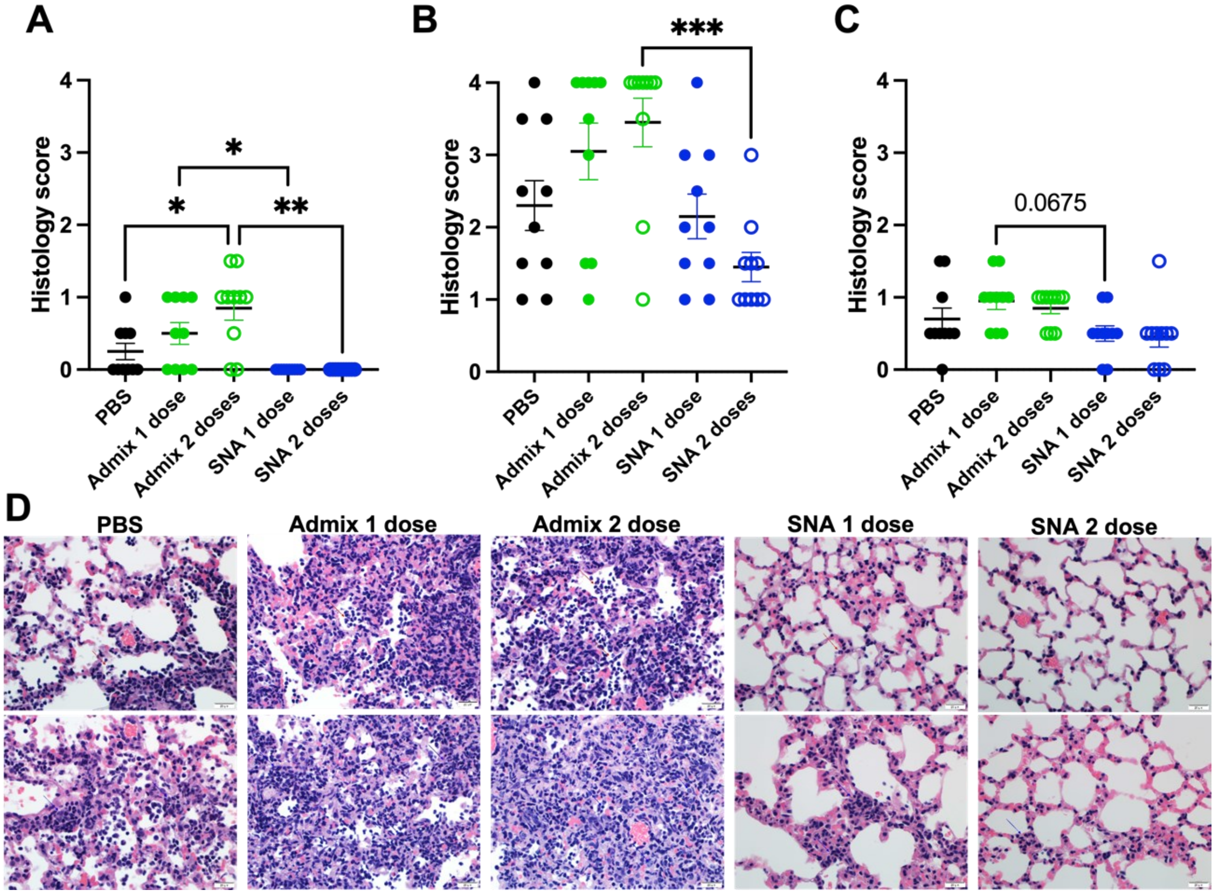

Figure 4.12. Histopathological analysis of mice post infection
Lung histopathology analysis from k18-hACE2 transgenic mice immunized with vaccines and challenged with a lethal infection of SARS-CoV-2. Lungs were collected on date of death (day 5 for PBS and admix vaccine either dose, and day 12 for SNA vaccine either dose). Scoring of (A) necrosis, (B), mononuclear infiltrates, and (C) edema. (D) Representative images of lungs stained with hematoxylin and eosin. Two representative images shown per group (magnification: 400x). Scale bar = 20 µm for all images. PBS group shows expansion of alveolar septae by inflammatory cells with solitary neutrophils in airspaces (red arrow, top image) and multiple foci of alveolar septal expansion by aggregates of mononuclear cells (blue arrows, bottom image). Admix 1 dose group shows dense inflammatory infiltrate including aggregates of neutrophils within airspaces (red arrow, top image) and diffuse expansion of alveolar septae by variably dense aggregates of mononuclear cells (blue arrows, bottom image). Admix 2 dose group shows dense inflammatory infiltrate including aggregates of neutrophils within airspaces (red arrow, top image) and diffuse mononuclear infiltrate consisting of variably sized lymphocytes with dense to open nuclear chromatin (blue arrows, bottom image) causing marked architectural distortion and expansion of alveolar septae. SNA 1 dose group shows rare, scattered neutrophils (red arrow, top image) sequestered in thin alveolar septae and foci of alveolar septal expansion by loose aggregates of mononuclear cells (blue arrows, bottom image). SNA 2 dose group shows thin alveolar septae with rare to absent neutrophils (top image) and focal expansion of alveolar septae by small loose aggregate of mononuclear cells (blue arrow, bottom image). $^*p<0.05$; $^{**}p<0.01$; $^{***}p<0.001$.

4.11. Comments on the Structure Function Relationships of SNA Infectious Disease Vaccines

This work establishes the SNA as an effective platform for antiviral vaccines. By utilizing the highly modular SNA architecture, we highlight the importance of packaging viral antigens to raise humoral immune responses that can effectively fight a live virus. This work has important implications on the design of next generation infectious disease vaccines. It illustrates that antibody production is tunable through simple chemical adjustments (*i.e.,* the adjuvant loading on a liposome), and that a simple change to the ratio of components can greatly alter immunoglobulin expression. This work offers alternative strategies to enhancing antibody responses than traditional approaches which involve administering multiple doses. Importantly, we also observed that a traditional approach of supplementing a vaccine with adjuvant to enhance an antibody response is not a consistently effective strategy. The results using the SNA, which compositionally is similar to the AS01b simple mixture in that both involve liposomal constructs, suggests that radial display of CpG adjuvant and co-delivery of vaccine components, which the SNA provides, leads to a more effective vaccine that can prevent mortality and attenuate lung injury. Future studies can investigate the dose dependent nature of vaccine efficacy and compare the SNA to alternative vaccine platforms in clinical trials. Consistently, the 3D arrangement of components on the SNA architecture leads to significant increases in vaccine functionality compared to numerous tested simple mixtures and underscores the important role that rational vaccinology will play in future vaccine design.

Taken together, this work underscores the SNA's potential to be used as a platform for infectious diseases, and that the concept of rational vaccinology holds equally as true for infectious disease as it does for cancer vaccine applications. Given the SNA's easily adaptable structure to contain any viral antigen and combinations thereof, modulate positions and tune the stoichiometry of each component, and remain stable at room temperature, the SNA is poised to be a rapidly accessible future platform for targets yet to be discovered. When considering the programmability of the SNA architecture, rapid translation to antigenic variants and human adjuvant sequences is easily feasible. Collectively, these results have broad implications for the development of vaccines for COVID-19 and potentially other infectious diseases.

CHAPTER FIVE

Nanoparticle Superlattices Through Template-Encoded DNA Dendrimers

Material in this chapter is based upon published work:

Cheng, H. F.*; Distler, M. E.*; Lee, B.; Zhou, W.; Weigand, S.; Mirkin, C. A., Nanoparticle Superlattices through Template-Encoded DNA Dendrimers. *J. Am. Chem. Soc.* **2021,** *143*, 17170-17179.

*Equal Author Contribution

5.1. Methods to Programmable and Dynamic Nanoparticle Assembly

Biopolymers assemble into hierarchical structures through sequence-defined intra- and intermolecular interactions. The specificity of these interactions renders these macromolecules powerful building blocks for materials design. Alternatively, many synthetic macromolecules, such as block copolymers,[248-251] dendrons,[252-255] or amphiphiles,[256-259] can undergo shape- or topology-controlled packing. These synthetic structures can associate with one another through dynamic, supramolecular interactions to yield nanoscale domains with adaptable sizes and shapes,[250-253, 255, 257, 259] enabling the formation of hierarchical materials that have unconventional, low-symmetry phases.[249-250, 252-253, 257-259] Developing nanoscale building blocks that are capable of forming both dynamic associations and sequence-defined interactions (akin to those found in biology) could afford novel structure types and provide important insights into how hierarchical architectures arise in both natural and synthetic systems.

Various macromolecular architectures have been utilized to mediate the assembly of nanoparticle building blocks.[260-261] In particular, colloidal crystal engineering with DNA has emerged as a powerful, sequence-defined approach to program nanoparticle assembly,[91] with control over phase symmetries, lattice parameters, crystal habits, and thermostabilities.[6, 115-116] In this approach, nanoparticles are functionalized with a dense shell of radially oriented oligonucleotides, which mediate inter-particle bonding *via* sequence-specific complementary base-pairing. These DNA-functionalized nanoscale building blocks, also known as programmable atom equivalents (PAEs),[262] are typically synthesized from nanoparticle cores that are structurally static. We hypothesized that by employing DNA-presenting supramolecules that can undergo dynamic structural reorganization, novel nanoparticle arrangements could be templated, and new lattice reconfiguration strategies could be enabled. We posited that such supramolecules should assemble through transient interactions that are orthogonal to the sequence-specific DNA hybridizations, which serve to direct the formation of nanoparticle superlattices.

Herein, we realized such supramolecular PAEs using a new type of DNA dendrimer composed of molecularly defined building blocks (**Figure 5.1. a**). We co-assembled these dendrimers with gold nanoparticle (AuNP)-based PAEs (**Figure 5.1. b**) and, by comprehensively screening the phase space, we identified five distinct crystal structures, one of which has no precedent in the field of colloidal crystal engineering. Our investigation of the nanoscale organization of these superlattices led to a serendipitous discovery: dendrimer PAEs that bear hydrophobic moieties at their core can undergo micelle-mediated association. The resulting colloidal crystals have three modes of organization: two that are programmed by DNA hybridization and one that is mediated by hydrophobic interactions. Each of these interactions can be toggled to control the assembly of these PAEs into various crystal structures.

5.2. Design and Synthesis of Supramolecular DNA Dendrimer PAEs

Dendritic architectures are excellent nanoscale building blocks[4,6,255] as they are molecularly precise, have a defined topology, and can be heavily functionalized. Dendritic DNA,[263-264] developed for drug delivery and chemical sensing,[265-268] can be synthesized with a precise architecture by assembling a large number of oligonucleotides that have deliberately designed, orthogonal sequences.[263-264, 267-268] To develop DNA dendrimers as a new type of building block in colloidal crystal engineering, we reasoned that our synthetic strategy should offer systematic, fine-tuned control over building block size, valency, and functionality.

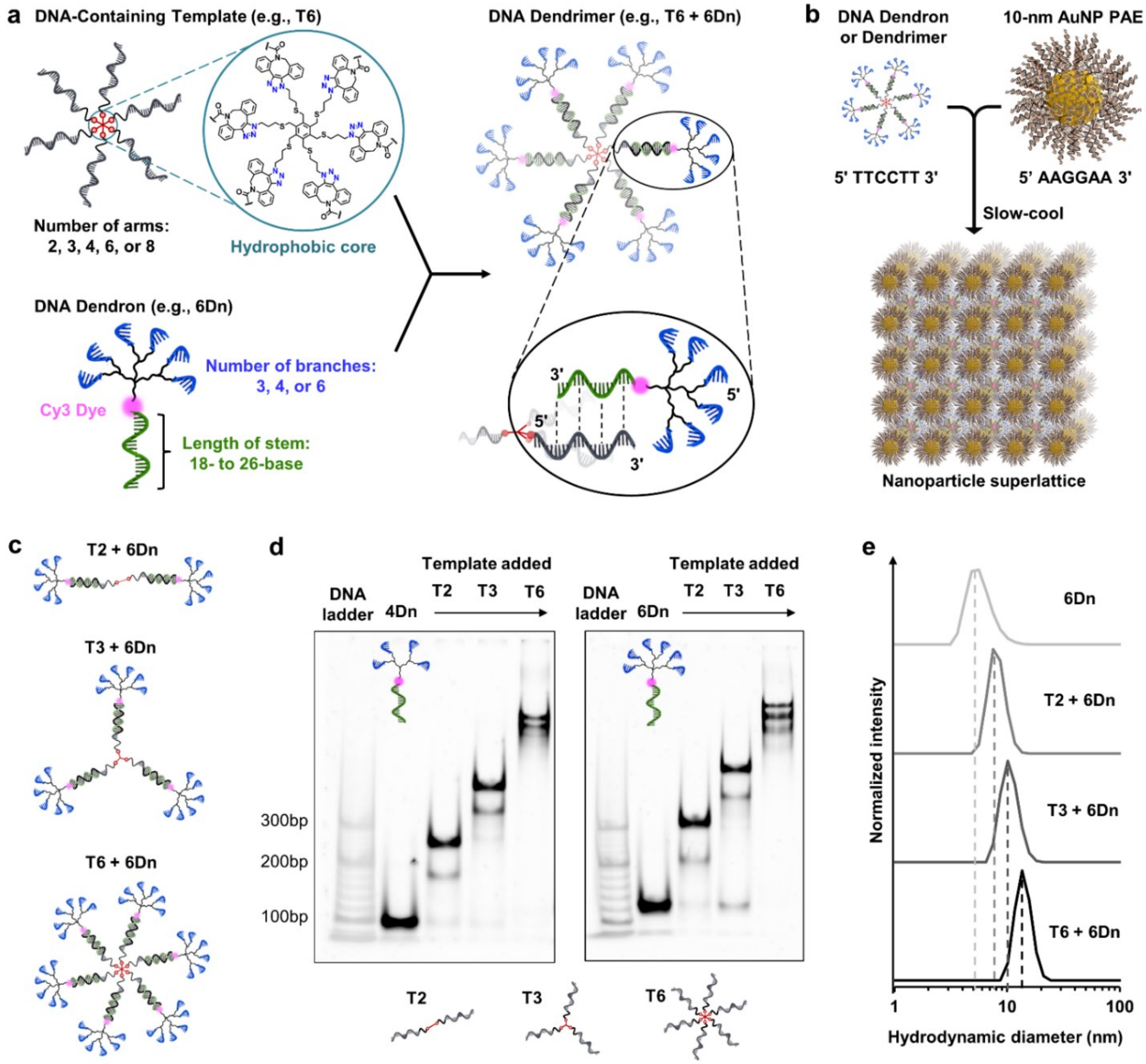

Figure 5.1. Bottom-up synthesis of supramolecular DNA dendrimers

(a) Left: DNA-containing templates have a hydrophobic core owing to the presence of dibenzocyclooctyne (DBCO) moieties. Depending on the structure of the molecular core, two to eight DNA strands can be installed (here, a six-arm DNA template is depicted). DNA dendrons can be synthesized with various branch numbers and stem lengths. Right: DNA dendrimers are assembled *via* hybridization between the template arms (black) and the dendron stems (green). (b) DNA dendrons or dendrimers were combined with 10-nm AuNP PAEs to form superlattices after slow-cooling. (c) A depiction of selected examples of DNA dendrimers. (d) Modular assembly of dendrons (4Dn and 6Dn) and templates (T2, T3, and T6) in 0.5 M NaCl results in defined DNA dendrimers that were characterized *via* 5% native polyacrylamide gel electrophoresis (PAGE). (e) Dynamic light scattering (DLS) shows that the hydrodynamic diameters (D_h) of these structures, dissolved in 0.5 M NaCl, 10 mM phosphate buffer, pH 7.4, increase with template valency. The dotted lines are there to guide the eye.

Our approach to preparing DNA dendrimers (**Figure 5.1. a**) uses two molecularly defined components (a template and a dendron) and one set of complementary DNA sequences. The DNA-containing templates were synthesized by conjugating multi-azide molecules with multiple copies of dibenzocyclooctyne (DBCO)-appended DNA,[269-270] yielding constructs with a range of valences (Ta, the number of arms, a = 2, 3, 4, 6, or 8). Each arm possesses an 18- to 20-base sequence designed to hybridize to the stems of the DNA dendrons, with melting temperatures (T_m) greater than 60 °C under assembly conditions (**Tables 5.1.-5.4.**). Each arm also has a six-base overhang that enables the resulting DNA dendrimer to be disassembled *via* toehold-mediated strand displacement (TMSD, *vide infra*).

Table 5.1. Linear oligonucleotides synthesized for this study

	DNA Sequence (5' to 3')	**Calc'd MW**	**Exp't MW**
PAE anchor	**Thiol-$(Sp18)_2$-AACGACTCATACTCACCT**	**6,403**	**6,425**
PAE linker	**AAGGAA-Sp18-AGGTGAGTATGAGTCGTT**	**7,834**	**7,869**
Temp_v1 (DBCO)	**DBCO-$(Sp18)_2$-TGGAGTGAATGGTAATAGTGAGTGGT**	**9,444**	**9,445**
Temp_v1 (hexynyl)	**Hexynyl-$(Sp18)_2$-TGGAGTGAATGGTAATAGTGAGTGGT**	**9,034**	**9,036**
Temp_v2 (DBCO)	**DBCO-$(Sp18)_2$-CATCCATCCTTATCAACT**	**6,613**	**6,618**
Block strand	**AACATCTAATCTACATCTACCACTCACTATTACCATTCACTCCA**	**13,218**	**13,234**
Unblock strand	**TGGAGTGAATGGTAATAGTGAGTGGTAGATGTAGATTAGATGTT**	**13,840**	**13,879**
Rigidifying strand	**TAGGTTGATAAG**	**3,725**	**3,776**

Table 5.2. DNA templates synthesized for this study

	Template arm sequence	Coupling yield* (%)	Calc’d MW (kDa)	Exp’t MW (kDa)
T2	**Temp_v1 (DBCO)**	**41**	**19.1**	**19.0**
T3	**Temp_v1 (DBCO)**	**64**	**28.6**	**28.5**
T4	**Temp_v1 (DBCO)**	**27**	**38.3**	**38.2**
T6	**Temp_v1 (DBCO)**	**23**	**57.5**	**59.5**
T8	**Temp_v1 (DBCO)**	**9**	**77.7**	**78.5**
T8’	**Temp_v1 (hexynyl)**	**7**	**74.4**	**72.6**
T2_v2	**Temp_v2 (DBCO)**	**50**	**13.4**	**13.7**
T4_v2	**Temp_v2 (DBCO)**	**54**	**26.9**	**27.1**
T6_v2	**Temp_v2 (DBCO)**	**23**	**40.5**	**41.0**

*Coupling yield is calculated by dividing the amount of DNA templates isolated by the theoretical maximum that could be synthesized, taking into account that ~30% of the chains are not terminated. A typical coupling reaction yields ~30-40 nmol of isolated product, sufficient for preparing more than 5,000 assemblies under the conditions described in this work.

Using various branching phosphoramidites,[151, 271] DNA dendrons were synthesized with three, four, or six branches (bDn, the number of branches, b = 3, 4, or 6) (**Figure 5.1. a**),[272] each featuring single-stranded sticky ends (5' TTCCTT 3') that can hybridize with AuNP PAEs bearing complementary sticky ends (5' AAGGAA 3') (Figure 1b). The dendrons have an 18- to 26-base stem that hybridizes with the arms on a template, enabling one to control the distance between the branches and the dendrimer core. For example, the dendrons 6Dn, 6Dn-L1, 6Dn-L2, and 6Dn-L3 have incrementally longer stems (**Table 5.3**). A Cy3-phosophoramidite was incorporated in the stem to enable quantification of dendron content. All DNA architectures were purified using denaturing polyacrylamide gel electrophoresis (PAGE) and characterized using matrix-assisted laser desorption ionization-time of flight mass spectroscopy (MALDI-TOF MS) (**Figure 5.2. and 5.3.**).

Table 5.3. DNA dendrons synthesized for this study

	DNA Sequence (5' to 3')	Isolated yield** (%)	Calc'd MW (kDa)	Exp't MW (kDa)
3Dn*	**TTCCTT-Sp18-Tr-Sp18-Cy3-Sp18-ACCACTCACTATTACCATTCCTT**	**7**	**14.9**	**14.9**
4Dn*	**TTCCTT-Sp18-D-Sp18-D-Sp18-Cy3-Sp18-ACCACTCACTATTACCATTCCTT**	**9**	**18.4**	**18.3**
6Dn*	**TTCCTT-Sp18-D-Sp18-Tr-Sp18-Cy3-Sp18-ACCACTCACTATTACCATTCCTT**	**4**	**23.4**	**23.1**
6Dn'	**TTCCTT-Sp18-D-Sp18-Tr-Sp18-Cy3-Sp18-ACCACTCACTATTACCAT**	**3**	**21.9**	**21.6**
6Dn-L1	**TTCCTT-Sp18-D-Sp18-Tr-Sp18-Cy3-Sp18-TCAACCTAACCACTCACTATTACCAT**	**4**	**24.3**	**24.0**
6Dn-L2	**TTCCTT-Sp18-D-Sp18-Tr-Sp18-Cy3-Sp18-CTTATCAACCTAACCACTCACTATTACCAT**	**5**	**25.5**	**25.2**
6Dn-L3	**TTCCTT-Sp18-D-Sp18-Tr-Sp18-Cy3-Sp18-CTTATCAACCTAACCACTCACTATTACCATTCACT**	**8**	**27.0**	**26.7**
6Dn_v2	**TTCCTT-Sp18-D-Sp18-Tr-Sp18-AGTTGATAAGGATGGAT**	**1*** **	**21.0**	**22.0**

*A 5' TTCCTT 3' sequence was appended at the 3' end of 3Dn, 4Dn, and 6Dn to augment dendron-AuNP PAE interactions. This modification improved the crystallinities and thermostabilities of the dendron-PAE assemblies, presumably by mitigating the repulsive contributions of the long stem regions.

**Assuming a coupling efficiency of 97%, a linear, 40-base DNA synthesis would be at ~20% isolated yield post-purification. The dendritic architecture and incorporation of specialty phosphoramidites decreases the synthetic yield. A standard 10-μmol synthesis would yield ~400 nmol of DNA dendrons, sufficient for preparing more than 9,000 assemblies under the conditions described in this work.

Table 5.4. Calculated melting temperatures (T_m) of anchor-linker pairs

	DNA Sequence (5' to 3')*	***T_m* / °C***
PAE anchor	**Thiol-$(Sp18)_2$-AACGACTCATACTCACCT**	**65**
PAE linker	**AAGGAA-Sp18-AGGTGAGTATGAGTCGTT**	
Temp_v1 (DBCO)	**DBCO-$(Sp18)_2$-TGGAGTGAATGGTAATAGTGAGTGGT**	**64**
6Dn	**TTCCTT-Sp18-D-Sp18-Tr-Sp18-Cy3-Sp18-ACCACTCACTATTACCATTCCTT**	
Temp_v1 (DBCO)	**DBCO-$(Sp18)_2$-TGGAGTGAATGGTAATAGTGAGTGGT**	**62**
6Dn'	**TTCCTT-Sp18-D-Sp18-Tr-Sp18-Cy3-Sp18-ACCACTCACTATTACCAT**	
Temp_v1 (DBCO)	**DBCO-$(Sp18)_2$-TGGAGTGAATGGTAATAGTGAGTGGT**	**62**
6Dn-L1	**TTCCTT-Sp18-D-Sp18-Tr-Sp18-Cy3-Sp18-TCAACCTAACCACTCACTATTACCAT**	
Temp_v1 (DBCO)	**DBCO-$(Sp18)_2$-TGGAGTGAATGGTAATAGTGAGTGGT**	**62**
6Dn-L2	**TTCCTT-Sp18-D-Sp18-Tr-Sp18-Cy3-Sp18-CTTATCAACCTAACCACTCACTATTACCAT**	
Temp_v1 (DBCO)	**DBCO-$(Sp18)_2$-TGGAGTGAATGGTAATAGTGAGTGGT**	**69**
6Dn-L3	**TTCCTT-Sp18-D-Sp18-Tr-Sp18-Cy3-Sp18-CTTATCAACCTAACCACTCACTATTACCATTCACT**	
Temp_v2 (DBCO)	**DBCO-$(Sp18)_2$-CATCCATCCTTATCAACT**	**60**
6Dn_v2	**TTCCTT-Sp18-D-Sp18-Tr-Sp18-AGTTGATAAGGATGGAT**	
Temp_v1 (DBCO)	**DBCO-$(Sp18)_2$-TGGAGTGAATGGTAATAGTGAGTGGT**	**72**
Block strand	**AACATCTAATCTACATCTACCACTCACTATTACCATTCACTCCA**	
Unblock strand	**TGGAGTGAATGGTAATAGTGAGTGGTAGATGTAGATTAGATGTT**	**80**
Block strand	**AACATCTAATCTACATCTACCACTCACTATTACCATTCACTCCA**	
6Dn-L2	**TTCCTT-Sp18-D-Sp18-Tr-Sp18-Cy3-Sp18-CTTATCAACCTAACCACTCACTATTACCAT**	**40**
Rigidifying strand	**TAGGTTGATAAG**	

*All melting temperatures are calculated on NUPACK (http://www.nupack.org/partition/new, accessed on April 16, 2021),[9-10] with [oligonucleotide] = 0.3 µM, [Na$^+$] = 0.5 M. The inputted sequences are bolded, and the base-pairs that were hybridized at room temperature are underlined. All sequences were checked to ensure that no secondary structures were expected to form at room temperature.

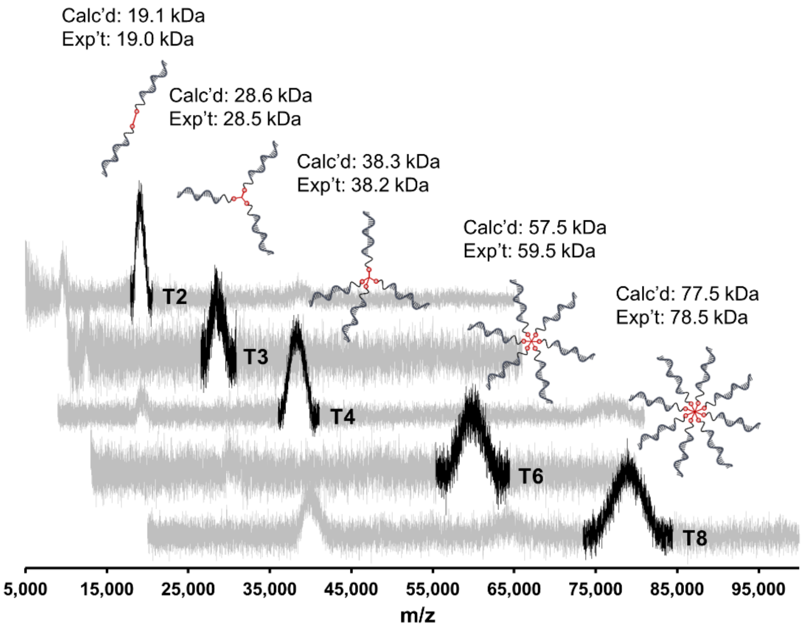

Figure 5.2. MALDI-TOF characterization of DNA templates
Stacked MALDI-TOF MS spectra of the DNA templates utilized in this work (linear and negative ion mode; matrix: dihydroxyacetone phosphate).

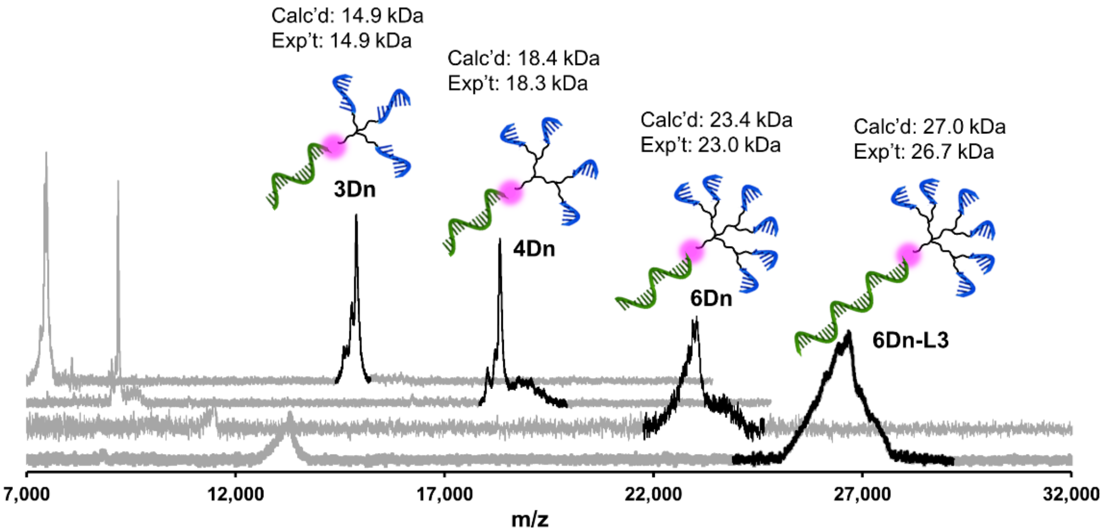

Figure 5.3. MALDI-TOF characterization of the DNA dendrons
Stacked MALDI-TOF MS spectra of selected DNA dendrons utilized in this work (linear and negative ion mode; matrix: dihydroxyacetone phosphate).

To establish that this hybridization-based approach can successfully produce supramolecular dendrimers (**Figure 5.1. c**), dendrons (4Dn and 6Dn) and templates (T2, T3, and T6) were stoichiometrically combined in 0.5 M NaCl, annealed from 64 °C to 4 °C, and characterized using 5% native PAGE. Discrete bands indicate the formation of DNA dendrimers, where a defined number of dendrons hybridized onto the template at near-stoichiometric ratios (**Figure 5.1. d**). Using dendrons with a greater number of branches or templates with a greater number of arms yielded larger dendrimers with lower electrophoretic mobilities. To probe the sizes of these structures in 0.5 M NaCl, 10 mM phosphate buffer, dynamic light scattering (DLS) measurements were performed. 6Dn alone has a hydrodynamic diameter (D_h) of 5.8 nm, and the D_h of the dendrimers increases with the template valency (**Figure 5.1. e**). These experiments confirm that this hybridization-based synthetic approach is effective in tuning the structure of DNA-presenting building blocks.

5.3. Nanoparticle Superlattice Assembly and Crystal Structure Analysis

To synthesize colloidal crystals, DNA dendrons or dendrimers were combined with 10-nm AuNP PAEs (**Figure 5.1. b**) in dendron/AuNP ratios of 16:1 or 24:1 (**Table 5.5.**), selected through initial empirical observations that these ratios yield well-formed aggregates. These mixtures were then made up to 100 μL at 0.5 M NaCl, 10 mM phosphate, and 0.015% sodium dodecyl sulfate (SDS), unless otherwise specified (**Table 5.6.**). The assemblies were heated to 60 °C, above the crystals' melting temperatures, and cooled to 22 °C at a rate of 0.1 °C per 10 min and characterized using small angle x-ray scattering (SAXS) in the solution state[273] and scanning transmission electron microscopy (STEM) in the solid state (after silica encapsulation, resin embedding, and ultramicrotomy).[274] We explored the phase space using different combinations of dendrons and templates (**Figure 5.4. a and Table 5.5.**) and identified five distinct crystalline phases: face-centered cubic (FCC, **Figure 5.4. b**), simple hexagonal (SH, **Figure 5.4. c**), simple cubic (SC, **Figure 5.4. d**), Ti_5Ga_4-type (**Figure 5.4. e**), and graphite-type (GT, **Figure 5.4. f**).[275]

Table 5.5. Phase space screening of dendron/dendrimer templated superlattices

Dendron	Template	Dendron/ AuNP ratio	Symmetry	Space group*	Lattice constant (nm)*	AuNP Wyckoff positions*
3Dn	N/A	16	FCC	Fm-3m	a = 42.8	4a
3Dn	T2	16	SH	P6/mmm	a = 32.3, c = 31.9	1a
3Dn	T3	16	SH	P6/mmm	a = 31.5, c = 30.9	1a
3Dn	T4	16	SH	P6/mmm	a = 31.6, c = 31.2	1a
3Dn	T6	16	SC	Pm-3m	a = 30.0	1a
3Dn	T8	16	SC, SH	Pm-3m	a = 29.3	1a
4Dn	N/A	16	FCC	Pm-3m	a = 46.1	4a
4Dn	T2	16	SH	P6/mmm	a = 32.4, c = 32.0	1a
4Dn	T3	16	SH	P6/mmm	a = 32.4, c = 32.0	1a
4Dn	T4	16	SH	P6/mmm	a = 33.3, c = 32.8	1a
4Dn	T6	16	SC, SH	P6/mmm	a = 33.3, c = 32.8	1a
4Dn	T8	16	SC, SH	Pm-3m	a = 31.3	1a
6Dn	N/A	16	FCC	Fm-3m	a = 45.5	4a
6Dn	T2	16	SH	P6/mmm	a = 32.6, c = 32.6	1a
6Dn	T3	16	SH	P6/mmm	a = 32.0, c = 32.4	1a
6Dn	T4	16	SH**	P6/mmm	a = 32.4, c = 32.1	1a
6Dn	T6	16	SC	Pm-3m	a = 30.6	1a
6Dn	T8	16	SC	Pm-3m	a = 31.3	1a
6Dn-L1	N/A	24	FCC	Fm-3m	a = 45.2	4a
6Dn-L1	T2	24	Ti_5Ga_4	P63/mcm	a = 72.3, c = 61.1	4d, 6g
6Dn-L1	T3	24	Ti_5Ga_4	P63/mcm	a = 72.3, c = 61.1	4d, 6g
6Dn-L1	T4	24	SC	Pm-3m	a = 30.2	1a
6Dn-L1	T6	24	SC	Pm-3m	a = 30.9	1a
6Dn-L1	T8	24	SC	Pm-3m	a = 30.7	1a
6Dn-L2	N/A	24	FCC	Fm-3m	a = 47.0	4a
6Dn-L2	T2	24	Ti_5Ga_4	P63/mcm	a = 73.0, c = 61.4	4d, 6g
6Dn-L2	T3	24	Ti_5Ga_4	P63/mcm	a = 72.7, c = 60.5	4d, 6g
6Dn-L2	T4	24	SC	Pm-3m	a = 31.0	1a
6Dn-L2	T6	24	GT, SC	Pm-3m	a = 31.6	1a
6Dn-L2	T8	24	GT, SC	Pm-3m	a = 31.2	1a
6Dn-L3	N/A	16	FCC	Fm-3m	a = 46.1	4a
6Dn-L3	T2	24	Ti_5Ga_4	P63/mcm	a = 73.2, c = 61.5	4d, 6g
6Dn-L3	T3	24	Ti_5Ga_4, SC	P63/mcm	a = 75.3, c = 62.7	4d, 6g
6Dn-L3	T4	24	Ti_5Ga_4, SC	Pm-3m	a = 31.1	1a
6Dn-L3	T6	24	GT, SC	P6/mmm	a = 36.0, c = 36.5	2d
6Dn-L3	T8	24	GT, SC	P6/mmm	a = 38.1, c = 36.7	2d

Assembly buffer: 0.5 M NaCl, 10 mM phosphate, 0.015 % SDS, pH 7.4.
200 equiv. of PAE linker strands were added per AuNP PAE (25 nM).
*The major phase’s space group, lattice parameters, and AuNP Wyckoff positions are reported.
**This sample contains some partially disordered *R*-3*m* phase.

Table 5.6. Effect of changing SDS concentration

Dendron	Template	Dendron/ AuNP ratio	SDS (%)	Symmetry*	Space group*	Lattice constant (nm)*
4Dn	T2	16	0	disordered	N/A	N/A
4Dn	T2	16	0.005	disordered	N/A	N/A
4Dn	T2	16	0.01	SC, SH	P6/mmm	a = 33.1, c = 32.8
4Dn	T2	16	0.02	SH	P6/mmm	a = 32.3, c = 32.0
4Dn	T2	16	0.04	SH	P6/mmm	a = 32.3, c = 32.0
6Dn	T6	16	0	SH (br)	P6/mmm	a = 31.7, c = 31.7
6Dn	T6	16	0.005	SH (br)	P6/mmm	a = 31.7, c = 31.7
6Dn	T6	16	0.01	SC	Pm-3m	a = 30.8
6Dn	T6	16	0.02	SC, SH	Pm-3m	a = 30.8
6Dn	T6	16	0.04	SC, SH	Pm-3m	a = 30.7
6Dn	T3	24	0	SH (br)	P6/mmm	a = 32.2, c = 31.7
6Dn	T3	24	0.005	SH (mixed)	P6/mmm	a = 32.0, c = 31.9
6Dn	T3	24	0.01	SC	Pm-3m	a = 31.0
6Dn	T3	24	0.02	SH	P6/mmm	a = 32.3, c = 32.1
6Dn	T3	24	0.04	SH	P6/mmm	a = 32.3, c = 32.1
6Dn-L2	T3	24	0	SH	P6/mmm	a = 32.2, c = 32.0
6Dn-L2	T3	24	0.005	SH	P6/mmm	a = 32.3, c = 32.1
6Dn-L2	T3	24	0.01	Ti_5Ga_4	P63/mcm	a = 73.5, c = 60.6
6Dn-L2	T3	24	0.02	Ti_5Ga_4 (br)	P63/mcm	a = 73.4, c = 60.9
6Dn-L2	T3	24	0.04	SC	Pm-3m	a = 33.7

The phases formed around the CMC of SDS (0.01%) are bolded. All assemblies are prepared in 0.5 M NaCl, 10 mM phosphate, pH 7.4.

*The major phase's space group and lattice parameters are reported.

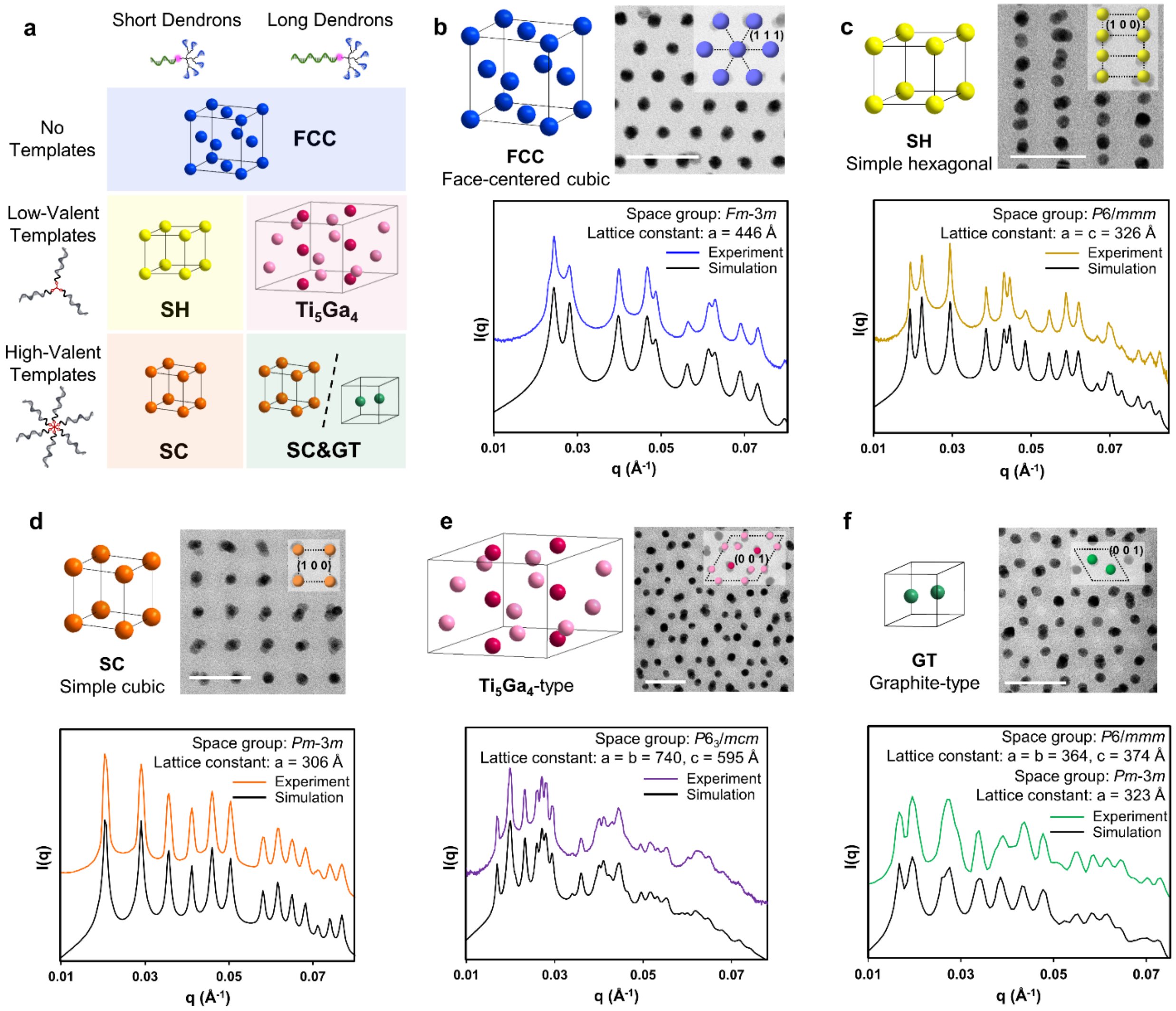

Figure 5.4. Superlattice phase symmetries and their characterization
(a) A depiction of the phase space: crystal structures depend on the presence and the identity of DNA-containing templates, as well as the stem length of the DNA dendrons (e.g., compared to 6Dn, 6Dn-L1 has an additional eight-base, non-hybridized region between the core and the branching region, while 6Dn-L2 and 6Dn-L3 have additional 12-base non-hybridized regions). (b)-(f), All structures were screened and characterized in the solution-state *via* small angle x-ray scattering (SAXS). Colored traces are experimental data, and black traces are simulated spectra. Representative samples were imaged *via* scanning transmission electron microscopy (STEM) after stabilization in the solid state. (b) Face-centered cubic (FCC). (c) Simple hexagonal (SH). (d) Simple cubic (SC). (e) Ti_5Ga_4-type. (f) A mixture of graphite-type (GT) and SC. Scale bars: 50 nm.

Most structures were pure and highly crystalline; however, the GT phase was always mixed with the SC phase in our system, and we also observed a partially disordered phase (**Figure 5.5.**) that is structurally related to the Ti_5Ga_4-type phase. The Ti_5Ga_4-type phase is of a low space group symmetry ($P6_3/mcm$), and has no precedent in colloidal crystal engineering, demonstrating how the catalogue of structures possible can be expanded by using DNA dendrimers as building blocks (*vide infra*). Additional crystal structure analysis can be found in **appendix 2**.

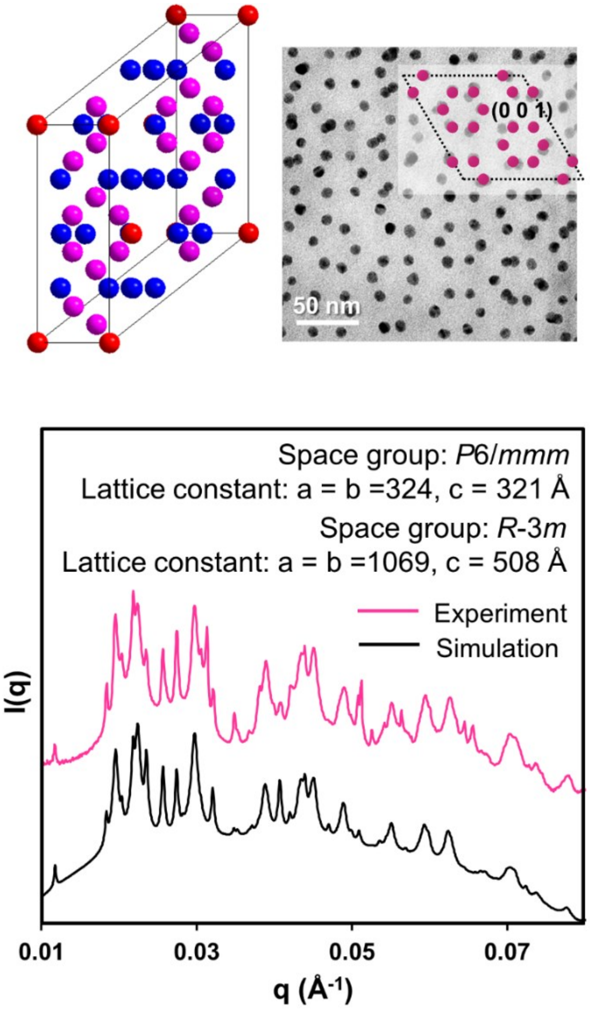

Figure 5.5. A mixture of SH and partially disordered R-3m phases
Top left: A structural model of the R-3m phase generated using all three Wyckoff positions. Top right: Cross-sectional ADF-STEM image shows a section where only the 18g Wyckoff position is occupied. Bottom: SAXS spectrum (pink) and simulation (black). The simulation was generated by summing contributions from a modeled SH structure and a modeled structure with R-3m phase, the latter of which was generated using partially occupied Wyckoff positions (bracketed are the relative contributions): 3a (1.25), 18g (0.5), 18 h (0.75).

DNA dendrons (e.g., 3Dn, 4Dn, and 6Dn) were assembled with 10-nm AuNP PAEs to form colloidal crystals with face-centered cubic (FCC) structures (**Figure 5.4. b**). FCC crystals have been observed when AuNP PAEs were assembled with low-valent electron equivalents (EEs)[276] that display metallic-type colloidal bonding. Due to their low valencies, DNA dendrons function as delocalized EEs (**Figure 5.6.**), bonding moieties that roam through and bind the AuNP PAE sublattice through sticky end interactions. The resulting structure is consistent with previous findings that FCC lattices are thermodynamically favorable in single-component nanoparticle systems,[277] stemming from the high symmetry and packing efficiency of the particles. A 5' TTCCTT 3' sequence was appended at the 3' end of the dendron stem in certain cases to augment dendron-AuNP PAE interactions. This sequence modification improved the crystallinities and thermostabilities of the dendron-PAE assemblies, presumably by mitigating the repulsive contributions of the long stem regions.

When two spherical PAEs with complementary sticky ends are assembled, the resulting crystal structures can be predicted using the complementary contact model (CCM).[6] The CCM assumes that superlattice formation maximizes the number of DNA duplexes (or "bonding") in the system. As such, crystal structures can be predicted by considering the size and linker ratios of the complementary building blocks. Thus, it is not surprising that, for 3Dn, 4Dn, and 6Dn, the crystal structure transitions from SH to SC as template valency increases (**Figure 5.2. a**). SH and SC are structural equivalents of AlB2 and CsCl, respectively, specifically observed when one of the two PAEs scatters x-rays to a much lesser extent, as in the case of a hollow spacer[275] or a DNA dendrimer (this work). However, based on the hydrodynamic diameters of the dendrimer formed from 6Dn and T6 (D_h = 14.0 nm, Figure 1e) and of the 10-nm AuNP PAE (D_h = 24.5 nm, **Figure**

5.7.), and their linker ratio, the CCM predicts the formation of an SH structure, not the experimentally observed SC lattice. The reason for this deviation is discussed below.

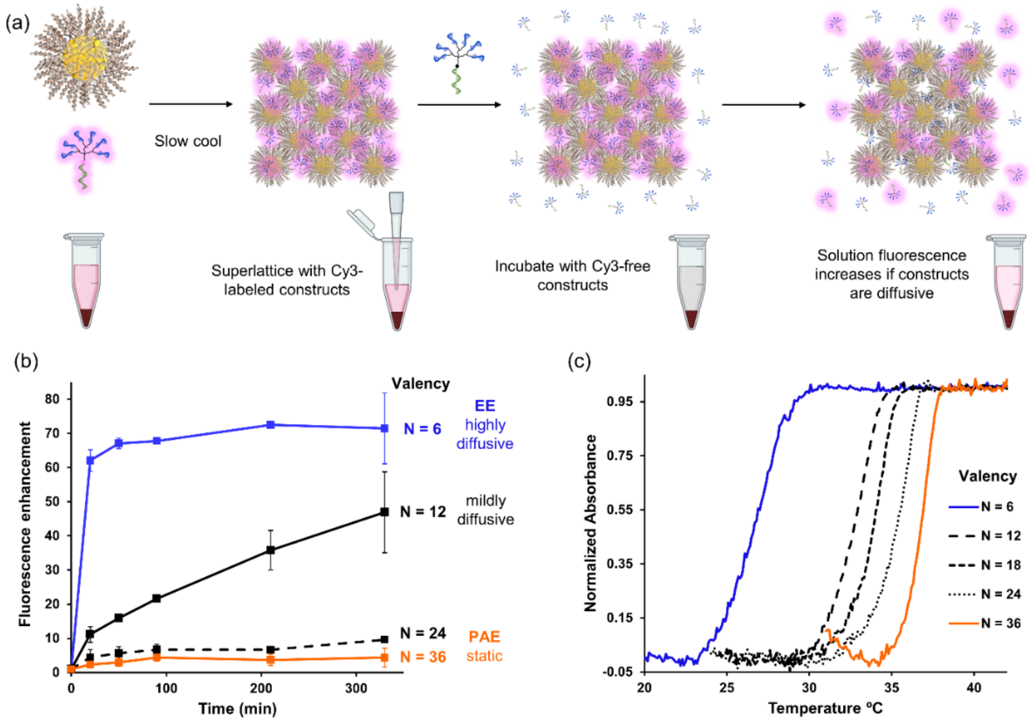

Figure 5.6. Determining DNA dendrimer diffusivity
(a) Experimental procedures used to track the rate of diffusion of dye-labeled constructs across the solution-superlattice interface. The rate of diffusion reflects the colloidal bonding character (e.g., metallic versus ionic) of the dendrons or dendrimers in the colloidal assemblies. (b) Low-valent dendron EEs diffuse quickly while high-valent dendrimer PAEs show negligible diffusion. The amount of Cy3-labeled dendrons (6Dn') used for sample preparation, as well as the amount of non-labeled dendrons (6Dn_v2), was kept constant across different samples (24 equiv. of the dendrons per AuNP). The error bars denote the standard deviation in fluorescence enhancement across three independent samples. (c) The melting temperatures (Tm) increase as template valency (N) increases. For N = 6, no templates were added (i.e., only 6Dn' was used). Corresponding templates were added stoichiometrically for superlattice sample preparation for other valencies (e.g., T2 was added for N = 12).

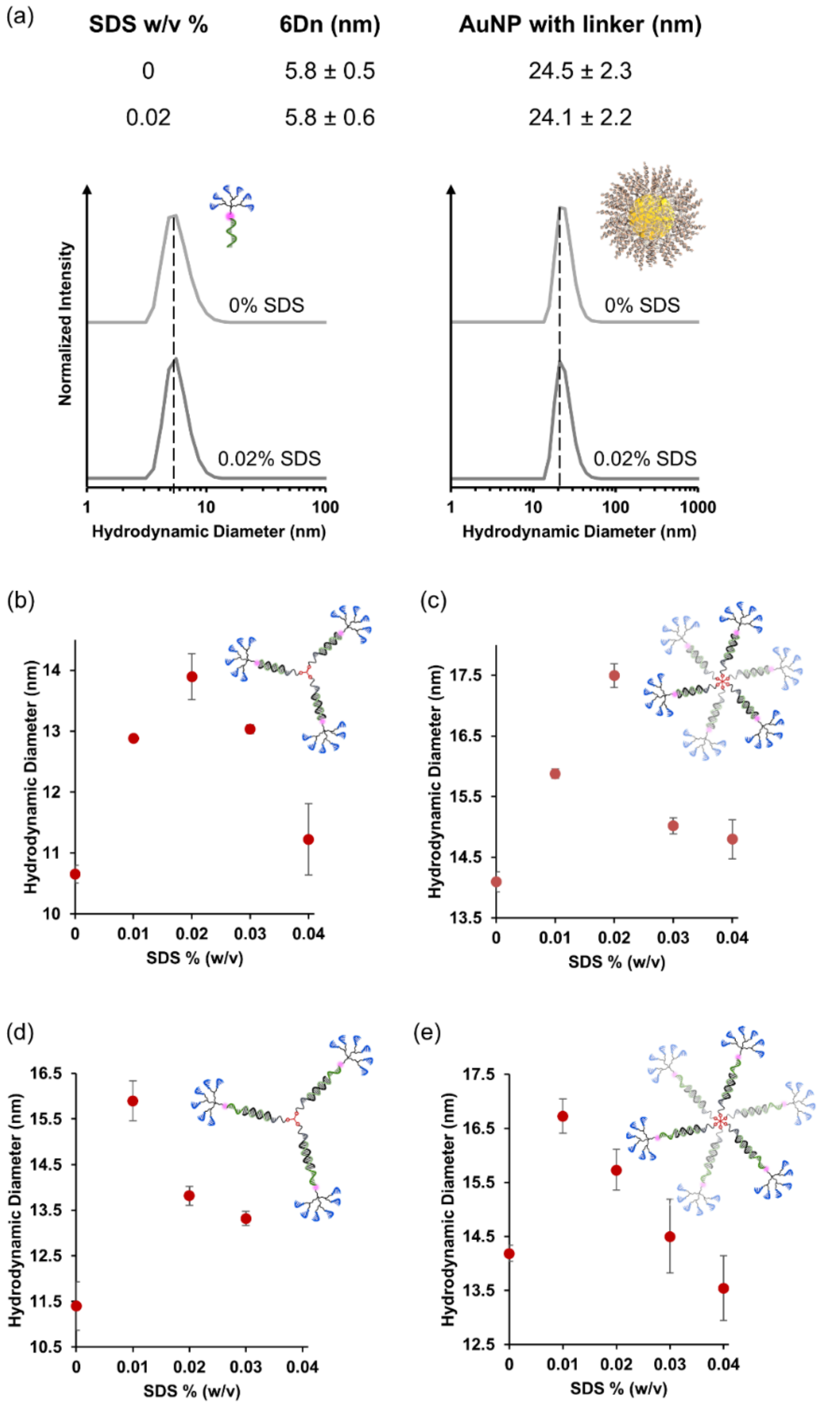

SDS w/v %	6Dn (nm)	AuNP with linker (nm)
0	5.8 ± 0.5	24.5 ± 2.3
0.02	5.8 ± 0.6	24.1 ± 2.2

Figure 5.7. DLS characterization of DNA structures used in this study
(a) The hydrodynamic diameters (Dh) of dendrons and AuNPs do not change with the addition of SDS in 0.5 M NaCl, 10 mM phosphate, pH 7.4 buffer. (b-e) Dh of dendrimers increase initially with SDS concentration, peak near the CMC of SDS (0.01 – 0.02 %), and then decrease with increasing SDS concentration. Due to the dynamic nature of dendrimer-dendrimer association in solution, the increase in Dh only reflects a fraction of the increase in the size of the effective building blocks in nanoparticle superlattices. Error bars denote the standard deviation in mean diameter from three measurements. (b) 6Dn and T3, (c) 6Dn and T6, (d) 6Dn-L2 and T3, and (e) 6Dn-L3 and T6.

5.4. Quantifying Superlattice Composition

We quantified the stoichiometric ratio of DNA dendrimer to AuNP in the superlattices to understand how DNA dendrimers direct nanoparticle assembly,[278] especially in the case of the aforementioned SC phase, which is an apparent departure from the CCM.[6] Specifically, the number of Cy3-labeled dendrons and 10-nm AuNP PAEs incorporated into the crystals were quantified using UV-vis spectroscopy (**Figure 5.8.**). When 6Dn was combined with T6 or T8, the resulting DNA dendrimers templated SC superlattices; analyzing the compositions of those crystals revealed that the DNA dendrimer to AuNP ratio is approximately 2:1. However, the SC phase should consist of two complementary PAEs of similar size in a 1:1 ratio.[6, 275] This finding suggests that two DNA dendrimers associate to give a discrete building block large enough in size to form an SC lattice when co-assembled with 10-nm AuNP PAEs.

Due to the presence of several hydrophobic moieties (e.g., DBCO) at the core of these dendrimers, we hypothesized that dendrimer-dendrimer association is enabled, at least in part, by

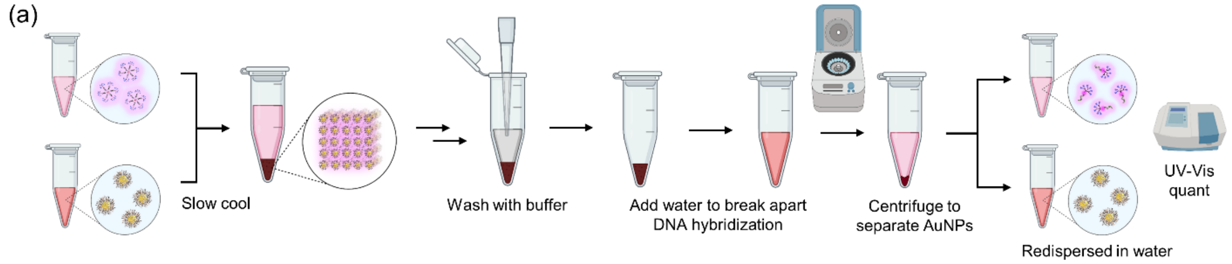

(b)

Sample	Input Dendron/AuNP	Crystal Dendron/AuNP	Structure (Stoichiometry)	No. of Dendrimers per lattice site
T3 + 6Dn	16	12.20 ± 1.09	SH (AB_2)	2.03 ± 0.18
T6 + 6Dn	16	14.13 ± 2.34	SC (AB)	2.35 ± 0.39
T8 + 6Dn	16	14.64 ± 0.99	SC (AB)	1.83 ± 0.12
T3 + 6Dn-L2	24	15.57 ± 1.14	Ti_5Ga_4-type (A_5B_4)	6.49 ± 0.48

Figure 5.8. Stoichiometric composition of resultant colloidal crystals
(a) A typical experiment for quantifying the ratio of Cy3-labeled dendron to AuNP within a colloidal crystal sample. The crystals are washed, disassembled, and centrifuged to separate the dendrons and 10-nm AuNPs. The dendrons and AuNPs were then separately quantified using their UV-vis absorbances. (b) A table showing the composition of colloidal crystals, quantified by the ratio of dendron per gold nanoparticles. Each entry represents the averages and standard deviation of three replicates. The number of dendrimers per lattice site is calculated by dividing the dendron to AuNP ratio by the template valency.

hydrophobic interactions. To test our hypothesis, we synthesized a template free of hydrophobic moieties by conjugating alkynyl-appended DNA onto a polyamidoamine (PAMAM)-based octa-azide core. PAMAM is hydrophilic, and, compared to DBCOs, linear alkynes yield triazole linkages that are significantly less hydrophobic. The resulting template (denoted as T8'), which is free of hydrophobic moieties, was combined with 6Dn and assembled with AuNP PAEs to yield SH superlattices, as predicted by the CCM (**Figure 5.9.**). On the contrary, SC superlattices were formed when the DBCO-containing T8 template was used, under identical assembly conditions. This result suggests that dendrimer-dendrimer association is likely mediated by hydrophobic interactions.

5.5. Micelle-Mediated Dendrimer-Dendrimer Association

We reasoned that SDS, added to the assembly buffer to enhance colloidal stability, can provide a confined, hydrophobic environment that brings together multiple dendrimers through micelle formation. Crucially, the critical micelle concentration (CMC) of SDS, in 0.5 M NaCl and at room temperature, is around 0.0094 to 0.015% (w/v).[279-281] Realizing our assemblies were prepared in the presence of SDS micelles, we hypothesized the following pathway for dendrimer-dendrimer association (**Figure 5.10. a**). Below the CMC of SDS, the DNA dendrimers do not associate with one another. At or just above the CMC of SDS, a small number of micelles form, and the hydrophobic moieties that define the core of the dendrimers insert into the micelles, mediating the association of two or more DNA dendrimers. Far above the CMC of SDS, the dendrimers are divided among many micelles, leading to less dendrimer-dendrimer association.

To test this hypothesis, we prepared assemblies by combining DNA dendrimers (6Dn and T6) with 10-nm AuNP PAEs and by adding an increasing amount of SDS (0, 0.005, 0.01, 0.02, and 0.04%) into assembly precursor solutions (**Table 5.6.**). *In situ* SAXS characterization of the resulting crystals revealed that, at 0 and 0.005% SDS (**Figure 5.10. b, left**), the CCM-predicted SH phases were formed, as dendrimer-dendrimer associations do not occur in the absence of micelles. At 0.01% SDS, the SC phase was formed exclusively, suggesting that micelle-

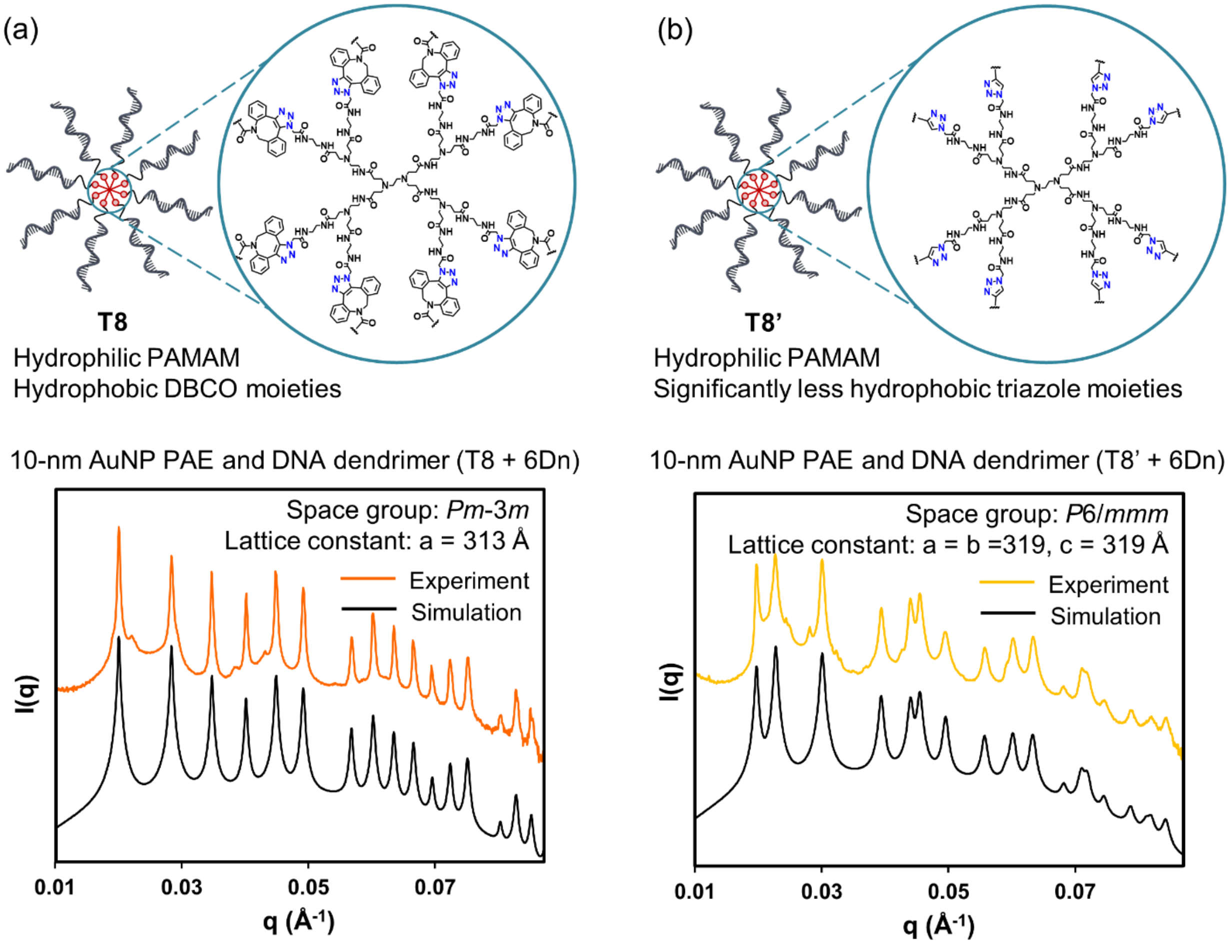

Figure 5.9. The effects of hydrophobic groups on NP assembly
The influence of hydrophobic moieties on dendrimer-dendrimer association and ultimately the superlattice crystal structure. Above: the molecular core and conjugation moieties of (a) T8 (DBCO moieties) and (b) T8' (hexynyl moieties) are highlight. Below: experimental (colored) and simulated (black) SAXS spectra of nanoparticle superlattices synthesized using (a) T8-templated dendrimer (DBCO moieties) and (b) T8'-templated dendrimer (hexynyl moieties). Both assemblies are prepared with 0.5 M NaCl, 10 mM phosphate, 0.015% SDS, pH 7.4 buffer.

dendrimers assemble near the CMC of SDS. As the concentration of SDS was increased further, the SH phase begins to reappear, consistent with our hypothesis. We note that there was still some SC phase at 0.04 % SDS, suggesting that the formation of high-valent micelle-dendrimers is promoted in high-concentration condensed states. We also characterized, using DLS, the solution hydrodynamic diameters of the DNA dendrimers as a function of SDS concentration using DLS. We observed considerable increases in D_h at 0.01 and 0.02% SDS (**Figure 5.7.**), consistent with our hypothesis that micelle-dendrimer formation is facilitated by a low concentration of SDS micelles. These experiments show that superlattice assembly can be guided along different pathways by controlling the degree of dendrimer-dendrimer association *via* surfactant concentration.

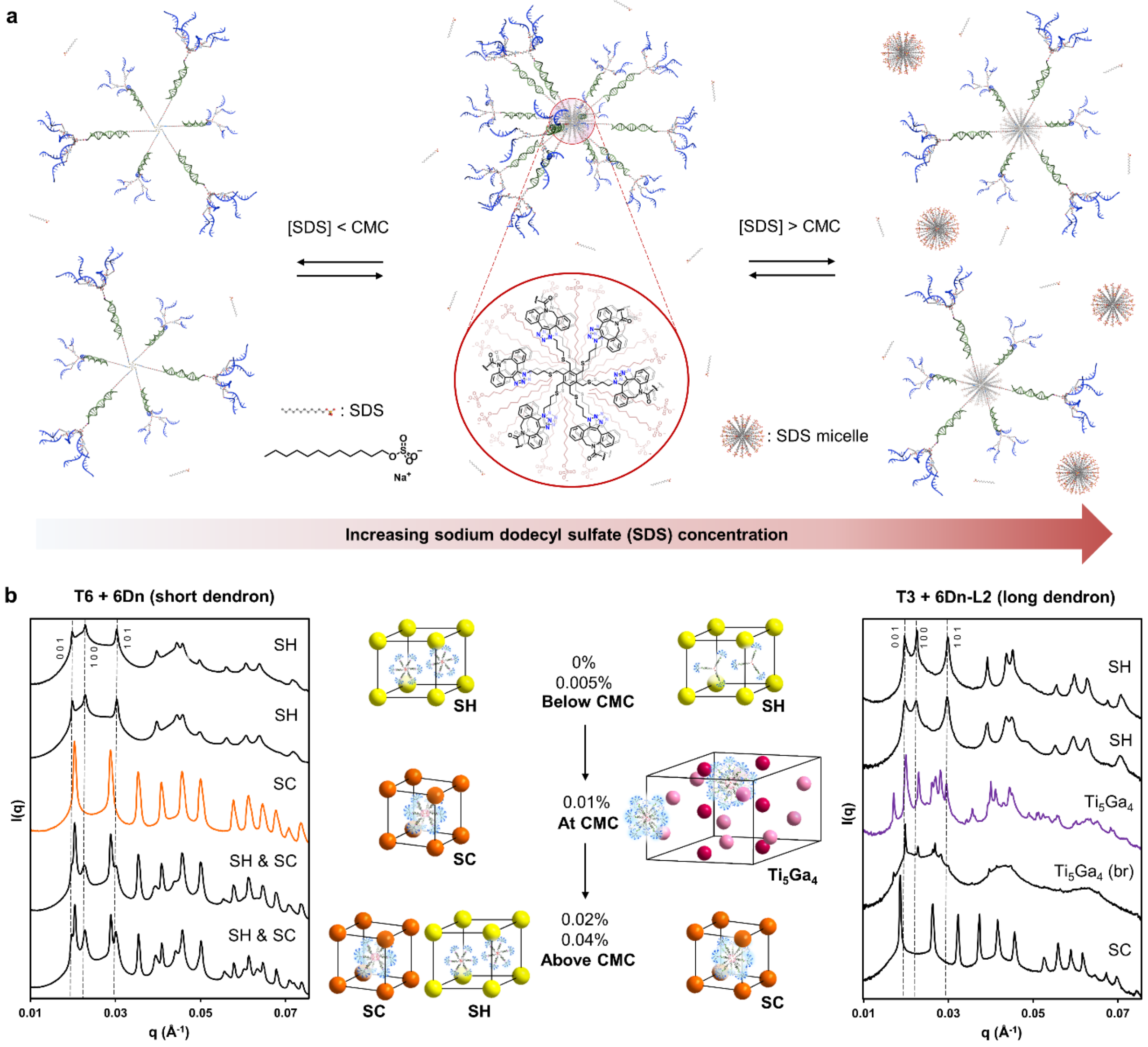

Figure 5.10. Surfactant-mediated DNA micelle-dendrimers

(a) Proposed pathway for dendrimer-dendrimer association. Surfactant sodium dodecyl sulfate (SDS) forms micelles at concentrations equal to or higher than the critical micelle concentration (CMC). These micelles encapsulate the hydrophobic cores of the templates, leading to dendrimer-dendrimer association at and slightly above the CMC. 3D models of DNA dendrimers and SDS micelles are drawn to scale. (b) From top to bottom: SAXS data collected at 0, 0.005, 0.01, 0.02, and 0.04% SDS. Left: T6 (0.1 µM) and 6Dn (0.6 µM). Right: T3 (0.2 µM) and 6Dn-L2 (0.6 µM), except for the sample at 0% SDS, whereby 1.5× concentrations were used to encourage aggregate formation. Center: observed crystal structures, represented by unit cells that depict DNA dendrimer and micelle-dendrimer locations. For clarity, not all micelle-dendrimers in the Ti_5Ga_4-type unit cell are drawn. Below the CMC, dendrimers do not associate with one another. At the CMC, the dendrimers associate to the greatest extent, significantly modulated by dendron stem length. Above the CMC, the dendrimers are distributed across a larger number of micelles, leading to less dendrimer-dendrimer association.

5.6. Understanding the Emergence of the Ti_5Ga_4-type Phase

We then addressed the question of whether the micelle-dendrimer size can be changed *via* structure design. Specifically, we hypothesized that a longer dendron stem would place the sterically bulky branches further from the dendrimer core, allowing more dendrimers to be inserted into a single micelle without prohibitive repulsion. To test this hypothesis, we added SDS into assembly precursor solutions containing 10-nm AuNP PAEs, T3 templates, and 6Dn-L2 (long dendron stem, **Figure 5.10. b, right**). SAXS revealed that below the CMC of SDS, the SH phase was formed, as individual DNA dendrimers are only large enough to template SH lattices. At 0.01% SDS (near the CMC), when the degree of dendrimer-dendrimer association should be at its highest, the Ti_5Ga_4-type phase was formed. Importantly, at 0.04% SDS, when presumably there is less dendrimer-dendrimer association, the SC phase was formed exclusively. In contrast, the assemblies prepared using T3 and 6Dn (short dendron) only yielded the SH phase at 0.04% SDS (**Figure 5.11.**). These results confirm our hypothesis that the dendron stem length in part determines the number of DNA dendrimers that can associate to form discrete micelle-dendrimers (**Figure 5.12.**). In a similar vein, GT phases are only observed when the DNA dendrimers are made up of a long dendron (6Dn-L2 or 6Dn-L3) and a high-valent template (T6 or T8). The presence of a large micelle-dendrimer is supported by the observation that the distances between complementary particles that are in contact are markedly longer in the GT phase than those in the SH or SC phases (**Figure 5.13.**).

In Ti_5Ga_4-type crystal structure, the AuNPs occupy two distinct Wyckoff positions: 4d (1/3, 2/3, 0) and 6g (1/4, 0, 1/4). To elucidate the locations of the DNA micelle-dendrimers, we constructed Voronoi polyhedra around the AuNPs (**Figure 5.14. a**). The polyhedra vertices meet at locations that possess the highest equidistant connectivity to the AuNPs. These locations, 2b (0, 0, 0) and 6g (3/5, 0, 1/4), pinpoint the most energetically favorable sites for the micelle-dendrimers. This analysis yields two important take-aways. First, the Ti_5Ga_4-type phase, which has a stoichiometry of A_5B_4 (where A is AuNP PAE and B is DNA micelle-dendrimer), resembles a class of intermetallic compounds with an archetype of Ti_5Ga_4 (**Table 5.7.**).[13-14] Second, the two Wyckoff positions for the micelle-dendrimers have distinct coordination numbers and distances from the AuNPs (**Figure 5.14. b**), indicating that they are occupied by micelle-dendrimers with different sizes. These non-degenerate micelle-dendrimers can only be accessed due to the dynamic nature of micelle-mediated, dendrimer-dendrimer association. Using the aforementioned quantification experiment (**Figure 5.8.**), we calculated that each B site contains an average of 6.49

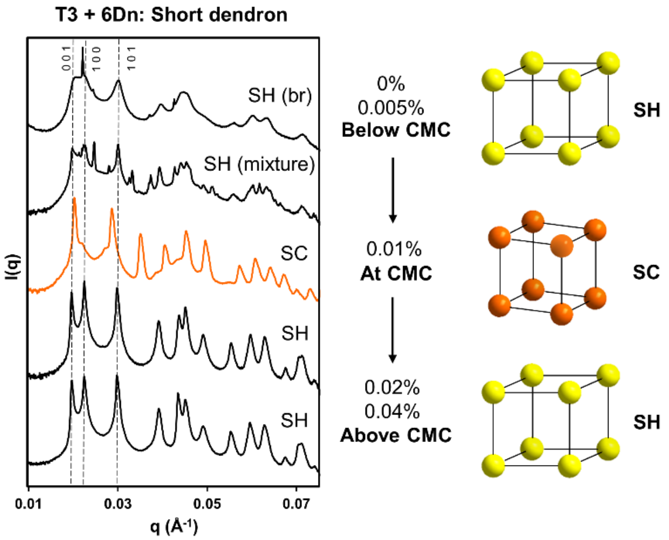

Figure 5.11. SDS concentration effects on assembly outcomes
10-nm AuNP PAEs were combined with DNA dendrimers made up of T3 and 6Dn (short stem). 0.4 µM of T3 and 1.2 µM of 6Dn were used, whereby 0.6 µM of T3 and 1.8 µM of 6Dn were used to encourage aggregates formation. From top to bottom: SAXS traces collected at 0, 0.005, 0.01, 0.02, and 0.04% SDS. The short dendron stem limits the degree of dendrimer-dendrimer association, and thus the SH phase was favored.

± 0.48 DNA dendrimers. We propose that the 2b site, with a lower coordination number and shorter distances from AuNPs, is occupied by a 5-mer, while the 6g site is occupied by a 7-mer. This averages to 6.5 DNA dendrimers per AuNP, matching the quantified composition.

The symmetry-breaking induced by these discrete micelle-dendrimers can also be highlighted by constructing a new set of Voronoi polyhedra around both the AuNPs and DNA micelle-dendrimers (**Figure 5.15.**). Two of these Voronoi polyhedra are Frank-Kasper (FK)-type, with a coordination number (CN) of 14, while the other two are pseudo-FK polyhedra with CNs of 13 and 17, respectively. Overall, the emergence of the Ti_5Ga_4-type phase is predicated on supramolecules undergoing further association, *via* transient interactions, into micellar architectures with discrete sizes. This type of symmetry-breaking mechanism, that is the transition from a simple to a complex packing structure caused by the formation of unequal-sized micelles, has been observed in soft

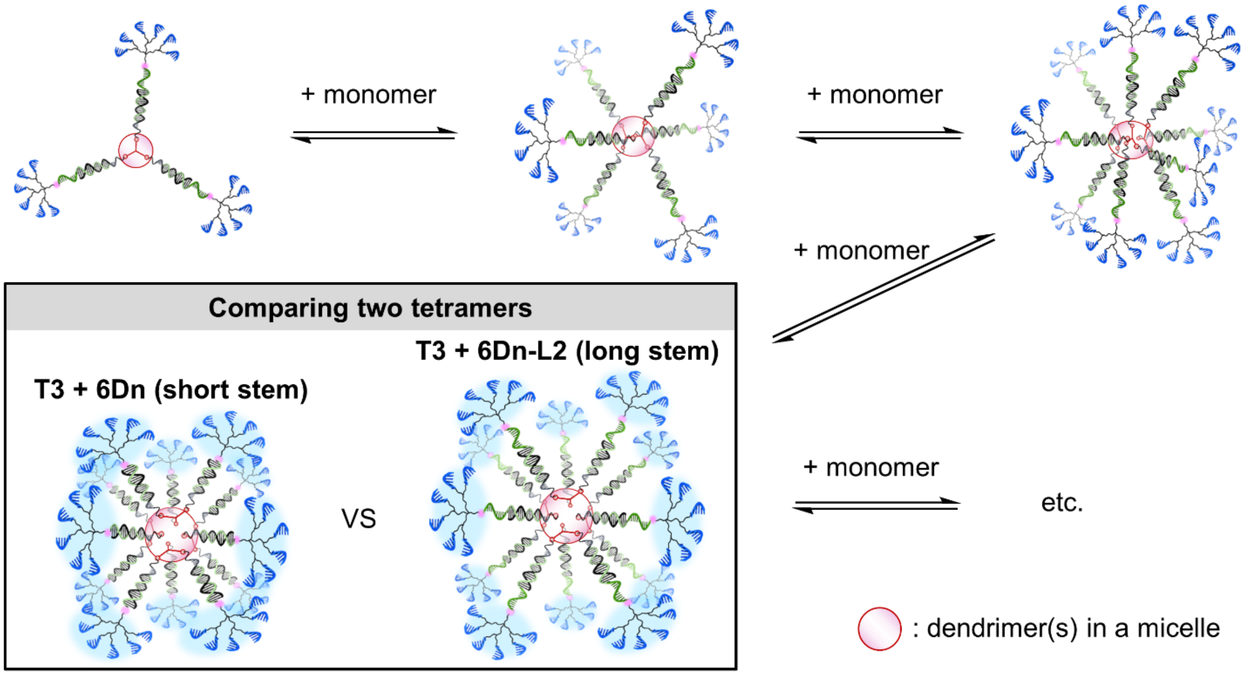

Figure 5.12. Model of DNA dendrimer association with different stem lengths
A model depicting the impact of dendron stem length on the degree of dendrimer association in the presence of SDS micelles. A longer stem relieves steric hindrance between dendron branches in a multi-mer. Thus, a longer dendron stem would enable a higher degree of dendrimer-dendrimer association and affect the resulting colloidal crystal structures.

matter[250, 259, 282] but is new to systems involving inorganic nanoparticles. Thus, reorganizable supra-structures offer new routes for expanding accessible structure types in nanoparticle assembly.

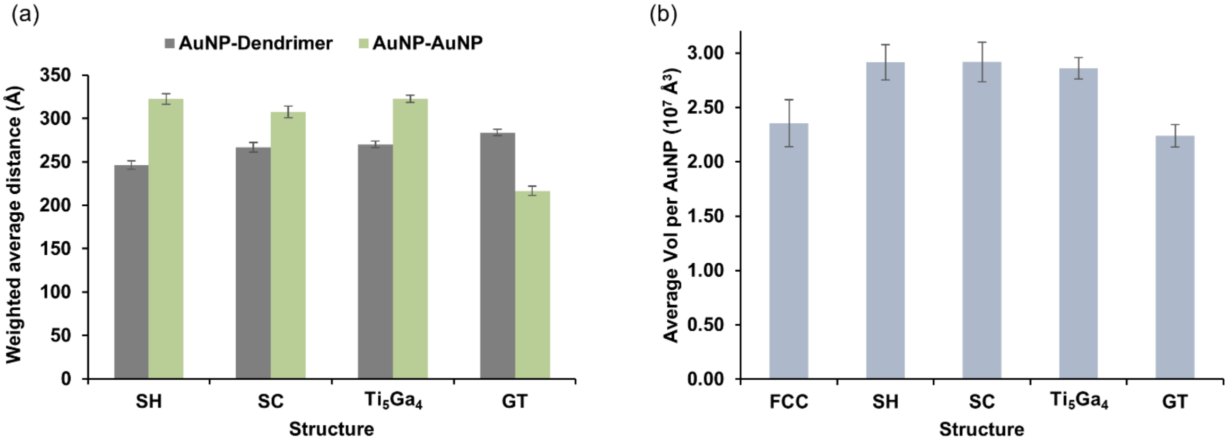

Figure 5.13. Changed in lattice parameters across the different crystal structures
(a) Weighted average distances, in the first coordination sphere, between DNA micelle-dendrimers and AuNPs (first, grey), and between AuNPs and AuNPs (second, green). n is the number of independently characterized structures. An increase in the average first-coordination distance between complementary particles (dark grey) indicates an increase in the average size of the DNA micelle-dendrimers that template that structure. SH: 246 ± 4.6 Å, 322 ± 6.2 Å, n = 10. SC: 267 ± 5.6 Å, 308 ± 6.6 Å, n = 12. Ti5Ga4: 270 ± 3.6 Å, 323 ± 4.3 Å, n = 10. GT: 284 ± 3.6 Å, 217 ± 5.2 Å, n = 7. (b) The average volume of a superlattice structure per AuNP. The low average volume per AuNP (thus a packing density of AuNPs) in the FCC phase is due to the absence of DNA templates and the structure's metallic bonding character. The high density of AuNPs in the GT phase is due to its A2B stoichiometry (i.e., for every DNA micelle-dendrimer there are two AuNPs).

Table 5.7. Colloidal Ti_5Ga_4-type phase compared to atomic Ti_5Ga_4

Comparing Ti_5Ga_4-type phase (upper) with the intermetallic structure Ti_5Ga_4 (bottom).[13-14] Coord.: coordination. CN: coordination number. The coordination distances to the bolded atoms are included for the intermetallic structure Ti_5Ga_4.

Site	Wyckoff position	Coordinates	Coord.	Coord. distances (Å)	Coord. partners	Polyhedra CN	Polyhedra vol (10^6 Å^3)
AuNP1	4d	1/3, 2/3, 0	Den_6	271	Six 6g	14	16.5
AuNP2	6g	1/4, 0, 1/4	Den_7	237	Two 2b	17	15.8
				259	Three 6g		
				317	Two 6g		
Den1	2b	0, 0, 0	$AuNP_6$	237	Six 6g	14	12.9
Den2	6g	3/5, 0, 1/4	$AuNP_9$	259	Four 4d	13	15.9
				271	Three 6g		
				317	Two 6g		
Site	Wyckoff position	Coordinates	Coord.	Coord. distances (Å)	Coord. partners	Polyhedra CN	Polyhedra vol (Å^3)
Ti1	4d	1/3, 2/3, 0	$Ti_8\mathbf{Ga_6}$	2.81	Six 6g	14	16.4
Ti2	6g	0.29, 0, 1/4	$Ti_8\mathbf{Ga_7}$	2.66	Two 2b	15	16.3
				2.59	One 6g		
				2.70	Two 6g		
				2.82	Two 6g		
Ga1	2b	0, 0, 0	$\mathbf{Ti_6}Ga_6$	2.66	Six 6g	14	15.6
Ga2	6g	0.62, 0, 1/4	$\mathbf{Ti_9}Ga_4$	2.81	Four 4d	13	16.1
				2.69	One 6g		
				2.70	Two 6g		
				2.82	Two 6g		

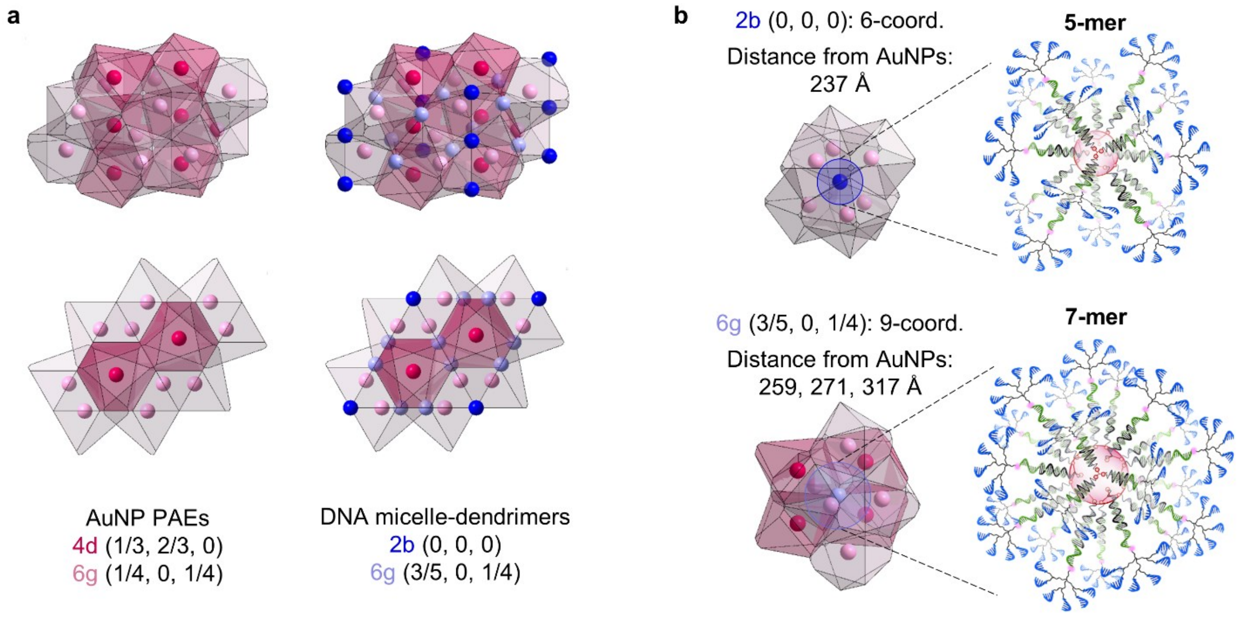

Figure 5.14. Structural analysis of Ti_5Ga_4-type phase

(a) Side and top-down views of a Ti_5Ga_4-type unit cell. Wyckoff positions of AuNPs are denoted by spheres in dark (4d) and pale (6g) pink, respectively. Voronoi polyhedra are constructed by considering the location of every AuNP. Within a unit cell, the polyhedra vertices meet at eight distinct locations that have the highest equidistant connectivity to the AuNPs. These are the proposed Wyckoff positions of DNA micelle-dendrimers, as denoted by the superimposed dark (0, 0, 0) and pale (3/5, 0, 1/4) blue spheres. (b) DNA micelle-dendrimers at 2b (left) are coordinated by six AuNPs at shorter distances, while those at 6g (right) are coordinated by nine AuNPs with longer distances. The significant difference in coordination environments can only be explained by the presence of micelle-dendrimers with distinct sizes and association numbers, specifically a 5-mer in 2b and a 7-mer in 6g.

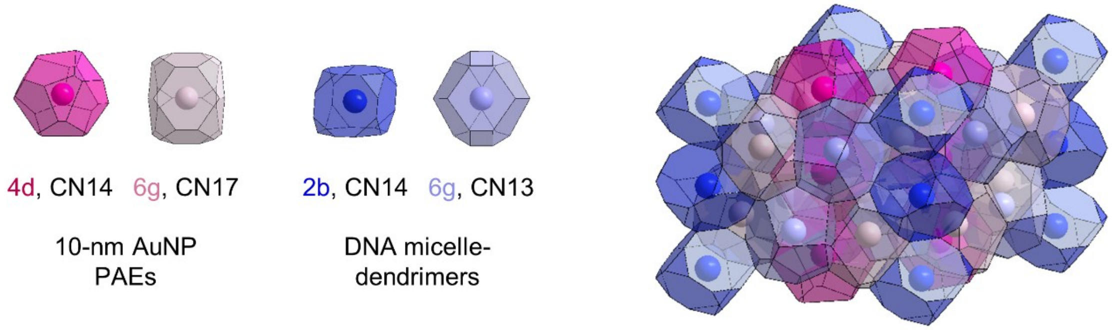

Figure 5.15. The symmetry breaking properties of discrete micelle DNA dendrimers

The symmetry-breaking induced by discrete DNA micelle-dendrimers can also be highlighted by constructing a new set of Voronoi polyhedra around both the AuNPs and DNA micelle-dendrimers. Two of these Voronoi polyhedra are Frank-Kasper (FK)-type, with a coordination number (CN) of 14, while the other two are pseudo-FK polyhedra with CNs of 13 and 17, respectively.

5.7. Reconfigurable Crystal Structures and Bonding Character

Having explored the phase space, we set out to design stimuli-responsive crystals with reconfigurable structures and thermostabilities. To disassemble the DNA dendrimer, we designed and synthesized a linear DNA strand (deactivating strand) that is a full complement to the template and would displace the DNA dendrons from the templates *via* TMSD,[283] yielding deactivated templates and functional dendron EEs (**Figure 5.16. a**). Native PAGE (lanes 6 and 7, **Figure 5.17.**) showed that a slight excess of deactivating strand is required to free the dendrons completely. The key to enabling multiple cycles of structural reconfiguration is that the deactivating strand was designed with its own toehold region, such that its perfect complement (the activating strand) would remove the deactivating strand from the template *via* TMSD (**Figure 5.16. a**). The liberated templates can combine with the dendrons to regenerate DNA dendrimers (lane 8, **Figure 5.17.**), thus completing one switching cycle.

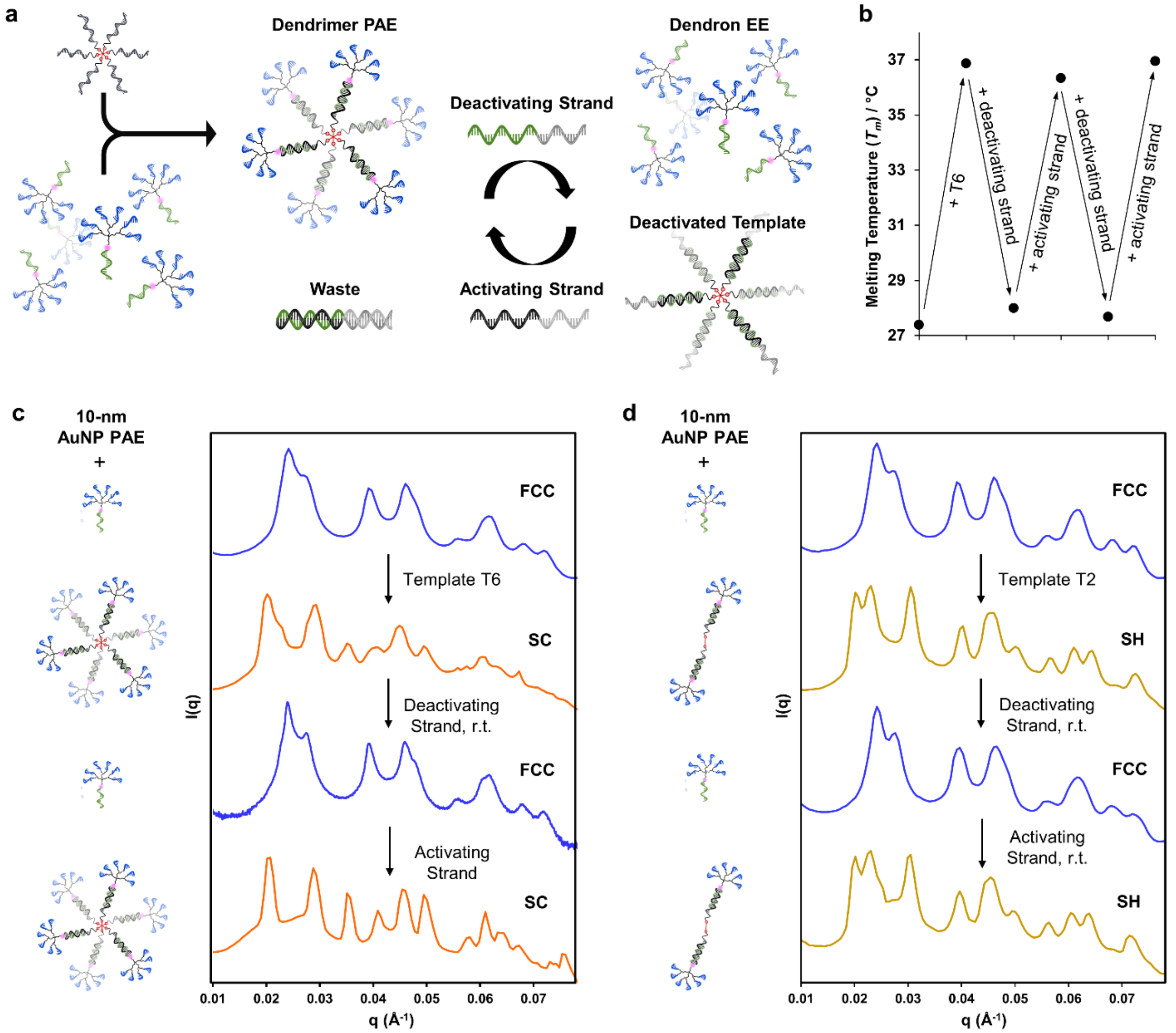

Figure 5.16. Colloidal crystals with switchable structures and thermostabilities
(a) Scheme outlining the design of switchable dendron/dendrimer architectures. DNA dendrons and templates can be reversibly assembled *via* toehold-mediated strand displacement reactions. (b) Consecutive additions of the template, the deactivating strand, and the activating strand enable one to reconfigure the thermostability of the colloidal crystal. Colloidal crystal structures were switched between FCC (blue traces) and (c) SC (orange traces) or (d) SH (yellow traces) over two full cycles in a single pot. For (d) heating and slow cooling is not required due to the diffusive nature of the DNA architectures involved, allowing the colloidal crystal structure to re-organize at room temperature.

We then studied the switchability of these dendritic architectures in the context of nanoparticle superlattices to determine whether this simple DNA design can enable both the thermostability and structure to be reversibly programmed. We started by studying superlattices that were prepared using 6Dn and 10-nm AuNP PAEs. The T_m of these crystals were characterized after the addition of a template (T6) and after consecutive additions of deactivating and activating strands. We observed changes in thermostability (**Figure 5.16. b**) that follow established dependence on construct valency (**Figure 5.6.**). *Via in situ* SAXS characterization, we confirmed that the phase symmetries change as expected (**Figure 5.16. c**). When 6Dn and 10-nm AuNP PAEs were assembled, an FCC lattice was formed. Then, upon the addition of a template (T6), the dendron EEs were assembled into dendrimer PAEs, and an SC lattice was formed after thermal annealing. Subsequent addition of the deactivating strand yielded an FCC lattice after annealing at room temperature, enabled by the diffusive nature of these low-valent dendrons. Finally, after the

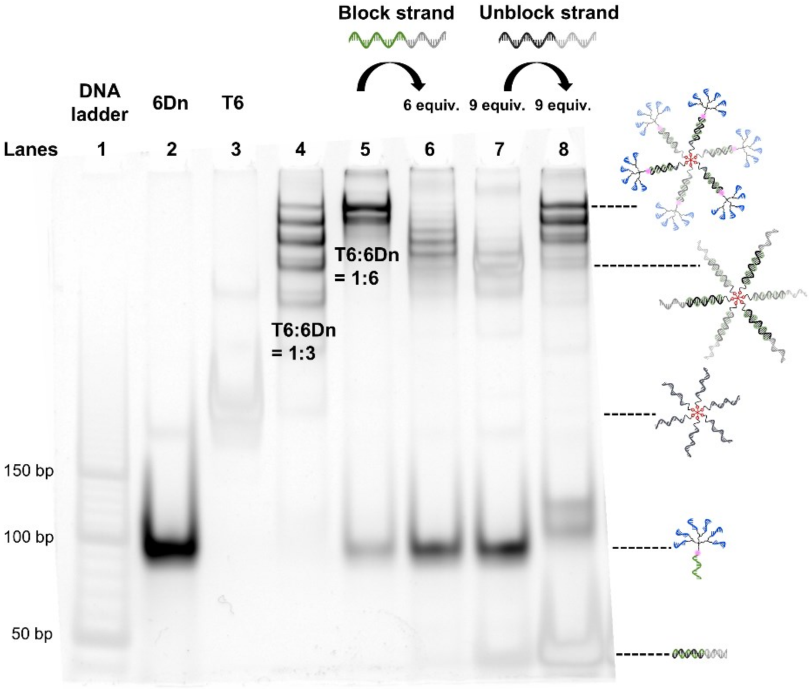

Figure 5.17. PAGE characterization of responsive DNA dendrimer design
Dendrons and templates are designed to enable toehold-mediated strand displacement reactions. A hybridization-enabled DNA dendrimer PAE can be reconfigured into individual dendron electron equivalents (EEs) using simple DNA strands (block strand and unblock strand) as stimuli. A 4.5% native PAGE showing the effect of adding block strand and unblock strand on the size of the resulting constructs. The gel is stained using GelRed and imaged on the Cy3-channel. As a result, the darker bands show the presence of Cy3 label (i.e., dendrons are part of the constructs). Lane 1: O'RangeRuler 10 bp DNA Ladder (ThermoFisher); lane 2: 6Dn; lane 3: T6; lane 4: one equiv. of T6 and three equiv. of 6Dn; lane 5: one equiv. of T6 and six equiv. of 6Dn; lane 6: one equiv. of T6, six equiv. of 6Dn, and six equiv. of block strand; lane 7: one equiv. of T6, six equiv. of 6Dn, and nine equiv. of block strand; lane 8: one equiv. of T6, six equiv. of 6Dn, nine equiv. of block strand, and nine equiv. of unblock strand.

addition of the activating strand and subsequent thermal annealing, the template re-hybridized with the dendron to regenerate the DNA dendrimer, reforming an SC lattice and completing two structure switching cycles. We further took advantage of the inherent diffusivity of low-valent templates (e.g., T2) and the resulting DNA dendrimers (**Figure 5.6.**) to switch crystal structures through two full cycles without having to heat or slow-cool the samples (**Figure 5.16. d**). The elegance of this room-temperature, isothermal phase symmetry reconfiguration is the simplicity of its operation and design, without having to use instruments for thermal processing,[284-287] or having to design complex DNA circuitry.[288]

The crystal structure reconfiguration is not limited to two structures only. By introducing a new template (e.g., T8) after a previously added template (e.g., T2) has been deactivated by the

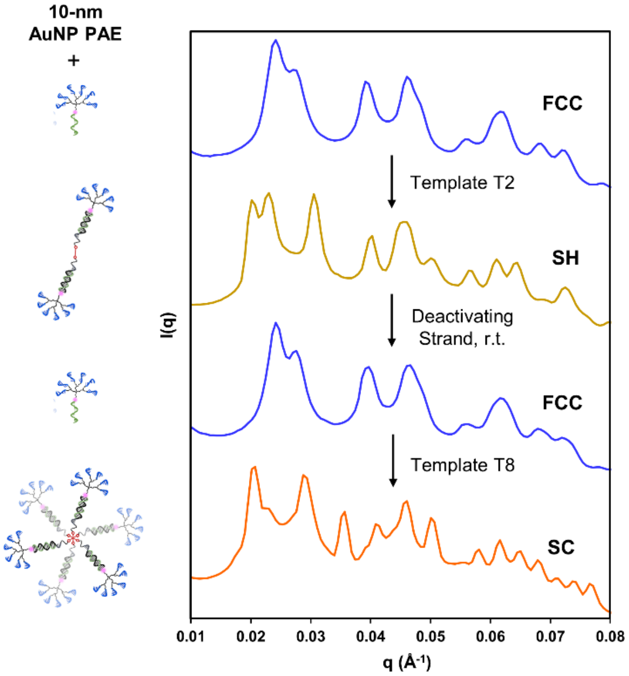

Figure 5.18. Switching a sample between three crystal structures in one pot
Consecutive additions of the template T2 and the block strand reconfigured the colloidal crystal structures from FCC (blue trace), to SH (yellow trace), and then back to FCC (blue trace). After each of the above additions, the samples were mixed gently via pipetting, and they were left at room temperature for 24 h. After the original template (T2) was inactivated by the addition of the block strand, a new template (T8) was added to reconfigure the sample into SC (orange trace) phase, after heating to 60 °C and slow-cooling to 22 °C.

action of the block strand, we successfully traversed between an FCC, an SH, and an SC lattice in one pot (**Figure 5.18.**). This type of structure reconfiguration also accommodates AuNP PAEs of different sizes. Using 5-nm AuNP PAEs, we successfully switched between an FCC lattice and an SC lattice (**Figure 5.19.**). Overall, these experiments demonstrate that both the structure and the thermostability of a colloidal crystal can be reversibly altered *via* a simple procedure, opening avenues for designing switchable and adaptive mesoscopic materials that are templated by highly modular DNA supramolecules.

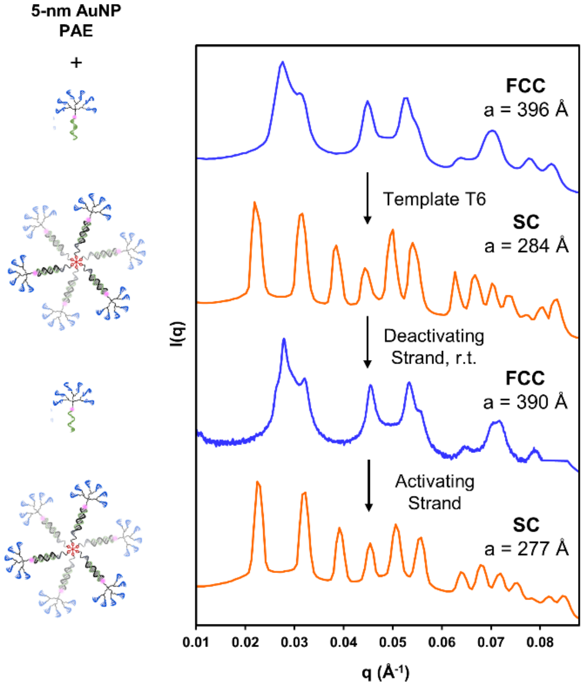

Figure 5.19. Reconfigurability of assemblies with 5 nm AuNP PAEs
Dendrimer-templated nanoparticle superlattices and structure reconfiguration is also applicable to 5-nm AuNPs. Here, consecutive addition of the template T6, the block strand, and the unblock strand allow one to reconfigure the colloidal crystal structures between FCC (blue traces) and SC (orange traces) over two full cycles in one pot. The samples were mixed gently after each addition. The sample is heated to 60 °C and slow-cooled to 22 °C at 0.1°C per min after the addition of the template and the unblock strand.

5.8. Comments on DNA Dendrimer PAEs

This work introduces a new type of DNA-mediated hierarchical assembly that has three levels of structural organization. Importantly, the assembly outcomes cannot be rationalized, and the lattice reconfiguration strategies cannot be realized, unless *all* of these underlying interactions are considered. This study highlights the fact that chemical components (e.g., surfactants) or functional groups (e.g., hydrophobic moieties) that seem inconsequential can assume structure-directing roles in extended assemblies. In particular, the advances described herein should encourage re-exploration of the surfactant literature for developing new strategies to program the assembly of nanomaterials. To conclude, utilizing both sequence-encoded and non-sequence-specific interactions to mediate dynamic and reconfigurable organizations of building blocks is an effective strategy for designing hierarchical materials. These structure-guiding principles should apply to both soft and hard matter, opening avenues for the deliberate introduction of transient interactions between building blocks to induce the formation of unconventional phases.

CHAPTER SIX

Symmetry-Breaking DNA Dendrimer Synthons in Colloidal Crystal Engineering with DNA

Material in this chapter is based upon:

Distler, M. E.; Landy, K. M.; Gibson, K. J.; Lee, B.; Weigand, S.; Mirkin, C. A., Symmetry-Breaking Dendrimer Synthons in Colloidal Crystal Engineering with DNA **2022,** *Submitted*.

6.1. The Challenges of Breaking Symmetry in Colloidal Crystals

Valence shell electron pair repulsion (VSEPR) theory defines the anisotropic bonding observed within molecules and crystalline solids,[289-291] and it rationalizes the low-symmetry structures that are often observed in nature. However, breaking symmetry in synthetic systems is challenging. This is particularly evident in the field of colloidal crystal engineering, where the commonly used isotropic nanoparticle (NP) building blocks favor the formation of closely packed, high symmetry crystal structures.[292-294] Efforts to introduce directional interactions in colloidal crystals primarily have relied on the use of anisotropic NPs.[295-302] Though effective, this approach relies on shape and size complementarity to determine crystal structure outcomes. Therefore, accessing different crystal structures requires changing a key feature of at least one of the nanoparticle components, which limits the scope of accessible structures and compositions.

Colloidal crystal engineering with DNA has the capability to address these limitations. NPs functionalized with a dense shell of radially oriented DNA, termed programmable atom equivalents (PAEs), can be assembled through sequence-specific DNA-DNA interactions.[115, 220] This approach enables features of the NP (i.e., size, shape, and composition) and the DNA to be modulated independently from each other. As a result, researchers have now made structures spanning over 70 different crystal symmetries, with programmable lattice parameters, crystal habits, and thermostabilities.[18] Nevertheless, symmetry breaking in DNA-mediated colloidal crystals also relies primarily on size and shape complementarity of the particles involved.[303-304] If symmetry breaking and orthogonal interactions could be decoupled from the features of the NP cores, then one could expand the scope of structural and compositional possibilities beyond what is currently possible with assemblies based purely on NP building blocks. Methods to achieve this level of control has resulted in unique low symmetry and diamond-family crystal structures by incorporating inorganic NPs into DNA origami cages that encode directional bonding.[299] Previous work has also shown that electron equivalents (EEs), DNA functionalized NPs that are defined by their small size, low valency, and mobility within a crystal structure, can break symmetry, but the design parameters are limited to DNA loading and relative concentrations of the EEs to the PAEs.[305-306] Furthermore, due to the inherent chemical isotropy of the EE cores, it is nearly impossible to specifically define directional, orthogonal interactions. We hypothesized that DNA dendrimers could be used as molecularly defined, symmetry-breaking synthons, capable of encoding anisotropic, orthogonal interactions in ways that cannot be achieved generally in particle-based systems.

Here, we report such capabilities using a new type of molecularly defined DNA dendrimer composed of a DNA junction (DJ) core and DNA dendron arms, termed DNA Junction PAEs (DJ PAEs). We co-assembled these DJ PAEs with gold nanoparticle (AuNP) PAEs and, by systematically screening the phase space, we identified three distinct colloidal crystal structures, one of which has never been reported in the field of colloidal crystal engineering (Si_2Sr). Through nucleic acid design, we synthesized DNA dendrimers capable of breaking symmetry and encoding orthogonal interactions into a single colloidal crystal, thereby enabling the synthesis of binary and ternary NP assemblies, with broken symmetries, that form independently of NP size, shape, and composition.

6.2. Design and Synthesis of DNA junction PAEs

Nanoscale dendritic architectures are promising as building blocks for novel materials because they can be easily synthesized and functionalized, are molecularly well-defined, and can have diverse topologies.[253, 307-308] Though dendritic DNA was originally developed for drug delivery and chemical sensing,[146, 198, 267, 309-311] we have shown how DNA dendrimers enable new capabilities in the field of nanoparticle assembly and colloidal crystal engineering.[199] In Chapter five, small organic molecular cores were used to covalently link DNA and then hybridize DNA dendrons.[199] This approach led to molecularly defined PAEs and novel control over DNA valency, but it still employs an isotropic core, which makes the introduction of anisotropic and orthogonal interactions difficult. We hypothesized that highly modular and chemically anisotropic cores with programmable size, valency, and orthogonality would be required to develop DNA dendrimers that are capable of breaking symmetry in colloidal crystals comprised of isotropically functionalized inorganic PAEs.

To synthesize such DNA dendrimers, two molecularly defined nucleic acid-based architectures were combined, a DNA junction core and a DNA dendron (**Figure 6.1. a)**. The junction cores are comprised of 36-base DNA strands that recognize and hybridize with the other core-forming sequences. Specifically, the first 18 bases (starting from the 5’ end) on each of the DNA strands, hybridize to form the junctions. Each of the junction-forming strands also have an 18-base overhang that is utilized for DNA dendron hybridization. The overhang region was designed to be 18 base pairs long so that, when hybridized, the melting temperatures (T_m) of these regions would be greater than 60 °C. This ensures that the DJ PAEs remain stable during colloidal crystal formation (typically at temperatures between 20 and 50 °C). The structures of these junction cores are highly programmable, and their sizes are directly related to the number of bases in the strands that comprise them (18 – 54 bp, 8 nm – 15 nm, respectively). Furthermore, a primary advantage of using the DJ PAE design, is the ability to introduce directional, orthogonal interactions. Through this approach, the overhang sequences can be independently designed, enabling orthogonal DNA dendrons to hybridize on each overhang of the junction.

Utilizing branching phosphoramidites, 9-branched DNA dendrons (9Dn) were synthesized with an 18-base stem that is designed to hybridize to the 18-base overhang of the two-way junction (2WJ) or three-way junction (3WJ) core. Indeed, when junction-forming strands and DNA dendrons are combined in an aqueous saline solution and annealed, DJ PAEs form (*vide infra*). Furthermore, each dendron has nine branches, each of which contains an identical single-stranded

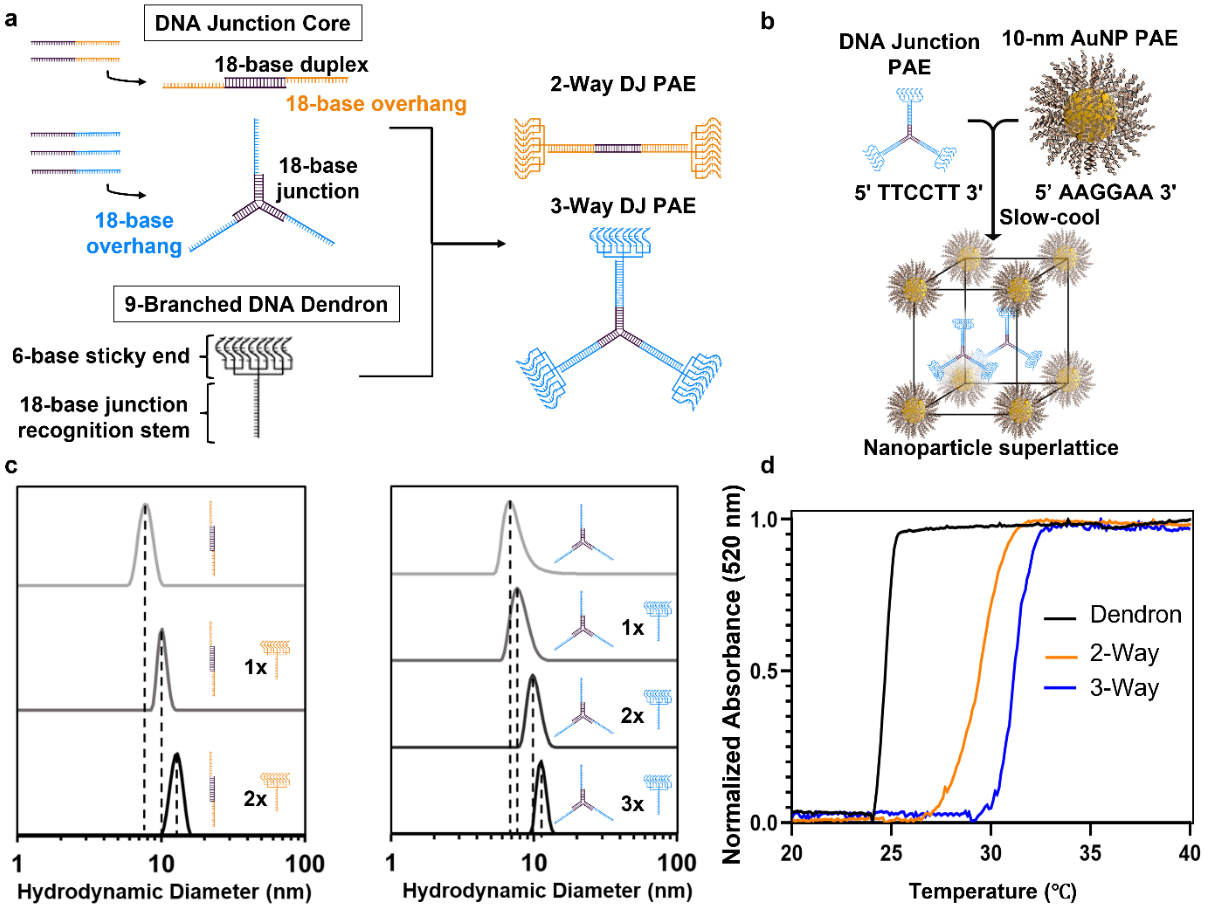

Figure 6.1. Bottom-up assembly of DJ PAEs

(a) DJ PAEs consist of a DNA junction core and a 9-branched DNA dendron that can be assembled into the 2WJ DJ PAE or a 3WJ DJ PAE structure via an annealing step. (b) DJ PAEs are coassembled with NP PAEs to produce colloidal crystals. (c) 2WJ and 3WJ DJ PAE formation can be characterized by DLS, as evidenced by the expected shifts in hydrodynamic diameter as a result of stepwise dendron addition. (d) Melting transitions of resultant colloidal crystals for 10-nm AuNP PAEs assembled with dendrons (black), 2WJ DJ PAEs (orange), and 3WJ DJ PAEs (blue) at ratios of 16:1 dendrons:AuNP PAEs. This trend held for all tested ratios.

sticky end, designed to hybridize with inorganic NPs that are fully modified with sticky end sequences complementary to those on the dendron (**Figure 6.1 b**). All DNA architectures were purified using either polyacrylamide gel electrophoresis (PAGE) or high-performance liquid chromatography (HPLC) and characterized using PAGE and matrix-assisted laser desorption/ionization time-of-flight mass spectrometry (MALDI-TOF MS) (**Table 6.1.-6.3.**).

Table 6.1. Anchor and linker strands

		DNA Sequence (5' - 3')	Calc'd MW	Exp't MW
10 nm Au 1	**A-1**	Thiol-(spacer18)2-AAC GAC TCA TAC TCA CCT	6403	6398
	L-1	AAGGAA-(spacer18)-AGG TGA GTA TGA GTC GTT	7868.7	7860
10 nm Au 2	**A-2**	Thiol-(spacer 18)2-CAT CCA TCC TTA TCA ACT	6370.6	6365
	L-2	AGAAGA-Spacer18-AGT TGA TAA GGA TGG ATG	7898.3	7888
10 nm Au 3	**A-3**	Thiol-(Spacer 18)2-ACT TAC ACT ACT CAT CTC	6370.6	6379
	L-3	GAAAAG-Sp-GAG ATG AGT AGT GTA AGT	7898.32	7902
10 nm Ag 1	**A-4**	5' Dithiol Serinol-(Spacer 18)2-CAT CCA TCC TTA TCA ACT	6256.3	6262
	L-2	same as above		
5 nm Au 1	**A-2**	same as above		
	L-2	same as above		
5 nm Au 2	**A-3**	same as above		
	L-3	same as above		

Table 6.2. DNA junction forming strands

		DNA Sequence (5' - 3')	Calc'd MW	Exp't MW
2WJ	**S1-O1**	GCG CAT AGT CCG AAT GGC AGT TGA TAG AGT TAG GTG	11220.3	11212
	S1-O2	GCG CAT AGT CCG AAT GGC ATG GTA ATA GTG AGT GGT	11220.3	11209
	S1-O3	GCG CAT AGT CCG AAT GGC GGT AGG TGT AAT GTG AAT	11220.3	11234
	S2-O1	GCC ATT CGG ACT ATG CGC AGT TGA TAG AGT TAG GTG	11171.3	11155
2WJ-L	**S1-O1-L**	GCG CAT AGT CCG AAT GGC GCG CAT AGT CCG AAT GGC AGT TGA TAG AGT TAG GTG	16806.9	16822
	S1-O2-L	GCG CAT AGT CCG AAT GGC GCG CAT AGT CCG AAT GGC AGT TGA TAG AGT TAG GTG	16806.9	16805
	S1-O3-L	GCG CAT AGT CCG AAT GGC GCG CAT AGT CCG AAT GGC GGT AGG TGT AAT GTG AAT	16806.9	16806
	S2-O1-L	GCC ATT CGG ACT ATG CGC GCC ATT CGG ACT ATG CGC AGT TGA TAG AGT TAG GTG	16708.8	16701
3WJ	**S3-O1**	CGT CAA TCC ACT ATG CGC AGT TGA TAG AGT TAG GTG	11115.2	11137
	S3-O2	CGT CAA TCC ACT ATG CGC ATG GTA ATA GTG AGT GGT	11115.2	11122
	S4-O1	CGC TGC TCA GGA TTG ACG AGT TGA TAG AGT TAG GTG	11211.3	11224
	S4-O3	CGC TGC TCA GGA TTG ACG GGT AGG TGT AAT GTG AAT	11211.3	11210
	S5-O1	GCG CAT AGT TGA GCA GCG AGT TGA TAG AGT TAG GTG	11260.3	11277
	S5-O2	GCG CAT AGT TGA GCA GCG ATG GTA ATA GTG AGT GGT	11260.3	11243
3WJ-L	**S3-O1-L**	CGT CAA TCC CGT CAA TCC ACT ATG CGC ACT ATG CGC AGT TGA TAG AGT TAG GTG	16596.8	16589
	S4-O1-L	CGC TGC TCA CGC TGC TCA GGA TTG ACG GGA TTG ACG AGT TGA TAG AGT TAG GTG	16788.9	16773
	S4-O3-L	CGC TGC TCA CGC TGC TCA GGA TTG ACG GGA TTG ACG GGT AGG TGT AAT GTG AAT	16788.9	16786
	S5-O1-L	GCG CAT AGT GCG CAT AGT TGA GCA GCG TGA GCA GCG AGT TGA TAG AGT TAG GTG	16886.9	16889
	S5-O2-L	GCG CAT AGT GCG CAT AGT TGA GCA GCG TGA GCA GCG ATG GTA ATA GTG AGT GGT	16886.9	16886

Table 6.3. DNA dendrons used in this study

		DNA Sequence (5' - 3')	**Calc'd MW (kDa)**	**Exp't MW (kDa)**
2WJ-S	**9Dn-O1-NJ**	TCTTCT-Tr-Tr-Sp-ATG GTA ATA GTG AGT GGT	23.78	23.80
	9Dn-O2	TTCCTT-Tr-Tr-Sp-ACC ACT CAC TAT TAC CAT	23.58	23.62
3WJ-S	**9Dn-O1-A**	TTCCTT-Tr-Tr-Sp-CGT CAA TCC ACT ATG CGC	23.63	23.65
	9Dn-O1-B	TTCCTT-Tr-Tr-Sp-CGC TGC TCA GGA TTG ACG	23.63	23.59
	9Dn-O1-C	TTCCTT-Tr-Tr-Sp-GCG CAT AGT TGA GCA GCG	23.63	23.60
Other Dendrons	**9Dn-O1**	TCTTCT-Tr-Tr-Sp-CAC CTA ACT CTA TCA ACT	23.58	23.53
	9Dn-O3	CTTTTC-Tr-Tr-Sp-ATT CAC ATT ACA CCT ACC	23.58	23.56
	9Dn-O4	TTCCTT-Tr-Tr-Sp-ATT CAC ATT ACA CCT ACC	23.58	23.58

First, DJ core formation was characterized. DNA junction-forming strands were stoichiometrically combined in 0.5 M NaCl, annealed from 90 to 20 °C over the course of one hour, and then analyzed using native PAGE (**Figure 6.2 and 6.3.**). It was critical that these junction cores be designed to have T_ms above that of the most stable DNA-mediated colloidal crystal (> 50 °C) to ensure that they would not de-hybridize during colloidal crystal assembly. Melting experiments were conducted using Sybr Green I, a DNA-intercalating dye, which fluoresces only in the presence of hybridized DNA. These experiments revealed that the 2WJs and 3WJs dehybridize at 77 and 60 °C, respectively; thus, these cores were appropriate to integrate within colloidal crystal assemblies (**Figure 6.4.**). Moreover, these experimentally determined T_ms were within 1 °C of the calculated values for the DNA designs (calculated using NUPACK). The T_m of the 2WJ is greater than that of the 3WJ because 18 bases are involved in hybridization to form the 2WJ, while, for the 3WJ, 9 bases hybridize to form each junction arm. Next, we characterized DNA dendron hybridization to these junction cores using dynamic light scattering (DLS) (**Figure**

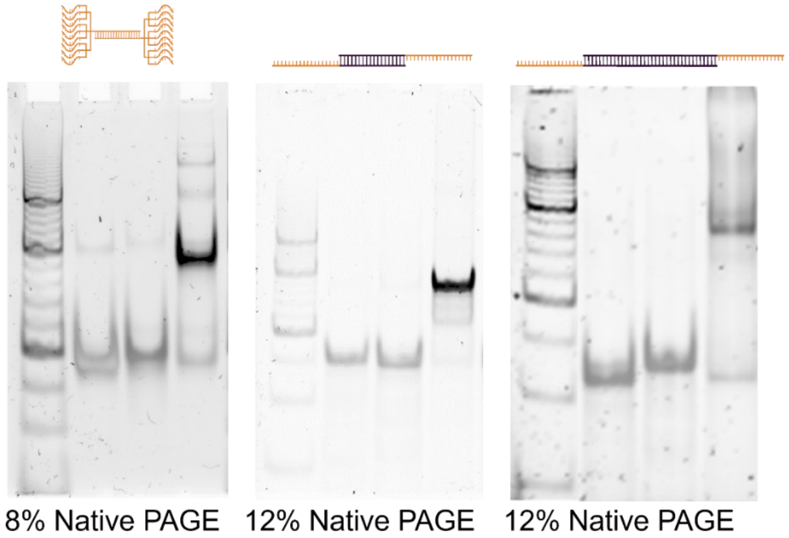

Figure 6.2. Two-way junction PAGE characterization
DNA junction forming strands were added in 1:1 ratios and annealed from 90-20 °C over the course of 1 h and characterized by PAGE. (left) DNA dendrons with stems that hybridize to form a 2WJ (18-base core, small). (middle) Linear DNA strands that hybridize to form a 2WJ (36-base core, medium. (right) Linear DNA strands that hybridize to form a 2WJ (54-base core, large).

6.1. c). DNA dendrons were added in a stepwise fashion at stoichiometric ratios relative to the number of overhangs available for binding. We observed that as the number of added dendrons increased, corresponding to one, two, or three DNA dendrons per DJ core (depending on the junction in use), the hydrodynamic diameter of the DJ PAE increased. These data confirm that DJ

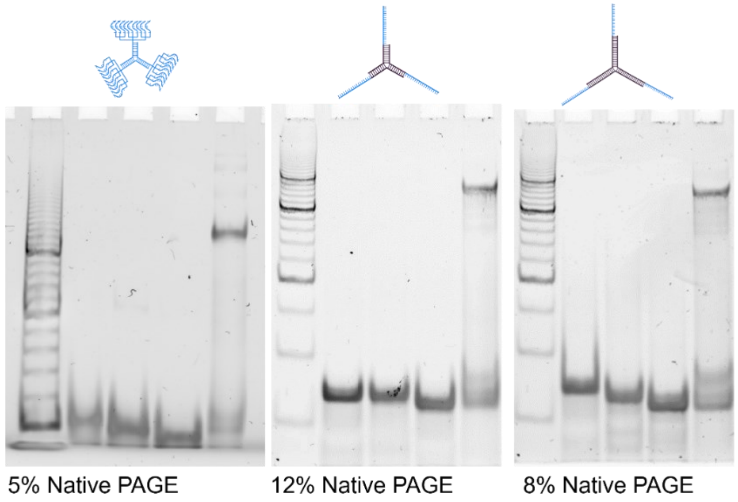

Figure 6.3. Three-way junction PAGE characterization
DNA junction forming strands were added in 1:1 ratios and annealed from 90-20 °C over the course of 1 h and characterized by PAGE. (left) DNA dendrons with stems that hybridize to form a 3WJ (18-base core, small). (middle) Linear DNA strands that hybridize to form a 3WJ (36-base core, medium. (right) Linear DNA strands that hybridize to form a 3WJ (54-base core, large).

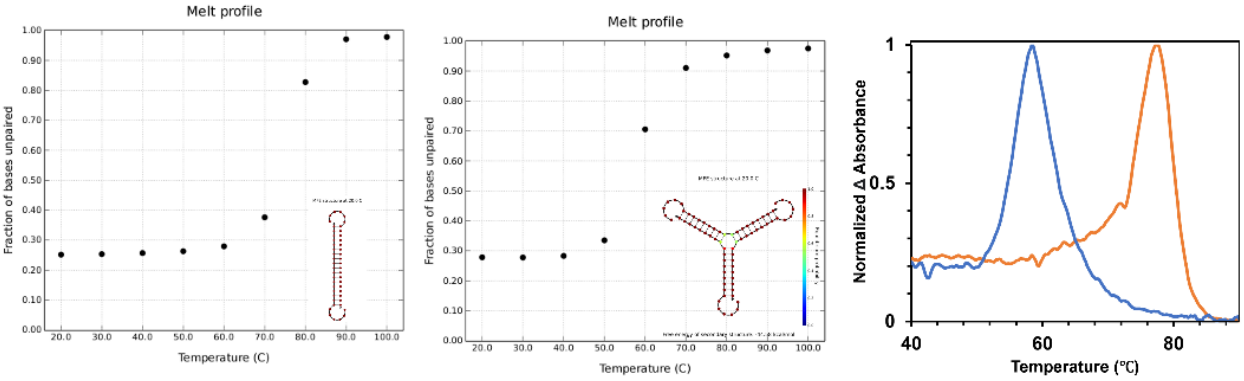

Figure 6.4. Thermostability of DNA junction design
Thermostability of DNA junction sequences were determined computationally and experimentally. (left) NUPACK simulation of the 2WJ melting transition. (middle) NUPACK simulation of the 3WJ melting transition. (right) Using a DNA intercalating dye, the melting temperatures of these DNA junctions were determined. When the DNA is duplexed, the intercalating dye will fluoresce and once the junctions melt, the dye will be quenched. By plotting the derivative, we can determine the melting temperature of the 2- way (orange) and 3-way (blue) junction. We found the 2WJ and 3WJ melted at 77 °C and 60 °C respectively. These values are within 1 °C of the calculated melting temperatures based on the DNA design.

PAE structures can be synthesized by combining the DNA dendrons in stoichiometric amounts with the DJ cores followed by annealing from 90 to 20 ºC over 1 h.

To synthesize colloidal crystals, DJ PAEs with appropriate sticky ends (5’ TTCCTT 3’) were combined with 10-nm AuNP PAEs (complementary sticky end: 5’ AAGGAA 3’) at DJ PAE/AuNP PAE ratios of 1:1, 2:1, 12:1, 16:1, or 24:1. These ratios were used because they produced stable colloidal crystals (based upon trial-and-error analysis, **Table 6.4**). Assembly solutions had a final volume of 100 mL at 0.5 M NaCl, 10 mM sodium phosphate, and 0.02% sodium dodecyl sulfate (SDS). The assemblies were heated to 50 °C and then cooled to 22 °C at a rate of 0.1 °C per 10 min. Importantly, the slow-cooling step was conducted at temperatures below the T_m of the DJ PAEs in order to avoid DJ PAE reorganization. The thermostabilities of the resulting colloidal crystals were characterized by conducting UV-vis melting experiments, in which the extinction of the AuNPs (at 520 nm) was measured as a function of increasing temperature (**Figure 6.1. d**). We compared the T_ms for colloidal crystals assembled from the 10-nm AuNPs PAEs and DNA dendrons only, 2WJ DJ PAEs, and 3WJ DJ PAEs (valencies: 9, 18, 27, respectively). We observed an increase in the colloidal crystal thermostability with increasing DJ PAE valency because a greater number of DNA-DNA interactions can be formed between the individual bonding units as valency increases (24.5 °C, 28.1 °C, 30.6 °C, for valencies of 9, 18, and 27, respectively). Based on the observed increase in thermostability, these data also indicate that the DJ PAE constructs form as expected.

Table 6.4. Concentration dependence of resultant colloidal crystal structures

Dendron	Junction	Dendron AuNP ratio	NP Size (nm)	Symmetry	Space group	Lattice constant (nm)
9Dn-O1	2WJ-M	1	5	mixed	*NA*	NA
9Dn-O1	2WJ-M	3	5	SH	*P6/mmm*	a=b=28.4, c=28.6
9Dn-O1	2WJ-M	6	5	SH	*P6/mmm*	a = b=28.4, c=28.6
9Dn-O1	2WJ-M	12	5	SH	*P6/mmm*	a = b=28.4, c=28.6
9Dn-O1	2WJ-L	1	5	Broad	*NA*	NA
9Dn-O1	2WJ-L	3	5	Broad	*NA*	NA
9Dn-O1	2WJ-L	6	5	Broad	*NA*	NA
9Dn-O1	2WJ-L	12	5	Si2Sr	*P 41 3 2*	a = 47.5
9Dn-O1	2WJ-M	24	10	mixed	*NA*	NA
9Dn-O1	2WJ-M	48	10	mixed	*NA*	NA
9Dn-O1	2WJ-M	96	10	SH	*P6/mmm*	a =b=30.5, c=30.1
9Dn-O1	2WJ-M	120	10	SH	*P6/mmm*	a =b=30.5, c=30.1
9Dn-O1	2WJ-L	24	10	SH	*P6/mmm*	a =b=31.2, c=31.0
9Dn-O1	2WJ-L	48	10	SH	*P6/mmm*	a =b=31.2, c=31.0
9Dn-O1	2WJ-L	96	10	SH	*P6/mmm*	a =b=31.2, c=31.0
9Dn-O1	2WJ-L	120	10	SH	*P6/mmm*	a =b=31.2, c=31.0
9Dn-O1	3WJ-M	1	5	mixed	*NA*	NA
9Dn-O1	3WJ-M	2	5	mixed	*NA*	NA
9Dn-O1	3WJ-M	6	5	SH	*P6/mmm*	a = b=28.9, c=28.4
9Dn-O1	3WJ-M	18	5	SH	*P6/mmm*	a = b=29.5, c=28.8
9Dn-O1	3WJ-L	1	5	mixed	*NA*	NA
9Dn-O1	3WJ-L	3	5	mixed	*NA*	NA
9Dn-O1	3WJ-L	6	5	Si2Sr	*P 41 3 2*	a = 47.5
9Dn-O1	3WJ-L	18	5	Si2Sr	*P 41 3 2*	a = 47.5
9Dn-O1	3WJ-M	12	10	mixed	*NA*	NA
9Dn-O1	3WJ-M	24	10	mixed	*NA*	NA
9Dn-O1	3WJ-M	48	10	SH	*P6/mmm*	a = b=29.4, c=29.0
9Dn-O1	3WJ-M	96	10	SH	*P6/mmm*	a = b=29.4, c=29.0
9Dn-O1	3WJ-L	12	10	SH	*P6/mmm*	a = b=31.4, c=27.5
9Dn-O1	3WJ-L	24	10	SH	*P6/mmm*	a = b=31.4, c=27.6
9Dn-O1	3WJ-L	48	10	SH	*P6/mmm*	a = b=31.4, c=27.7
9Dn-O1	3WJ-L	96	10	SH	*P6/mmm*	a = b=31.4, c=27.8

6.3. Investigating the bonding properties of DJ PAEs with identical sticky ends

The complementary contact model (CCM) allows one to predict the resulting crystal structures when two PAEs assemble.[117] This model predicts that the most thermodynamically favorable crystal structure is the one that maximizes the number of DNA duplexes (or "bonds") in the system. According to the CCM, the relative sizes and DNA loading of the two PAEs dictate the crystal structure. Therefore, we explored our system's design space by changing the sizes and valencies of the junction cores and the sizes of the AuNP PAEs. Specifically, three different sized DJ PAEs were designed: (1) the stems of the dendrons form the DNA junctions (18-base core, small), (2) the junction core strands consisted of 36 bases total (medium), and (3) the junction core strands consisted of 54 bases total (large) (**Table 6.2**). These DJ PAEs, where the same sticky ends were presented on each junction arm, were assembled with 5-nm or 10-nm AuNP PAEs. The resulting structures were characterized using small-angle X-ray scattering (SAXS) in the solution state and scanning transmission electron microscopy (STEM) in the solid state (after silica encapsulation, resin embedding, and ultramicrotomy).[312] In this design space, we identified three distinct crystalline phases: face-centered cubic (FCC), simple hexagonal (SH), and Si_2Sr (**Figure 6.5.**). Most of the assemblies were structurally pure and highly crystalline; however, the Si_2Sr phase was often (though not always) formed with SH structural character, as well. The low-symmetry ($P\ 4_1\ 3\ 2$) Si_2Sr phase has not previously been reported in the field of colloidal crystal engineering, and thus, this work expands the library of crystal structures attainable when DNA dendrimer-based PAEs are utilized.

FCC crystal structures are typically observed when PAEs are assembled with small, low-valent bonding elements, termed "electron equivalents" (EEs) due to their metallic-like bonding characteristics. [306, 313] Previously, we discovered that, due to their low valencies, 3-, 4-, and 6-branched dendrons also function as EEs, whereby they are delocalized and mobile throughout a crystal lattice of PAEs.[199] When individual 9-branched DNA dendrons (9Dn, no junction in Figure 2a,b) were assembled with 5-nm or 10-nm AuNP PAEs, FCC structures formed (**Figure 6.5. c**). Thus, the 9Dn can also be considered an EE, as evidenced by its propensity to form an FCC crystal with both 5-nm and 10-nm particles and the low T_m of the resultant colloidal crystal (**Figure 6.1. d, black**). Furthermore, these results are consistent with previous findings that conclude that FCC symmetry is the most thermodynamically stable phase in single-component colloidal crystals due to the high symmetry and packing efficiency of the particles.[199] The small DJ PAEs (18-base core) continued to produce FCC crystal structures when assembled with 5-nm and 10-nm AuNP PAEs. This can be rationalized by the small size of the DJ PAEs (hydrodynamic diameter of 5 nm) relative to the size of the inorganic NP PAEs.

According to the CCM, when two components of different sizes assemble, an SH crystal structure maximizes the number of DNA hybridization events. In this case, the medium DJ PAEs (36-base core) have hydrodynamic diameters of approximately 8 nm, for both the 2WJ and 3WJ cores, while the 5-nm AuNP PAEs have a hydrodynamic diameter of approximately 20 nm, post-DNA functionalization. Thus, an SH crystal structure is expected based on the relative sizes of the components. Indeed, when the medium 2WJ and 3WJ DJ PAEs were assembled with 5-nm PAEs, an SH crystal structure formed (**Figure 6.5. d**).

When two PAEs of similar sizes are assembled, a CsCl crystal structure is expected to be observed; however, when one of the particles does not diffract electrons as strongly as the other, this appears as a simple cubic (SC) structure by SAXS and STEM. Nevertheless, when large DJ PAEs (54-base core, 15 nm in size) are assembled with 5-nm PAEs (hydrodynamic diameter of 20 nm), a Si_2Sr ($P\,4_1\,3\,2$) crystal structure is observed, which has never been reported in the field of colloidal crystal engineering. The Si_2Sr ($P\,4_1\,3\,2$) is a primitive cubic crystal structure, similar to the commonly observed SC structure (Figure 2e). We postulate that its formation is due to the compressibility of the DJ PAEs compared to the inorganic NP PAEs that are commonly used in DNA-mediated colloidal crystal engineering. The compressibility of the DJ PAEs allows them to

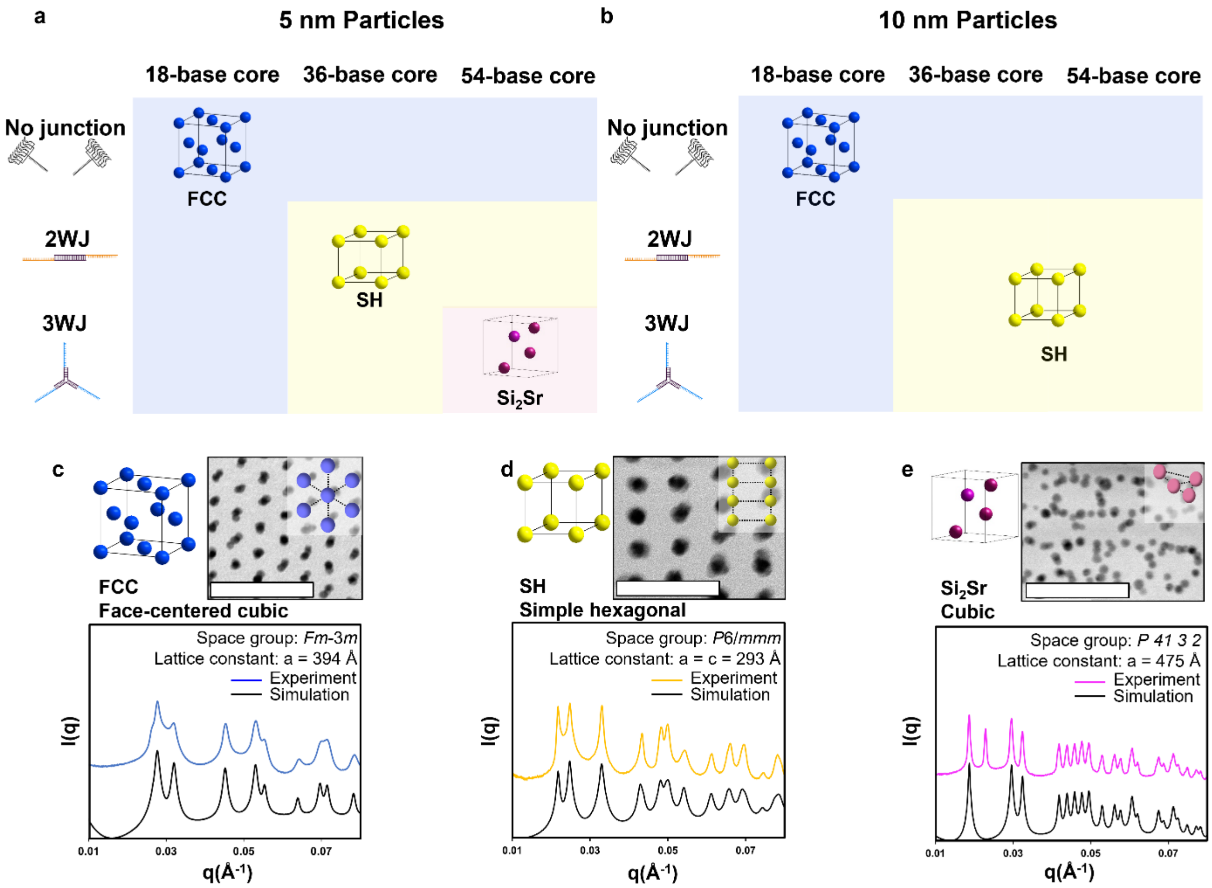

Figure 6.5. Exploring the phase space of DJ PAE-templated colloidal crystals
DJ PAEs of increasing size were synthesized and assembled with AuNP PAEs. Phase diagram of resultant colloidal crystals as a function of DJ PAE size and valency, when assembled with 5-nm (a) or 10-nm (b) AuNP PAEs. Based on the relative size of DJ PAEs:AuNP PAEs, three colloidal crystal structures were accessed – FCC (c), SH (d), and Si_2Sr (e), as characterized by SAXS and STEM. Scale bars: 50 nm

contract and form low-symmetry structures that maximize DNA duplex formation. These types of low-symmetry structures are more commonly observed in crystalline soft materials due to this very reason.[314-315] We believe that by combining soft-core PAEs (e.g., DJ PAEs) with hard-core PAEs (i.e., inorganic NP PAEs), low-symmetry colloidal crystals, such as Si_2Sr and potentially other structures, can be realized, creating an exciting path for future experimentation.

When these DJ PAEs were assembled with 10-nm AuNP PAEs (hydrodynamic diameter of 25 nm), a different trend was observed due to the relative sizes of the two PAEs. Specifically, for the small DJ PAEs (5 nm), we observed an FCC structure and for the medium- and large-sized DJ PAEs (8 nm and 15 nm, respectively), SH structures were observed (**Figure 6.5. b**). The largest DJ PAE size investigated remains small enough, compared to the 10-nm AuNP PAE, to fall within the SH regime. Nevertheless, with increasing DJ PAE size, the lattice parameters and unit cell

Table 6.5. DNA phase space exploration with DJ PAEs

Dendron	Junction	Dendron/AuNP ratio	NP Size (nm)	Symmetry	Space group	Lattice constant (nm)
9Dn-O1	N/A	12/24/48	5	FCC	*Fm-3m*	a = 42.5
9Dn-O1	2WJ-S	12/24/48	5	FCC	*Fm-3m*	a = 39.3
9Dn-O1	2WJ-M	3/6/12	5	SH	*P6/mmm*	a = b=28.7, c=28.9
9Dn-O1	2WJ-L	12	5	Si2Sr	*P 41 3 2*	a = 47.5
9DnO1	3WJ-S	12/24/48	5	FCC	*Fm-3m*	a=41.2
9Dn-O1	3WJ-M	6/18	5	SH	*P6/mmm*	a =b=28.8, c = 28.4
9Dn-O1	3WJ-L	6/18	5	Si2Sr	*P 41 3 2*	a = 47.5
9Dn-O1	N/A	24/48/96/120	10	FCC	*Fm*-3*m*	a = 45.4
9Dn-O1	2WJ-S	24/48/96/120	10	FCC	*Fm-3m*	a = 42.5
9Dn-O1	2WJ-M	96/120	10	SH	*P6/mmm*	a =b=30.4, c=30.1
9Dn-O1	2WJ-L	96/120	10	SH	*P6/mmm*	a =b=31.2, c=31.0
9Dn-O1	3WJ-S	12/24/48/96	10	FCC	*Fm-3m*	a=43.3
9Dn-O1	3WJ-M	12/24/48/96	10	SH	*P6/mmm*	a =b= 31.3, c = 25.5
9Dn-O1	3WJ-L	12/24/48/96	10	SH	*P6/mmm*	a = b=35.3, c = 26.5

volume consistently increased (**Table 6.5**). Thus, this approach allows one to access multiple crystal structures as well as readily shift the spacing between particles by tuning the DNA length.

6.4. Symmetry-breaking DJ PAEs in Binary NP Assemblies

Binary DNA-mediated nanoparticle assemblies often form a CsCl crystal structure (when the components are similar sizes) or an AlB_2 (when the components are different sizes), whereby one particle type would occupy the centered positions of the unit cell (like the chloride or boron), while the other particle type would occupy the corner positions of the unit cell (like the cesium or aluminum), in accordance with the CCM.[117, 316] Under these conditions, the PAEs are isotropically functionalized with DNA, forming high symmetry crystal structures. We hypothesized that these isotropic NPs could be organized into more complex crystal structures if we break symmetry by anisotropically presenting two orthogonal DNA sticky ends within a single colloidal crystal. We explored this hypothesis using a 2WJ DJ PAE. In this case, the junction-forming sequences were the same; however, the 18-base overhang regions were designed to be orthogonal such that only one specific dendron could hybridize to each overhang. Furthermore, the two dendrons were designed to have orthogonal sticky ends (5’ TTCCTT 3’ or 5’ TCTTCT 3’) on their branches. After forming this DJ PAE, we then introduced the two orthogonally functionalized NPs, with each particle decorated with a complementary sequence to one of the dendrons (5’ AAGGAA 3’ or 5’ AGAAGA 3’) (**Figure 6.6. a**). Therefore, in this system, two distinct binding interactions are possible.

We started by exploring this binary system using medium DJ PAEs and two different 10-nm AuNP PAEs. While the DJ PAEs are key components for directing the formation of colloidal crystals and therefore can be considered a third component in these structures, we have chosen to characterize the number of components based on the number of easily interchangeable inorganic NP PAEs that define the crystal structure. The distribution of these particles within the crystal structure was determined using SAXS and STEM. Through experimentation and simulation, the crystal structure was determined to be a large-lattice parameter (72 nm) SH crystal (**Figure 6.6. b**, middle). The SAXS patterns, along with the large lattice parameter could only be rationalized if both components were organized in specific locations within the unit cell: AuNP 1 at the (0,0,0) positions and AuNP 2 at the (0,0,1/2) positions (**Figure 6.6. b, right**). While the STEM data

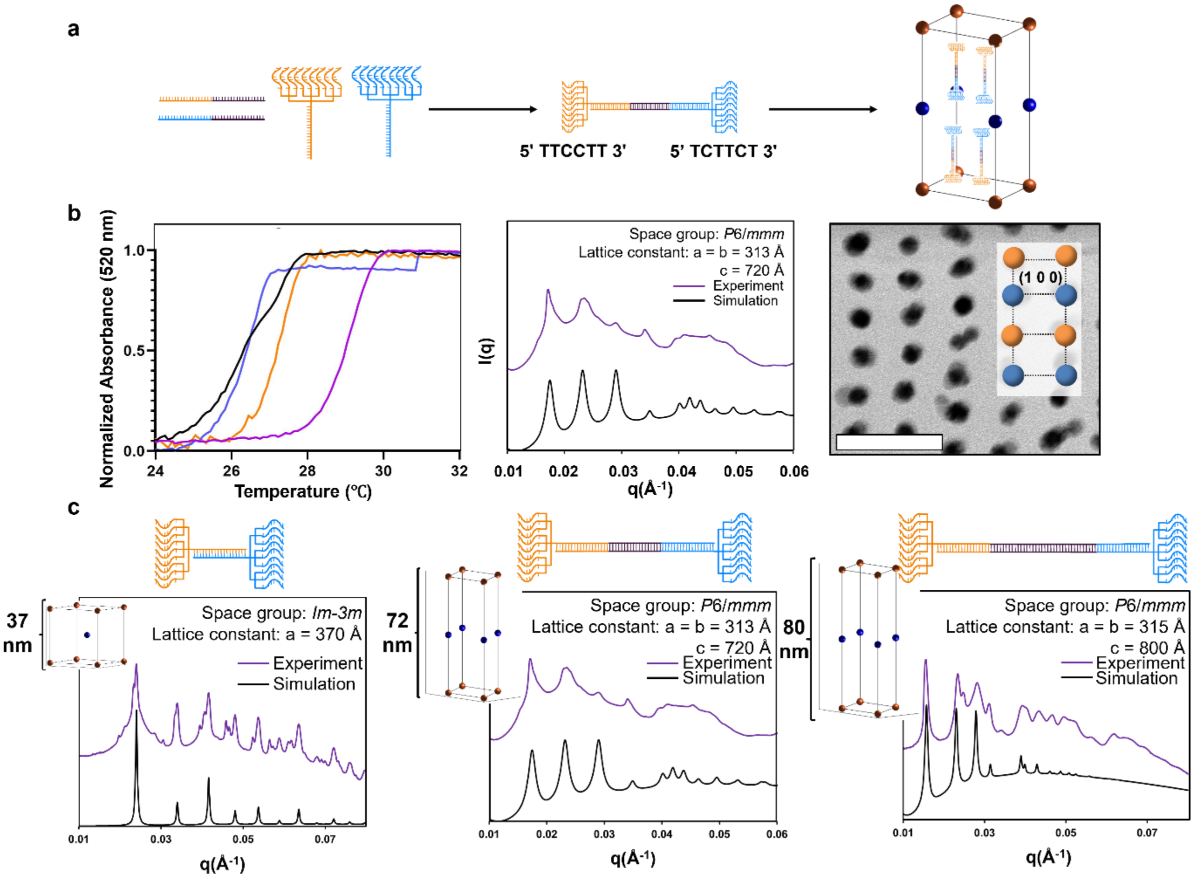

Figure 6.6. Symmetry breaking in binary NP assemblies
(a) DJ PAEs were designed such that the junction core contains orthogonal overhangs to which unique DNA dendrons could bind in order to direct the assembly of two different components. (b) Two 10-nm AuNP PAEs, functionalized with orthogonal DNA sequences, were assembled using the DJ PAE and characterized by UV-vis melt experiments, SAXS, and STEM. Melt experiments were conducted on multiple samples: AuNP PAE 1 and dendron 1 (black), AuNP PAE 2 and dendron 2 (orange), AuNP PAE 1+2 and dendron 1+2 (black), and AuNP PAE 1+2 and full 2WJ DJ PAE (purple). Scale bar = 50 nm. (c) The impact of anisotropy on the resultant crystal structures were observed by assembling two components using the small, medium, and large DJ PAEs and measuring changes in crystal structure and lattice parameter by SAXS.

corroborate these results, further experimentation was necessary to confirm that this was indeed, the local particle distribution (*vide infra*).

Melting experiments were also conducted to confirm that the DJ PAE can program the assembly of two components into a single colloidal crystal. The T_ms of assemblies of each individual dendron (no junction) and their respective complementary AuNP PAEs melted at 26.2 °C and 27 °C, respectively (**Figure 6.6. b left, blue and orange**); the sticky ends were designed such that there was a measurable difference between those two transitions, which allows the two interactions to be differentiated from one another. Importantly, when these two types of dendrons and these two types of NPs were assembled in the same solution, but without the 2WJ core, two melting transitions were observed – one that matches that of the blue trace and one that matches that of the orange trace (**Figure 6.6. b left, black**). These data indicate that even if both dendrons are present in solution, the two components phase separate to form the expected FCC structures, whereby each dendron assembles with its complementary AuNP PAE into a distinct lattice, as confirmed by SAXS (**Figure 6.7. and 6.8.**). Finally, only when all of these components are mixed together with the 2WJ core, does a completely new melting transition appear as a single, sharp transition, at a higher T_m than was observed for the other samples (Figure 3b left, purple). These results confirm that the two components have been incorporated into a single colloidal crystal as a result of the DJ PAE design.

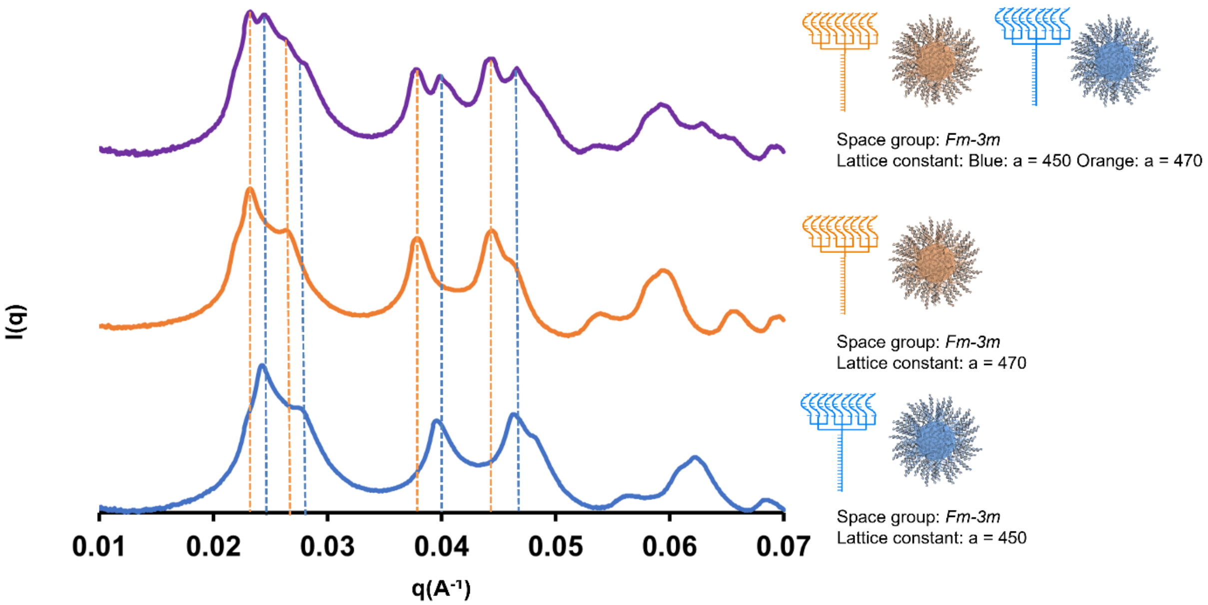

Figure 6.7. SAXS of two component assemblies (2x 10 nm AuNP) without the DJ core
(a) When both dendrons and 10 nm AuNP PAEs are assembled in the absence the 2WJ core, two different FCC crystal structures form. The blue and orange traces match the FCC structures of either NP and the purple trace is when both are assembled in the same solution without the DJ core. This indicates that, without the junction core, the two particles phase separate into their own crystal structures.

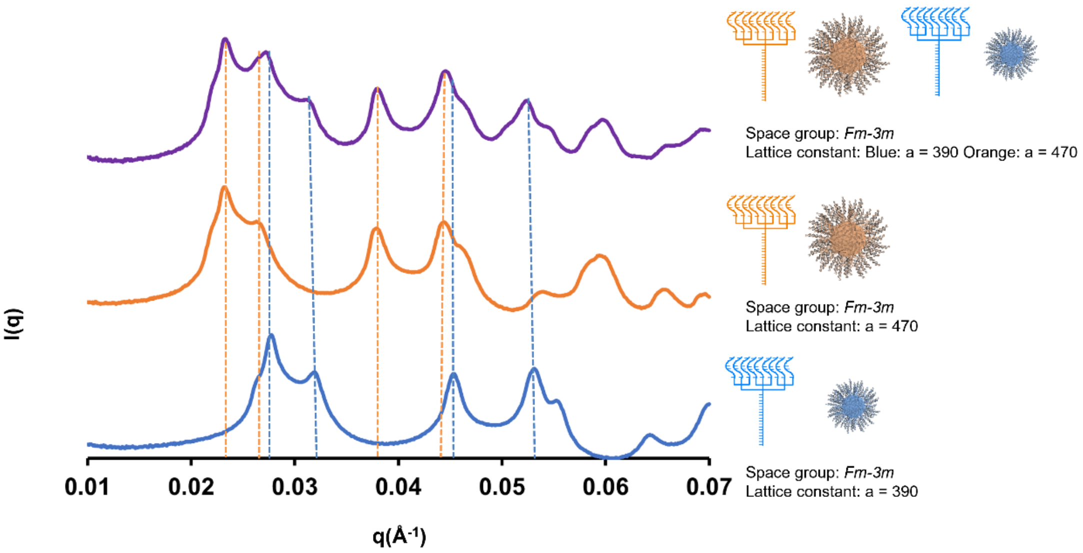

Figure 6.8.. SAXS of two component assemblies (10 nm and 5 nm AuNP) without the DJ core
(a) When both dendrons and 10 or 5 nm AuNP PAEs are assembled in the absence the 2WJ core, two different FCC crystal structures form. The blue and orange traces match the FCC structures of either NP and the purple trace is when both are assembled in the same solution without the DJ core. This indicates that, without the junction core, the two particles phase separate into their own crystal structures.

After demonstrating that the 2WJ DJ PAE can be used to program the assembly of two components into a single colloidal crystal, we then explored the impact of DJ PAE length on the resultant colloidal crystal structure and NP localization. To do this, we designed the small, medium, and large 2WJ DJ PAEs with orthogonal dendrons on each side (**Figure 6.6 c**). The small 2WJ DJ PAEs and the 10-nm AuNP PAEs formed a primarily CsCl crystal structure that is commonly observed in two-component DNA-mediated NP assemblies (**Figure 6.6. c, left**). However, as the distance between the two dendrons increased using the medium DJ PAE, the particles organized into an SH crystal structure, due to the increased anisotropy of the DJ PAEs (**Figure 6.6. c, middle**). Finally, when the size of the DJ PAE was increased further (large), an SH crystal structure was observed with a larger lattice parameter than in the medium DJ PAE structure (**Figure 6.6. c, right**). However, the increase was only observed in one dimension of the unit cell. Specifically, the *a* and *b* dimensions of the unit cell remained virtually unchanged (31.4 nm), but the *c* dimension increased by approximately 8 nm, matching the expected size increase based on the number of added bases. This single dimension expansion further supports the likely crystal structure and orientation of the DJ PAE within the unit cell. Furthermore, this means that DJ PAEs can be used to specifically program a single dimension of the unit cell independently, potentially opening new avenues for the design of programmable colloidal crystals and even pseudo-two-dimensional materials.

Next, we sought to confirm the local NP organization in these binary systems by assembling particles that could be distinguished within the crystal structure by SAXS and STEM. We assembled 10-nm AuNP PAEs with 5-nm AuNP PAEs. As was seen in the two-component system comprised of 10-nm NPs above, increased thermostability was observed when the junction core was used to build the colloidal crystal (27.8 °C) as compared to when colloidal crystals with individual dendrons and particles were prepared (25.2 °C and 24.8°C) (**Figure 6.9. a, left**). Using SAXS, we observed a diffraction pattern that represents an SH crystal structure similar to that seen when only 10-nm particles were used (**Figure 6.9. a, middle**). Compared to the SH structure formed from two 10-nm Au PAEs, the lattice parameters were slightly smaller, owing to the presence of smaller 5-nm Au PAEs (**Table 6.4.**). Furthermore, by adjusting the DJ PAE size, we again confirmed single dimension increases in the lattice parameters (**Figure 6.10.**). Finally, STEM was used to confirm this distribution with a sectioned sample (**Figure 6.9.a, right**). Here, the (100) plane clearly shows layers of 10-nm and 5-nm particles distributed as expected, based on the simulations and SAXS data.

To confirm that this organization was not an artifact of having two different sized NP PAEs and to conclusively determine the location of the two components, we repeated this experiment using 10-nm AuNP PAEs and 10-nm AgNP PAEs. The melt data again confirmed that the use of the 2WJ DJ PAE results in a significant increase in the thermostability of resultant crystals compared to when individual dendrons and particles were used (**Figure 6.9. b, left**). AgNPs tend to have fewer surface-bound DNA strands per particle than do AuNPs because their affinity for the thiol functional group of the DNA strands is lower.[317] As a result, crystals comprised of AgNP PAEs have relatively lower thermostabilities than do crystals comprised of AuNP PAEs (**Figure 6.9. b, left, blue and orange**). Nevertheless, when all of the particles are assembled together, the peaks in the simulated diffraction pattern of the expected crystal structure overlap with those of the experimental pattern, indicating that the same SH structure does indeed form (**Figure 6.9. b, middle**). STEM and energy dispersive X-ray spectroscopy (EDS) also confirmed this assignment. When imaging thin sections of the crystal, we observed bands of particles with two different zcontrasts; the AuNPs appear brighter because they more strongly scatter the electron beam (**Figure 6.9. b, right**). EDS data also support this result (**Figure 6.9. c**). Ultimately, we have demonstrated that the 2WJ DJ PAEs provide unique control over the structure and lattice parameters of binary colloidal crystals and are capable breaking symmetry to alter NP organization within the unit cell.

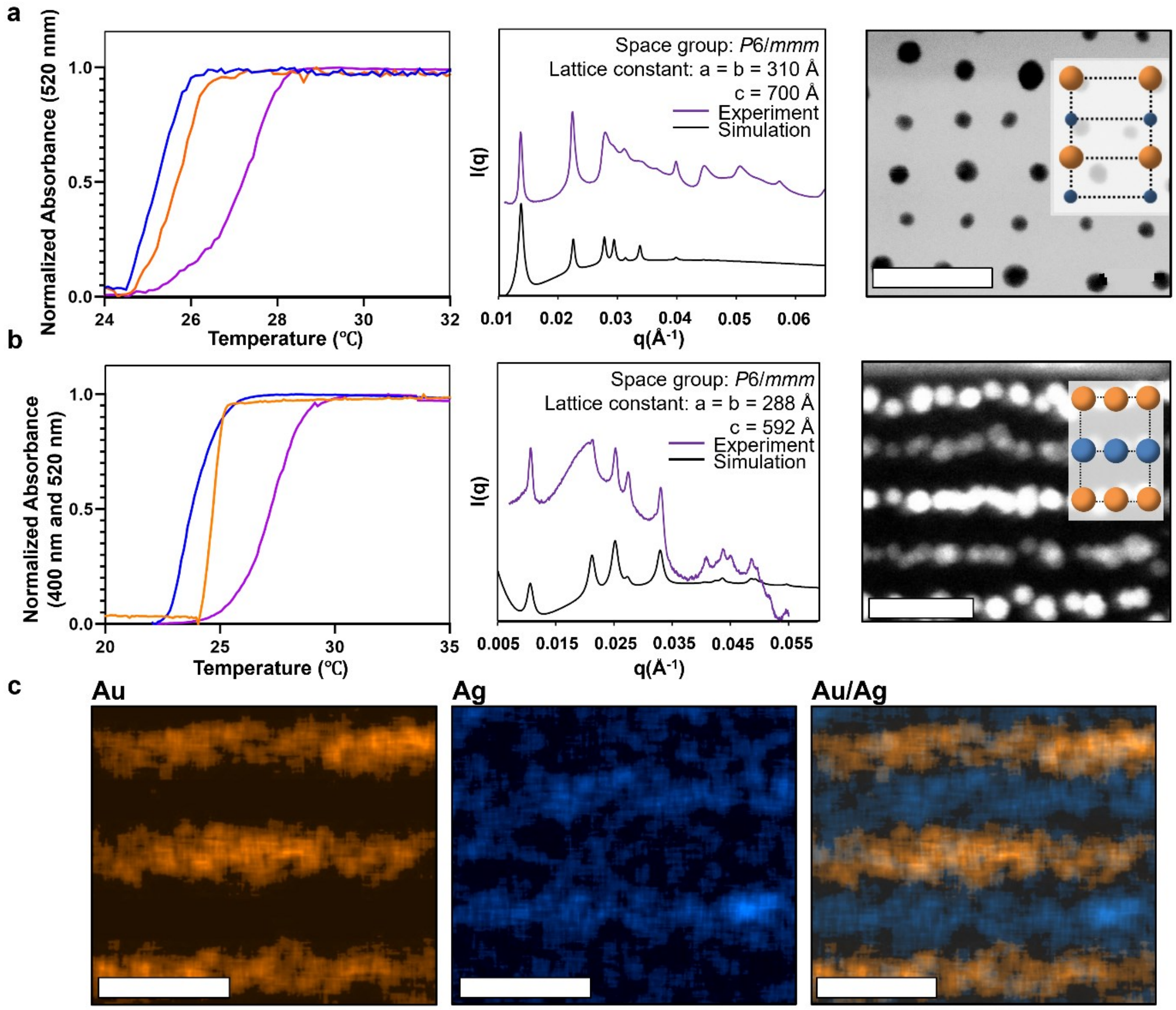

Figure 6.9. Assembly of two-component colloidal crystals to confirm NP localization
(a) A 10-nm AuNP PAE and a 5-nm AuNP PAE were assembled and characterized by UV-vis melting experiments, SAXS, and STEM. Melting experiments were conducted on: 10-nm PAE and dendron 1 (orange), 5-nm PAE and dendron 2 (blue), and both PAEs and full 2WJ DJ PAE (purple). (b) A 10-nm AuNP PAE and a 10-nm AgNP PAE were assembled and characterized by UV-vis melt experiments, SAXS, and STEM. Melting experiments were conducted on Au PAE and dendron 1 (orange), Ag PAE and dendron 2 (blue), both PAEs and full 2WJ DJ PAE (purple). (c) EDS was conducted on the resultant Au/Ag NP assemblies to conclusively demonstrate local NP organization. Au particles are represented in orange and Ag particles are represented in blue. Scale bar: 50 nm.

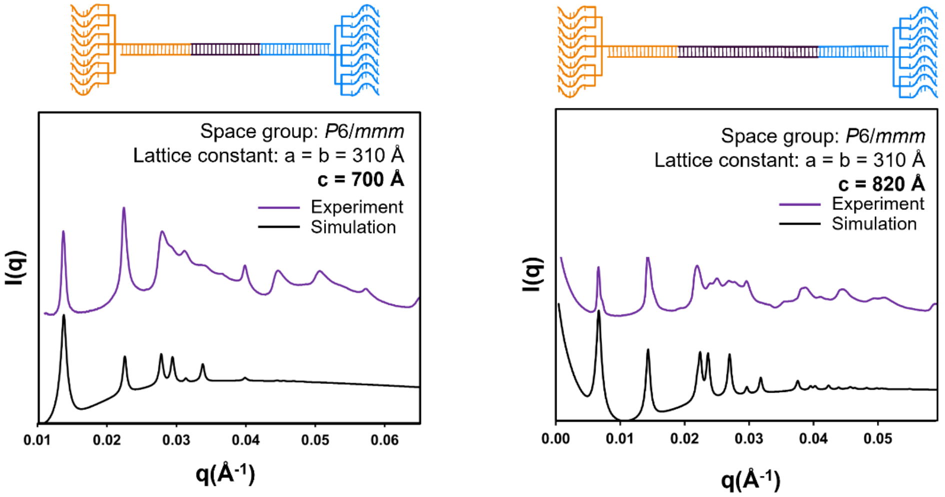

Figure 6.10. Tuning binary NP assemblies in a single dimension
Increasing the anisotropic presentation of the two orthogonal sequences allows us to tune the unit cell lattice parameters regardless of NP size, shape, and composition. This figure demonstrates this point using a 10 nm and 5 nm AuNP assembly. As we shift from the medium to long DJ PAE, the *c* dimension of the unit cell increases by 8.2 nm, while the *a* and *b* dimensions do not change.

6.5. Realizing Ternary NP Assemblies Through Symmetry-breaking DJ PAEs

Ternary colloidal crystals represent a long-standing challenge in the field of colloidal crystal engineering because it is difficult to program the local organization of each component. One way this has been achieved is by relying on specific nanoparticle sizes. For example, DNA-mediated approaches to three-component systems have been realized by using nanoparticle size differences to fit a third component into specific interstitial positions of a binary lattice.[318] Based on the observations from the 2WJ DJ PAE, we hypothesized that a 3WJ DJ PAE could be used to program the assembly of three components into a single colloidal crystal independent of NP size. Without a symmetry breaking DJ PAE, programming three orthogonal DNA interactions in a single structure is not possible and the introduction of a third particle would require the same DNA sticky ends as another particle, which would likely result in a statistically disorganized crystal structure. As discussed previously, though it is a necessary component of the crystal structure, the

DJ PAE is not counted toward the total number of components. As a result, we classify these assemblies as ternary, though they are arguably quaternary structures. Utilizing a similar design as described above with the 2WJ DJ PAEs, 3WJ DJ PAEs with orthogonal dendrons and sticky ends were prepared (**Figure 6.11. a**). Based on the SAXS data and multiple simulations, it was determined that the crystal structure was hexagonal and matches the proposed unit cell depicted (**Figure 6.11. a right and c**). In this structure, one of the components occupies the (1/3, -1/3, 1/2) positions (pink) in the unit cell, while the other two components have an equal chance of occupying the (0, 0, 0) positions of the unit cell (blue/orange). Furthermore, STEM images of sectioned samples reveal that this is indeed, the crystal structure based on the characteristic (100) plane that was observed (**Figure 6.11. d**). Thus, we have demonstrated that DJ PAEs can be used to create the first ternary colloidal crystals that form without relying on different sized particles.

We again characterized the thermostabilities of the resultant colloidal crystals. The dendrons were designed such that when they assemble with their respective AuNP PAEs, the T_ms transitions would vary slightly. When all of the dendrons and their corresponding NP PAEs were

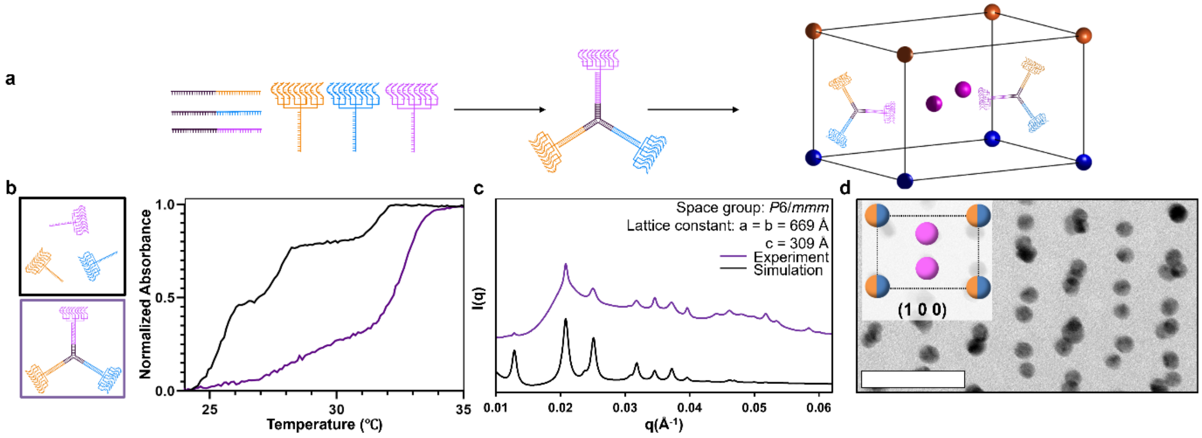

Figure 6.11.. Assembly of three-component colloidal crystals
(a) DJ PAEs were designed such that the junction core contains orthogonal overhangs to which unique DNA dendrons can bind in order to direct the assembly of three different components. (b) UV-vis melt experiments were conducted with the junction core (purple) and without the junction core (black), demonstrating that only when the full DJ PAE is present, does a single colloidal crystal with all three components form. (c) SAXS data and simulations confirm that the resultant crystal structure is hexagonal with the depicted nanoparticle distribution. (d) STEM further supports this conclusion. The characteristic (100) plane of this crystal structure was imaged. Scale bar: 50 nm.

mixed in the assembly solution, with no DJ core present, we observed phase separation of the three different resultant FCC structures, as confirmed by SAXS (**Figure 6.12.**). This is evidenced by the three distinct melting transitions that are observed in the UV-vis trace (**Figure 6.11. b, black**). On the other hand, when the full 3WJ DJ PAE was formed, a distinct and singular melting transition was observed (**Figure 6.11. b, purple**), indicating that indeed, a single colloidal crystal had formed from the three NP components. A gradual increase in extinction was observed from 25 to 30 °C, which is likely due to the range of interaction strengths between the DNA dendrons and their respective NP PAEs. Here, we demonstrate that due to the programmable anisotropy and orthogonality of the DJ PAE, the first ternary colloidal crystals that can form independently of NP size were synthesized. Further experimentation will lead to a greater understanding of design parameters to tune nanoparticle localization and ultimately expand beyond three component systems.

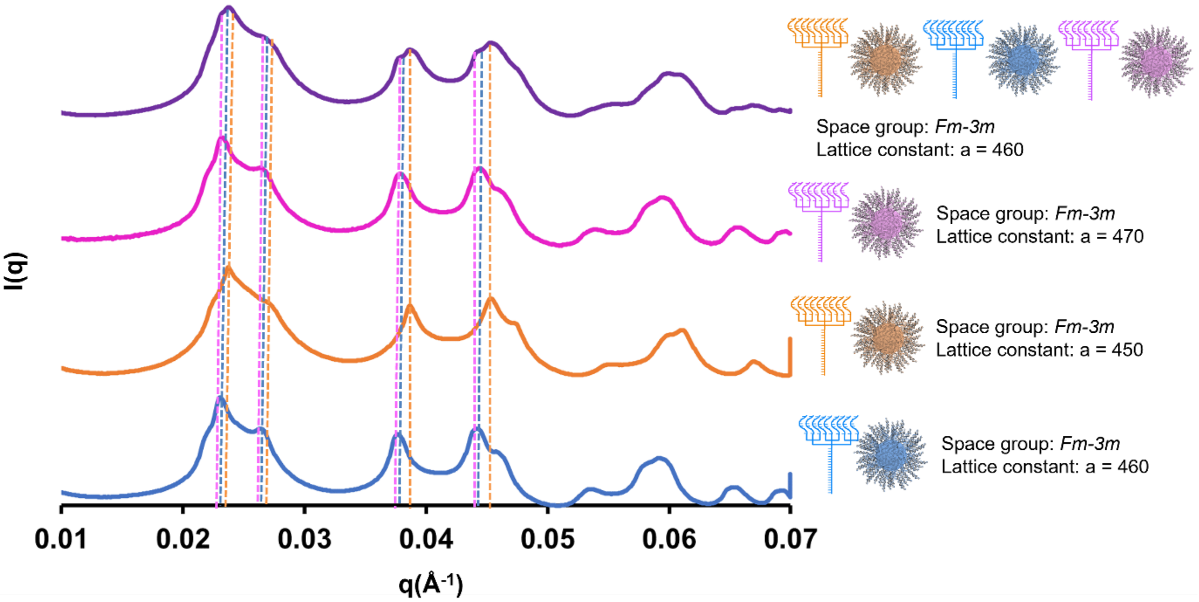

Figure 6.12. SAXS of three component assemblies without the DJ core
When three different 10-nm AuNP PAES are assembled in the absence the 3WJ core, three different FCC crystal structures form. Due to the individual particles being the same size, this results in a broad FCC structure (purple trace). The assemblies consisting of induvial components all have lattice parameters within that range (blue, orange and pink trace). This indicates that, without the junction core, the three particles phase separate into their own crystal structures.

6.6. Comments on breaking symmetry in colloidal crystals using DNA dendrimers

This work introduces a new type of DNA-based building block that functions as a symmetry-breaking synthon to encode anisotropic and orthogonal information within NP assemblies. DJ PAEs can be readily designed to have specific sizes and architectures that play key roles in dictating assembly outcomes. When all sticky ends on the DNA dendrimers are identical, the relative size between the DJ PAEs and NP PAEs can be tuned to access three distinct colloidal crystal structures in accordance with the CCM, including a structure that is novel to the field of colloidal crystal engineering. As a symmetry-breaking synthon, these molecular entities allow us to fine-tune anisotropy and orthogonality in ways that cannot be seen in particle-based systems. Using this approach, binary assemblies with novel structural control were realized and the first ternary colloidal crystals that form independent of NP size were made. Importantly, none of these assembly outcomes can be rationalized without considering the effects of directional interactions. This work forms a foundation for developing and studying colloidal crystals with unique, low symmetry structures as well as multicomponent colloidal alloys that can have a significant impact on the development of modern materials.

CHAPTER SEVEN

Conclusions

7.1. Conclusions

This thesis presents new methods to gain fine-tuned control over DNA ligand architecture and utilize this control to access new capabilities in therapeutics and materials design. In biology, these lessons include: (1) how DNA dendron valency and design affect cellular uptake, resistance to degradation, and delivery of conjugated cargo; (2) how molecular vaccine structure can be tuned and harnessed to elevate adjuvant and antigen delivery and function to induce a specific and powerful immune response against a desired cancer target; (3) how SNA structure can dictate infectious disease vaccine efficacy. In materials, these lessons include (1) how fine-tuned control over DNA dendron/dendrimer valency and size can lead to novel programmability over resultant colloidal crystals; (2) how DNA dendrons can be interfaced with multiple different cores to build molecularly defined, nanoscale building blocks; (3) how DNA dendrons can encode anisotropic and orthogonal interactions within a single colloidal crystal, providing new insights and capabilities for building low symmetry colloidal alloys. This work utilizes the vast design space and chemical addressability of oligonucleotides as programmable materials, and our findings emphasize the impact of controlling DNA ligand architecture for both improved therapeutics and materials design.

In Chapter two, we introduced the DNA dendron as a molecularly defined mimic of the SNA that can be used as a general approach to deliver functional biomolecules into cells. By achieving robust synthetic yields and developing functionalization procedures, we demonstrate the promise for many potential applications. We explore critical DNA dendron design parameters (*e.g.,* valency and length) and investigate how they impact cellular uptake, resistance to degradation, and delivery of functional cargo (e.g., small molecules, DNA/RNA, peptides, and proteins). DNA dendrons provide a simple, effective, and biocompatible approach to deliver various diagnostic and therapeutic biomaterials to living systems. The DNA dendron is poised to have a significant impact on the development of next generation diagnostic tools, vaccines, and therapeutics.

In Chapter three, we utilized the DNA dendron as a molecularly defined platform for vaccine design. By leveraging the fine-tuned structural control of the dendron, established in chapter two, we investigated how DNA dendron design impacts the delivery of functional adjuvant CpG sequences, and how to maximize cellular uptake and the resultant immune response, *ex vivo* and *in vivo*. We observed that the CpG sequence as the dendron stem, and the poly-T sequences as the branches was the most efficient method of delivering functional adjuvant to cells. Importantly, as the CPG no longer needed to occupy the branches for effective functioning, the branch sequences have the potential to be further tuned to improve dendron uptake (*e.g.,* the use of G-rich sequences). By conjugating an antigenic peptide derived from cervical cancer (due to HPV) to the dendron, a molecularly defined cancer vaccine was synthesized. We investigated how peptide conjugation to different parts of the dendron modulates dendron uptake and immune activation and that the vaccines produced a robust and specific immune response against the cancer target. Finally, we harnessed a particular structural design that has antigenic peptide conjugated to each dendron branch to reduce tumor burden and extend animal survival, *in vivo*. Taken together, this work explores the structure-function relationships of DNA-dendron based vaccines in a molecularly defined manner. Due to the modularity of this molecular vaccine, whereby the antigenic cancer target can be switched with relative ease, these design rules can be applied to develop vaccines that treat a variety of cancers.

In Chapter four, we established the SNA as an effective antiviral vaccine platform. By utilizing the highly modular SNA architecture, we highlight the importance of packaging viral antigens to raise humoral immune responses that can effectively protect against a live virus. This work has important implications for the design of next generation infectious disease vaccines. It illustrates that antibody production is tunable through simple chemical adjustments (*e.g.,* the adjuvant loading on a liposome) and that a change to the ratio of components can greatly alter immunoglobulin expression levels. This work offers alternative strategies to enhance antibody responses *versus* traditional approaches, which involve administering multiple doses. Importantly, we also observed that a common approach of supplementing a vaccine with adjuvant to enhance an antibody response is not effective at robust antibody generation. The results confirm that radial display of CpG adjuvant and co-delivery of vaccine components leads to an effective vaccine that prevents mortality and attenuates lung injury. Taken together, this work underscores the SNA's potential as a platform for infectious disease vaccines and highlights the role that structure-function relationships can play in revolutionizing vaccine development for rapidly emerging diseases.

Chapter five utilizes the DNA dendron in the assembly of nanoparticles into colloidal crystals. By combining the DNA dendrons with DNA-containing templates, a new type of DNA-mediated hierarchical assembly that has three levels of structural organization was achieved. Importantly, the assembly outcomes cannot be rationalized and the lattice reconfiguration strategies cannot be realized unless all of these underlying interactions are considered. This study highlights the fact that chemical components (e.g., surfactants) or functional groups (e.g., hydrophobic moieties) that seem inconsequential can assume structure-directing roles in extended assemblies. In particular, the advances described should encourage re-exploration of the surfactant literature for developing new strategies to program the assembly of nanomaterials. Utilizing both sequence-encoded and non-sequence-specific interactions to mediate dynamic and reconfigurable organizations of building blocks is an effective strategy for designing hierarchical materials. These structure-guiding principles should apply to both soft and hard matter, opening avenues for the deliberate introduction of transient interactions between building blocks to induce the formation of unconventional phases.

In Chapter six, we build upon the lessons learned to develop a DNA dendrimer building block as a symmetry-breaking synthon to encode anisotropic and orthogonal information within NP assemblies. These DNA Junction PAEs (DJ PAEs) can be readily designed to have specific sizes and architectures that play key roles in dictating assembly outcomes. When all sticky ends on the DNA dendrimers are identical, the relative size between the DJ PAEs and NP PAEs can be tuned to access three distinct colloidal crystal structures in accordance with the CCM, including a structure that is novel to the field of colloidal crystal engineering. As a symmetry-breaking synthon, these molecular entities allow for fine-tuned anisotropy and orthogonality in ways that cannot be achieved in strictly particle-based systems. Using this approach, binary assemblies with novel structural control were realized; also, the first ternary colloidal crystals that form independent of NP size were realized. Importantly, none of these assembly outcomes can be rationalized without considering the effects of directional interactions. This work forms a foundation for developing and studying colloidal crystals with unique, low symmetry structures as well as multicomponent colloidal alloys that can have a significant impact on the development of modern materials.

The use of DNA as a ligand to program materials properties is an evolving field. Recently, many have studied how DNA design (*i.e.,* length, flexibility, and sequence) impacts nanoparticle properties in biological and materials settings. The next step in this evolution is to gain control over DNA ligand presentation, specifically valency (number), anisotropy (direction), and orthogonality (interaction). By accessing this level of control, novel capabilities can be achieved across multiple fields. The work presented in this thesis develops a method by which we can investigate the effects of DNA ligand presentation control. The DNA dendron enables programmability of valency, anisotropy, and orthogonality, and the work presented here highlights the potential to utilize this control to create new functional therapeutics and materials.

REFERENCES

1. Chen, G.; Gibson, K. J.; Liu, D.; Rees, H. C.; Lee, J.-H.; Xia, W.; Lin, R.; Xin, H. L.; Gang, O.; Weizmann, Y., Regioselective surface encoding of nanoparticles for programmable self-assembly. *Nature Materials* **2019,** *18* (2), 169.
2. Kim, Y.-Y.; Bang, Y.; Lee, A.-H.; Song, Y.-K., Multivalent traptavidin–DNA conjugates for the programmable assembly of nanostructures. *ACS Nano* **2019,** *13* (2), 1183.
3. Tikhomirov, G.; Hoogland, S.; Lee, P. E.; Fischer, A.; Sargent, E. H.; Kelley, S. O., DNA-based programming of quantum dot valency, self-assembly and luminescence. *Nature Nanotechnology* **2011,** *6* (8), 485.
4. Si, K. J.; Chen, Y.; Shi, Q.; Cheng, W., Nanoparticle superlattices: The roles of soft ligands. *Advanced Science* **2018,** *5* (1), 1700179.
5. Rossi, L. M.; Fiorio, J. L.; Garcia, M. A. S.; Ferraz, C. P., The role and fate of capping ligands in colloidally prepared metal nanoparticle catalysts. *Dalton Transactions* **2018,** *47* (17), 5889.
6. Macfarlane, R. J.; Lee, B.; Jones, M. R.; Harris, N.; Schatz, G. C.; Mirkin, C. A., Nanoparticle superlattice engineering with DNA. *Science* **2011,** *334* (6053), 204.
7. Si, K. J.; Sikdar, D.; Chen, Y.; Eftekhari, F.; Xu, Z.; Tang, Y.; Xiong, W.; Guo, P.; Zhang, S.; Lu, Y.; Bao, Q.; Zhu, W.; Premaratne, M.; Cheng, W., Giant plasmene nanosheets, nanoribbons, and origami. *ACS Nano* **2014,** *8* (11), 11086.
8. Wang, H.; Chen, L.; Shen, X.; Zhu, L.; He, J.; Chen, H., Unconventional chain-growth mode in the assembly of colloidal gold nanoparticles. *Angewandte Chemie International Edition* **2012,** *51* (32), 8021.
9. Zadeh, J. N.; Steenberg, C. D.; Bois, J. S.; Wolfe, B. R.; Pierce, M. B.; Khan, A. R.; Dirks, R. M.; Pierce, N. A., Nupack: Analysis and design of nucleic acid systems. *J. Comput. Chem.* **2011,** *32* (1), 170.
10. Lu, Z.; Long, Y.; Cun, X.; Wang, X.; Li, J.; Mei, L.; Yang, Y.; Li, M.; Zhang, Z.; He, Q., A size-shrinkable nanoparticle-based combined anti-tumor and anti-inflammatory strategy for enhanced cancer therapy. *Nanoscale* **2018,** *10* (21), 9957.
11. Mosqueira, V. C. F.; Legrand, P.; Morgat, J.-L.; Vert, M.; Mysiakine, E.; Gref, R.; Devissaguet, J.-P.; Barratt, G., Biodistribution of long-circulating peg-grafted nanocapsules in mice: Effects of peg chain length and density. *Pharmaceutical Research* **2001,** *18* (10), 1411.
12. Yao, G.; Li, J.; Li, Q.; Chen, X.; Liu, X.; Wang, F.; Qu, Z.; Ge, Z.; Narayanan, R. P.; Williams, D.; Pei, H.; Zuo, X.; Wang, L.; Yan, H.; Feringa, B. L.; Fan, C., Programming nanoparticle valence bonds with single-stranded DNA encoders. *Nature Materials* **2020,** *19* (7), 781.
13. Schubert, K.; Meissner, H. G.; Poetzschke, M.; Rossteutscher, W.; Stolz, E., Structure data on metallic phases. Vii. *Nuturwissenschaften* **1962,** *49*, 57.
14. Rieger, W.; Nowotny, H.; Benesovsky, F., Phases with octahedral units of transition metals. *Monatsh. Chem.* **1965,** *96* (1), 232.
15. Peng, X.; Manna, L.; Yang, W.; Wickham, J.; Scher, E.; Kadavanich, A.; Alivisatos, A. P., Shape control of cdse nanocrystals. *Nature* **2000,** *404* (6773), 59.
16. Jishkariani, D.; Diroll, B. T.; Cargnello, M.; Klein, D. R.; Hough, L. A.; Murray, C. B.; Donnio, B., Dendron-mediated engineering of interparticle separation and self-assembly in dendronized gold nanoparticles superlattices. *Journal of the American Chemical Society* **2015,** *137* (33), 10728.
17. Takara, K.; Hatakeyama, H.; Ohga, N.; Hida, K.; Harashima, H., Design of a dual-ligand system using a specific ligand and cell penetrating peptide, resulting in a synergistic effect on selectivity and cellular uptake. *International Journal of Pharmaceutics* **2010,** *396* (1), 143.
18. Laramy, C. R.; O’Brien, M. N.; Mirkin, C. A., Crystal engineering with DNA. *Nature Reviews Materials* **2019,** *4* (3), 201.
19. Macfarlane, R. J.; O'Brien, M. N.; Petrosko, S. H.; Mirkin, C. A., Nucleic acid-modified nanostructures as programmable atom equivalents: Forging a new “table of elements”. *Angewandte Chemie International Edition* **2013,** *52* (22), 5688.
20. Li, N.; Zhao, P.; Astruc, D., Anisotropic gold nanoparticles: Synthesis, properties, applications, and toxicity. *Angewandte Chemie International Edition* **2014,** *53* (7), 1756.
21. Chen, X.; Zhao, D.; Zhao, L.; An, Y.; Ma, R.; Shi, L.; He, Q.; Chen, L., Optic and catalytic properties of gold nanoparticles tuned by homopolymers. *Science in China Series B: Chemistry* **2009,** *52* (9), 1372.
22. Kumar, D.; Saini, N.; Jain, N.; Sareen, R.; Pandit, V., Gold nanoparticles: An era in bionanotechnology. *Expert opinion on drug delivery* **2013,** *10* (3), 397.

23. Sardar, R.; Funston, A. M.; Mulvaney, P.; Murray, R. W., Gold nanoparticles: Past, present, and future. *Langmuir* **2009,** *25* (24), 13840.

24. Njoki, P. N.; Lim, I.-I. S.; Mott, D.; Park, H.-Y.; Khan, B.; Mishra, S.; Sujakumar, R.; Luo, J.; Zhong, C.-J., Size correlation of optical and spectroscopic properties for gold nanoparticles. *The Journal of Physical Chemistry C* **2007,** *111* (40), 14664.

25. Jain, P. K.; Lee, K. S.; El-Sayed, I. H.; El-Sayed, M. A., Calculated absorption and scattering properties of gold nanoparticles of different size, shape, and composition: Applications in biological imaging and biomedicine. *The journal of physical chemistry B* **2006,** *110* (14), 7238.

26. Hua, Y.; Chandra, K.; Dam, D. H. M.; Wiederrecht, G. P.; Odom, T. W., Shape-dependent nonlinear optical properties of anisotropic gold nanoparticles. *The journal of physical chemistry letters* **2015,** *6* (24), 4904.

27. Cuenya, B. R., Synthesis and catalytic properties of metal nanoparticles: Size, shape, support, composition, and oxidation state effects. *Thin Solid Films* **2010,** *518* (12), 3127.

28. Heuer-Jungemann, A.; Feliu, N.; Bakaimi, I.; Hamaly, M.; Alkilany, A.; Chakraborty, I.; Masood, A.; Casula, M. F.; Kostopoulou, A.; Oh, E.; Susumu, K.; Stewart, M. H.; Medintz, I. L.; Stratakis, E.; Parak, W. J.; Kanaras, A. G., The role of ligands in the chemical synthesis and applications of inorganic nanoparticles. *Chemical Reviews* **2019,** *119* (8), 4819.

29. Ling, D.; Hackett, M. J.; Hyeon, T., Surface ligands in synthesis, modification, assembly and biomedical applications of nanoparticles. *Nano Today* **2014,** *9* (4), 457.

30. Pellegrino, T.; Kudera, S.; Liedl, T.; Muñoz Javier, A.; Manna, L.; Parak, W. J., On the development of colloidal nanoparticles towards multifunctional structures and their possible use for biological applications. *small* **2005,** *1* (1), 48.

31. Ji, X.; Song, X.; Li, J.; Bai, Y.; Yang, W.; Peng, X., Size control of gold nanocrystals in citrate reduction: The third role of citrate. *Journal of the American Chemical Society* **2007,** *129* (45), 13939.

32. Frens, G., Controlled nucleation for the regulation of the particle size in monodisperse gold suspensions. *Nature physical science* **1973,** *241* (105), 20.

33. Jana, N. R.; Gearheart, L.; Murphy, C. J., Seeding growth for size control of 5− 40 nm diameter gold nanoparticles. *Langmuir* **2001,** *17* (22), 6782.

34. Sau, T. K.; Murphy, C. J., Room temperature, high-yield synthesis of multiple shapes of gold nanoparticles in aqueous solution. *Journal of the American Chemical Society* **2004,** *126* (28), 8648.

35. Pérez-Juste, J.; Pastoriza-Santos, I.; Liz-Marzán, L. M.; Mulvaney, P., Gold nanorods: Synthesis, characterization and applications. *Coordination chemistry reviews* **2005,** *249* (17-18), 1870.

36. Gao, J.; Bender, C. M.; Murphy, C. J., Dependence of the gold nanorod aspect ratio on the nature of the directing surfactant in aqueous solution. *Langmuir* **2003,** *19* (21), 9065.

37. Dinkel, R.; Braunschweig, B. r.; Peukert, W., Fast and slow ligand exchange at the surface of colloidal gold nanoparticles. *The journal of physical chemistry C* **2016,** *120* (3), 1673.

38. Feng, Y.; Xing, S.; Xu, J.; Wang, H.; Lim, J. W.; Chen, H., Probing the kinetics of ligand exchange on colloidal gold nanoparticles by surface-enhanced raman scattering. *Dalton Transactions* **2010,** *39* (2), 349.

39. Dreaden, E. C.; Alkilany, A. M.; Huang, X.; Murphy, C. J.; El-Sayed, M. A., The golden age: Gold nanoparticles for biomedicine. *Chemical Society Reviews* **2012,** *41* (7), 2740.

40. Zhu, T.; Vasilev, K.; Kreiter, M.; Mittler, S.; Knoll, W., Surface modification of citrate-reduced colloidal gold nanoparticles with 2-mercaptosuccinic acid. *Langmuir* **2003,** *19* (22), 9518.

41. Larson, I.; Chan, D.; Drummond, C. J.; Grieser, F., Use of atomic force microscopy force measurements to monitor citrate displacement by amines on gold in aqueous solution. *Langmuir* **1997,** *13* (9), 2429.

42. Hühn, J.; Carrillo-Carrion, C.; Soliman, M. G.; Pfeiffer, C.; Valdeperez, D.; Masood, A.; Chakraborty, I.; Zhu, L.; Gallego, M.; Yue, Z., Selected standard protocols for the synthesis, phase transfer, and characterization of inorganic colloidal nanoparticles. *Chemistry of Materials* **2017,** *29* (1), 399.

43. Erathodiyil, N.; Ying, J. Y., Functionalization of inorganic nanoparticles for bioimaging applications. *Accounts of chemical research* **2011,** *44* (10), 925.

44. Kango, S.; Kalia, S.; Celli, A.; Njuguna, J.; Habibi, Y.; Kumar, R., Surface modification of inorganic nanoparticles for development of organic–inorganic nanocomposites—a review. *Progress in Polymer Science* **2013,** *38* (8), 1232.

45. Albanese, A.; Tang, P. S.; Chan, W. C. W., The effect of nanoparticle size, shape, and surface chemistry on biological systems. *Annual Review of Biomedical Engineering* **2012,** *14* (1), 1.

46. Yoo, J.; Park, C.; Yi, G.; Lee, D.; Koo, H., Active targeting strategies using biological ligands for nanoparticle drug delivery systems. *Cancers (Basel)* **2019,** *11* (5), 640.

47. Nel, A. E.; Mädler, L.; Velegol, D.; Xia, T.; Hoek, E. M. V.; Somasundaran, P.; Klaessig, F.; Castranova, V.; Thompson, M., Understanding biophysicochemical interactions at the nano–bio interface. *Nature Materials* **2009,** *8* (7), 543.

48. Kolate, A.; Baradia, D.; Patil, S.; Vhora, I.; Kore, G.; Misra, A., Peg — a versatile conjugating ligand for drugs and drug delivery systems. *Journal of Controlled Release* **2014,** *192*, 67.

49. Tan, S. J.; Jana, N. R.; Gao, S.; Patra, P. K.; Ying, J. Y., Surface-ligand-dependent cellular interaction, subcellular localization, and cytotoxicity of polymer-coated quantum dots. *Chemistry of Materials* **2010,** *22* (7), 2239.

50. Ishida, M.; Watanabe, H.; Takigawa, K.; Kurishita, Y.; Oki, C.; Nakamura, A.; Hamachi, I.; Tsukiji, S., Synthetic self-localizing ligands that control the spatial location of proteins in living cells. *Journal of the American Chemical Society* **2013,** *135* (34), 12684.

51. Pearce, A. K.; Fuchs, A. V.; Fletcher, N. L.; Thurecht, K. J., Targeting nanomedicines to prostate cancer: Evaluation of specificity of ligands to two different receptors in vivo. *Pharmaceutical Research* **2016,** *33* (10), 2388.

52. Fiandra, L.; Mazzucchelli, S.; De Palma, C.; Colombo, M.; Allevi, R.; Sommaruga, S.; Clementi, E.; Bellini, M.; Prosperi, D.; Corsi, F., Assessing the in vivo targeting efficiency of multifunctional nanoconstructs bearing antibody-derived ligands. *ACS Nano* **2013,** *7* (7), 6092.

53. Liu, Y.; Hui, Y.; Ran, R.; Yang, G.-Z.; Wibowo, D.; Wang, H.-F.; Middelberg, A. P. J.; Zhao, C.-X., Synergetic combinations of dual-targeting ligands for enhanced in vitro and in vivo tumor targeting. *Advanced Healthcare Materials* **2018,** *7* (15), 1800106.

54. Cunningham-Rundles, C.; Zhuo, Z.; Griffith, B.; Keenan, J., Biological activities of polyethylene-glycol immunoglobulin conjugates resistance to enzymatic degradation. *Journal of Immunological Methods* **1992,** *152* (2), 177.

55. Otsuka, H.; Nagasaki, Y.; Kataoka, K., Pegylated nanoparticles for biological and pharmaceutical applications. *Advanced Drug Delivery Reviews* **2003,** *55* (3), 403.

56. Lynch, I.; Dawson, K. A., Protein-nanoparticle interactions. *Nano Today* **2008,** *3* (1), 40.

57. Walkey, C. D.; Olsen, J. B.; Guo, H.; Emili, A.; Chan, W. C. W., Nanoparticle size and surface chemistry determine serum protein adsorption and macrophage uptake. *Journal of the American Chemical Society* **2012,** *134* (4), 2139.

58. Lundqvist, M.; Stigler, J.; Cedervall, T.; Berggård, T.; Flanagan, M. B.; Lynch, I.; Elia, G.; Dawson, K., The evolution of the protein corona around nanoparticles: A test study. *ACS Nano* **2011,** *5* (9), 7503.

59. Mahmoudi, M.; Lynch, I.; Ejtehadi, M. R.; Monopoli, M. P.; Bombelli, F. B.; Laurent, S., Protein−nanoparticle interactions: Opportunities and challenges. *Chemical Reviews* **2011,** *111* (9), 5610.

60. Batra, J.; Robinson, J.; Mehner, C.; Hockla, A.; Miller, E.; Radisky, D. C.; Radisky, E. S., Pegylation extends circulation half-life while preserving in vitro and in vivo activity of tissue inhibitor of metalloproteinases-1 (timp-1). *PLoS One* **2012,** *7* (11), e50028.

61. Ginn, C.; Khalili, H.; Lever, R.; Brocchini, S., Pegylation and its impact on the design of new protein-based medicines. *Future Medicinal Chemistry* **2014,** *6* (16), 1829.

62. Pelaz, B.; del Pino, P.; Maffre, P.; Hartmann, R.; Gallego, M.; Rivera-Fernández, S.; de la Fuente, J. M.; Nienhaus, G. U.; Parak, W. J., Surface functionalization of nanoparticles with polyethylene glycol: Effects on protein adsorption and cellular uptake. *ACS Nano* **2015,** *9* (7), 6996.

63. Shimizu, T.; Abu Lila, A. S.; Awata, M.; Kubo, Y.; Mima, Y.; Hashimoto, Y.; Ando, H.; Okuhira, K.; Ishima, Y.; Ishida, T., A cell assay for detecting anti-peg immune response against peg-modified therapeutics. *Pharmaceutical Research* **2018,** *35* (11), 1.

64. Wan, X.; Zhang, J.; Yu, W.; Shen, L.; Ji, S.; Hu, T., Effect of protein immunogenicity and peg size and branching on the anti-peg immune response to pegylated proteins. *Process Biochemistry* **2017,** *52*, 183.

65. Veronese, F. M., Peptide and protein pegylation: A review of problems and solutions. *Biomaterials* **2001,** *22* (5), 405.

66. Derakhshankhah, H.; Jafari, S., Cell penetrating peptides: A concise review with emphasis on biomedical applications. *Biomedicine & Pharmacotherapy* **2018,** *108*, 1090.

67. Jafari, S.; Dizaj, S. M.; Adibkia, K., Cell-penetrating peptides and their analogues as novel nanocarriers for drug delivery. *BioImpacts: BI* **2015,** *5* (2), 103.

68. Guidotti, G.; Brambilla, L.; Rossi, D., Cell-penetrating peptides: From basic research to clinics. *Trends in pharmacological sciences* **2017,** *38* (4), 406.

69. Kang, J.-H.; Jung, M.-Y.; Yin, X.; Andrianifahanana, M.; Hernandez, D. M.; Leof, E. B., Cell-penetrating peptides selectively targeting smad3 inhibit profibrotic tgf-β signaling. *The Journal of clinical investigation* **2017,** *127* (7), 2541.

70. Tanaka, G.; Kawaguchi, Y.; Kuwata, K.; Takeuchi, T.; Nakase, I.; Futaki, S., Photoaffinity labeling methods to explore internalization mechanisms of arginine-rich cell-penetrating peptides. In *Photoaffinity labeling for structural probing within protein*, Springer: 2017; pp 225.

71. Lundberg, P.; Langel, Ü., A brief introduction to cell-penetrating peptides. *Journal of Molecular Recognition* **2003,** *16* (5), 227.

72. Oikawa, K.; Islam, M. M.; Horii, Y.; Yoshizumi, T.; Numata, K., Screening of a cell-penetrating peptide library in escherichia coli: Relationship between cell penetration efficiency and cytotoxicity. *Acs Omega* **2018,** *3* (12), 16489.

73. Xie, J.; Bi, Y.; Zhang, H.; Dong, S.; Teng, L.; Lee, R. J.; Yang, Z., Cell-penetrating peptides in diagnosis and treatment of human diseases: From preclinical research to clinical application. *Frontiers in pharmacology* **2020,** *11*, 697.

74. Nie, Z.; Petukhova, A.; Kumacheva, E., Properties and emerging applications of self-assembled structures made from inorganic nanoparticles. *Nature Nanotechnology* **2010,** *5* (1), 15.

75. Lee, M. S.; Yee, D. W.; Ye, M.; Macfarlane, R. J., Nanoparticle assembly as a materials development tool. *Journal of the American Chemical Society* **2022,** *144* (8), 3330.

76. Liu, G. L.; Yin, Y.; Kunchakarra, S.; Mukherjee, B.; Gerion, D.; Jett, S. D.; Bear, D. G.; Gray, J. W.; Alivisatos, A. P.; Lee, L. P.; Chen, F. F., A nanoplasmonic molecular ruler for measuring nuclease activity and DNA footprinting. *Nature Nanotechnology* **2006,** *1* (1), 47.

77. Jin, Y.; Gao, X., Plasmonic fluorescent quantum dots. *Nature Nanotechnology* **2009,** *4* (9), 571.

78. Lee, J.; Hernandez, P.; Lee, J.; Govorov, A. O.; Kotov, N. A., Exciton–plasmon interactions in molecular spring assemblies of nanowires and wavelength-based protein detection. *Nature Materials* **2007,** *6* (4), 291.

79. Lee, H.; Sun, E.; Ham, D.; Weissleder, R., Chip–nmr biosensor for detection and molecular analysis of cells. *Nature Medicine* **2008,** *14* (8), 869.

80. Nie, Z.; Fava, D.; Kumacheva, E.; Zou, S.; Walker, G. C.; Rubinstein, M., Self-assembly of metal–polymer analogues of amphiphilic triblock copolymers. *Nature Materials* **2007,** *6* (8), 609.

81. He, J.; Liu, Y.; Babu, T.; Wei, Z.; Nie, Z., Self-assembly of inorganic nanoparticle vesicles and tubules driven by tethered linear block copolymers. *Journal of the American Chemical Society* **2012,** *134* (28), 11342.

82. Sau, T. K.; Murphy, C. J., Self-assembly patterns formed upon solvent evaporation of aqueous cetyltrimethylammonium bromide-coated gold nanoparticles of various shapes. *Langmuir* **2005,** *21* (7), 2923.

83. Durand-Gasselin, C.; Capelot, M.; Sanson, N.; Lequeux, N., Tunable and reversible aggregation of poly(ethylene oxide-st-propylene oxide) grafted gold nanoparticles. *Langmuir* **2010,** *26* (14), 12321.

84. Sardar, R.; Bjorge, N. S.; Shumaker-Parry, J. S., Ph-controlled assemblies of polymeric amine-stabilized gold nanoparticles. *Macromolecules* **2008,** *41* (12), 4347.

85. Guo, Y.; Ma, Y.; Xu, L.; Li, J.; Yang, W., Conformational change induced reversible assembly/disassembly of poly-l-lysine-functionalized gold nanoparticles. *The Journal of Physical Chemistry C* **2007,** *111* (26), 9172.

86. Si, S.; Mandal, T. K., Ph-controlled reversible assembly of peptide-functionalized gold nanoparticles. *Langmuir* **2007,** *23* (1), 190.

87. Watson, J. D.; Crick, F. H., The structure of DNA. *Cold Spring Harb Symp Quant Biol* **1953,** *18*, 123.

88. Caruthers, M. H., Robert letsinger: The father of synthetic DNA chemistry. *Proceedings of the National Academy of Sciences* **2014,** *111* (51), 18098.

89. Reese, C. B., Oligo-and poly-nucleotides: 50 years of chemical synthesis. *Organic & biomolecular chemistry* **2005,** *3* (21), 3851.

90. Alivisatos, A. P.; Johnsson, K. P.; Peng, X.; Wilson, T. E.; Loweth, C. J.; Bruchez, M. P.; Schultz, P. G., Organization of 'nanocrystal molecules' using DNA. *Nature* **1996,** *382* (6592), 609.

91. Mirkin, C. A.; Letsinger, R. L.; Mucic, R. C.; Storhoff, J. J., A DNA-based method for rationally assembling nanoparticles into macroscopic materials. *Nature* **1996,** *382* (6592), 607.

92. Young, K. L.; Ross, M. B.; Blaber, M. G.; Rycenga, M.; Jones, M. R.; Zhang, C.; Senesi, A. J.; Lee, B.; Schatz, G. C.; Mirkin, C. A., Using DNA to design plasmonic metamaterials with tunable optical properties. *Advanced Materials* **2014,** *26* (4), 653.

93. Zhang, C.; Macfarlane, R. J.; Young, K. L.; Choi, C. H. J.; Hao, L.; Auyeung, E.; Liu, G.; Zhou, X.; Mirkin, C. A., A general approach to DNA-programmable atom equivalents. *Nature Materials* **2013,** *12* (8), 741.

94. Banga, R. J.; Meckes, B.; Narayan, S. P.; Sprangers, A. J.; Nguyen, S. T.; Mirkin, C. A., Cross-linked micellar spherical nucleic acids from thermoresponsive templates. *Journal of the American Chemical Society* **2017,** *139* (12), 4278.
95. Banga, R. J.; Chernyak, N.; Narayan, S. P.; Nguyen, S. T.; Mirkin, C. A., Liposomal spherical nucleic acids. *Journal of the American Chemical Society* **2014,** *136* (28), 9866.
96. Brodin, J. D.; Sprangers, A. J.; McMillan, J. R.; Mirkin, C. A., DNA-mediated cellular delivery of functional enzymes. *Journal of the American Chemical Society* **2015,** *137* (47), 14838.
97. Wang, S.; Chen, Y.; Wang, S.; Li, P.; Mirkin, C. A.; Farha, O. K., DNA-functionalized metal–organic framework nanoparticles for intracellular delivery of proteins. *Journal of the American Chemical Society* **2019,** *141* (6), 2215.
98. Banga, R. J.; Krovi, S. A.; Narayan, S. P.; Sprangers, A. J.; Liu, G.; Mirkin, C. A.; Nguyen, S. T., Drug-loaded polymeric spherical nucleic acids: Enhancing colloidal stability and cellular uptake of polymeric nanoparticles through DNA surface-functionalization. *Biomacromolecules* **2017,** *18* (2), 483.
99. Cutler, J. I.; Auyeung, E.; Mirkin, C. A., Spherical nucleic acids. *Journal of the American Chemical Society* **2012,** *134* (3), 1376.
100. Cutler, J. I.; Auyeung, E.; Mirkin, C. A., Spherical nucleic acids. *J Am Chem Soc* **2012,** *134* (3), 1376.
101. Choi, C. H. J.; Hao, L.; Narayan, S. P.; Auyeung, E.; Mirkin, C. A., Mechanism for the endocytosis of spherical nucleic acid nanoparticle conjugates. *Proceedings of the National Academy of Sciences* **2013,** *110* (19), 7625.
102. Seferos, D. S.; Prigodich, A. E.; Giljohann, D. A.; Patel, P. C.; Mirkin, C. A., Polyvalent DNA nanoparticle conjugates stabilize nucleic acids. *Nano Letters* **2009,** *9* (1), 308.
103. Kusmierz, C. D.; Bujold, K. E.; Callmann, C. E.; Mirkin, C. A., Defining the design parameters for in vivo enzyme delivery through protein spherical nucleic acids. *ACS Central Science* **2020,** *6* (5), 815.
104. Jensen, S. A.; Day, E. S.; Ko, C. H.; Hurley, L. A.; Luciano, J. P.; Kouri, F. M.; Merkel, T. J.; Luthi, A. J.; Patel, P. C.; Cutler, J. I.; Daniel, W. L.; Scott, A. W.; Rotz, M. W.; Meade, T. J.; Giljohann, D. A.; Mirkin, C. A.; Stegh, A. H., Spherical nucleic acid nanoparticle conjugates as an rnai-based therapy for glioblastoma. *Science Translational Medicine* **2013,** *5* (209), 209ra152.
105. Yamankurt, G.; Stawicki, R. J.; Posadas, D. M.; Nguyen, J. Q.; Carthew, R. W.; Mirkin, C. A., The effector mechanism of sirna spherical nucleic acids. *Proceedings of the National Academy of Sciences* **2020,** *117* (3), 1312.
106. Radovic-Moreno, A. F.; Chernyak, N.; Mader, C. C.; Nallagatla, S.; Kang, R. S.; Hao, L.; Walker, D. A.; Halo, T. L.; Merkel, T. J.; Rische, C. H.; Anantatmula, S.; Burkhart, M.; Mirkin, C. A.; Gryaznov, S. M., Immunomodulatory spherical nucleic acids. *Proceedings of the National Academy of Sciences* **2015,** *112* (13), 3892.
107. Kapadia, C. H.; Melamed, J. R.; Day, E. S., Spherical nucleic acid nanoparticles: Therapeutic potential. *Biodrugs* **2018,** *32* (4), 297.
108. Wang, S.; Qin, L.; Yamankurt, G.; Skakuj, K.; Huang, Z.; Chen, P.-C.; Dominguez, D.; Lee, A.; Zhang, B.; Mirkin, C. A., Rational vaccinology with spherical nucleic acids. *Proceedings of the National Academy of Sciences* **2019,** *116* (21), 10473.
109. Teplensky, M. H.; Distler, M. E.; Kusmierz, C. D.; Evangelopoulos, M.; Gula, H.; Elli, D.; Tomatsidou, A.; Nicolaescu, V.; Gelarden, I.; Yeldandi, A.; Batlle, D.; Missiakas, D.; Mirkin, C. A., Spherical nucleic acids as an infectious disease vaccine platform. *Proceedings of the National Academy of Sciences* **2022,** *119* (14), e2119093119.
110. Teplensky, M. H.; Dittmar, J. W.; Qin, L.; Wang, S.; Evangelopoulos, M.; Zhang, B.; Mirkin, C. A., Spherical nucleic acid vaccine structure markedly influences adaptive immune responses of clinically utilized prostate cancer targets. *Advanced Healthcare Materials* **2021,** *10* (22), 2101262.
111. Meckes, B.; Banga, R. J.; Nguyen, S. T.; Mirkin, C. A., Enhancing the stability and immunomodulatory activity of liposomal spherical nucleic acids through lipid-tail DNA modifications. *Small* **2018,** *14* (5).
112. Skakuj, K.; Wang, S.; Qin, L.; Lee, A.; Zhang, B.; Mirkin, C. A., Conjugation chemistry-dependent t-cell activation with spherical nucleic acids. *Journal of the American Chemical Society* **2018,** *140* (4), 1227.
113. Wang, Z.-G.; Ding, B., Engineering DNA self-assemblies as templates for functional nanostructures. *Accounts of Chemical Research* **2014,** *47* (6), 1654.
114. Tan, L. H.; Xing, H.; Lu, Y., DNA as a powerful tool for morphology control, spatial positioning, and dynamic assembly of nanoparticles. *Accounts of Chemical Research* **2014,** *47* (6), 1881.
115. Park, S. Y.; Lytton-Jean, A. K. R.; Lee, B.; Weigand, S.; Schatz, G. C.; Mirkin, C. A., DNA-programmable nanoparticle crystallization. *Nature* **2008,** *451* (7178), 553.

116. Nykypanchuk, D.; Maye, M. M.; van der Lelie, D.; Gang, O., DNA-guided crystallization of colloidal nanoparticles. *Nature* **2008,** *451* (7178), 549.

117. Macfarlane, R. J.; Lee, B.; Jones, M. R.; Harris, N.; Schatz, G. C.; Mirkin, C. A., Nanoparticle superlattice engineering with DNA. *Science* **2011,** *334* (6053), 204.

118. Chen, G.; Gibson, K. J.; Liu, D.; Rees, H. C.; Lee, J. H.; Xia, W.; Lin, R.; Xin, H. L.; Gang, O.; Weizmann, Y., Regioselective surface encoding of nanoparticles for programmable self-assembly. *Nat Mater* **2019,** *18* (2), 169.

119. Tikhomirov, G.; Hoogland, S.; Lee, P. E.; Fischer, A.; Sargent, E. H.; Kelley, S. O., DNA-based programming of quantum dot valency, self-assembly and luminescence. *Nat Nanotechnol* **2011,** *6* (8), 485.

120. Chen, B.; Jia, Y.; Gao, Y.; Sanchez, L.; Anthony, S. M.; Yu, Y., Janus particles as artificial antigen-presenting cells for t cell activation. *ACS Applied Materials & Interfaces* **2014,** *6* (21), 18435.

121. Dalal, C.; Jana, N. R., Multivalency effect of tat-peptide-functionalized nanoparticle in cellular endocytosis and subcellular trafficking. *The Journal of Physical Chemistry B* **2017,** *121* (14), 2942.

122. Poon, Z.; Chen, S.; Engler, A. C.; Lee, H. I.; Atas, E.; von Maltzahn, G.; Bhatia, S. N.; Hammond, P. T., Ligand-clustered "patchy" nanoparticles for modulated cellular uptake and in vivo tumor targeting. *Angew Chem Int Ed Engl* **2010,** *49* (40), 7266.

123. McMillan, J. R.; Hayes, O. G.; Winegar, P. H.; Mirkin, C. A., Protein materials engineering with DNA. *Accounts of Chemical Research* **2019,** *52* (7), 1939.

124. Alladin-Mustan, B. S.; Liu, Y.; Li, Y.; de Almeida, D. R. Q.; Yuzik, J.; Mendes, C. F.; Gibbs, J. M., Reverse transcription lesion-induced DNA amplification: An instrument-free isothermal method to detect rna. *Anal Chim Acta* **2021,** *1149*, 238130.

125. Ding, F.; Mou, Q.; Ma, Y.; Pan, G.; Guo, Y.; Tong, G.; Choi, C. H. J.; Zhu, X.; Zhang, C., A crosslinked nucleic acid nanogel for effective sirna delivery and antitumor therapy. *Angew Chem Int Ed* **2018,** *57* (12), 3064.

126. Acar, H.; Ting, J. M.; Srivastava, S.; LaBelle, J. L.; Tirrell, M. V., Molecular engineering solutions for therapeutic peptide delivery. *Chem Soc Rev* **2017,** *46* (21), 6553.

127. Fu, A.; Tang, R.; Hardie, J.; Farkas, M. E.; Rotello, V. M., Promises and pitfalls of intracellular delivery of proteins. *Bioconjugate Chemistry* **2014,** *25* (9), 1602.

128. Patil, S. D.; Rhodes, D. G.; Burgess, D. J., DNA-based therapeutics and DNA delivery systems: A comprehensive review. *The AAPS Journal* **2005,** *7* (1), E61.

129. Pal Singh, P.; Vithalapuram, V.; Metre, S.; Kodipyaka, R., Lipoplex-based therapeutics for effective oligonucleotide delivery: A compendious review. *J Liposome Res* **2020,** *30* (4), 313.

130. Stewart, K. M.; Horton, K. L.; Kelley, S. O., Cell-penetrating peptides as delivery vehicles for biology and medicine. *Org Biomol Chem* **2008,** *6* (13), 2242.

131. Yousif, L. F.; Stewart, K. M.; Horton, K. L.; Kelley, S. O., Mitochondria-penetrating peptides: Sequence effects and model cargo transport. *ChemBioChem* **2009,** *10* (12), 2081.

132. Xu, Z. P.; Zeng, Q. H.; Lu, G. Q.; Yu, A. B., Inorganic nanoparticles as carriers for efficient cellular delivery. *Chem Eng Sci* **2006,** *61* (3), 1027.

133. McMillan, J.; Batrakova, E.; Gendelman, H. E., Cell delivery of therapeutic nanoparticles. *Prog Mol Biol Transl Sci* **2011,** *104*, 563.

134. Wang, D.; Lu, X.; Jia, F.; Tan, X.; Sun, X.; Cao, X.; Wai, F.; Zhang, C.; Zhang, K., Precision tuning of DNA- and poly(ethylene glycol)-based nanoparticles via coassembly for effective antisense gene regulation. *Chemistry of materials : a publication of the American Chemical Society* **2017,** *29* (23), 9882.

135. Kohata, A.; Hashim, P. K.; Okuro, K.; Aida, T., Transferrin-appended nanocaplet for transcellular sirna delivery into deep tissues. *Journal of the American Chemical Society* **2019,** *141* (7), 2862.

136. Dass, C. R., Cytotoxicity issues pertinent to lipoplex-mediated gene therapy in-vivo. *J Pharm Pharmacol* **2002,** *54* (5), 593.

137. Khazanov, E.; Simberg, D.; Barenholz, Y., Lipoplexes prepared from cationic liposomes and mammalian DNA induce cpg-independent, direct cytotoxic effects in cell cultures and in mice. *J Gene Med* **2006,** *8* (8), 998.

138. Kristensen, M.; Birch, D.; Mørck Nielsen, H., Applications and challenges for use of cell-penetrating peptides as delivery vectors for peptide and protein cargos. *Int J Mol Sci* **2016,** *17* (2), 185.

139. Choi, C. H.; Hao, L.; Narayan, S. P.; Auyeung, E.; Mirkin, C. A., Mechanism for the endocytosis of spherical nucleic acid nanoparticle conjugates. *Proc Natl Acad Sci U S A* **2013,** *110* (19), 7625.

140. Banga, R. J.; Chernyak, N.; Narayan, S. P.; Nguyen, S. T.; Mirkin, C. A., Liposomal spherical nucleic acids. *J Am Chem Soc* **2014,** *136* (28), 9866.

141. Banga, R. J.; Meckes, B.; Narayan, S. P.; Sprangers, A. J.; Nguyen, S. T.; Mirkin, C. A., Cross-linked micellar spherical nucleic acids from thermoresponsive templates. *J Am Chem Soc* **2017,** *139* (12), 4278.

142. Brodin, J. D.; Sprangers, A. J.; McMillan, J. R.; Mirkin, C. A., DNA-mediated cellular delivery of functional enzymes. *J Am Chem Soc* **2015,** *137* (47), 14838.

143. Jensen, S. A.; Day, E. S.; Ko, C. H.; Hurley, L. A.; Luciano, J. P.; Kouri, F. M.; Merkel, T. J.; Luthi, A. J.; Patel, P. C.; Cutler, J. I.; Daniel, W. L.; Scott, A. W.; Rotz, M. W.; Meade, T. J.; Giljohann, D. A.; Mirkin, C. A.; Stegh, A. H., Spherical nucleic acid nanoparticle conjugates as an rnai-based therapy for glioblastoma. *Science Translational Medicine* **2013,** *5* (209), 209ra152.

144. Yamankurt, G.; Stawicki, R. J.; Posadas, D. M.; Nguyen, J. Q.; Carthew, R. W.; Mirkin, C. A., The effector mechanism of sirna spherical nucleic acids. *Proceedings of the National Academy of Sciences* **2020,** *117* (3), 1312.

145. Radovic-Moreno, A. F.; Chernyak, N.; Mader, C. C.; Nallagatla, S.; Kang, R. S.; Hao, L.; Walker, D. A.; Halo, T. L.; Merkel, T. J.; Rische, C. H.; Anantatmula, S.; Burkhart, M.; Mirkin, C. A.; Gryaznov, S. M., Immunomodulatory spherical nucleic acids. *Proceedings of the National Academy of Sciences* **2015,** *112* (13), 3892.

146. Li, Y.; Tseng, Y. D.; Kwon, S. Y.; d'Espaux, L.; Bunch, J. S.; McEuen, P. L.; Luo, D., Controlled assembly of dendrimer-like DNA. *Nature materials* **2004,** *3* (1), 38.

147. Evanko, D., Hybridization chain reaction. *Nat Methods* **2004,** *1* (3), 186.

148. Qu, Y.; Yang, J.; Zhan, P.; Liu, S.; Zhang, K.; Jiang, Q.; Li, C.; Ding, B., Self-assembled DNA dendrimer nanoparticle for efficient delivery of immunostimulatory cpg motifs. *ACS Appl Mater Interfaces* **2017,** *9* (24), 20324.

149. Zhao, Y.; Hu, S.; Wang, H.; Yu, K.; Guan, Y.; Liu, X.; Li, N.; Liu, F., DNA dendrimer-streptavidin nanocomplex: An efficient signal amplifier for construction of biosensing platforms. *Anal Chem* **2017,** *89* (12), 6907.

150. Li, Y.; Tseng, Y. D.; Kwon, S. Y.; D'Espaux, L.; Bunch, J. S.; McEuen, P. L.; Luo, D., Controlled assembly of dendrimer-like DNA. *Nat Mater* **2004,** *3* (1), 38.

151. Shchepinov, M. S.; Udalova, I. A.; Bridgman, A. J.; Southern, E. M., Oligonucleotide dendrimers: Synthesis and use as polylabelled DNA probes. *Nucleic Acids Res* **1997,** *25* (22), 4447.

152. Meng, H.-M.; Zhang, X.; Lv, Y.; Zhao, Z.; Wang, N.-N.; Fu, T.; Fan, H.; Liang, H.; Qiu, L.; Zhu, G.; Tan, W., DNA dendrimer: An efficient nanocarrier of functional nucleic acids for intracellular molecular sensing. *ACS Nano* **2014,** *8* (6), 6171.

153. Caruthers, M. H., The chemical synthesis of DNA/rna: Our gift to science. *J Biol Chem* **2013,** *288* (2), 1420.

154. Bruno, B. J.; Miller, G. D.; Lim, C. S., Basics and recent advances in peptide and protein drug delivery. *Ther Deliv* **2013,** *4* (11), 1443.

155. Kukutsch, N. A.; Roßner, S.; Austyn, J. M.; Schuler, G.; Lutz, M. B., Formation and kinetics of mhc class i-ovalbumin peptide complexes on immature and mature murine dendritic cells. *J Invest Dermatol* **2000,** *115* (3), 449.

156. Falo, L. D.; Kovacsovics-Bankowski, M.; Thompson, K.; Rock, K. L., Targeting antigen into the phagocytic pathway in vivo induces protective tumour immunity. *Nat Med* **1995,** *1* (7), 649.

157. Fifis, T.; Gamvrellis, A.; Crimeen-Irwin, B.; Pietersz, G. A.; Li, J.; Mottram, P. L.; McKenzie, I. F. C.; Plebanski, M., Size-dependent immunogenicity: Therapeutic and protective properties of nano-vaccines against tumors. *The Journal of Immunology* **2004,** *173* (5), 3148.

158. Kovacsovics-Bankowski, M.; Clark, K.; Benacerraf, B.; Rock, K. L., Efficient major histocompatibility complex class i presentation of exogenous antigen upon phagocytosis by macrophages. *Proceedings of the National Academy of Sciences* **1993,** *90* (11), 4942.

159. Reddy, S. T.; Rehor, A.; Schmoekel, H. G.; Hubbell, J. A.; Swartz, M. A., In vivo targeting of dendritic cells in lymph nodes with poly(propylene sulfide) nanoparticles. *Journal of Controlled Release* **2006,** *112* (1), 26.

160. Tran, K. K.; Shen, H., The role of phagosomal ph on the size-dependent efficiency of cross-presentation by dendritic cells. *Biomaterials* **2009,** *30* (7), 1356.

161. Wang, S.; Qin, L.; Yamankurt, G.; Skakuj, K.; Huang, Z.; Chen, P.-C.; Dominguez, D.; Lee, A.; Zhang, B.; Mirkin, C. A., Rational vaccinology with spherical nucleic acids. *Proceedings of the National Academy of Sciences* **2019,** *116* (21), 10473.

162. Radovic-Moreno, A. F.; Chernyak, N.; Mader, C. C.; Nallagatla, S.; Kang, R. S.; Hao, L.; Walker, D. A.; Halo, T. L.; Merkel, T. J.; Rische, C. H.; Anantatmula, S.; Burkhart, M.; Mirkin, C. A.; Gryaznov, S. M., Immunomodulatory spherical nucleic acids. *Proc Natl Acad Sci U S A* **2015,** *112* (13), 3892.

163. King, C., Thymosin apha 1–a peptide immune modulator with a broad range of clinical applications. *Clinical & Experimental Pharmacology* **2013,** *03*.

164. Wu, X.; Jia, J.; You, H., Thymosin alpha-1 treatment in chronic hepatitis b. *Expert Opin Biol Ther* **2015,** *15* (sup1), 129.

165. Li, J.; Liu, C. H.; Wang, F. S., Thymosin alpha 1: Biological activities, applications and genetic engineering production. *Peptides* **2010,** *31* (11), 2151.

166. Sherman, K. E., Thymosin α 1 for treatment of hepatitis c virus: Promise and proof. *Annals of the New York Academy of Sciences* **2010,** *1194* (1), 136.

167. Chadwick, D.; Pido-Lopez, J.; Pires, A.; Imami, N.; Gotch, F.; Villacian, J. S.; Ravindran, S.; Paton, N. I., A pilot study of the safety and efficacy of thymosin alpha 1 in augmenting immune reconstitution in hiv-infected patients with low cd4 counts taking highly active antiretroviral therapy. *Clinical and experimental immunology* **2003,** *134* (3), 477.

168. Matteucci, C.; Grelli, S.; Balestrieri, E.; Minutolo, A.; Argaw-Denboba, A.; Macchi, B.; Sinibaldi-Vallebona, P.; Perno, C. F.; Mastino, A.; Garaci, E., Thymosin alpha 1 and hiv-1: Recent advances and future perspectives. *Future Microbiology* **2017,** *12* (2), 141.

169. Costantini, C.; Bellet, M. M.; Pariano, M.; Renga, G.; Stincardini, C.; Goldstein, A. L.; Garaci, E.; Romani, L., A reappraisal of thymosin alpha1 in cancer therapy. *Frontiers in oncology* **2019,** *9*, 873.

170. Wu, M.; Ji, J.-J.; Zhong, L.; Shao, Z.-Y.; Xie, Q.-F.; Liu, Z.-Y.; Wang, C.-L.; Su, L.; Feng, Y.-W.; Liu, Z.-F.; Yao, Y.-M., Thymosin α1 therapy in critically ill patients with covid-19: A multicenter retrospective cohort study. *International immunopharmacology* **2020,** *88*, 106873.

171. Liu, Y.; Pan, Y.; Hu, Z.; Wu, M.; Wang, C.; Feng, Z.; Mao, C.; Tan, Y.; Liu, Y.; Chen, L.; Li, M.; Wang, G.; Yuan, Z.; Diao, B.; Wu, Y.; Chen, Y., Thymosin alpha 1 reduces the mortality of severe coronavirus disease 2019 by restoration of lymphocytopenia and reversion of exhausted t cells. *Clinical Infectious Diseases* **2020,** *71* (16), 2150.

172. Ancell, C. D.; Phipps, J.; Young, L., Thymosin alpha-1. *American Journal of Health-System Pharmacy* **2001,** *58* (10), 879.

173. King, R.; Tuthill, C., Chapter seven - immune modulation with thymosin alpha 1 treatment. In *Vitamins and hormones*, Litwack, G., Ed. Academic Press: 2016; Vol. 102, pp 151.

174. Hirano, T.; Kishimoto, T., Interleukin-6. In *Peptide growth factors and their receptors i*, Sporn, M. B.; Roberts, A. B., Eds. Springer Berlin Heidelberg: Berlin, Heidelberg, 1990; pp 633.

175. Chu, W.-M., Tumor necrosis factor. *Cancer Lett* **2013,** *328* (2), 222.

176. Ashley, C. E.; Carnes, E. C.; Phillips, G. K.; Padilla, D.; Durfee, P. N.; Brown, P. A.; Hanna, T. N.; Liu, J.; Phillips, B.; Carter, M. B., The targeted delivery of multicomponent cargos to cancer cells by nanoporous particle-supported lipid bilayers. *Nature materials* **2011,** *10* (5), 389.

177. Coulie, P. G.; Van den Eynde, B. J.; Van Der Bruggen, P.; Boon, T., Tumour antigens recognized by t lymphocytes: At the core of cancer immunotherapy. *Nature Reviews Cancer* **2014,** *14* (2), 135.

178. Irvine, D. J.; Swartz, M. A.; Szeto, G. L., Engineering synthetic vaccines using cues from natural immunity. *Nature materials* **2013,** *12* (11), 978.

179. Khalil, D. N.; Smith, E. L.; Brentjens, R. J.; Wolchok, J. D., The future of cancer treatment: Immunomodulation, cars and combination immunotherapy. *Nature reviews Clinical oncology* **2016,** *13* (5), 273.

180. Zhang, L.; Gu, F.; Chan, J.; Wang, A.; Langer, R.; Farokhzad, O., Nanoparticles in medicine: Therapeutic applications and developments. *Clin Pharmacol Ther* **2008,** *83* (5), 761.

181. Zhang, Y.; Lin, S.; Wang, X.-Y.; Zhu, G., Nanovaccines for cancer immunotherapy. *WIREs Nanomedicine and Nanobiotechnology* **2019,** *11* (5), e1559.

182. Zhu, G.; Zhang, F.; Ni, Q.; Niu, G.; Chen, X., Efficient nanovaccine delivery in cancer immunotherapy. *ACS Nano* **2017,** *11* (3), 2387.

183. Couvreur, P., Nanoparticles in drug delivery: Past, present and future. *Adv Drug Del Rev* **2013,** *65* (1), 21.

184. Kemp, J. A.; Shim, M. S.; Heo, C. Y.; Kwon, Y. J., "Combo" nanomedicine: Co-delivery of multi-modal therapeutics for efficient, targeted, and safe cancer therapy. *Adv Drug Del Rev* **2016,** *98*, 3.

185. Wong, K. K.; Li, W. A.; Mooney, D. J.; Dranoff, G., Advances in therapeutic cancer vaccines. *Adv Immunol* **2016,** *130*, 191.

186. Anselmo, A. C.; Mitragotri, S., Nanoparticles in the clinic: An update post covid-19 vaccines. *Bioengineering & translational medicine* **2021,** *6* (3), e10246.

187. Sallam, M. A.; Prakash, S.; Kumbhojkar, N.; Shields IV, C. W.; Mitragotri, S., Formulation-based approaches for dermal delivery of vaccines and therapeutic nucleic acids: Recent advances and future perspectives. *Bioengineering & Translational Medicine* **2021,** *6* (3), e10215.

188. Sahdev, P.; Ochyl, L. J.; Moon, J. J., Biomaterials for nanoparticle vaccine delivery systems. *Pharm Res* **2014,** *31* (10), 2563.

189. Gu, L.; Mooney, D. J., Biomaterials and emerging anticancer therapeutics: Engineering the microenvironment. *Nature Reviews Cancer* **2016,** *16* (1), 56.

190. Koshy, S. T.; Mooney, D. J., Biomaterials for enhancing anti-cancer immunity. *Curr Opin Biotechnol* **2016,** *40*, 1.

191. Tzeng, A.; Kauke, M. J.; Zhu, E. F.; Moynihan, K. D.; Opel, C. F.; Yang, N. J.; Mehta, N.; Kelly, R. L.; Szeto, G. L.; Overwijk, W. W., Temporally programmed cd8α+ dc activation enhances combination cancer immunotherapy. *Cell Rep* **2016,** *17* (10), 2503.

192. Rincon-Restrepo, M.; Mayer, A.; Hauert, S.; Bonner, D. K.; Phelps, E. A.; Hubbell, J. A.; Swartz, M. A.; Hirosue, S., Vaccine nanocarriers: Coupling intracellular pathways and cellular biodistribution to control cd4 vs cd8 t cell responses. *Biomaterials* **2017,** *132*, 48.

193. Irvine, D. J.; Aung, A.; Silva, M., Controlling timing and location in vaccines. *Adv Drug Del Rev* **2020,** *158*, 91.

194. Mehta, N. K.; Pradhan, R. V.; Soleimany, A. P.; Moynihan, K. D.; Rothschilds, A. M.; Momin, N.; Rakhra, K.; Mata-Fink, J.; Bhatia, S. N.; Wittrup, K. D., Pharmacokinetic tuning of protein–antigen fusions enhances the immunogenicity of t-cell vaccines. *Nature biomedical engineering* **2020,** *4* (6), 636.

195. Radovic-Moreno, A. F.; Chernyak, N.; Mader, C. C.; Nallagatla, S.; Kang, R. S.; Hao, L.; Walker, D. A.; Halo, T. L.; Merkel, T. J.; Rische, C. H., Immunomodulatory spherical nucleic acids. *Proceedings of the National Academy of Sciences* **2015,** *112* (13), 3892.

196. Meckes, B.; Banga, R. J.; Nguyen, S. T.; Mirkin, C. A., Enhancing the stability and immunomodulatory activity of liposomal spherical nucleic acids through lipid-tail DNA modifications. *Small* **2018,** *14* (5), 1702909.

197. Liu, H.; Irvine, D. J., Guiding principles in the design of molecular bioconjugates for vaccine applications. *Bioconjugate chemistry* **2015,** *26* (5), 791.

198. Distler, M. E.; Teplensky, M. H.; Bujold, K. E.; Kusmierz, C. D.; Evangelopoulos, M.; Mirkin, C. A., DNA dendrons as agents for intracellular delivery. *Journal of the American Chemical Society* **2021,** *143* (34), 13513.

199. Cheng, H. F.; Distler, M. E.; Lee, B.; Zhou, W.; Weigand, S.; Mirkin, C. A., Nanoparticle superlattices through template-encoded DNA dendrimers. *Journal of the American Chemical Society* **2021,** *143* (41), 17170.

200. Reed, S. G.; Bertholet, S.; Coler, R. N.; Friede, M., New horizons in adjuvants for vaccine development. *Trends Immunol* **2009,** *30* (1), 23.

201. Kawamoto, Y.; Liu, W.; Yum, J. H.; Park, S.; Sugiyama, H.; Takahashi, Y.; Takakura, Y., Enhanced immunostimulatory activity of covalent DNA dendrons. *ChemBioChem* **2022,** *23* (4), e202100583.

202. Lanier, L. L.; O'Fallon, S.; Somoza, C.; Phillips, J. H.; Linsley, P. S.; Okumura, K.; Ito, D.; Azuma, M., Cd80 (b7) and cd86 (b70) provide similar costimulatory signals for t cell proliferation, cytokine production, and generation of ctl. *The Journal of Immunology* **1995,** *154* (1), 97.

203. Comberlato, A.; Koga, M. M.; Nüssing, S.; Parish, I. A.; Bastings, M. M. C., Spatially controlled activation of toll-like receptor 9 with DNA-based nanomaterials. *Nano Lett* **2022,** *22* (6), 2506.

204. Chowell, D.; Krishna, S.; Becker, P. D.; Cocita, C.; Shu, J.; Tan, X.; Greenberg, P. D.; Klavinskis, L. S.; Blattman, J. N.; Anderson, K. S., Tcr contact residue hydrophobicity is a hallmark of immunogenic cd8+ t cell epitopes. *Proceedings of the National Academy of Sciences* **2015,** *112* (14), E1754.

205. Fröhlich, E., The role of surface charge in cellular uptake and cytotoxicity of medical nanoparticles. *International journal of nanomedicine* **2012,** *7*, 5577.

206. Sainte-Marie, G., The lymph node revisited: Development, morphology, functioning, and role in triggering primary immune responses. *The Anatomical Record* **2010,** *293* (2), 320.

207. Ali Khan, A.; Mudassir, J.; Mohtar, N.; Darwis, Y., Advanced drug delivery to the lymphatic system: Lipid-based nanoformulations. *Int J Nanomedicine* **2013,** *8*, 2733.

208. Hawley, A. E.; Davis, S. S.; Illum, L., Targeting of colloids to lymph nodes: Influence of lymphatic physiology and colloidal characteristics. *Adv Drug Del Rev* **1995,** *17* (1), 129.

209. Liu, J.; Wong, H.-L.; Moselhy, J.; Bowen, B.; Wu, X. Y.; Johnston, M. R., Targeting colloidal particulates to thoracic lymph nodes. *Lung Cancer* **2006,** *51* (3), 377.

210. Excler, J.-L.; Saville, M.; Berkley, S.; Kim, J. H., Vaccine development for emerging infectious diseases. *Nat Med* **2021,** *27* (4), 591.

211. Marston, H. D.; Folkers, G. K.; Morens, D. M.; Fauci, A. S., Emerging viral diseases: Confronting threats with new technologies. *Sci Transl Med* **2014,** *6* (253), 253ps10.

212. Morens, D. M.; Fauci, A. S., Emerging infectious diseases: Threats to human health and global stability. *PLoS pathogens* **2013,** *9* (7), e1003467.
213. Dolgin, E., How protein-based covid vaccines could change the pandemic. *Nature* **2021,** *599* (7885), 359.
214. Wong, S. S.; Webby, R. J., Traditional and new influenza vaccines. *Clin Microbiol Rev* **2013,** *26* (3), 476.
215. Tregoning, J. S.; Russell, R. F.; Kinnear, E., Adjuvanted influenza vaccines. *Hum Vaccin Immunother* **2018,** *14* (3), 550.
216. Wei, C.-J.; Crank, M. C.; Shiver, J.; Graham, B. S.; Mascola, J. R.; Nabel, G. J., Next-generation influenza vaccines: Opportunities and challenges. *Nature Reviews Drug Discovery* **2020,** *19* (4), 239.
217. Kanekiyo, M.; Wei, C.-J.; Yassine, H. M.; McTamney, P. M.; Boyington, J. C.; Whittle, J. R. R.; Rao, S. S.; Kong, W.-P.; Wang, L.; Nabel, G. J., Self-assembling influenza nanoparticle vaccines elicit broadly neutralizing h1n1 antibodies. *Nature* **2013,** *499* (7456), 102.
218. Yamankurt, G.; Berns, E. J.; Xue, A.; Lee, A.; Bagheri, N.; Mrksich, M.; Mirkin, C. A., Exploration of the nanomedicine-design space with high-throughput screening and machine learning. *Nature biomedical engineering* **2019,** *3* (4), 318.
219. Qin, L.; Wang, S.; Dominguez, D.; Long, A.; Chen, S.; Fan, J.; Ahn, J.; Skakuj, K.; Huang, Z.; Lee, A.; Mirkin, C.; Zhang, B., Development of spherical nucleic acids for prostate cancer immunotherapy. *Front Immunol* **2020,** *11*, 1333.
220. Mirkin, C. A.; Letsinger, R. L.; Mucic, R. C.; Storhoff, J. J., A DNA-based method for rationally assembling nanoparticles into macroscopic materials. *Nature* **1996,** *382* (6592), 607.
221. Callmann, C. E.; Cole, L. E.; Kusmierz, C. D.; Huang, Z.; Horiuchi, D.; Mirkin, C. A., Tumor cell lysate-loaded immunostimulatory spherical nucleic acids as therapeutics for triple-negative breast cancer. *Proceedings of the National Academy of Sciences of the United States of America* **2020,** *117* (30), 17543.
222. Palm, A.-K. E.; Henry, C., Remembrance of things past: Long-term b cell memory after infection and vaccination. *Frontiers in immunology* **2019,** *10*, 1787.
223. Siegrist, C.-A., Chapter 2 - vaccine immunology. In *Vaccines (fifth edition)*, Plotkin, S. A.; Orenstein, W. A.; Offit, P. A., Eds. W.B. Saunders: Edinburgh, 2008; pp 17.
224. Chapter 14 - b cell memory and plasma cell development. In *Molecular biology of b cells (second edition)*, Alt, F. W.; Honjo, T.; Radbruch, A.; Reth, M., Eds. Academic Press: London, 2015; pp 227.
225. Agematsu, K.; Nagumo, H.; Yang, F.-C.; Nakazawa, T.; Fukushima, K.; Ito, S.; Sugita, K.; Mori, T.; Kobata, T.; Morimoto, C.; Komiyama, A., B cell subpopulations separated by cd27 and crucial collaboration of cd27+ b cells and helper t cells in immunoglobulin production. *Eur J Immunol* **1997,** *27* (8), 2073.
226. Arens, R.; Nolte, M. A.; Tesselaar, K.; Heemskerk, B.; Reedquist, K. A.; van Lier, R. A. W.; van Oers, M. H. J., Signaling through cd70 regulates b cell activation and igg production. *The Journal of Immunology* **2004,** *173* (6), 3901.
227. Ezan, E., Pharmacokinetic studies of protein drugs: Past, present and future. *Adv Drug Deliv Rev* **2013,** *65* (8), 1065.
228. Lau, E. H.; Tsang, O. T.; Hui, D. S.; Kwan, M. Y.; Chan, W.-h.; Chiu, S. S.; Ko, R. L.; Chan, K. H.; Cheng, S.; Perera, R. A., Neutralizing antibody titres in sars-cov-2 infections. *Nature communications* **2021,** *12* (1), 1.
229. Garçon, N.; Di Pasquale, A., From discovery to licensure, the adjuvant system story. *Hum Vaccin Immunother* **2017,** *13* (1), 19.
230. Reed, S. G.; Orr, M. T.; Fox, C. B., Key roles of adjuvants in modern vaccines. *Nat Med* **2013,** *19* (12), 1597.
231. Sarkar, I.; Garg, R.; van Drunen Littel-van den Hurk, S., Selection of adjuvants for vaccines targeting specific pathogens. *Expert review of vaccines* **2019,** *18* (5), 505.
232. CDC Adjuvants and vaccines. https://www.cdc.gov/vaccinesafety/concerns/adjuvants.html.
233. Meckes, B.; Banga, R. J.; Nguyen, S. T.; Mirkin, C. A., Enhancing the stability and immunomodulatory activity of liposomal spherical nucleic acids through lipid-tail DNA modifications. *Small* **2018,** *14* (5), 1702909.
234. Callmann, C. E.; Kusmierz, C. D.; Dittmar, J. W.; Broger, L.; Mirkin, C. A., Impact of liposomal spherical nucleic acid structure on immunotherapeutic function. *ACS Central Science* **2021,** *7* (5), 892.
235. CDC Sars-cov-2 variant classifications and definitions. https://www.cdc.gov/coronavirus/2019-ncov/variants/variant-info.html.
236. Lundgren, D. H.; Hwang, S. I.; Wu, L.; Han, D. K., Role of spectral counting in quantitative proteomics. *Expert Rev Proteomics* **2010,** *7* (1), 39.

237. Schroeder, H. W., Jr.; Cavacini, L., Structure and function of immunoglobulins. *J Allergy Clin Immunol* **2010,** *125* (2 Suppl 2), S41.
238. The UniProt, C., Uniprot: The universal protein knowledgebase in 2021. *Nucleic Acids Res* **2021,** *49* (D1), D480.
239. Barros-Martins, J.; Hammerschmidt, S. I.; Cossmann, A.; Odak, I.; Stankov, M. V.; Morillas Ramos, G.; Dopfer-Jablonka, A.; Heidemann, A.; Ritter, C.; Friedrichsen, M.; Schultze-Florey, C.; Ravens, I.; Willenzon, S.; Bubke, A.; Ristenpart, J.; Janssen, A.; Ssebyatika, G.; Bernhardt, G.; Münch, J.; Hoffmann, M.; Pöhlmann, S.; Krey, T.; Bošnjak, B.; Förster, R.; Behrens, G. M. N., Immune responses against sars-cov-2 variants after heterologous and homologous chadox1 ncov-19/bnt162b2 vaccination. *Nat Med* **2021**.
240. McCray, P. B., Jr.; Pewe, L.; Wohlford-Lenane, C.; Hickey, M.; Manzel, L.; Shi, L.; Netland, J.; Jia, H. P.; Halabi, C.; Sigmund, C. D.; Meyerholz, D. K.; Kirby, P.; Look, D. C.; Perlman, S., Lethal infection of k18-hace2 mice infected with severe acute respiratory syndrome coronavirus. *J Virol* **2007,** *81* (2), 813.
241. Hassler, L.; Wysocki, J.; Gelarden, I.; Tomatsidou, A.; Gula, H.; Nicoleascu, V.; Randall, G.; Henkin, J.; Yeldandi, A.; Batlle, D., A novel soluble ace2 protein totally protects from lethal disease caused by sars-cov-2 infection. *bioRxiv* **2021**, 2021.03.12.435191.
242. Zheng, J.; Wong, L.-Y. R.; Li, K.; Verma, A. K.; Ortiz, M. E.; Wohlford-Lenane, C.; Leidinger, M. R.; Knudson, C. M.; Meyerholz, D. K.; McCray, P. B., Jr.; Perlman, S., Covid-19 treatments and pathogenesis including anosmia in k18-hace2 mice. *Nature* **2021,** *589* (7843), 603.
243. Winkler, E. S.; Bailey, A. L.; Kafai, N. M.; Nair, S.; McCune, B. T.; Yu, J.; Fox, J. M.; Chen, R. E.; Earnest, J. T.; Keeler, S. P.; Ritter, J. H.; Kang, L.-I.; Dort, S.; Robichaud, A.; Head, R.; Holtzman, M. J.; Diamond, M. S., Sars-cov-2 infection of human ace2-transgenic mice causes severe lung inflammation and impaired function. *Nat Immunol* **2020,** *21* (11), 1327.
244. Golden, J. W.; Cline, C. R.; Zeng, X.; Garrison, A. R.; Carey, B. D.; Mucker, E. M.; White, L. E.; Shamblin, J. D.; Brocato, R. L.; Liu, J.; Babka, A. M.; Rauch, H. B.; Smith, J. M.; Hollidge, B. S.; Fitzpatrick, C.; Badger, C. V.; Hooper, J. W., Human angiotensin-converting enzyme 2 transgenic mice infected with sars-cov-2 develop severe and fatal respiratory disease. *JCI Insight* **2020,** *5* (19).
245. Silvas Jesus, A.; Vasquez Desarey, M.; Park, J.-G.; Chiem, K.; Allué-Guardia, A.; Garcia-Vilanova, A.; Platt Roy, N.; Miorin, L.; Kehrer, T.; Cupic, A.; Gonzalez-Reiche Ana, S.; Bakel Harm, v.; García-Sastre, A.; Anderson, T.; Torrelles Jordi, B.; Ye, C.; Martinez-Sobrido, L.; Parrish Colin, R., Contribution of sars-cov-2 accessory proteins to viral pathogenicity in k18 human ace2 transgenic mice. *J Virol 95* (17), e00402.
246. Moreau, G. B.; Burgess, S. L.; Sturek, J. M.; Donlan, A. N.; Petri, W. A.; Mann, B. J., Evaluation of k18-hace2 mice as a model of sars-cov-2 infection. *Am J Trop Med Hyg* **2020,** *103* (3), 1215.
247. Wang, J.; Li, Q.; Yin, Y.; Zhang, Y.; Cao, Y.; Lin, X.; Huang, L.; Hoffmann, D.; Lu, M.; Qiu, Y., Excessive neutrophils and neutrophil extracellular traps in covid-19. *Front Immunol* **2020,** *11* (2063).
248. Matsen, M. W.; Bates, F. S., Origins of complex self-assembly in block copolymers. *Macromolecules* **1996,** *29* (23), 7641.
249. Lee, S.; Bluemle, M. J.; Bates, F. S., Discovery of a frank-kasper σ phase in sphere-forming block copolymer melts. *Science* **2010,** *330* (6002), 349.
250. Lee, S.; Leighton, C.; Bates, F. S., Sphericity and symmetry breaking in the formation of frank-kasper phases from one component materials. *Proc. Natl. Acad. Sci. U. S. A.* **2014,** *111* (50), 17723.
251. Peterca, M.; Percec, V., Recasting metal alloy phases with block copolymers. *Science* **2010,** *330* (6002), 333.
252. Balagurusamy, V. S. K.; Ungar, G.; Percec, V.; Johansson, G., Rational design of the first spherical supramolecular dendrimers self-organized in a novel thermotropic cubic liquid-crystalline phase and the determination of their shape by x-ray analysis. *J. Am. Chem. Soc.* **1997,** *119* (7), 1539.
253. Ungar, G.; Liu, Y.; Zeng, X.; Percec, V.; Cho, W.-D., Giant supramolecular liquid crystal lattice. *Science* **2003,** *299* (5610), 1208.
254. Rosen, B. M.; Wilson, C. J.; Wilson, D. A.; Peterca, M.; Imam, M. R.; Percec, V., Dendron-mediated self-assembly, disassembly, and self-organization of complex systems. *Chem. Rev.* **2009,** *109* (11), 6275.
255. Sun, H.-J.; Zhang, S.; Percec, V., From structure to function via complex supramolecular dendrimer systems. *Chem. Soc. Rev.* **2015,** *44* (12), 3900.
256. Yu, X.-F.; Zhong, S.; Li, X.-P.; Tu, Y.-F.; Yang, S.-G.; Van Horn, R. M.; Ni, C.-Y.; Pochan, D. J.; Quirk, R. P.; Wesdemiotis, C.; Zhang, W.-B.; Cheng, S. Z. D., A giant surfactant of polystyrene-(carboxylic acid-functionalized polyhedral oligomeric silsesquioxane) amphiphile with highly stretched polystyrene tails in micellar assemblies. *J. Am. Chem. Soc.* **2010,** *132* (47), 16741.

257. Huang, M.; Hsu, C.-H.; Wang, J.; Mei, S.; Dong, X.; Li, Y.; Li, M.; Liu, H.; Zhang, W.; Aida, T.; Zhang, W.-B.; Yue, K.; Cheng, S. Z. D., Selective assemblies of giant tetrahedra via precisely controlled positional interactions. *Science* **2015,** *348* (6233), 424.

258. Yue, K.; Huang, M.; Marson, R. L.; He, J.; Huang, J.; Zhou, Z.; Wang, J.; Liu, C.; Yan, X.; Wu, K.; Guo, Z.; Liu, H.; Zhang, W.; Ni, P.; Wesdemiotis, C.; Zhang, W.-B.; Glotzer, S. C.; Cheng, S. Z. D., Geometry induced sequence of nanoscale frank-kasper and quasicrystal mesophases in giant surfactants. *Proc. Natl. Acad. Sci. U. S. A.* **2016,** *113* (50), 14195.

259. Su, Z.; Hsu, C.-H.; Gong, Z.; Feng, X.; Huang, J.; Zhang, R.; Wang, Y.; Mao, J.; Wesdemiotis, C.; Li, T.; Seifert, S.; Zhang, W.; Aida, T.; Huang, M.; Cheng, S. Z. D., Identification of a frank-kasper z phase from shape amphiphile self-assembly. *Nat. Chem.* **2019,** *11* (10), 899.

260. Shenhar, R.; Norsten, T. B.; Rotello, V. M., Polymer-mediated nanoparticle assembly: Structural control and applications. *Adv. Mater.* **2005,** *17* (6), 657.

261. Wang, Y.; Desroches, G. J.; Macfarlane, R. J., Ordered polymer composite materials: Challenges and opportunities. *Nanoscale* **2021,** *13* (2), 426.

262. Macfarlane, R. J.; O'Brien, M. N.; Petrosko, S. H.; Mirkin, C. A., Nucleic acid-modified nanostructures as programmable atom equivalents: Forging a new "table of elements". *Angew. Chem., Int. Ed.* **2013,** *52* (22), 5688.

263. Nilsen, T. W.; Grayzel, J.; Prensky, W., Dendritic nucleic acid structures. *J. Theor. Biol.* **1997,** *187* (2), 273.

264. Li, Y.; Tseng, Y. D.; Kwon, S. Y.; d'Espaux, L.; Bunch, J. S.; McEuen, P. L.; Luo, D., Controlled assembly of dendrimer-like DNA. *Nat Mater* **2004,** *3* (1), 38.

265. Li, Y.; Cu, Y. T. H.; Luo, D., Multiplexed detection of pathogen DNA with DNA-based fluorescence nanobarcodes. *Nat. Biotechnol.* **2005,** *23* (7), 885.

266. Lee, J. B.; Roh, Y. H.; Um, S. H.; Funabashi, H.; Cheng, W.; Cha, J. J.; Kiatwuthinon, P.; Muller, D. A.; Luo, D., Multifunctional nanoarchitectures from DNA-based abc monomers. *Nat. Nanotechnol.* **2009,** *4* (7), 430.

267. Rattanakiat, S.; Nishikawa, M.; Funabashi, H.; Luo, D.; Takakura, Y., The assembly of a short linear natural cytosine-phosphate-guanine DNA into dendritic structures and its effect on immunostimulatory activity. *Biomaterials* **2009,** *30* (29), 5701.

268. Lu, J.; Hu, P.; Cao, L.; Wei, Z.; Xiao, F.; Chen, Z.; Li, Y.; Tian, L., Genetically encoded and biologically produced all-DNA nanomedicine based on one-pot assembly of DNA dendrimers for targeted gene regulation. *Angew. Chem., Int. Ed.* **2021,** *60* (10), 5377.

269. Thaner, R. V.; Eryazici, I.; Farha, O. K.; Mirkin, C. A.; Nguyen, S. B. T., Facile one-step solid-phase synthesis of multi-topic organic-DNA hybrids via "click" chemistry. *Chem. Sci.* **2014,** *5* (3), 1091.

270. Cheng, H. F.; Wang, S.; Mirkin, C. A., Electron-equivalent valency through molecularly well-defined multivalent DNA. *J. Am. Chem. Soc.* **2021,** *143* (4), 1752.

271. Shchepinov, M. S.; Mir, K. U.; Elder, J. K.; Frank-Kamenetskii, M. D.; Southern, E. M., Oligonucleotide dendrimers: Stable nano-structures. *Nucleic Acids Res.* **1999,** *27* (15), 3035.

272. Distler, M. E.; Teplensky, M. H.; Bujold, K. E.; Kusmierz, C. D.; Evangelopoulos, M.; Mirkin, C. A., DNA dendrons as agents for intracellular delivery. *J. Am. Chem. Soc.* **2021,** *143* (34), 13513.

273. Li, T.; Senesi, A. J.; Lee, B., Small angle x-ray scattering for nanoparticle research. *Chem. Rev.* **2016,** *116* (18), 11128.

274. Auyeung, E.; Macfarlane, R. J.; Choi, C. H. J.; Cutler, J. I.; Mirkin, C. A., Transitioning DNA-engineered nanoparticle superlattices from solution to the solid state. *Adv. Mater.* **2012,** *24* (38), 5181.

275. Auyeung, E.; Cutler, J. I.; Macfarlane, R. J.; Jones, M. R.; Wu, J.; Liu, G.; Zhang, K.; Osberg, K. D.; Mirkin, C. A., Synthetically programmable nanoparticle superlattices using a hollow three-dimensional spacer approach. *Nat. Nanotechnol.* **2012,** *7* (1), 24.

276. Girard, M.; Du, J. S.; Huang, Z.; Dravid, V. P.; Mirkin, C. A.; Olvera, d. l. C. M.; Girard, M.; Olvera, d. l. C. M.; Girard, M.; Wang, S.; Du, J. S.; Das, A.; Huang, Z.; Dravid, V. P.; Mirkin, C. A.; Olvera, d. l. C. M.; Wang, S.; Das, A.; Mirkin, C. A.; Olvera, d. l. C. M.; Lee, B., Particle analogs of electrons in colloidal crystals. *Science* **2019,** *364* (6446), 1174.

277. Whetten, R. L.; Shafigullin, M. N.; Khoury, J. T.; Schaaff, T. G.; Vezmar, I.; Alvarez, M. M.; Wilkinson, A., Crystal structures of molecular gold nanocrystal arrays. *Acc. Chem. Res.* **1999,** *32* (5), 397.

278. Wang, M. X.; Brodin, J. D.; Millan, J. A.; Seo, S. E.; Girard, M.; Olvera de la Cruz, M.; Lee, B.; Mirkin, C. A., Altering DNA-programmable colloidal crystallization paths by modulating particle repulsion. *Nano Lett.* **2017,** *17* (8), 5126.

279. Emerson, M. F.; Holtzer, A., On the ionic strength dependence of micelle number. Ii. *J. Phys. Chem.* **1967,** *71* (6), 1898.

280. Hayashi, S.; Ikeda, S., Micelle size and shape of sodium dodecyl sulfate in concentrated sodium chloride solutions. *J. Phys. Chem.* **1980,** *84* (7), 744.

281. Stellner, K. L.; Scamehorn, J. F., Hardness tolerance of anionic surfactant solutions. 1. Anionic surfactant with added monovalent electrolyte. *Langmuir* **1989,** *5* (1), 70.

282. Kim, S. A.; Jeong, K.-J.; Yethiraj, A.; Mahanthappa, M. K., Low-symmetry sphere packings of simple surfactant micelles induced by ionic sphericity. *Proc. Natl. Acad. Sci. U. S. A.* **2017,** *114* (16), 4072.

283. Zhang, D. Y.; Seelig, G., Dynamic DNA nanotechnology using strand-displacement reactions. *Nat. Chem.* **2011,** *3* (2), 103.

284. Zhang, Y.; Pal, S.; Srinivasan, B.; Vo, T.; Kumar, S.; Gang, O., Selective transformations between nanoparticle superlattices via the reprogramming of DNA-mediated interactions. *Nat. Mater.* **2015,** *14* (8), 840.

285. Kim, Y.; Macfarlane, R. J.; Jones, M. R.; Mirkin, C. A., Transmutable nanoparticles with reconfigurable surface ligands. *Science* **2016,** *351* (6273), 579.

286. Zhu, J.; Kim, Y.; Lin, H.; Wang, S.; Mirkin, C. A., Ph-responsive nanoparticle superlattices with tunable DNA bonds. *J. Am. Chem. Soc.* **2018,** *140* (15), 5061.

287. Oh, J. S.; Yi, G.-R.; Pine, D. J., Reconfigurable self-assembly and kinetic control of multiprogrammed DNA-coated particles. *ACS Nano* **2020,** *14* (4), 4595.

288. Zhou, X.; Yao, D.; Hua, W.; Huang, N.; Chen, X.; Li, L.; He, M.; Zhang, Y.; Guo, Y.; Xiao, S.; Bian, F.; Liang, H., Programming colloidal bonding using DNA strand-displacement circuitry. *Proc. Natl. Acad. Sci. U. S. A.* **2020,** *117* (11), 5617.

289. Gillespie, R., The valence-shell electron-pair repulsion (vsepr) theory of directed valency. *J Chem Educ* **1963,** *40* (6), 295.

290. Lewis, G. N., The atom and the molecule. *Journal of the American Chemical Society* **1916,** *38* (4), 762.

291. Pauling, L. *The nature of the chemical bond: And the structure of molecules and crystals; an introduction to modern structural chemistry*; 1940.

292. Kalsin, A. M.; Fialkowski, M.; Paszewski, M.; Smoukov, S. K.; Bishop, K. J.; Grzybowski, B. A., Electrostatic self-assembly of binary nanoparticle crystals with a diamond-like lattice. *Science* **2006,** *312* (5772), 420.

293. Shevchenko, E. V.; Talapin, D. V.; Kotov, N. A.; O'Brien, S.; Murray, C. B., Structural diversity in binary nanoparticle superlattices. *Nature* **2006,** *439* (7072), 55.

294. Boles, M. A.; Engel, M.; Talapin, D. V., Self-assembly of colloidal nanocrystals: From intricate structures to functional materials. *Chem Rev* **2016,** *116* (18), 11220.

295. Glotzer, S. C.; Solomon, M. J., Anisotropy of building blocks and their assembly into complex structures. *Nature materials* **2007,** *6* (8), 557.

296. Damasceno, P. F.; Engel, M.; Glotzer, S. C., Predictive self-assembly of polyhedra into complex structures. *Science* **2012,** *337* (6093), 453.

297. Wang, Y.; Wang, Y.; Breed, D. R.; Manoharan, V. N.; Feng, L.; Hollingsworth, A. D.; Weck, M.; Pine, D. J., Colloids with valence and specific directional bonding. *Nature* **2012,** *491* (7422), 51.

298. Huang, M.; Hsu, C.-H.; Wang, J.; Mei, S.; Dong, X.; Li, Y.; Li, M.; Liu, H.; Zhang, W.; Aida, T., Selective assemblies of giant tetrahedra via precisely controlled positional interactions. *Science* **2015,** *348* (6233), 424.

299. Liu, W.; Tagawa, M.; Xin, H. L.; Wang, T.; Emamy, H.; Li, H.; Yager, K. G.; Starr, F. W.; Tkachenko, A. V.; Gang, O., Diamond family of nanoparticle superlattices. *Science* **2016,** *351* (6273), 582.

300. Lin, H.; Lee, S.; Sun, L.; Spellings, M.; Engel, M.; Glotzer, S. C.; Mirkin, C. A., Clathrate colloidal crystals. *Science* **2017,** *355* (6328), 931.

301. Yi, C.; Liu, H.; Zhang, S.; Yang, Y.; Zhang, Y.; Lu, Z.; Kumacheva, E.; Nie, Z., Self-limiting directional nanoparticle bonding governed by reaction stoichiometry. *Science* **2020,** *369* (6509), 1369.

302. He, M.; Gales, J. P.; Ducrot, É.; Gong, Z.; Yi, G.-R.; Sacanna, S.; Pine, D. J., Colloidal diamond. *Nature* **2020,** *585* (7826), 524.

303. O'Brien, M. N.; Jones, M. R.; Lee, B.; Mirkin, C. A., Anisotropic nanoparticle complementarity in DNA-mediated co-crystallization. *Nature Materials* **2015,** *14* (8), 833.

304. Laramy, C. R.; Lopez-Rios, H.; O'Brien, M. N.; Girard, M.; Stawicki, R. J.; Lee, B.; de la Cruz, M. O.; Mirkin, C. A., Controlled symmetry breaking in colloidal crystal engineering with DNA. *ACS Nano* **2019,** *13* (2), 1412.

305. Wang, S.; Lee, S.; Du, J. S.; Partridge, B. E.; Cheng, H. F.; Zhou, W.; Dravid, V. P.; Lee, B.; Glotzer, S. C.; Mirkin, C. A., The emergence of valency in colloidal crystals through electron equivalents. *Nature Materials* **2022,** *21* (5), 580.

306. Girard, M.; Wang, S.; Du, J. S.; Das, A.; Huang, Z.; Dravid, V. P.; Lee, B.; Mirkin, C. A.; Olvera de la Cruz, M., Particle analogs of electrons in colloidal crystals. *Science* **2019,** *364* (6446), 1174.

307. Balagurusamy, V.; Ungar, G.; Percec, V.; Johansson, G., Rational design of the first spherical supramolecular dendrimers self-organized in a novel thermotropic cubic liquid-crystalline phase and the determination of their shape by x-ray analysis. *Journal of the American Chemical Society* **1997,** *119* (7), 1539.

308. Peterca, M.; Percec, V., Materials science. Recasting metal alloy phases with block copolymers. *Science* **2010,** *330* (6002), 333.

309. Nilsen, T. W.; Grayzel, J.; Prensky, W., Dendritic nucleic acid structures. *J Theor Biol* **1997,** *187* (2), 273.

310. Lee, J. B.; Roh, Y. H.; Um, S. H.; Funabashi, H.; Cheng, W.; Cha, J. J.; Kiatwuthinon, P.; Muller, D. A.; Luo, D., Multifunctional nanoarchitectures from DNA-based abc monomers. *Nature nanotechnology* **2009,** *4* (7), 430.

311. Lu, J.; Hu, P.; Cao, L.; Wei, Z.; Xiao, F.; Chen, Z.; Li, Y.; Tian, L., Genetically encoded and biologically produced all-DNA nanomedicine based on one-pot assembly of DNA dendrimers for targeted gene regulation. *Angew Chem* **2021,** *133* (10), 5437.

312. Auyeung, E.; Macfarlane, R. J.; Choi, C. H. J.; Cutler, J. I.; Mirkin, C. A., Transitioning DNA-engineered nanoparticle superlattices from solution to the solid state. *Adv Mater* **2012,** *24* (38), 5181.

313. Cheng, H. F.; Wang, S.; Mirkin, C. A., Electron-equivalent valency through molecularly well-defined multivalent DNA. *Journal of the American Chemical Society* **2021,** *143* (4), 1752.

314. Das, S.; Mondal, A.; Reddy, C. M., Harnessing molecular rotations in plastic crystals: A holistic view for crystal engineering of adaptive soft materials. *Chem Soc Rev* **2020,** *49* (24), 8878.

315. Kim, S. A.; Jeong, K.-J.; Yethiraj, A.; Mahanthappa, M. K., Low-symmetry sphere packings of simple surfactant micelles induced by ionic sphericity. *Proceedings of the National Academy of Sciences* **2017,** *114* (16), 4072.

316. Brodin, J. D.; Auyeung, E.; Mirkin, C. A., DNA-mediated engineering of multicomponent enzyme crystals. *Proc Natl Acad Sci U S A* **2015,** *112* (15), 4564.

317. Lee, J.-S.; Lytton-Jean, A. K. R.; Hurst, S. J.; Mirkin, C. A., Silver nanoparticle−oligonucleotide conjugates based on DNA with triple cyclic disulfide moieties. *Nano Lett* **2007,** *7* (7), 2112.

318. Macfarlane, R. J.; Jones, M. R.; Lee, B.; Auyeung, E.; Mirkin, C. A., Topotactic interconversion of nanoparticle superlattices. *Science* **2013,** *341* (6151), 1222.

APPENDICES

Appendix 1: DNA Dendrons as Agents for Intracellular Delivery (chapter one)

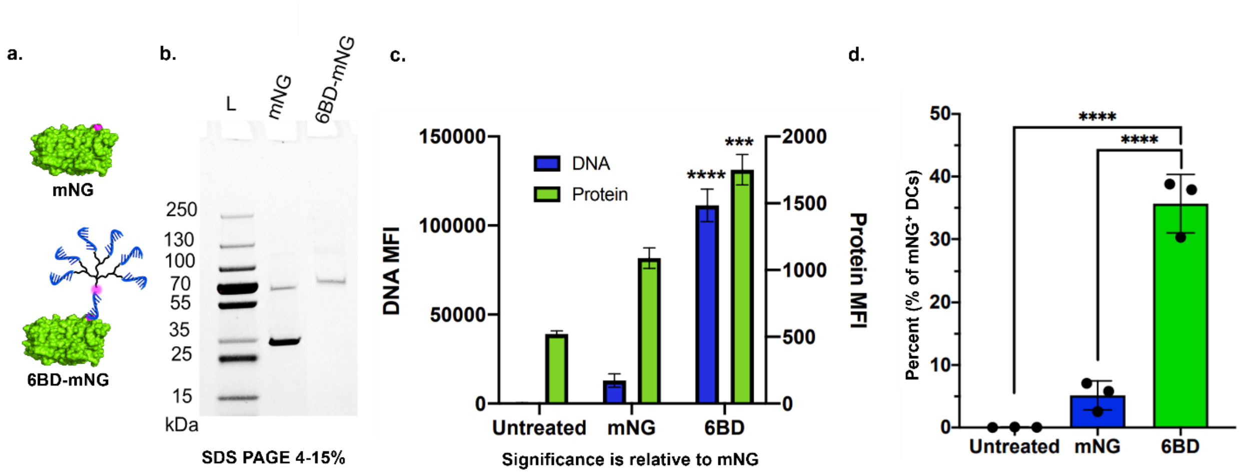

Figure A1.1. A single DNA dendron used for protein delivery
(a,b) A single DNA dendron was conjugated to the single surface cysteine on the fluorescent protein mNG and characterized by PAGE. (C,D) The single DNA dendron is able facilitate cellular uptake of the protein cargo as evidenced by the fluorescence intensity of cells treated with mNG and the percent of cells positive for mNG. DCs were treated at 250 nM for 1 h. This data demonstrates how the dendron can be used as a potentially universal tag for the cellular delivery of nanoscale materials.

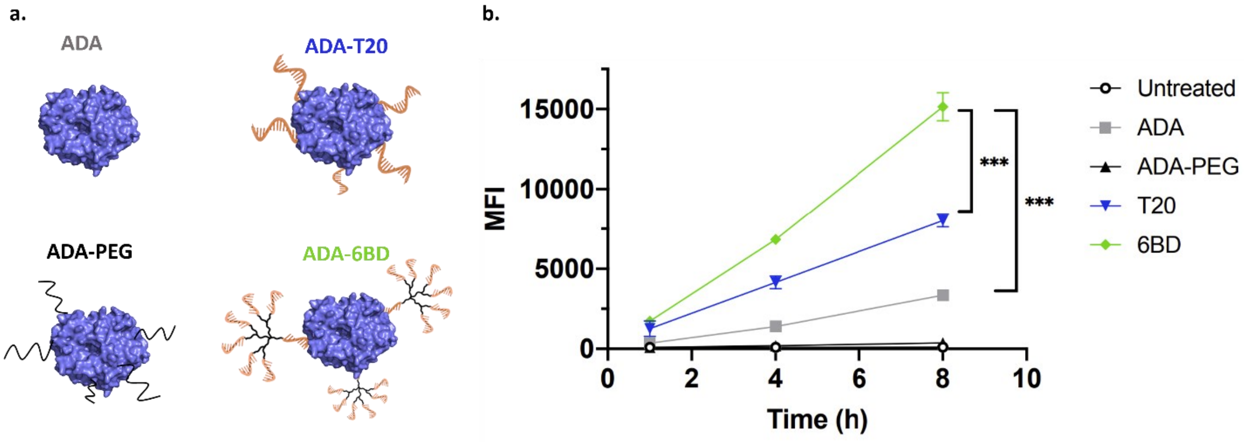

Figure A1.2. DNA dendrons to maximize DNA loading on proteins
(a) Four DNA dendrons were designed from the clinically relevant adenosine deaminase (ADA) protein: unfunctionalized ADA, PEGylated ADA (clinical formulation), ADA protein SNA, and ADA dendron SNA. (b) Cellular uptake, over multiple timepoints, indicates that the DNA dendron functionalized ADA is capable of significantly more efficient cellular uptake than the typical ProSNA design and the current clinical formulation (PEGylated form).

Appendix 2: Nanoparticle Superlattices Through Template-Encoded DNA Dendrimers (chapter 5)

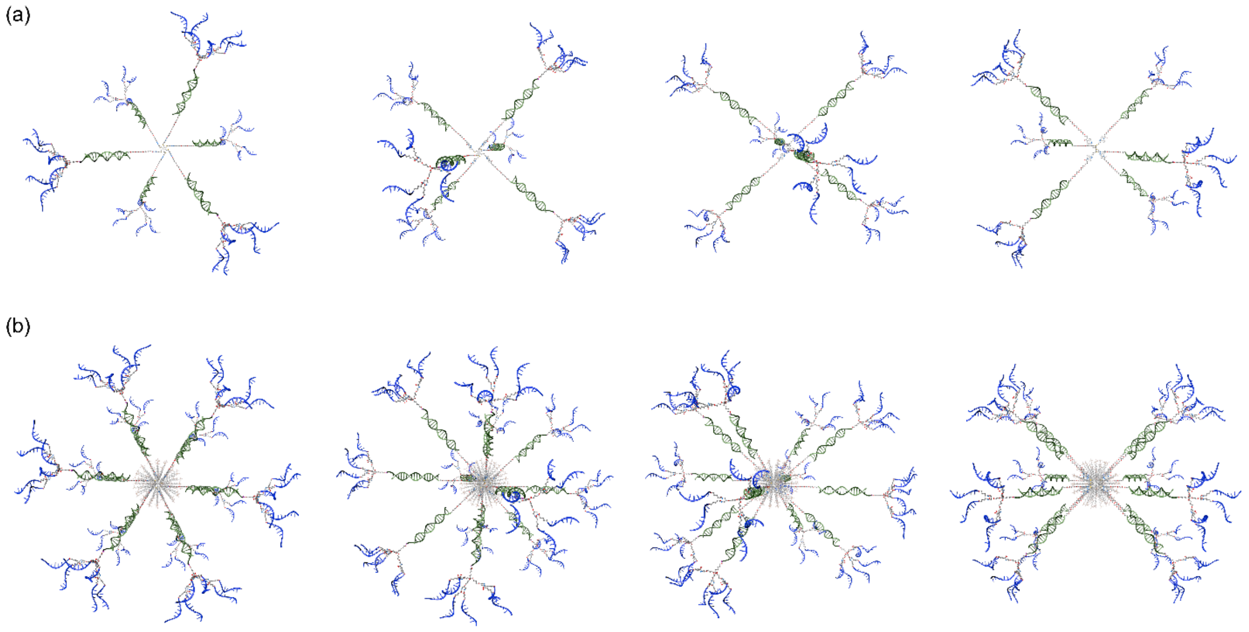

Figure A2.1. 3D models of DNA dendrimers
(a) 3D models of a DNA dendrimer (a six-arm templated combined with six copies of six-branch dendrons), rotated by a 30° interval from left to right. (b) 3D models of a DNA micelle-dendrimer made up of two DNA dendrimers and a SDS micelle, rotated by a 30° interval from left to right. The SDS micelles and the DNA dendrimers were drawn to scale. Models were created using Cinema 4DTM.

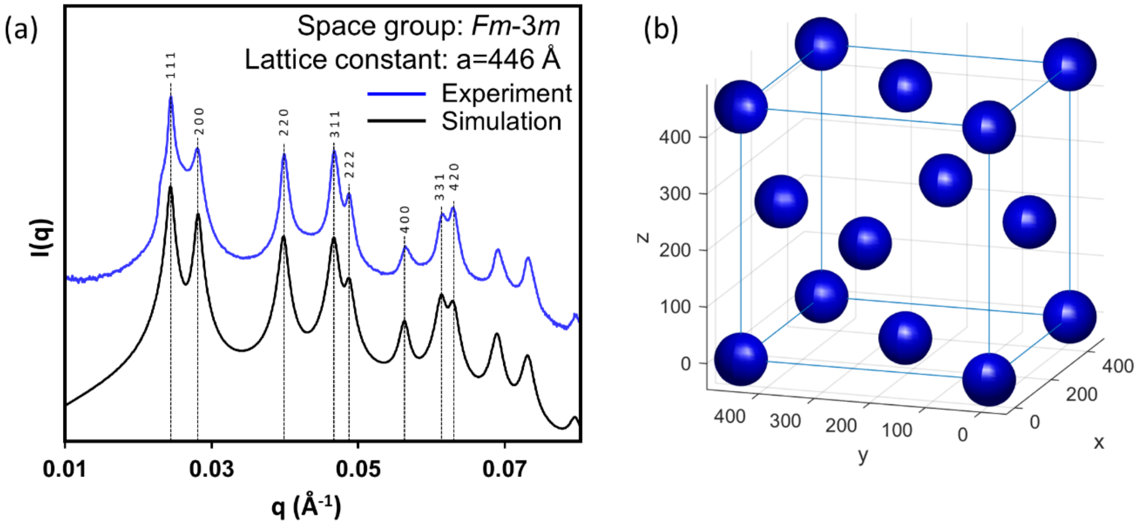

Figure A2.2. SAXS characterization – face centered cubic (FCC)
(a) Azimuthally averaged 1D SAXS spectra of a representative FCC phase (blue: experiment, black: simulation). The first eight scattering peaks and their corresponding Miller indices (*hkl*) are labeled (black dashed lines). (b) Structural model of AuNP sublattice in FCC phase symmetry used to generate the simulated spectrum.

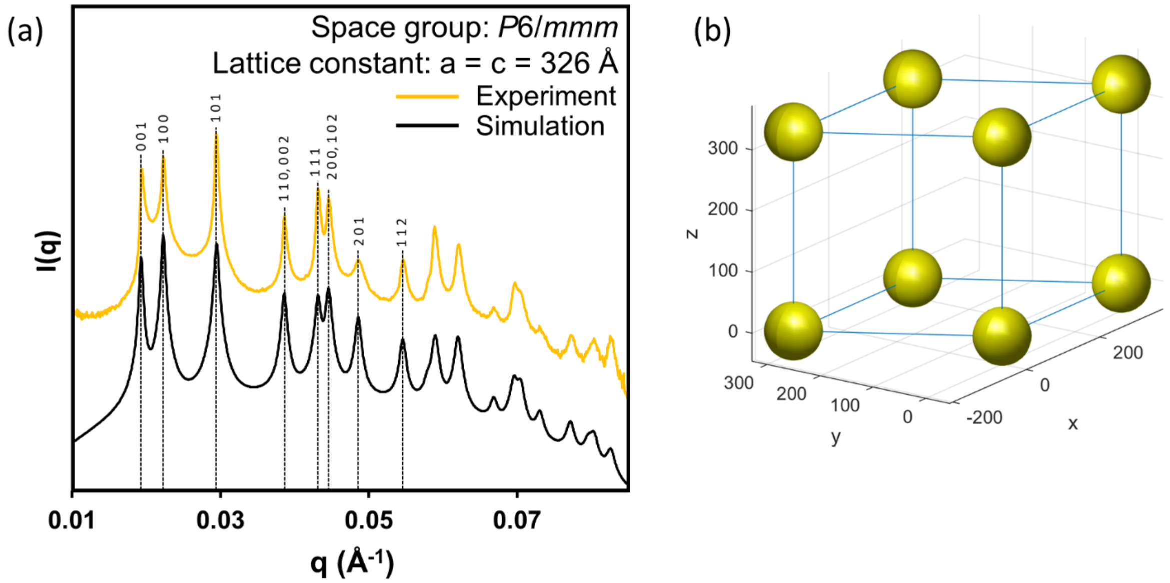

Figure A2.3. SAXS characterization – simple hexagonal (SH)
(a) Azimuthally averaged 1D SAXS spectra of a representative SH phase (yellow: experiment, black: simulation). first eight scattering peaks and their corresponding Miller indices (hkl) are labeled (black dashed lines). (b) The structural model of the AuNP sublattice in SH phase symmetry used to generate the simulated spectrum.

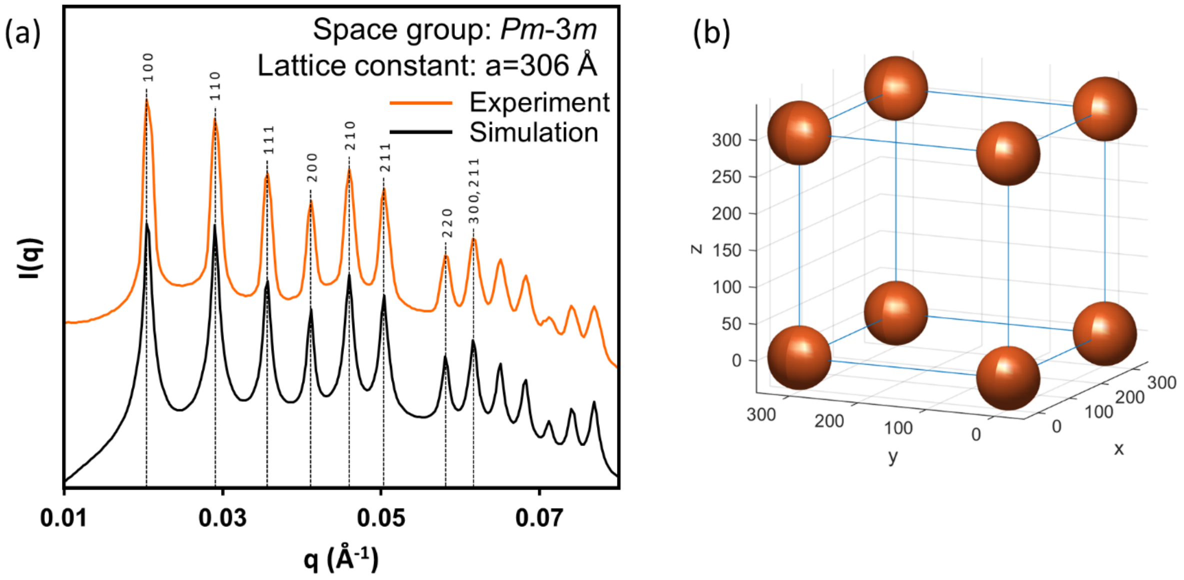

Figure A2.4. SAXS characterization – Simple cubic (SC)
(a) Azimuthally averaged 1D SAXS spectra of a representative FCC phase (blue: experiment, black: simulation). The first eight scattering peaks and their corresponding Miller indices (hkl) are labeled (black dashed lines). (b) Structural model of AuNP sublattice in FCC phase symmetry used to generate the simulated spectrum.

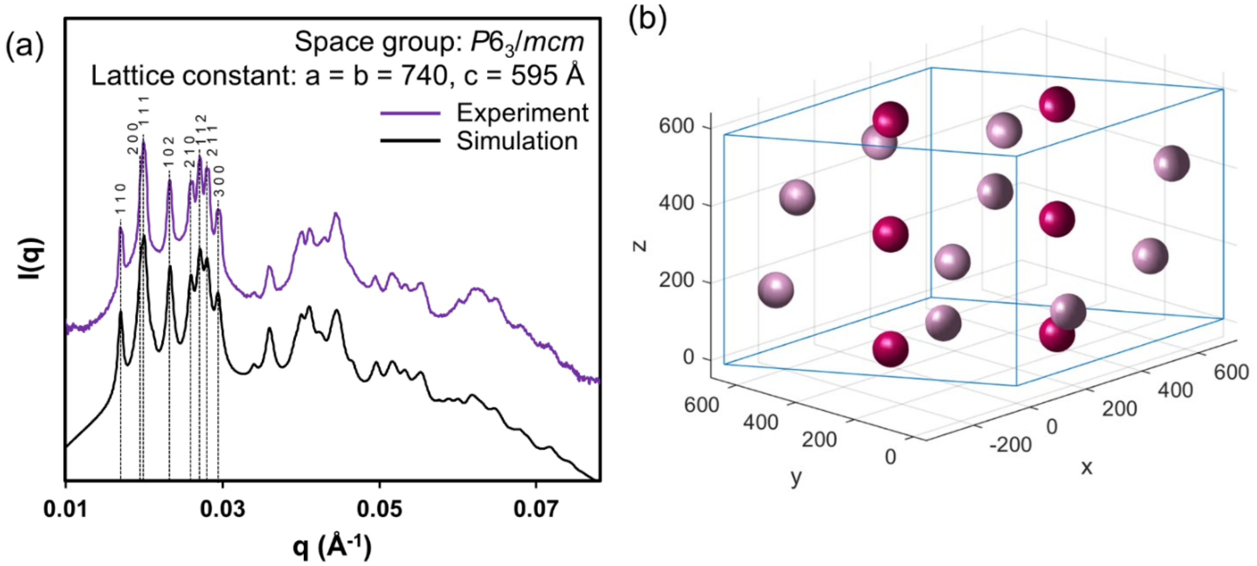

Figure A2.5. SAXS characterization – Ti_5Ga_4-type phase
(a) Azimuthally averaged 1D SAXS spectra of a representative Ti5Ga4-type phase (purple: experiment, black: simulation). The first eight scattering peaks and their corresponding Miller indices (hkl) are labeled (black dashed lines). (b) The structural model of the AuNP sublattice in Ti5Ga4-type phase symmetry used to generate the simulated spectrum.

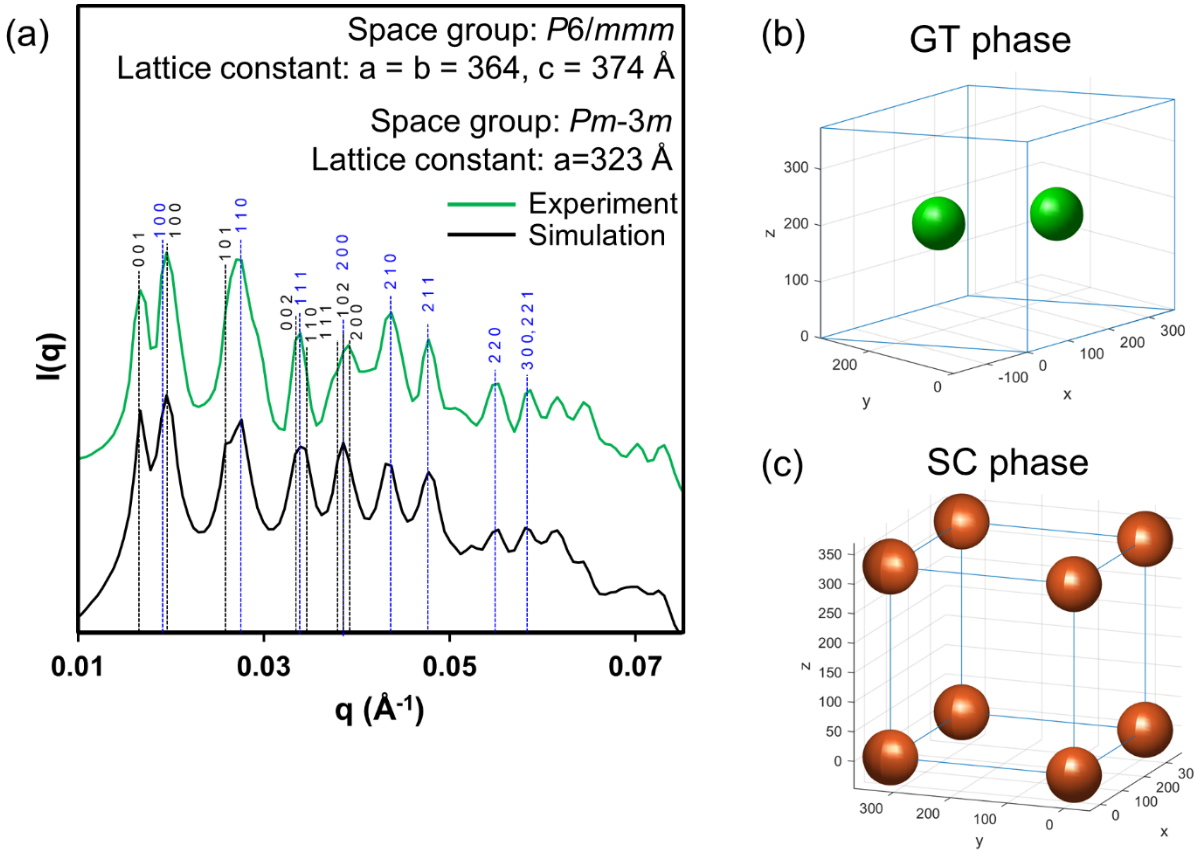

Figure A2.6. SAXS characterization – graphite-type (GT) and simple cubic (SC)
(a) Azimuthally averaged 1D SAXS spectra of a representative mixture of GT and SC phases (green: experiment, black: simulation of GT phase). For each phase, the first eight scattering peaks and their corresponding Miller indices (hkl) are labeled (black dashed lines for GT phase and blue dashed lines for SC phase). The structural models of the AuNP sublattice in (b) GT and (c) SC phase symmetries used to generate the simulated spectrum.

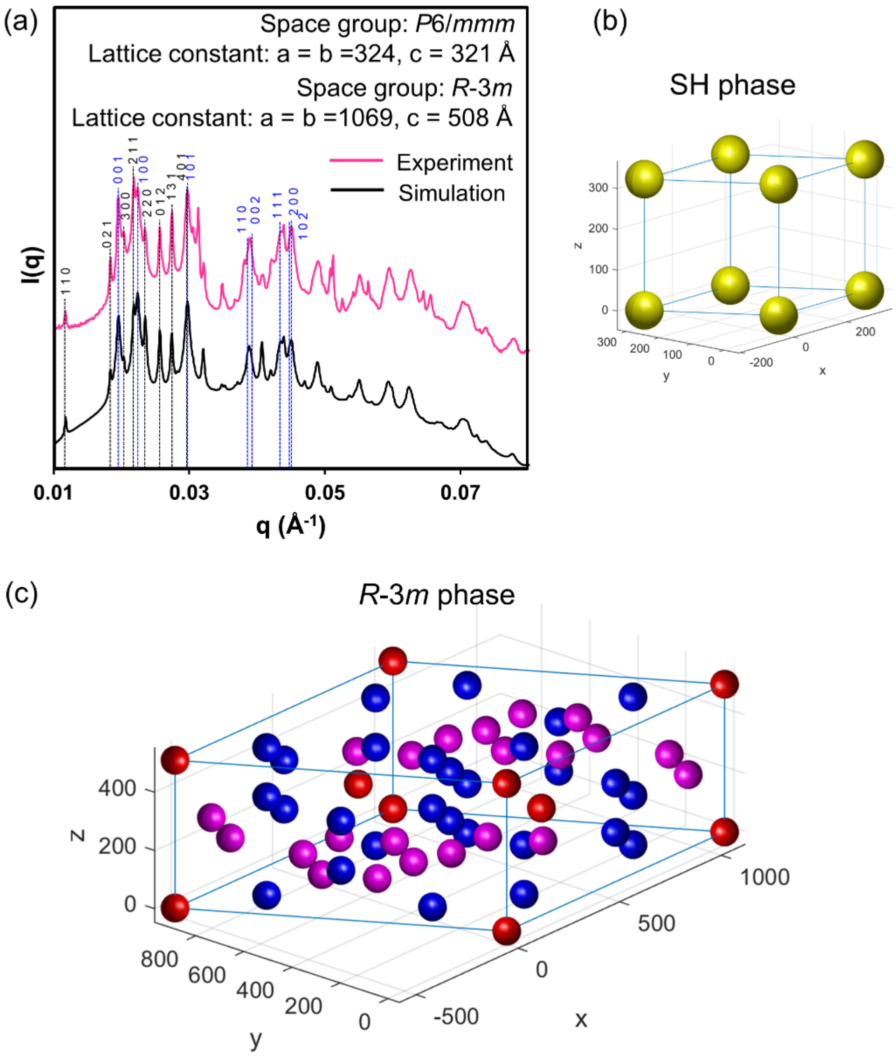

Figure A2.7. SAXS characterization – partially disordered R-3m phase

(a) Azimuthally averaged 1D SAXS spectra of a representative mixture of a SH phase and a partially disordered R-3m phase (pink: experiment, black: simulation). The first eight scattering peaks and their corresponding Miller indices (hkl) are labeled (black dashed lines for SH phase and blue dashed lines for partially disordered R-3m phase). The structural models of the AuNP sublattice in (b) SH and (c) partially disordered R-3m phase symmetries used to generate the simulated spectrum. All AuNP positions (including partially occupied ones) are depicted in the latter image..

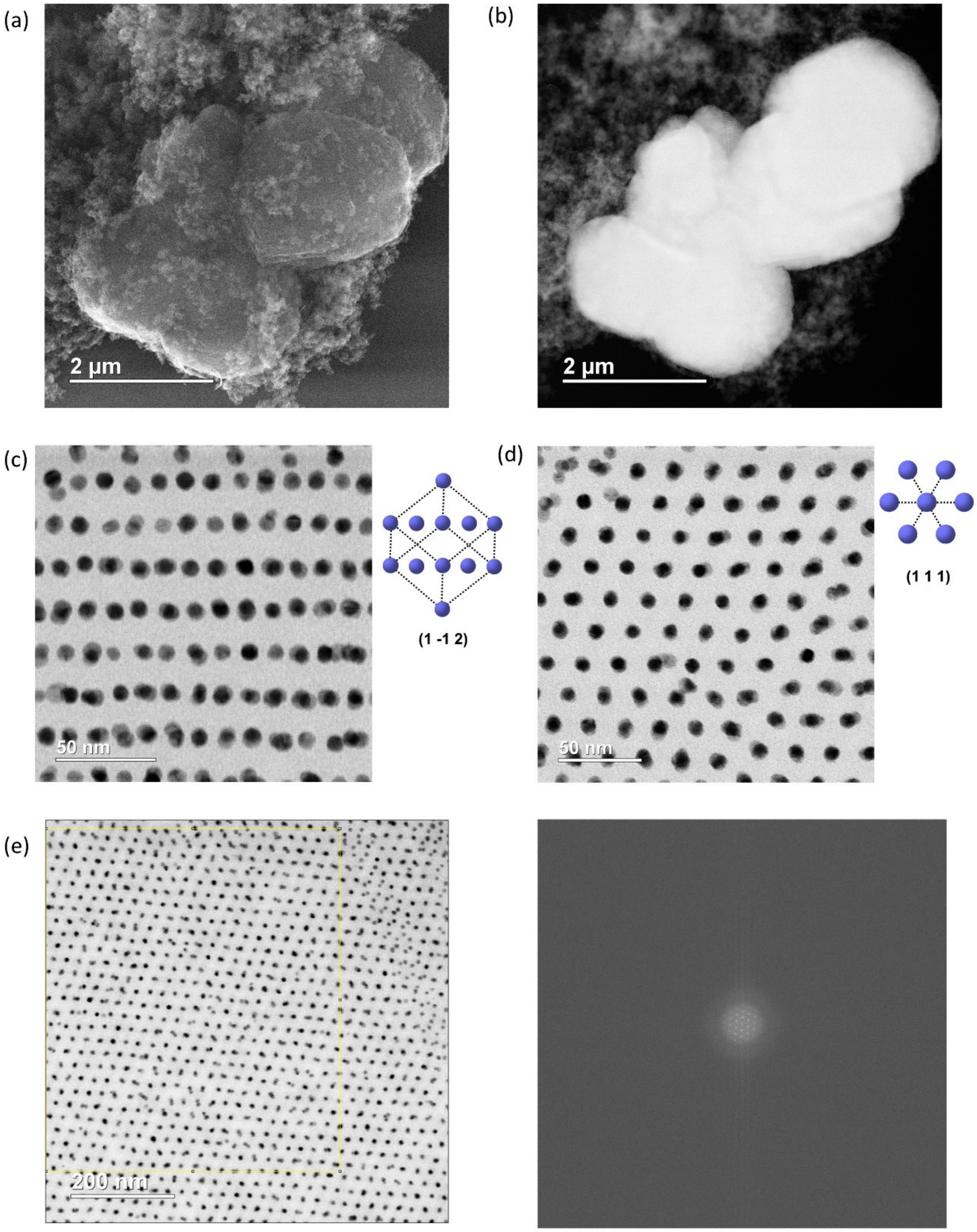

Figure A2.8. STEM characterization – face centered cubic (FCC)
(a) Representative SE-STEM and (b) ADF-STEM images of FCC phase crystals after silica encapsulation. Cross-sectional ABF-STEM image and 2D projection of the structural model (dotted black line represents unit cell edges) along the (c) [1 -1 2] and (d) [1 1 1] zone axes of a ultramicrotomed FCC phase superlattice. (e) The boxed region of a low-magnification ABF-STEM image (left) was Fourier-transformed to yield a diffractogram (right).

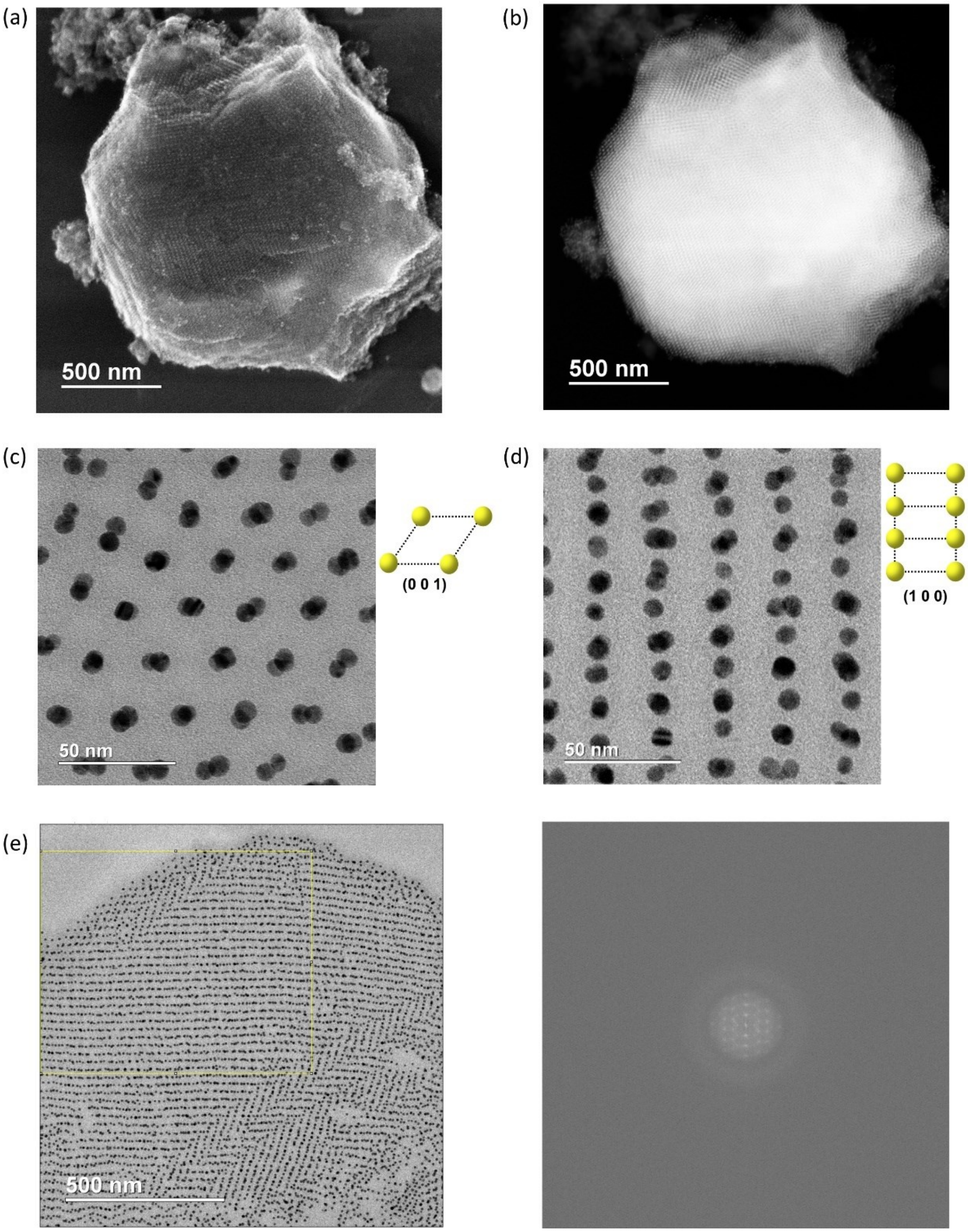

Figure A2.9. STEM characterization – simple hexagonal (SH)
(a) Representative SE-STEM and (b) ADF-STEM images of a SH phase crystal after silica encapsulation. The shape of the crystal is roughly hexagonal as the SH phase has multiple lattice planes with hexagonal patterns. Cross-sectional ABF-STEM image and 2D projection of the structural model (dotted black line represents unit cell edges) along the (c) [0 0 1] and (d) [1 0 0] zone axes of a ultramicrotomed SH phase superlattice. (e) The boxed region of a low-magnification ABF-STEM image (left) was Fourier-transformed to yield a diffractogram (right).

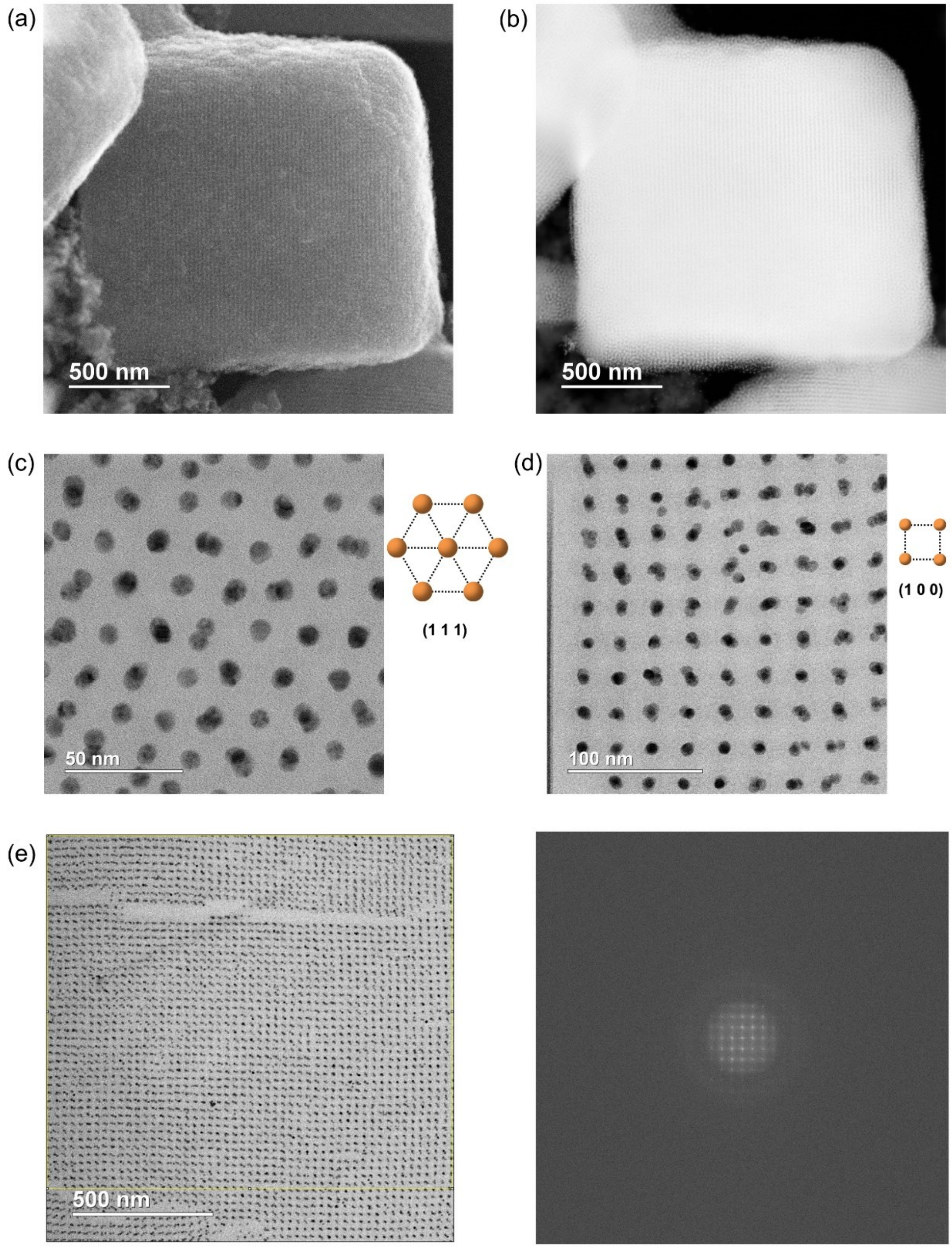

Figure A2.10. STEM characterization – simple cubic (SC)
(a) Representative SE-STEM and (b) ADF-STEM images of a SC phase crystal after silica encapsulation. The cubic shape of the crystal reflects its simple cubic symmetry. Cross-sectional ABF-STEM image and 2D projection of the structural model (dotted black line represents unit cell edges) along the (c) [1 1 1] and (d) [1 0 0] zone axes of a ultramicrotomed SC phase superlattice. (e) The boxed region of a low-magnification ABF-STEM image (left) was Fourier-transformed to yield a diffractogram (right).

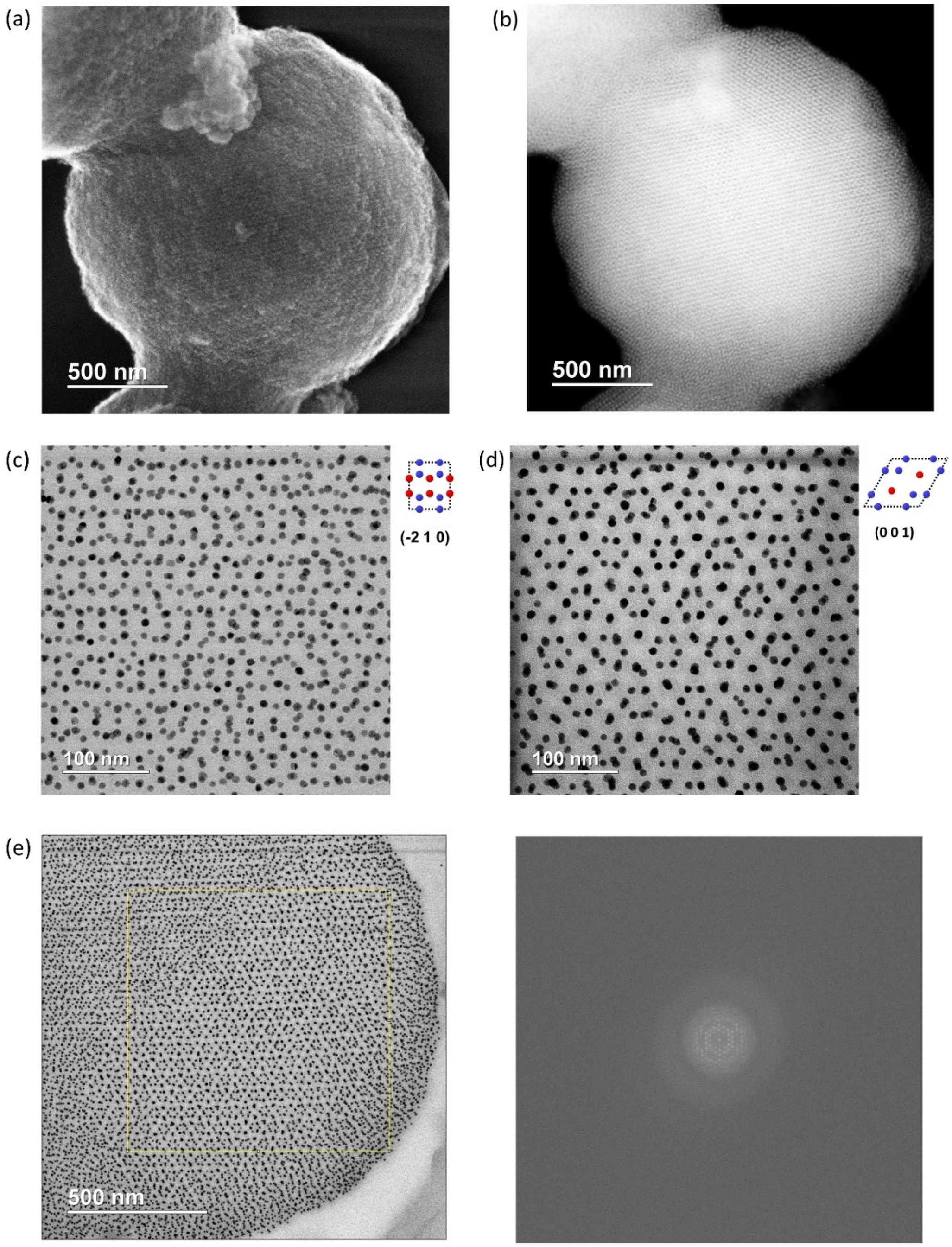

Figure A2.11. STEM characterization – Ti_5Ga_4-type

(a) Representative SE-STEM and (b) ADF-STEM images after silica encapsulation of a Ti5Ga4-type phase crystal. Due to the Ti5Ga4-type phase's low symmetry, the crystals do not present any particular low-energy facets and thus grow to form non-faceted, spherical micro-crystallites. Cross-sectional ABF-STEM image and 2D projection of the structural model (red: 4d, blue: 6g, dotted black line represents unit cell edges) along the (c) [-2 1 0] and (d) [0 0 1] zone axes of a ultramicrotomed Ti5Ga4-type phase superlattice. (e) The boxed region of a low-magnification ABF-STEM image (left) was Fourier-transformed to yield a diffractogram (right).

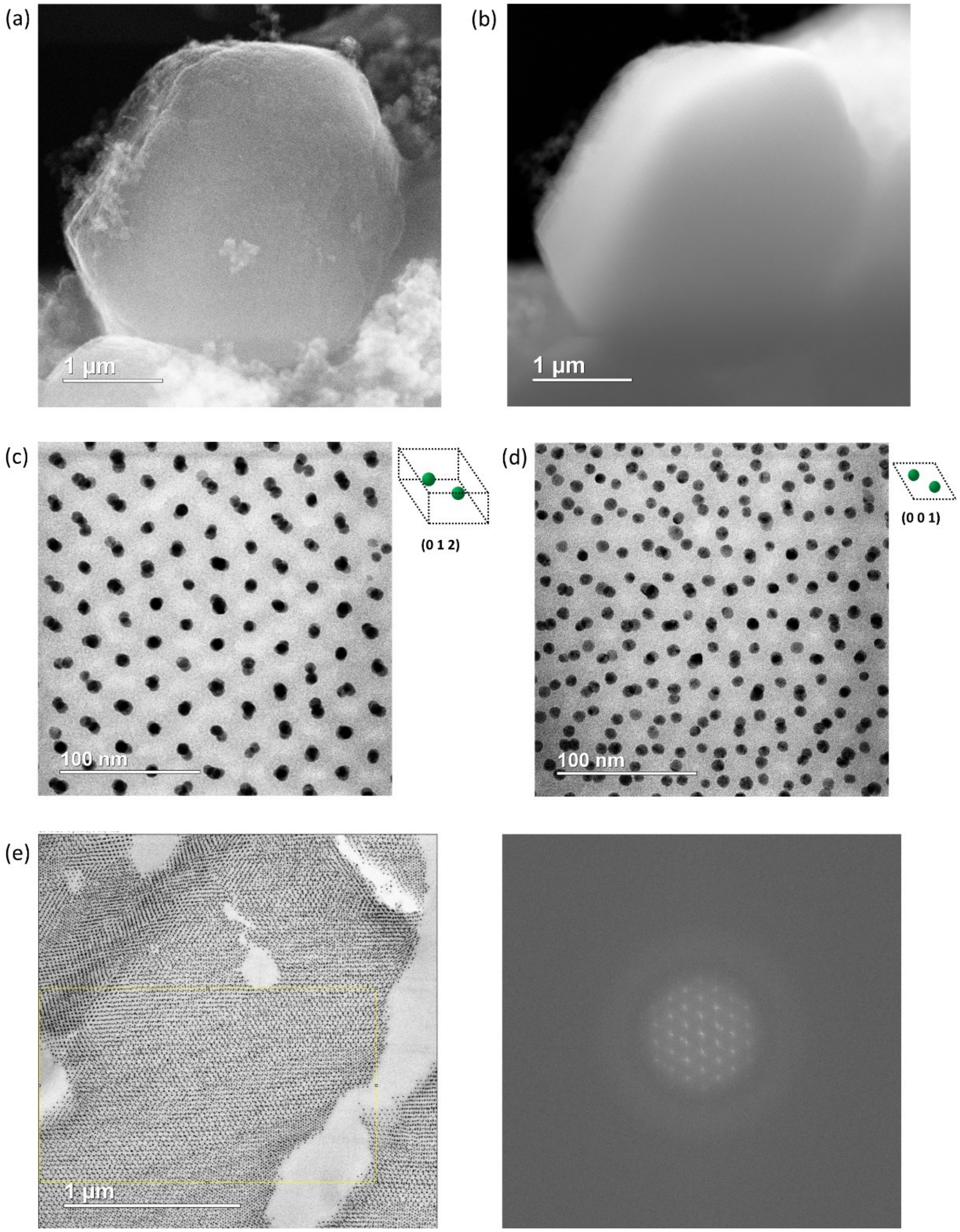

Figure A2.12. STEM characterization – Graphite type (GT)
(a) Representative SE-STEM and (b) ADF-STEM images of a GT phase crystal after silica encapsulation. The shape of the crystal is roughly hexagonal as the GT phase has multiple lattice planes with hexagonal patterns. Cross-sectional ABF-STEM image and 2D projection of the structural model (dotted black line represents unit cell edges) along the (c) [0 1 2] and (d) [0 0 1] zone axes of a ultramicrotomed GT phase superlattice. (e) The boxed region of a low-magnification ABF-STEM image (left) was Fourier-transformed to yield a diffractogram (right).

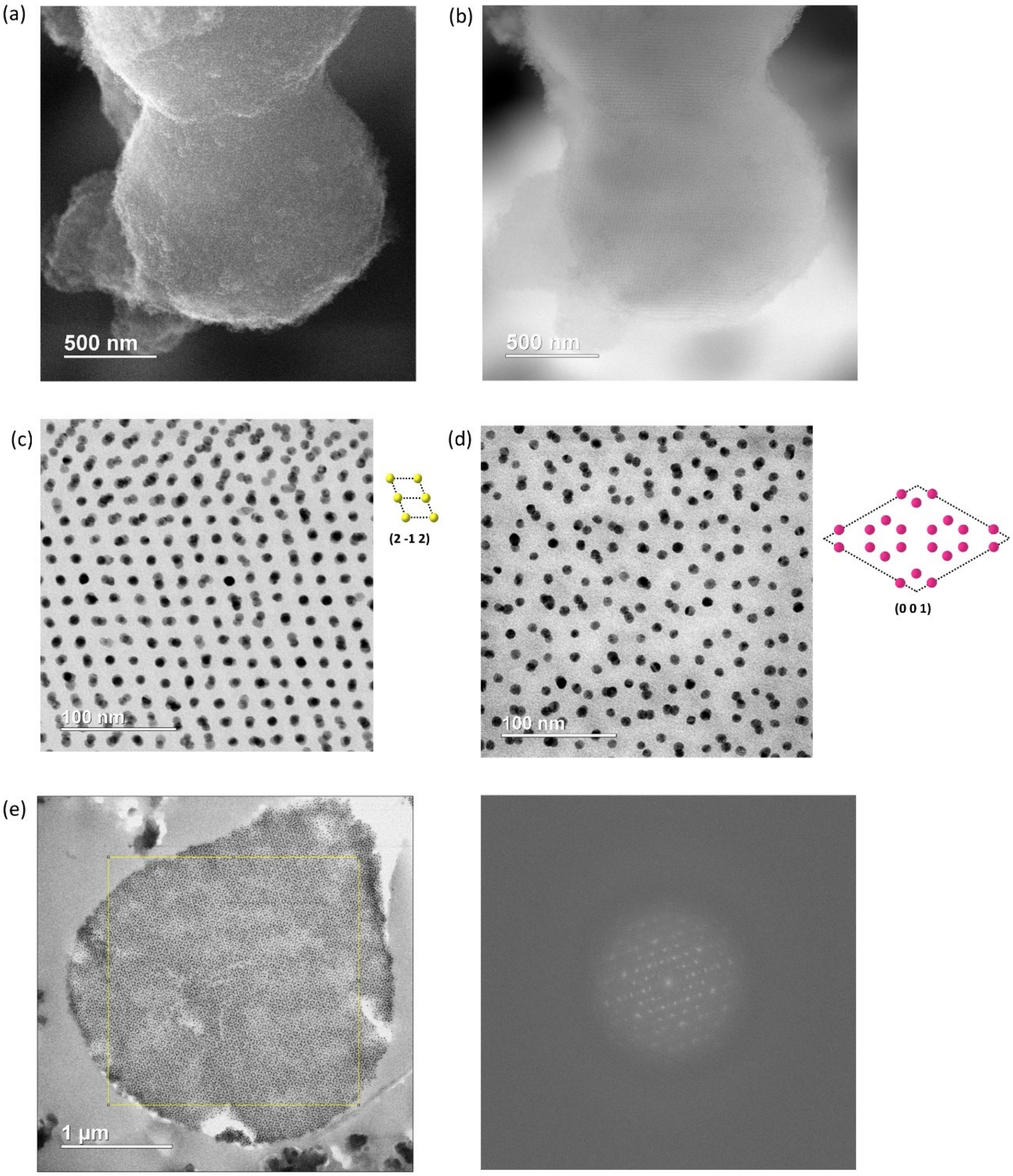

Figure A2.13. STEM characterization – Partially disordered R-3*m* phase
(a) Representative SE-STEM and (b) ADF-STEM images of the partially disordered R-3m phase crystals after silica encapsulation. Due to R-3m's low symmetry, the crystals do not present any particular low-energy facets and thus grow to form non-faceted, spherical micro-crystallites. The colloidal crystal sample is comprised of nanoparticle superlattices in SH and partially disordered R-3m phases. Cross-sectional ABF-STEM image and 2D projection of the structural model (dotted black line represents unit cell edges) along the (c) [2 -1 2] zone axis of a ultramicrotomed SH phase superlattice and (d) along the [0 0 1] zone axis of a ultramicrotomed R-3mphase superlattice. (e) The boxed region of a low-magnification ABF-STEM image (left) was Fourier-transformed to yield a diffractogram (right).